

5-2018

Modeling and Mitigation of Wireless Communications Interference for Spectrum Sharing with Radar

David P. Zilz
Purdue University

Follow this and additional works at: https://docs.lib.purdue.edu/open_access_dissertations

Recommended Citation

Zilz, David P., "Modeling and Mitigation of Wireless Communications Interference for Spectrum Sharing with Radar" (2018). *Open Access Dissertations*. 1858.
https://docs.lib.purdue.edu/open_access_dissertations/1858

This document has been made available through Purdue e-Pubs, a service of the Purdue University Libraries.
Please contact epubs@purdue.edu for additional information.

MODELING AND MITIGATION OF WIRELESS COMMUNICATIONS
INTERFERENCE FOR SPECTRUM SHARING WITH RADAR

A Dissertation

Submitted to the Faculty

of

Purdue University

by

David P. Zilz

In Partial Fulfillment of the

Requirements for the Degree

of

Doctor of Philosophy

May 2018

Purdue University

West Lafayette, Indiana

THE PURDUE UNIVERSITY GRADUATE SCHOOL
STATEMENT OF COMMITTEE APPROVAL

Dr. Mark R. Bell, Chair

Department of Electrical and Computer Engineering

Dr. Charles A. Bouman

Department of Electrical and Computer Engineering

Dr. David J. Love

Department of Electrical and Computer Engineering

Dr. James V. Krogmeier

Department of Electrical and Computer Engineering

Dr. Michael D. Zoltowski

Department of Electrical and Computer Engineering

Approved by:

Dr. Venkataramanan Balakrishnan

Head of the Graduate Program

ACKNOWLEDGMENTS

The author would like to acknowledge and thank the many people who contributed to this dissertation. First, the author cannot thank enough Professor Mark Bell of Purdue University for his invaluable guidance and encouragement as doctoral advisor. The author also thanks the rest his doctoral committee, consisting of Professors Charles Bouman, James Krogmeier, David Love, and Michael Zoltowski of Purdue University, for their contributions to this project.

This dissertation constitutes part of a larger team effort on a National Science Foundation grant. The author thanks Narueporn Nartasilpa, Sara Shahi, Ahmad Salim, Professor Daniela Tuninetti, Professor Natasha Devroye, and Professor Danilo Erricolo of the University of Illinois, Chicago, for their collaboration on this project and on the summary report [1]. This work was supported by the National Science Foundation under the Enhancing Access to Radio Spectrum (EARS) program, 1443971-EECS-Grant 107277. The contents of this article are solely the responsibility of the author (and the other authors of the related publications in the open literature) and do not necessarily represent the official views of the NSF.

Several people contributed to the work in Chapter 2. Dr. Muralidhar Rangaswamy and his research team at the Air Force Research Laboratory provided helpful constructive criticisms and suggestions, as did the anonymous reviewers of [2], significantly enhancing the quality of presentation. Tracy Mavity facilitated the online publishing of the contents of Appendix C [3].

A key insight in Chapter 3 was provided by Professors David Gleich and Michael Zoltowski of Purdue University, suggesting the use a generalized eigendecomposition to jointly diagonalize $\tilde{\mathbf{G}}(f)$ and $\tilde{\mathbf{E}}^{-1}(f)$ in Theorem 7 [4].

Finally, significant computational resources were required to perform the analysis in this dissertation. The author owes deep gratitude to Professor James Krogmeier,

Professor David Love, Stephen Larew, Dennis Ogbe, and the rest of the Flexible and Efficient Spectrum Usage Preeminent Team at Purdue University for their help with computational resources. In addition, most of this work was completed using open-source scientific computing software, such as the Julia programming language [5] and its packages (*e.g.*, [6–15]), as well as Python and several of its scientific computing packages (*e.g.*, [16–20]).

TABLE OF CONTENTS

	Page
LIST OF FIGURES	vii
ABBREVIATIONS	xi
ABSTRACT	xiii
1 INTRODUCTION	1
1.1 Motivation	1
1.2 Previous work	4
1.2.1 Research Direction 1: Transmit scheduling and power control . .	5
1.2.2 Research Direction 2: Waveform design	6
1.2.3 Research Direction 3: Receiver design	7
1.2.4 Research Direction 4: Upper and lower joint performance bounds	8
1.2.5 Summary of previous work	8
1.3 Contributions	9
1.3.1 Chapter 2: Modeling communications interference and its ef-	
fects on radar	9
1.3.2 Chapter 3: Mitigating communications interference to radar via	
signal processing	11
1.4 Summary	12
2 STATISTICAL MODELING OF WIRELESS COMMUNICATIONS INTER-	
FERENCE AND ITS EFFECTS ON ADAPTIVE-THRESHOLD RADAR	
DETECTION	14
2.1 Introduction	14
2.1.1 Motivation	14
2.1.2 Overview	15
2.2 Statistical models of wireless interference	16
2.2.1 Theoretical models in the literature	16

	Page
2.2.2 An empirical investigation of interference statistics	18
2.2.3 Conclusions and proposed interference model	28
2.3 Effects of interference on radar: Analysis	30
2.3.1 Model	30
2.3.2 Mathematical preliminaries	36
2.3.3 ROC equations for fixed-threshold detector	43
2.3.4 ROC equations for cell-averaging adaptive-threshold detector . .	45
2.4 Effects of interference on radar: Results	49
2.4.1 Effects of non-Gaussian statistical behavior	49
2.4.2 Effects of changing INR	54
2.5 Conclusions	55
3 OPTIMAL LINEAR DETECTION OF SIGNALS IN CYCLOSTATION- ARY, LINEARLY-MODULATED, DIGITAL COMMUNICATIONS INTER- FERENCE	59
3.1 Introduction	59
3.1.1 Motivation	59
3.1.2 Overview	60
3.2 Linear whitening of stationary LMDC interference	61
3.3 Linear whitening of cyclostationary LMDC interference	63
3.3.1 Pulse-shape synchronized case	63
3.3.2 Asynchronous case	72
3.3.3 Representation of whitener as FRESH filter	90
3.3.4 Extension of whitener to a mixture of stationary and cyclosta- tionary LMDC interference	94
3.4 Performance analysis	95
3.4.1 Theoretical analysis of deflection	96
3.4.2 Statistical models for LMDC parameters	98
3.4.3 Method of evaluating expectation in (3.107)	99
3.4.4 Choice of waveforms	100

	Page
3.4.5 Implementation of whiteners	100
3.4.6 Results	101
3.5 Conclusions	105
4 CONCLUSIONS	107
4.1 Summary of contributions	107
4.2 Connections between Chapters 2–3	108
4.3 Directions for future work	110
REFERENCES	111
A Practical considerations in numerical integration	119
B Agreement of Monte Carlo simulation with numerical integration	121
C Full set of calculated P_{FA} and P_{D} for fixed-threshold radar detector and cell-averaging adaptive-threshold radar detector	123
D Understanding the ROC crossing caused by slow interference	157
E Detailed derivation from the development of the cyclostationary LMDC whitener	160
F Proof on positive semidefiniteness	162
G Monte Carlo validation of whiteners	165
VITA	171

LIST OF FIGURES

Figure	Page
1.1 United States Frequency Allocation Chart. Available on NTIA's website at ntia.gov . This chart is current as of February 2018.	2
2.1 Simulation results for single-user OFDM with slow, Rician multipath fading. (a) The CDFs in (a) are of $n_s = 10^3$ i.i.d. realizations of A_I for one of a total of 48 simulations. (b)–(d) The empirical CDFs in (b)–(d) are of the goodness-of-approximation metrics d_{KS} , ρ_{kurt} , and κ_{model} , κ_{emp} for the entire population of 48 simulations.	25
2.2 Simulation results for multiple OFDM users transmitting with slow Rayleigh fading from random locations. (a) The CDFs in (a) are of $n_s = 10^3$ i.i.d. realizations of A_I for one of a total of 12 simulations. (b)–(d) The results in (b)–(d) are kurtoses κ_{model} , κ_{emp} for 12 different simulations. (Note: Due to very heavy algebraic tails in the above simulations, the fitted Student- t model often has an undefined kurtosis.)	27
2.3 Block diagram for radar receiver	31
2.4 Block diagram for cell-averaging adaptive-threshold decision rule	34
2.5 ROCs for both detectors under impulsive and heavy-tailed interference. . .	50
2.6 Rare crossing of non-Gaussian and Gaussian ROCs, for the case of slow, impulsive interference	54
2.7 Radar P_D and P_{FA} versus INR for the case of the cell-averaging processor with 27 cells, slow Gaussian (Rayleigh) interference, a fixed threshold scalar τ , and SNR = 17 dB.	56
3.1 Interpretation of the cyclostationary whitener of Theorem 7 as the <i>form</i> of a multiuser detector followed by an interference canceler, cf [94, p. 235, 244, 295].	88
3.2 FRESH filter implementation of the cyclostationary whitener of Theorem 7. A FRESH filter essentially consists of a bank of frequency shifters followed by LTI filters.	93

Figure	Page
3.3	Estimated deflection (output SINR) \hat{d}_s and \hat{d}_c versus input INR, for $s(t)$ having time-bandwidth product $\Pi = 100$. (a) $N = 1$ and $g(t) = g_1(t)$ (half-sine pulse shape). (b) $N = 1$ and $g(t) = g_2(t)$ (half-cosine pulse shape). (c) $N = 2$ and $g(t) = g_1(t)$ (half-sine pulse shape). (d) $N = 2$ and $g(t) = g_2(t)$ (half-cosine pulse shape). (e) $N = 3$ and $g(t) = g_1(t)$ (half-sine pulse shape). (f) $N = 3$ and $g(t) = g_2(t)$ (half-cosine pulse shape).102
3.4	Estimated deflection (output SINR) \hat{d}_s and \hat{d}_c versus input INR, for $s(t)$ having time-bandwidth product $\Pi = 50$. (a) $N = 1$ and $g(t) = g_1(t)$ (half-sine pulse shape). (b) $N = 1$ and $g(t) = g_2(t)$ (half-cosine pulse shape). (c) $N = 2$ and $g(t) = g_1(t)$ (half-sine pulse shape). (d) $N = 2$ and $g(t) = g_2(t)$ (half-cosine pulse shape). (e) $N = 3$ and $g(t) = g_1(t)$ (half-sine pulse shape). (f) $N = 3$ and $g(t) = g_2(t)$ (half-cosine pulse shape).103
B.1	Z-scores of Monte Carlo estimates of P_{FA} and P_D , assuming the values for P_{FA} and P_D obtained by numerical integration are correct. Six values of z_{P_D} are not computable since the corresponding numerically integrated values of P_D are barely greater than unity, by a negligible amount that is consistent with the Monte Carlo estimates (which are unity or barely less than unity) and do not affect conclusions drawn by the ROC plots. . . . 121
C.1	ROCs for fixed-threshold test with impulsive interference (INR = -10 dB; SNR = 0, 5, 10, 15 dB) 124
C.2	ROCs for fixed-threshold test with impulsive interference (INR = -5 dB; SNR = 0, 5, 10, 15 dB) 125
C.3	ROCs for fixed-threshold test with impulsive interference (INR = 0 dB; SNR = 0, 5, 10, 15 dB) 126
C.4	ROCs for fixed-threshold test with impulsive interference (INR = 5 dB; SNR = 0, 5, 10, 15 dB) 127
C.5	ROCs for fixed-threshold test with heavy-tailed interference (INR = -10 dB; SNR = 0, 5, 10, 15 dB) 128
C.6	ROCs for fixed-threshold test with heavy-tailed interference (INR = -5 dB; SNR = 0, 5, 10, 15 dB) 129
C.7	ROCs for fixed-threshold test with heavy-tailed interference (INR = 0 dB; SNR = 0, 5, 10, 15 dB) 130
C.8	ROCs for fixed-threshold test with heavy-tailed interference (INR = 5 dB; SNR = 0, 5, 10, 15 dB) 131
C.9	ROCs for cell-averaging processor with “fast,” impulsive interference (INR = -10 dB; SNR = 0, 5, 10, 15 dB) 132

Figure	Page
C.10 ROCs for cell-averaging processor with “fast,” impulsive interference (INR = -5 dB; SNR = 0, 5, 10, 15 dB)	133
C.11 ROCs for cell-averaging processor with “fast,” impulsive interference (INR = 0 dB; SNR = 0, 5, 10, 15 dB)	134
C.12 ROCs for cell-averaging processor with “fast,” impulsive interference (INR = 5 dB; SNR = 0, 5, 10, 15 dB)	135
C.13 ROCs for cell-averaging processor with “fast,” heavy-tailed interference (INR = -10 dB; SNR = 0, 5, 10, 15 dB)	136
C.14 ROCs for cell-averaging processor with “fast,” heavy-tailed interference (INR = -5 dB; SNR = 0, 5, 10, 15 dB)	137
C.15 ROCs for cell-averaging processor with “fast,” heavy-tailed interference (INR = 0 dB; SNR = 0, 5, 10, 15 dB)	138
C.16 ROCs for cell-averaging processor with “fast,” heavy-tailed interference (INR = 5 dB; SNR = 0, 5, 10, 15 dB)	139
C.17 ROCs for cell-averaging processor with “slow,” impulsive interference (INR = -10 dB; SNR = 0, 5, 10, 15 dB)	140
C.18 ROCs for cell-averaging processor with “slow,” impulsive interference (INR = -5 dB; SNR = 0, 5, 10, 15 dB)	141
C.19 ROCs for cell-averaging processor with “slow,” impulsive interference (INR = 0 dB; SNR = 0, 5, 10, 15 dB)	142
C.20 ROCs for cell-averaging processor with “slow,” impulsive interference (INR = 5 dB; SNR = 0, 5, 10, 15 dB)	143
C.21 ROCs for cell-averaging processor with “slow,” heavy-tailed interference (INR = -10 dB; SNR = 0, 5, 10, 15 dB)	144
C.22 ROCs for cell-averaging processor with “slow,” heavy-tailed interference (INR = -5 dB; SNR = 0, 5, 10, 15 dB)	145
C.23 ROCs for cell-averaging processor with “slow,” heavy-tailed interference (INR = 0 dB; SNR = 0, 5, 10, 15 dB)	146
C.24 ROCs for cell-averaging processor with “slow,” heavy-tailed interference (INR = 5 dB; SNR = 0, 5, 10, 15 dB)	147
C.25 P_D and P_{FA} versus INR for fixed-threshold test (SNR = 5, 10, 15, 20 dB, baseline $P_{FA} = 10^{-4}$)	148
C.26 P_D and P_{FA} versus INR for fixed-threshold test (SNR = 5, 10, 15, 20 dB, baseline $P_{FA} = 10^{-8}$)	149

Figure	Page
C.27 P_D and P_{FA} versus INR for fixed threshold test (SNR = 5, 10, 15, 20 dB, baseline $P_{FA} = 10^{-12}$)	150
C.28 P_D and P_{FA} versus INR for cell-averaging processor with “fast” interference (SNR = 5, 10, 15, 20 dB, baseline $P_{FA} = 10^{-4}$)	151
C.29 P_D and P_{FA} versus INR for cell-averaging processor with “fast” interference (SNR = 5, 10, 15, 20 dB, baseline $P_{FA} = 10^{-8}$)	152
C.30 P_D and P_{FA} versus INR for cell-averaging processor with “fast” interference (SNR = 5, 10, 15, 20 dB, baseline $P_{FA} = 10^{-12}$)	153
C.31 P_D and P_{FA} versus INR for cell-averaging processor with “slow” interference (SNR = 5, 10, 15, 20 dB, baseline $P_{FA} = 10^{-4}$)	154
C.32 P_D and P_{FA} versus INR for cell-averaging processor with “slow” interference (SNR = 5, 10, 15, 20 dB, baseline $P_{FA} = 10^{-8}$)	155
C.33 P_D and P_{FA} versus INR for cell-averaging processor with “slow” interference (SNR = 5, 10, 15, 20 dB, baseline $P_{FA} = 10^{-12}$)	156
D.1 Diagram explaining the crossing of the ROCs in Figure 2.6 for Gaussian versus impulsive interference, for the case of the cell-averaging processor with slow interference.	157
D.2 The distributions under H_1 (top) and H_0 (bottom) of many i.i.d. samples of $ X ^2$ and Z for the cell-averaging processor with slow interference. The top figure corresponds to the qualitative description of Figure D.1.	158
G.1 Empirical cumulative distribution functions (CDFs) of whiteness measures for Figure 3.3. (a) $\{p_{s,\ell}\}_{\ell=1}^{L'}$ and $\{p_{c,\ell}\}_{\ell=1}^{L'}$ for INRs of 0, 10, 20, and 30 dB. (b) $\{\nu_{s,\ell}\}_{\ell=1}^{L'}$ and $\{\nu_{c,\ell}\}_{\ell=1}^{L'}$ for INRs of 0, 10, 20, and 30 dB, along with the reference set $\{\nu_{\text{ref},\ell}\}_{\ell=1}^{L''}$	169
G.2 Empirical cumulative distribution functions (CDFs) of whiteness measures for Figure 3.4. (a) $\{p_{s,\ell}\}_{\ell=1}^{L'}$ and $\{p_{c,\ell}\}_{\ell=1}^{L'}$ for INRs of 0, 10, 20, and 30 dB. (b) $\{\nu_{s,\ell}\}_{\ell=1}^{L'}$ and $\{\nu_{c,\ell}\}_{\ell=1}^{L'}$ for INRs of 0, 10, 20, and 30 dB, along with the reference set $\{\nu_{\text{ref},\ell}\}_{\ell=1}^{L''}$	170

ABBREVIATIONS

AWGN	Additive White Gaussian Noise
AWS	Advanced Wireless Services
C-AWGN	Circularly-Symmetric, Complex-Valued Additive White Gaussian Noise
CBRS	Citizens Broadband Radio Service
cdf	Cumulative Distribution Function
CDMA	Code Division Multiple Access
CFAR	Constant False Alarm Rate
CLT	Central Limit Theorem
CUT	Cell Under Test
DFT	Discrete Fourier Transform
FCC	Federal Communications Commission
FDMA	Frequency Division Multiple Access
FFT	Fast Fourier Transform
FRESH	Frequency-Shift
i.i.d.	Independent, Identically Distributed
INR	Interference-to-Noise Ratio
LFM	Linear Frequency Modulation
LMDC	Linearly Modulated Digital Communications
LPTV	Linear, Periodically Time-Varying
LTI	Linear, Time-Invariant
LTV	Linear, Time-Varying
MAC	Multiple Access Channel
MIMO	Multiple-Input, Multiple-Output

NTIA	National Telecommunications and Information Administration
OFDM	Orthogonal Frequency Division Multiplexing
PAM	Pulse Amplitude Modulation
pdf	Probability Density Function
QAM	Quadrature Amplitude Modulation
QPSK	Quadrature Phase Shift Keying
RF	Radio Frequency
ROC	Receiver Operating Characteristic
SINR	Signal-to-Interference-Plus-Noise Ratio
SIRV	Spherically Invariant Random Vector
SNR	Signal-to-Noise Ratio
TDMA	Time Division Multiple Access
VoIP	Voice over Internet Protocol

ABSTRACT

Zilz, David P. Ph.D., Purdue University, May 2018. Modeling and Mitigation of Wireless Communications Interference for Spectrum Sharing with Radar. Major Professor: Mark R. Bell.

Due to both economic incentives and policy mandates, researchers increasingly face the challenge of enabling spectrum sharing between radar and wireless communications systems. In the past eight years, researchers have begun to suggest a wide variety of approaches to radar-communications spectrum sharing, ranging from transmitter design to receiver design, from spatial to temporal to other-dimensional multiplexing, and from cooperative to non-cooperative sharing. Within this diverse field of innovation, this dissertation makes two primary contributions. First, a model for wireless communications interference and its effects on adaptive-threshold radar detection is proposed. Based on both theoretical and empirical study, we find evidence for both Gaussian and non-Gaussian communications interference models, depending on the modeling situation. Further, such interference can impact radar receivers via two mechanisms—model mismatch and boost to the underlying noise floor—and both mechanisms deserve attention. Second, an innovative signal processing algorithm is proposed for radar detection in the presence of cyclostationary, linearly-modulated, digital communications (LMDC) interference (such as OFDM or CDMA) and a stationary background component. The proposed detector consists of a novel whitening filter followed by the traditional matched filter. Performance results indicate that the proposed cyclostationary-based detector outperforms a standard equivalent detector based on a stationary interference model, particularly when the number of cyclostationary LMDC transmitters is small and their interference-to-noise ratio (INR) is large relative to the stationary background.

1. INTRODUCTION

1.1 Motivation

As growing numbers of wireless devices and networks crowd a finite radio frequency (RF) spectrum [21,22] (*cf.* Figure 1.1), researchers and policy makers seek innovative ways to use the spectrum more efficiently. Proposed solutions to spectrum scarcity include cognitive radio [23–25], small cells [26,27], massive multiple-input multiple-output (MIMO) antenna arrays [28–32], millimeter-wave communications [33–35], and spectrum sharing between different types of RF systems. Within the latter category, policy changes have already begun to form in U.S. policy calling for spectrum sharing between commercial wireless and government systems, including radar. Together, these economic drivers and policy trends motivate research into radar-communications spectrum sharing.

A major effort at spectrum sharing between commercial wireless and government systems began in 2010, when the President of the United States issued a memorandum directing that 500 MHz of electromagnetic spectrum be made available for wireless broadband use over the subsequent 10 years [36]. In addition, the President directed steps to facilitate research on “innovative spectrum-sharing technologies, including those that are secure and resilient.” Three years later, the President issued a further memorandum praising existing efforts which would “almost double the amount of spectrum available for wireless broadband,” and yet the President called for even more spectrum to be made available [37]. Among other measures, the latter memorandum encouraged the sharing of federally used spectrum—“subject to adequate interference protection for [f]ederal users, especially users with national security, law enforcement, and safety-of-life responsibilities.”

[illegible]

2

Following these presidential memoranda, U.S. policies have already been implemented requiring forms of spectrum sharing between commercial and government systems [38–42] (*cf.* [43]). For example, in 2014 the FCC made 65 MHz of additional spectrum available to commercial wireless use in the 1695–1710 MHz, 1755–1780 MHz, and 2155–2180 MHz frequency bands, naming these frequency bands “Advanced Wireless Services 3” (AWS-3). Within the AWS-3 bands, 40 MHz was “made available for commercial use pursuant to collaboration among the wireless industry and [f]ederal agencies,” as several government agencies had incumbent access to this portion of the spectrum. Although many of the incumbent government systems had plans to relocate out of the AWS-3 bands, a few intended to remain indefinitely, necessitating some form of spectrum sharing [39, 40].

Another new policy aimed at spectrum sharing was adopted in 2015, when the FCC opened the 3550–3700 MHz frequency band, which historically has been used by several military radar systems, to commercial use as a “Commercial Broadband Radio Service” (CBRS) [41]. The CBRS establishes a three-tier system of spectrum access in the 3.5-GHz band, consisting of an Incumbent tier (which includes government radar systems), a Priority Access tier, and a General Authorized Access tier. As stated in the general rules of the newly adopted Part 96, “Priority Access ... and General Authorized Access users must not cause harmful interference to Incumbent users and must accept interference from Incumbent users[;] General Authorized Access users must not cause harmful interference to Priority Access [users] and must accept interference from [them]” [41]. The lower two tiers must register with a Spectrum Access System, a database which controls access to the spectrum in a coordinated manner. Protection for Incumbent users is accomplished via geographic exclusion zones within which lower-tier users may not access the CBRS band. For example, shipborne radars are protected from interference through the enforcement of exclusion zones along the coasts of the continental United States. Although initial exclusion zone proposals assumed that lower-tier users would be deployed in macro-cell networks, by changing to a small cell specification, the exclusion zones were reduced significantly in size [42].

The FCC rules also allow for potential lower-tier operation within the exclusion zones in the future, but such operation would be conditioned on a suitable spectrum sensing system reliably determining that no Incumbent users would be negatively impacted by such lower-tier operation [41]. Thus, the 3.5-GHz CBRS incorporates several innovative spectrum management approaches, including the use of spectrum sensing, database-driven spectrum access, and spectrum sharing between commercial wireless systems and government systems including radar.

When spectrum policy changes to allow new users into a frequency band, the incumbent users must either relocate to a new band or find some way of coexisting with the new users. Many radar systems are constrained by various engineering objectives in the frequencies at which they perform well (*cf.* [44]), and so when wireless communications systems gain licenses to use the radars' spectral allocations, it may become necessary for such radar systems to share spectrum. Such sharing must simultaneously satisfy the engineering requirements of both the radar and the wireless communications systems.

Thus, due to both economic incentives and public policy mandates, radar and wireless communications systems are finding increasing impetus to share spectrum effectively. This is a relatively new application in asymmetric multiple access and presents interesting challenges and exciting opportunities to RF engineers.

1.2 Previous work

In order for radar and wireless communications systems to share spectrum effectively, both systems must transmit and receive signals in a manner that minimizes the negative effects of interference from each system to the other. This constitutes a type of multiple access in that both radar and communications users desire to use a common wireless channel simultaneously; however, in contrast to more familiar multiple access scenarios, such as multi-user cellular communications, the radar-communications problem involves *asymmetric* multiple access.

Because the design objectives of radar and communications are very different—sensing on the one hand, and point-to-point transmission of information on the other—the signals and signal processing which optimize the performance of either system tend to look very different from each other. For example, radar systems often use linear frequency modulated (LFM) signals because of their ease of pulse compression, Doppler tolerance, and constant modulus (which is important for energy efficiency in high-power amplifiers); broadband communications systems, on the other hand, often use orthogonal frequency division multiplexing (OFDM) signals in order to achieve frequency diversity and high data rates. Just as different engineering objectives historically have resulted in different designs for radar and communications systems that are spectrally separated, it is likely that this asymmetry similarly will carry over to radar and communications systems that share a common frequency band.

Whereas the design and optimization of radar and communications *separately* has reached a fair level of maturity, the *joint* design and optimization of radar and communications signals and systems is a relatively new application. As such, one could get the impression that approaches to the radar-communications spectrum sharing problem are diverse to the extent of seeming *ad hoc* at times; a systematic strategy for spectrum sharing has yet to emerge in the literature. Nevertheless, four general categories of spectrum sharing research seem to exist in the literature, and this section outlines these in order to place this dissertation in the context of existing work.

1.2.1 Research Direction 1: Transmit scheduling and power control

The first approach for achieving radar-communications spectrum sharing uses transmit scheduling and power control to limit interference from one system to the other [42, 45–51]. The recent adoption of the CBRS in the 3.5-GHz band is an example of this type of radar-communications spectrum sharing [41]. Often this approach uses a primary-secondary strategy, in which the radar (or communications) systems

are granted primary and unlimited access to a given spectrum band, and the communications (or radar) systems are granted secondary access to that band, on the condition that they do not unacceptably interfere with the primary systems. By properly scheduling their transmissions in time and space and/or controlling their transmitted power, the secondary users avoid harmful interference to the primary users. For example, [45] examines a situation in which communications devices share spectrum as secondary users with a rotating radar as a primary user, with secondary users restricted to a maximum level of interference to radar. By evaluating quality of service metrics, the authors of [45] find that applications such as non-interactive video on demand, peer-to-peer file sharing, file transfers, automatic meter reading, and web browsing could potentially operate successfully in this type of shared spectrum, while applications such as real-time transfers of small files and voice over internet protocol (VoIP) are less suited to this type of spectrum sharing. Similarly, the authors of [47] investigate primary-secondary sharing between a rotating radar and WiFi devices, and they compute geographic protection zones required to prevent unacceptably harmful interference to the primary, radar users. In [49], the authors propose signal processing techniques to enable secondary users to transmit opportunistically when primary, rotating radar systems are directed away from them. Other issues involved in this kind of primary-secondary spectrum sharing involve methods by which opportunities for secondary transmission (“white spaces”) are detected, and methods of protecting the primary users’ operational privacy when information about the primary users (*e.g.*, locations of military radars) requires some level of secrecy; these applications are considered in [50] and [51], respectively.

1.2.2 Research Direction 2: Waveform design

While the first approach to spectrum sharing uses transmit scheduling and power control to limit interference between radar and communications systems, the second approach makes fundamental changes to the transmitted radar and communications

waveforms in order to enhance each system’s performance and/or reduce interference from one system to the other. [52–57]. For example, [53] considers the joint design of radar and communications waveforms as a resource allocation problem. Specifically, the authors of [53] discuss the problem of allocating a finite set of signal basis functions (OFDM subcarriers, in this particular paper) to the two modalities of radar and communications. Since each basis function is assumed to be used for either radar or communications (but not both) in this paper, the joint allocation involves an inherent trade-off between radar performance and communications performance. After observing that brute-force computation of a Pareto-optimal basis allocation has exponential computational complexity, the authors of [53] propose two intuitive, iterative algorithms that assign basis functions one at a time to either modality. Other waveform design approaches also have been proposed in the literature. For example, the authors of [55], citing [58], use water-filling in the frequency domain to design radar waveforms in the presence of legacy communications systems such that the effects of harmful interference to and from the communications systems are reduced. Alternatively, [56] proposes a MIMO technique for transmitting radar and communications signals simultaneously from a single transmit array. The proposed signaling strategy transmits radar signals in the array main lobe while using side lobe control and waveform diversity to communicate a stream of data bits to communications receivers located in the side lobes of the array.

1.2.3 Research Direction 3: Receiver design

While the first and second approaches to radar-communications spectrum sharing address the transmit side of the problem through transmit scheduling, power control, and waveform design, the third approach examines the receive side of the problem by designing signal processing algorithms that mitigate interference [57, 59–61]. For example, radar signal processing is proposed in [59, 60] that uses spatial filtering to suppress interference from a certain class of wireless interference in both the main

and side lobes of a MIMO radar receiver. Conversely, [61] derives optimal and approximately optimal detectors of communications symbols in the presence of radar interference.

1.2.4 Research Direction 4: Upper and lower joint performance bounds

Finally, in addition to the above three technical approaches to radar-communications spectrum sharing, another research direction investigates performance bounds on radar-communications spectrum sharing. Two types of performance bounds have been proposed in the literature—baseline “lower” bounds, and information-theoretic “upper” bounds. Baseline bounds investigate the performance of legacy radar and communications systems that share spectrum without modifying their transmitter or receiver designs [1]; as such, these constitute “lower” performance bounds in that the radar and communications systems can hopefully improve in performance as they are modified to facilitate spectrum sharing. On the other hand, information-theoretic bounds establish upper limits of the joint performance of radar and communications systems using various spectrum sharing strategies (*cf.* [62] and related works). These information-theoretic bounds have the form of multiple-access channel (MAC) rate upper bounds; however, since channel capacity is not an operationally meaningful performance metric for radar systems, the MAC bounds of radar-communications spectrum sharing involve novel information-theoretic analysis compared with traditional MAC analysis.

1.2.5 Summary of previous work

All four of the above Research Directions are likely to play a role in improving spectral efficiency through radar-communications spectrum sharing. Given fixed waveform and receiver designs, Research Direction 1 optimizes spectral efficiency by exploiting existing spectral white spaces in time and space—that is, with proper transmit scheduling and power control, new users can take advantage of spatial and

temporal gaps in existing spectrum usage by opportunistically accessing the spectrum. Research Directions 2–3 may further improve spectral efficiency through the design of novel signals and signal processors that outperform legacy systems in spectrum sharing environments. These improvements should improve on the baseline, lower performance bounds of legacy systems, and will not outperform the fundamental information-theoretic upper performance limits (which are still in the process of being formulated). Therefore, spectrum sharing constitutes a multi-faceted research program, with rich opportunity for innovation in technology as well as policy.

1.3 Contributions

Within the context of the above Research Directions 1–4, this dissertation makes the following contributions. The focus of this dissertation is on the radar side of the spectrum sharing application, examining the problem of radar detection in the presence of wireless communications interference.

1.3.1 Chapter 2: Modeling communications interference and its effects on radar

Chapter 2 addresses in part the following research questions.

Q1: What are good statistical models for wireless communications interference to radar?

Q2: Given these models of wireless communications interference, what are the effects of such interference on some standard radar detectors?

For question [Q1], we find theoretical and empirical support for both Gaussian and non-Gaussian interference models, depending on the modeling application. For question [Q2], we specifically analyze the probability of false alarm P_{FA} and probability of detection P_{D} for two types of radar detectors—a simple fixed-threshold detector, and a cell-averaging adaptive-threshold radar detector, which has constant false alarm

rate (CFAR) in additive white Gaussian noise (AWGN) only. These detector architectures are chosen for the sake of analytical tractability, but we speculate that many of our qualitative conclusions may generalize to other receiver types as well. Given these receiver architectures, we find two categories of answers to [Q2]. First, model mismatch between wireless communications interference and AWGN, due to either non-Gaussian interference statistics or non-white interference coherence time, can cause unexpected behavior in the two radar detectors analyzed, which are optimized for detection in AWGN only. Second, even when interference is well modeled as AWGN, it boosts the noise floor of the radar detector, and this can cause significant and insidious detection losses at relatively low interference-to-noise ratio (INR) (*e.g.*, about -6 to -2 dB mean INR at the output of the matched filter).

Chapter 2 contributes to Research Directions 1–4 in the following ways. First, it contributes to Research Direction 1 (transmit scheduling and power control) by suggesting novel, statistically-based interference protection criteria to govern the power control of wireless communications transmitters interfering with a radar receiver. When a radar operates as primary user in a spectrum band shared with wireless communications transmitters as secondary users, the communications transmitters must control their transmitted power so that the aggregate received interference at the radar receiver does not cause unacceptable degradation in the radar’s performance. In such a scenario, it becomes necessary to specify the types and levels of secondary-to-primary interference that are acceptable. In other words, one must specify metrics to quantify the aggregate effects of communications interference to radar, as well as thresholds below which these metrics must remain in order to ensure reliable radar operation. Toward this end, we find that when communications interference is not well modeled as AWGN, mean INR is not sufficient to characterize interference effects on radar, and additional interference characteristics, such as kurtosis/impulsiveness and coherence time, are important for describing aggregate interference effects on radar detection. Therefore, secondary transmitters’ power control strategies may need to

consider these additional metrics when computing levels of interference to radar that are acceptable.

Second, in proposing a statical model for wireless communications interference to radar, Chapter 2 contributes to Research Direction 3 (receiver design) by suggesting radar receiver architectures for spectrum sharing applications. For example, when wireless communications interference to radar is non-Gaussian, radar performance may benefit from non-linear detectors that are optimized for non-Gaussian interference. In addition, the similarities between the interference models studied in Chapter 2 and radar clutter models suggest that the radar clutter literature may provide useful insights transferable to the spectrum sharing application.

Finally, since Chapter 2 assumes that the communications and radar systems use standard legacy signal and system designs, this chapter contributes to Research Direction 4 (joint performance bounds) by providing baseline, lower bounds on the joint performance of spectrally coexistent radar and communications systems. In other words, since the signals and systems in Chapter 2 are not optimized for spectrum sharing, the detection performance of the radar receiver likely can improve upward from the results of Chapter 2 as the signals and systems are adapted to accommodate spectrum sharing.

1.3.2 Chapter 3: Mitigating communications interference to radar via signal processing

While Chapter 2 investigates statistical models of wireless communications interference and its effects on legacy radar systems, Chapter 3 addresses in part the following research question.

Q3: What are some novel radar detectors that outperform standard legacy detectors in the presence of wireless communications interference?

Chapter 3 specifically focuses on radar detection in the presence of cyclostationary, linearly modulated, digital communications (LMDC) interference, which includes sig-

naling schemes such as OFDM and CDMA. The proposed detector consists of a novel whitening filter followed by the traditional matched filter, and as such it optimizes the statistical deflection among the class of all linear detectors. The novel whitening filter derived in Chapter 3 is shown to have equivalent mathematical representations as (i) the *form* of a multiuser detector followed by an interference canceler, and (ii) a frequency-shift (FRESH) filter. Performance results suggest that the proposed cyclostationary-based detector outperforms an equivalent detector based on a stationary model of the LMDC interference, particularly when the number of cyclostationary LMDC signals is small and their INR is large relative to the stationary background.

Thus, Chapter 3 contributes to Research Direction 3 (receiver design) by proposing a novel radar receiver that outperforms standard detection algorithms in the presence of a certain class of wireless communications interference. In the process, Chapter 3 also suggests further study of time-varying signal processing, synchronization, and multiuser detection in radar receivers sharing spectrum with wireless communications devices.

1.4 Summary

We have seen that the proliferation of wireless RF devices has provided economic and political incentive for radar and wireless communications systems to share spectrum effectively. As an asymmetric multiple access problem, the essence of radar-communications spectrum sharing is interference management. The research on this topic in the open literature tends to be grouped in four general categories—transmit scheduling and power control, waveform design, receiver design, and joint performance bounds. This dissertation contributes two chapters of original research on the radar side of the spectrum sharing application—one chapter focused on the statistical modeling of wireless communications interference and its effects on some standard, legacy radar detectors, and another chapter that proposes a novel algorithm for radar detection in the presence of wireless communications interference. Finally, a conclud-

ing chapter summarizes the findings of this dissertation, drawing connections between different facets of the results, and proposing future directions for spectrum sharing research.

2. STATISTICAL MODELING OF WIRELESS COMMUNICATIONS INTERFERENCE AND ITS EFFECTS ON ADAPTIVE-THRESHOLD RADAR DETECTION

2.1 Introduction

This chapter proposes a statistical model for wireless communications interference to radar, and it evaluates the effects of such interference on some conventional radar detectors. The analysis and results of this chapter are also being published in [1–3].

2.1.1 Motivation

One spectrum sharing approach suggests that radars could be allowed to transmit as primary users in a frequency band, while communications users could be given secondary spectrum access provided that their aggregate power (as received by the radar receivers) remains below some specified interference-to-noise ratio (INR) [45, 47, 63]. As pointed out by NTIA [64, p. 10], such an approach begs several questions: (i) Is INR the only or best criterion for ensuring that interference from wireless communications systems does not adversely impact radar performance? (ii) What INR thresholds should be specified?

In answering these questions, one could reason that the composite interference would appear Gaussian to the radar in many situations [47] (see Section 2.2.1 below). Since Gaussian interference in Gaussian noise affects detection solely through the signal-to-interference-plus-noise ratio (SINR), one may reason further that INR is a sufficient criterion for interference management, and that very low-INR Gaussian

interference would have only a minor impact on radar detection. We will investigate the validity of these arguments in this chapter.

In [64], researchers experimentally studied the effects of communications-like interference on many fielded radar systems ranging from air search to maritime radionavigation to meteorological sensing. The researchers found that all radars in the study experienced negative effects at INRs in the range -10 dB to -2 dB [64, p. 136]. The researchers also found that low-level interference effects were “insidious,” with no overt indications of interference to the radar operator [64, p. 137]. For example, [64, p. 58] shows a radar display in which several targets are missing due to interference at an INR of -3 dB, but the display shows no indications that interference is present (such as the false alarm “strokes” seen at higher INRs).

2.1.2 Overview

Motivated by the NTIA study, we propose a model for understanding and extending the NTIA results in order to assess: (i) The appropriateness of Gaussian models for communications interference; (ii) The appropriateness of INR as an interference protection criterion; and (iii) The potential levels of INR thresholds required to ensure radar reliability. We briefly outline the primary contributions of this chapter.

We propose a statistical model for wireless communications interference that is motivated by existing interference and clutter models in the literature and supported by original simulations. Importantly, we find that both Gaussian and non-Gaussian models are applicable and deserve consideration, depending on the modeling situation. Section 2.2 addresses this preliminary step of interference modeling.

After this step, we propose a statistical model for the effects of wireless communications interference on radar detection. Our model takes the form of equations for the probability of false alarm P_{FA} and probability of detection P_D for two classes of radar detectors—a fixed-threshold test, and a cell-averaging adaptive-threshold test (which has a CFAR in AWGN only). These admittedly simple receiver architectures

are chosen for the sake of analytical tractability, although we speculate that many of our qualitative conclusions may generalize to other receiver types as well. Section 2.3 develops this analysis of P_{FA} and P_{D} for these two types of radar detectors.

Finally, the performance curves resulting from our model (presented and discussed in Section 2.4) generate several insights for spectrum sharing research, namely: (i) Non-Gaussian interference can cause some adaptive-threshold radar detectors to lose their CFAR, often to a disastrous extent; (ii) The performance of adaptive-threshold radar detectors can vary significantly based on the coherence time of the interference; and (iii) Relatively low-INR Gaussian interference can cause insidious drops in P_{D} in adaptive-threshold detectors, similarly to the results observed by NTIA. Together, these insights have important ramifications for spectrum sharing policy and technology.

2.2 Statistical models of wireless interference

In order to assess the statistical effects of wireless communications interference on radar detection, one must first specify a statistical model for the interference. Toward this end, this section surveys some common classes of theoretical interference models before turning to original empirical investigation. We find that while a Gaussian model describes wireless communications interference in some cases, important non-Gaussian models also have both theoretical and empirical justification, particularly when modeling random network and wireless propagation effects.

2.2.1 Theoretical models in the literature

As discussed in the Introduction, in many situations a Gaussian model for wireless communications interference seems justified theoretically by the Central Limit Theorem (CLT). Consider the following three scenarios: (i) In single-user OFDM interference, many i.i.d. subcarrier symbols are effectively added via a discrete Fourier transform (DFT), so that the resulting time-domain transmitted symbols may have

Gaussian statistics by the CLT (*cf.* [47]). (ii) When single-user pulse amplitude modulation (PAM) interference is processed via a matched filter, and when the matched filter is of sufficiently long duration to include many i.i.d. PAM pulses, then the output of the matched filter may have Gaussian statistics by the CLT. (iii) In multi-user interference, if the number of i.i.d. interfering transmitters is deterministic and sufficiently large, then the composite interference received by a nearby receiver may have Gaussian statistics by the CLT (*cf.* [47]).

While arguments such as these provide a justification for Gaussian interference models in many cases, important non-Gaussian models also have theoretical justification. For example, [65,66] generalize a CLT argument to derive a non-Gaussian model for radar clutter. (Although the authors specifically address radar clutter modeling in these works rather than interference modeling, the statistical-physical argument is the same for both, so the argument is easily extended to the interference case.) The authors of [65,66] show that if the number of scatterers is sufficiently large and *random* (fluctuating) rather than *deterministic* (fixed), then the composite radar clutter is well-modeled as a spherically invariant random vector (SIRV). This argument provides theoretical justification for many non-Gaussian models that have been found to fit empirical radar clutter data well, such as the K distribution.

Other theoretical non-Gaussian interference models have been proposed as well. For example, alpha-stable interference models have been derived in [67–69] by assuming a marked Poisson point process model for the interfering sources. We note that while the mathematically simple form of alpha-stable interference models is attractive, they violate physical reasoning by having infinite second-order moments. Several authors have pointed out that the reason for these unbounded second-order moments lies in a physically incorrect path loss model, but physically reasonable corrections to the path loss model lose the mathematical simplicity of the alpha-stable models [67, 70–72]. Because the behavior of the cell-averaging radar detector studied in this chapter depends critically on finite second-order moments, in our empirical mod-

eling approach we will modify the path loss model in order to avoid the unrealistic, infinite moments of alpha-stable models.

Like the alpha-stable models, the Middleton interference models are derived theoretically by assuming a marked Poisson point process model for the interfering sources [73,74]. Middleton develops two classes of models, called Class-A and Class-B, to describe different interference scenarios. In the process of forcing finite second-order moments in the Class-B model, the probability density function (pdf) becomes mathematically cumbersome, its mean-square value becomes ill-defined, and the physical meaning of some of its parameters becomes unclear. The Class-A pdf, on the other hand, does not suffer from these deficiencies. The Class-A pdf has the following form:¹

$$f_{A_I}(a) = e^{-A} \sum_{m=0}^{\infty} \frac{A^m}{m!} \frac{a}{\sigma_m^2} \exp \left\{ -\frac{a^2}{2\sigma_m^2} \right\} 1_{[0,\infty)}(a), \quad (2.1)$$

where

$$1_G(x) = \begin{cases} 1, & x \in G, \\ 0, & x \notin G, \end{cases} \quad (2.2)$$

$$\sigma_m^2 = \frac{\Omega}{2} \frac{m/A + \Gamma}{1 + \Gamma}. \quad (2.3)$$

2.2.2 An empirical investigation of interference statistics

In order to supplement the foregoing theoretical interference models and gain additional insight into the statistical behavior of wireless communications interference, we conduct an empirical investigation of interference statistics. In our empirical approach, we simulate an electromagnetic interference environment using standard models for transmitted signals and electromagnetic propagation, process the resulting interference using a radar matched-filter, and fit statistical distributions to the resulting random variable.

¹Here, A is the “Impulsive Index,” related to the number of interfering signals; Γ is the ratio of Gaussian power to non-Gaussian power; and Ω is the average power in the entire interference (Gaussian plus non-Gaussian). Since our analysis treats the Gaussian noise separately from the interference, we would generally take $\Gamma \rightarrow 0$.

In simulating wireless communications interference, we focus on OFDM signals due to the prevalence of OFDM in modern broadband communications. In our simulations, sources of OFDM signals are generated randomly in time and space via a Poisson point process model, in accordance with the modeling framework of the alpha-stable and Middleton models. Once the signals are generated, we apply standard wireless channel models of (i) Rician fading, and (ii) a path loss function of $1/(1+r)^\nu$ as a function of radial distance r .² This path loss function behaves as $1/r^\nu$ in the far field—which is a standard model—but tends to unity as $r \rightarrow 0$ in order to satisfy energy conservation and avoid the problems of the alpha-stable interference models (see above). Shadowing is not investigated in this investigation, but could be included in future work given a sufficiently reliable statistical model.

After generating OFDM signals in a Poisson point process, passing them through Rician fading channels, applying path loss, and summing the results, the composite interference is processed using a matched filter. The impulse response of the matched filter is chosen to be a linear frequency-modulated (LFM) chirp due to the prevalence of LFM waveforms in radar systems.

Finally, we fit four candidate pdfs to the simulated data—the Rayleigh, Weibull, and K distributions, and a version of the Student- t distribution—and we use two metrics to evaluate goodness-of-approximation. We do not perform a hypothesis test for goodness-of-fit (such as a Kolmogorov-Smirnov test); rather, since the true interference distribution is unknown and potentially intractable, we assess the four candidate distributions merely as mathematically tractable approximations to the true distribution. For our first metric of goodness-of-approximation, we use the Kolmogorov-Smirnov *distance* (*not* the *p-value*, since we do not apply the K-S hypothesis test). Our second metric is the ratio of model kurtosis to empirical kurtosis, chosen since kurtosis is one measure of the heaviness of the tail of a distribution, and tail probabilities play a large role in determining the false alarm rates of radar detectors.

²A more complete model for the path loss would be $1/(1+r/r_0)^\nu$, with r_0 depending on the systems and environment of interest. Here we simply normalize with $r_0 = 1$ for simplicity.

The matched-filtered composite interference is found to be well modeled by a K distribution for a single OFDM user with slow multipath fading and a fixed transmitter location. When transmitter location is modeled as random, the K distribution generally underestimates the heaviness of the tails in the empirical data, but it still provides a significantly better fit than a Rayleigh distribution. For these reasons we will adopt a K distribution model for heavy-tailed interference. In the case of random transmitter location, we choose to underestimate the heaviness of the interference tails because, as we will see in Section 2.4, K distribution tails can cause significant detrimental effects on radar detection, so we reason that the heavier, empirical tails would produce even *worse* effects on radar detection. In other words, by underestimating the tail heaviness, we can qualitatively bound the problems caused by heavy tails in order to make stronger conclusions about the effects of non-Gaussian interference on radar detection.

Simulation setup

We simulate wireless communications interference as follows.

First, we generate P locations for wireless communications transmitters according to the following procedure inspired by a Poisson point process.

1. Specify an average number of interfering transmitters as P_{avg} .
2. If $P_{\text{avg}} = 1$, then set the number P of interfering sources equal to 1.
3. If $P_{\text{avg}} < 1$, generate the number P of interfering sources as a Bernoulli random variable which assumes a value of 1 with probability P_{avg} , and 0 otherwise.
4. If $P_{\text{avg}} > 1$, generate the number P of interfering sources as a Poisson random variable with mean P_{avg} . Optionally, repeat until a nonzero value of P is obtained.

At each point in the process, we place a wireless transmitter, and we denote the radial distance from the p -th transmitter to the radar receiver as R_p , where $p \in \{1, \dots, P\}$.

We choose each R_p by generating a random point uniformly distributed over a sector of a circle of radius R_{\max} , and set the radial distance R_p to be the distance from this point to the origin of the circle.

Then for each p -th transmitter we generate a random OFDM transmitted signal as follows. Out of a total of M subcarriers, M_{nz} are assigned nonzero data symbols from some symbol constellation such as QPSK or 16-QAM; the other subcarriers are assigned an amplitude of zero. The M_{nz} data-carrying subcarriers are selected from the M possible subcarriers at random in comb, contiguous, or fully randomized patterns. Then, given the M subcarrier amplitudes $\{\tilde{C}_{k,p}\}_{k=0}^{M-1}$, the OFDM pulse amplitudes $\{C_{m,p}\}_{m=0}^{M-1}$ are obtained via an inverse DFT:

$$C_{m,p} = \frac{1}{\sqrt{M}} \sum_{k=0}^{M-1} \tilde{C}_{k,p} e^{i2\pi km/M}. \quad (2.4)$$

The $\{C_{m,p}\}_{m=0}^{M-1}$ have a length- $(L'-1)$ cyclic prefix appended to the beginning of each length- M OFDM block, where L' is chosen to be just long enough to fill the delay spread of the wireless channel, discussed below. The resulting $M + (L' - 1)$ pulse amplitudes are modulated onto an analog pulse shape $g(t)$:

$$C_p(t) = \sum_{m=-(L'-1)}^{M-1} C_{m,p} g(t - mT_c), \quad (2.5)$$

where T_c is the pulse symbol duration.

Once the OFDM signals $C_p(t)$ are generated, they each undergo the wireless propagation effects of Rician fading and path loss. Rician fading is expressed as the convolution with a linear, time-varying (LTV) impulse response as follows:

$$I_p(t) = \sum_{\ell=0}^{L-1} H_{\ell,p}(t) C_p(t - \ell T_{cc}), \quad (2.6)$$

where T_{cc} denotes the coherence time of the signal $C_p(t)$ and is taken to be a fraction of the pulse symbol duration T_c , and $L'/L = T_{cc}/T_c$. The channel taps $\{H_{\ell,p}(t)\}_{\ell=0}^{L-1}$ are usually independent complex-valued Gaussian random processes; only the first tap $H_{0,p}(t)$ may be a convex combination of a complex Gaussian random process

and a deterministic line-of-sight component (Rician fading). The delay-power profile across ℓ is taken to be exponentially decaying; the Doppler spectrum (corresponding to the autocorrelation over t) is set to be rectangular for convenience.

Finally, the Rician-faded signals $I_p(t)$ undergo some path loss $1/(1 + R_p)^\nu$,³ and arrive at the receiver with some random delay τ_p and phase ϕ_p , the latter of which is taken to be uniformly distributed on $[0, 2\pi)$. The sum of these signals is

$$I(t) = \sum_{p=1}^P \frac{1}{(1 + R_p)^\nu} I_p(t - \tau_p) e^{i\phi_p}. \quad (2.7)$$

The composite interference $I(t)$ is passed through a matched filter to form a statistic I :

$$I = A_I e^{i\Theta_I} = \int_{-\infty}^{\infty} I(t) s^*(t) dt, \quad (2.8)$$

where

$$s(t) = e^{i\pi\beta t^2} 1_{[0, T_{\text{LFM}}]}(t) \quad (2.9)$$

is an LFM chirp with duration T_{LFM} and chirp rate β , and A_I and Θ_I are the amplitude and phase of I , respectively.

Statistical analysis

For our statistical analysis, we generate many independent, identically distributed (i.i.d.) trials of the amplitude $A_I = |I|$ according to (2.4)-(2.9), fit several statistical distributions to the resulting empirical data, and use two different goodness-of-approximation metrics to evaluate how well each of the candidate distributions approximates the empirical distribution of the simulated data.

³Note that even for a fixed path loss exponent ν , this path loss $1/(1 + R_p)^\nu$ is random via the random locations R_p .

Four distributions are tested as candidate approximations of the empirical data: the Rayleigh, Weibull, K , and circular Student- t distributions. The respective pdfs of the distributions are:

$$f_{\text{Rayleigh}}(a; \sigma_R) = \frac{a}{\sigma_R^2} \exp \left\{ -\frac{a^2}{2\sigma_R^2} \right\} 1_{[0, \infty)}(a), \quad (2.10)$$

$$f_{\text{Weibull}}(a; k_W, \sigma_W) = \left(\frac{k_W}{\sigma_W} \right) \left(\frac{a}{\sigma_W} \right)^{k_W-1} \cdot \exp \left\{ -\left(\frac{a}{\sigma_W} \right)^{k_W} \right\} 1_{[0, \infty)}(a), \quad (2.11)$$

$$f_K(a; \alpha_K, \lambda_K) = \frac{4}{\lambda \Gamma(\alpha_K)} \left(\frac{a}{\lambda_K} \right)^{\alpha_K} \cdot K_{\alpha_K-1} \left(\frac{2a}{\lambda_K} \right) 1_{[0, \infty)}(a), \quad (2.12)$$

$$f_{\text{Circ-}t}(a; \alpha_T, \sigma_T) = \frac{2\alpha_T a}{\sigma_T^2} \left[1 + \left(\frac{a}{\sigma_T} \right)^2 \right]^{-\alpha_T-1} 1_{[0, \infty)}(a), \quad (2.13)$$

where $\Gamma(\cdot)$ is the (complete) gamma function, $K_\nu(\cdot)$ is the modified Bessel function of the second kind. The latter three distributions allow for heavier tails than the Rayleigh distribution, but also include the Rayleigh distribution as a special or limiting case. Both the Weibull and K distributions have exponential tails and have been used in radar clutter modeling [65, 75]. What we are calling the circular Student- t distribution has heavier, algebraic tails, and it corresponds to the amplitude of a complex random variable whose real and imaginary parts follow the familiar Student- t distribution and whose phase is uniform on $[0, 2\pi)$.

The parameters of the four candidate distributions are fit to the empirical simulated A_I values. The Rayleigh and Weibull distributions are fit using the “stats” routines from the Python package “scipy;” the K distribution is fit using an expectation-maximization implementation of maximum-likelihood estimation according to [76]; the circular Student- t distribution is fit using maximum-likelihood.

Finally, we use two metrics to evaluate goodness-of-approximation. The first is the Kolmogorov-Smirnov distance (*not p-value*—see above), defined as:

$$d_{\text{KS}} = \sup_{A_I \in \mathbb{R}} |F_{\text{emp}}(A_I) - F_{\text{model}}(A_I)|, \quad (2.14)$$

where $F_{\text{emp}}(A_I)$ and $F_{\text{model}}(A_I)$ are the empirical and model cumulative distribution functions (cdfs) of the random variable A_I . We choose the second metric to be the ratio of model kurtosis to empirical kurtosis:

$$\rho_{\text{kurt}} = \frac{\kappa_{\text{model}}}{\kappa_{\text{emp}}}, \quad (2.15)$$

$$\kappa_{\text{model}} = \frac{\int_{-\infty}^{\infty} a^4 f_{\text{model}}(a) da}{\left(\int_{-\infty}^{\infty} a^2 f_{\text{model}}(a) da \right)^2}, \quad (2.16)$$

$$\kappa_{\text{emp}} = \frac{1/n_s \sum_{j=1}^{n_s} a_j^4}{\left(1/n_s \sum_{j=1}^{n_s} a_j^2 \right)^2}, \quad (2.17)$$

where $f_{\text{model}}(a)$ is the candidate approximation for the pdf for A_I , and a_1, \dots, a_{n_s} are n_s i.i.d. realizations of A_I .

Statistical results

As discussed in the introduction to this sub-section, we will choose the K distribution (2.12) to model heavy-tailed wireless communications interference. Here we present simulation results justifying use of the K distribution for wireless communications interference.

We perform two sets of simulations. For the first set, we run 48 simulations of single-user OFDM interference with slow Rician fading and fixed transmitter location R_1 .⁴ The results from this first set of simulations are shown in Figure 2.1. Sub-Figure (a) illustrates empirical and model cdfs $F_{\text{emp}}(A_I)$ and $F_{\text{model}}(A_I)$ for one representative of the 48 simulations, where $F_{\text{model}}(\cdot)$ covers the cases of Rayleigh, Weibull, K , and circular Student- t models. In Sub-Figure (a), the Rayleigh model has fitted parameter

⁴The simulations in Figure 2.1 use the following parameter values, with an asterisk denoting the particular parameter values of Sub-Figure (a): $n_s = 10^3$ i.i.d. trials, a sample period of $T_{cc} = 1/128$ ms; radar filter matched to an LFM chirp with chirp rate $\beta = -30 \text{ ms}^{-2}$ and duration $T_{\text{LFM}} = 1$ ms; one ($P = P_{\text{avg}} = 1$) OFDM user transmitting two frequency-hopping OFDM blocks, with i.i.d. QPSK symbols modulated onto $M_{\text{nz}} = 16, 32, 64,^*$ or 128 out of a total of $M = 128$ subcarriers, arranged in frequency in contiguous,* comb, or random patterns, with $T_c = 4/128$ ms-duration pulse symbols having a root-raised-cosine pulse shape with a roll-off factor of 0.4, a cyclic prefix just long enough to cover the frequency-selective multipath channel, and a random delay-of-arrival τ_p uniformly distributed on $[-T_c(128 + \text{cyclic prefix length}), 0]$; a slow Ricean fading multipath channel with K-factors of 0^* or 10^6 and delay spreads of $LT_{cc} = 6/128$ ms or $12/128$ ms.*

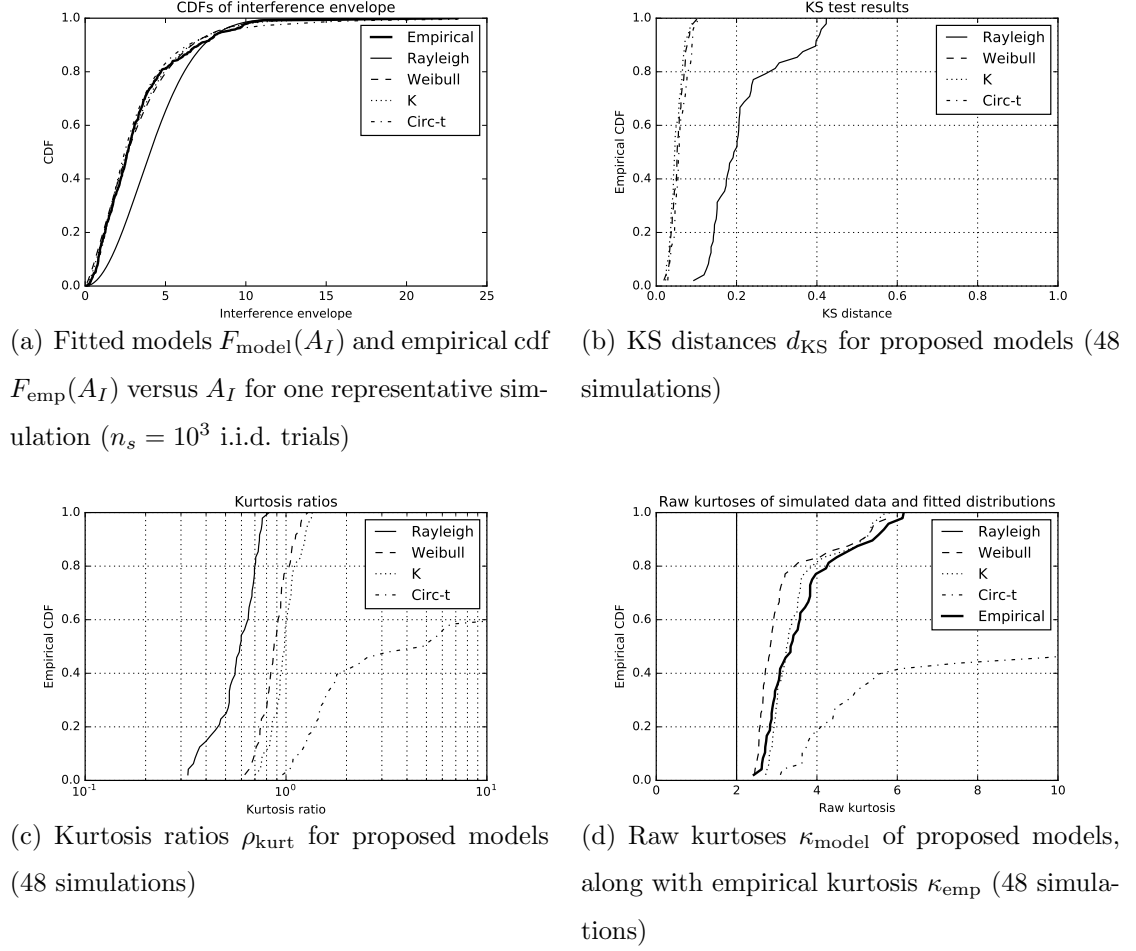


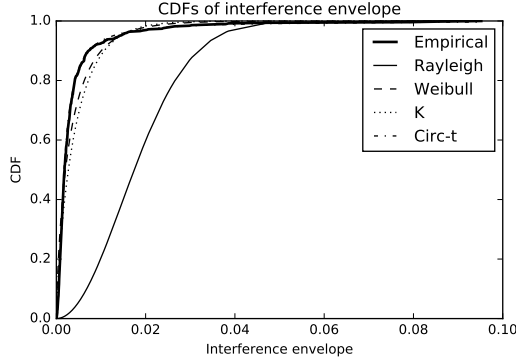
Figure 2.1. Simulation results for single-user OFDM with slow, Rician multipath fading. (a) The CDFs in (a) are of $n_s = 10^3$ i.i.d. realizations of A_I for one of a total of 48 simulations. (b)–(d) The empirical CDFs in (b)–(d) are of the goodness-of-approximation metrics d_{KS} , ρ_{kurt} , and κ_{model} , κ_{emp} for the entire population of 48 simulations.

$\sigma_R = 3.43$, the Weibull model has fitted parameters $k_W = 1.30$, $\sigma_W = 3.51$, the K model has fitted parameters $\alpha_K = 1.02$, $\lambda_K = 4.07$, and the circular Student- t model has fitted parameters $\alpha_T = 1.33$, $\sigma_T = 2.97$. Note the relatively poor fit of the Rayleigh model, which has a K-S distance of $d_{\text{KS}} = 0.27$ in this simulation. As shown in Sub-Figure (b), all three non-Rayleigh distributions are better approximations of the data than the Rayleigh distribution, in the sense of K-S distance d_{KS} . In

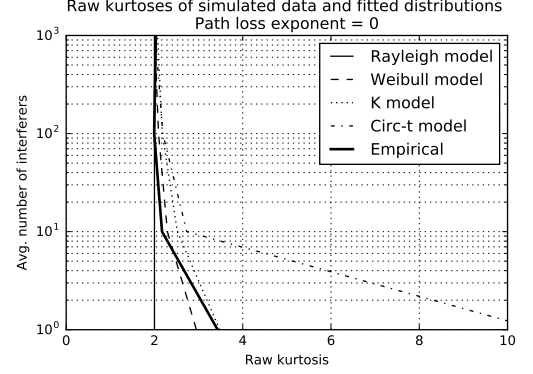
terms of the kurtosis ratio ρ_{kurt} , Sub-Figure (c) indicates that the K distribution is the best approximation, with the Weibull distribution as a close second-best; in addition, while the Rayleigh distribution under-estimates tail heaviness, the circular Student- t distribution over-estimates the tail heaviness of the empirical data. Finally, Sub-Figure (d) shows the kurtoses κ_{emp} and κ_{model} used to compute ρ_{kurt} , where κ_{model} ranges over the Rayleigh, Weibull, K , and circular Student- t models. In Sub-Figure (d), we see again that the K distribution gives the best approximation of tail heaviness. Further, for this set of simulations, reasonable values of kurtosis range from about 3 to about 5, corresponding to K distribution shape parameters of about $\alpha_K = 2$ to about $\alpha_K = 0.67$.

For the second set of simulations we run 12 scenarios of multi-user OFDM interference with random transmitter locations R_p (and hence random path loss $(1 + R_p)^{-\nu}$), and the results are presented in Figure 2.2.⁵ Again, for the sake of illustration, Sub-Figure (a) shows the empirical and model cdfs $F_{\text{emp}}(A_I)$ and $F_{\text{model}}(A_I)$ for one of the 12 simulations, where $F_{\text{model}}(\cdot)$ covers the cases of Rayleigh, Weibull, K , and circular Student- t models. In Sub-Figure (a), the Rayleigh model has fitted parameters $\sigma_R = 0.01$, the Weibull model has fitted parameters $k_W = 0.76$, $\sigma_W = 0.0033$, the K model has fitted parameters $\alpha_K = 0.37$, $\lambda_K = 0.01$, and the circular Student- t model has fitted parameters $\alpha_T = 0.65$, $\sigma_T = 0.0013$. Note the poor fit of the Rayleigh model, which has a K-S distance of $d_{\text{KS}} = 0.79$ in this particularly extreme simulation in Sub-Figure (a). Sub-Figures (b)–(d) present the empirical and model kurtoses κ_{emp} and κ_{model} , where once again κ_{model} ranges over the Rayleigh, Weibull, K , and

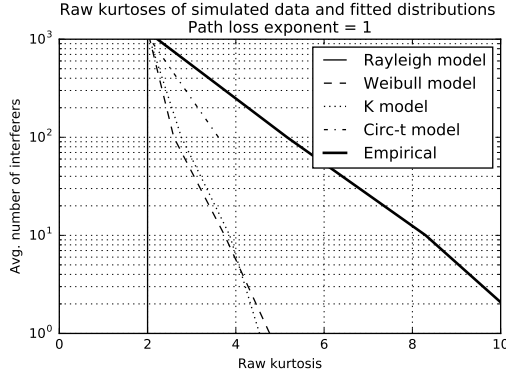
⁵The simulations in Figure 2.2 use the following parameter values, with an asterisk denoting the particular parameter values of Sub-Figure (a): $n_s = 10^3$ i.i.d. trials, a sample period of $T_{cc} = 1/128$ ms; a radar filter matched to an LFM chirp with chirp rate $\beta = -30 \text{ ms}^{-2}$ and duration $T_{\text{LFM}} = 1$ ms; average numbers of users P_{avg} of 1,* 10, 100, or 1000 users transmitting two frequency-hopping OFDM blocks each, with i.i.d. QPSK symbols modulated onto $M_{\text{nz}} = 8$ out of a total of $M = 32$ available subcarriers, arranged in a comb pattern in frequency, with $T_c = 4/128$ ms-duration pulse symbols having a root-raised-cosine pulse shape with a roll-off factor of 0.4, a cyclic prefix just long enough to cover the frequency-selective multipath channel, and a random delay-of-arrival τ_p uniformly distributed on $[-T_c(32 + \text{cyclic prefix length}), 0]$; a slow Rayleigh fading multipath channel having a delay spread of $LT_{cc} = 6/128$ ms; and users distributed randomly over a sector of a circle of radius $R_{\text{max}} = 10^2$, with amplitude path loss exponents ν of 0, 1, and 1.5.*



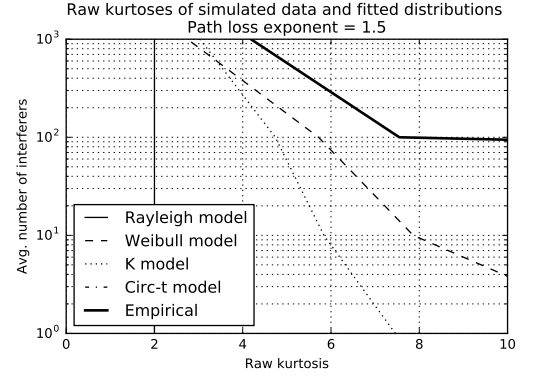
(a) Fitted models $F_{\text{model}}(A_I)$ and empirical cdf $F_{\text{emp}}(A_I)$ versus A_I for one representative simulation ($n_s = 10^3$ i.i.d. trials)



(b) Raw kurtoses κ_{model} of proposed models, along with empirical kurtosis κ_{emp} , for the case of $\nu = 0$ (4 simulations)



(c) Raw kurtoses κ_{model} of proposed models, along with empirical kurtosis κ_{emp} , for the case of $\nu = 1$ (4 simulations)



(d) Raw kurtoses κ_{model} of proposed models, along with empirical kurtosis κ_{emp} , for the case of $\nu = 1.5$ (4 simulations)

Figure 2.2. Simulation results for multiple OFDM users transmitting with slow Rayleigh fading from random locations. (a) The CDFs in (a) are of $n_s = 10^3$ i.i.d. realizations of A_I for one of a total of 12 simulations. (b)–(d) The results in (b)–(d) are kurtoses κ_{model} , κ_{emp} for 12 different simulations. (Note: Due to very heavy algebraic tails in the above simulations, the fitted Student- t model often has an undefined kurtosis.)

circular Student- t models; these sub-figures present kurtosis results for the respective cases of no path loss ($\nu = 0$), path loss due to spherical propagation ($\nu = 1$), and path loss due to more severe propagation ($\nu = 1.5$) such as could occur in urban

environments. In all three Sub-Figures (b)–(d), the empirical kurtosis κ_{emp} (shown in bold solid lines) converges toward a Rayleigh kurtosis of $\kappa = 2$ as the average number of interferers P_{avg} increases from 1 to 1000. However, this convergence is slower for more severe path loss—in fact, the tail heaviness is roughly the same in the case of $\nu = 1.5$, $P_{\text{avg}} = 1000$ as it is in the case of $\nu = 0$ and $P_{\text{avg}} = 1$ (single-user with no path loss). This makes sense, because severe path loss causes only the interfering sources closest to the receiver to dominate in the composite received interference signal, so that the *effective* number of interfering sources is much less than the actual number of sources. Finally, note that both the K and Weibull distributions provide good approximations for the empirical data when $\nu = 0$ (Sub-Figure (b)) but underestimate the tail heaviness of the empirical data for the cases $\nu = 1, 1.5$ (Sub-Figures (c)–(d)). As we discussed in the introduction to this sub-section, we choose to use the K distribution’s underestimation of the tail heaviness in order to qualitatively bound the effect of non-Gaussian wireless communications interference on radar in the rest of the chapter. For the cases of $\nu = 1, 1.5$, reasonable values of kurtosis range from about 4 to more than 7, corresponding to K distribution shape parameters of about $\alpha_K = 1$ to $\alpha_K < 0.4$.

2.2.3 Conclusions and proposed interference model

The foregoing simulations suggest the following conclusions about statistical interference modeling: (i) Although single-user OFDM interference may have Gaussian statistics *conditioned on the wireless channel*, when one averages over random multipath fading effects, heavy-tailed statistics (such as modeled by the K distribution) can result. (ii) Although multi-user interference may converge to Gaussian statistics *conditioned on a fixed, large number of sources*, when one averages over random path loss effects induced by random transmitter locations, heavy-tailed statistics can result, and this can significantly slow CLT convergence. Further, recall from the theoretical discussion of [65,66] that: (iii) When one models the number of interfering sources as

random (rather than fixed) and large, then non-Gaussian statistics (such as modeled by the K distribution) can result.

In all three cases, non-Gaussian models result from averaging over fluctuating wireless propagation effects (such as multipath fading) or fluctuating network effects (such as transmitters turning ON and OFF or changing locations). Whether one chooses to condition on a fixed realization of such effects or average over a fluctuating ensemble of such effects likely will depend on the specific modeling application of interest.

Based on the foregoing statistical discussion, we propose the following pdf for the envelope of the matched-filtered interference A_I :

$$f_{A_I}(a) = (1 - p)\delta(a) + p \frac{4}{\lambda \Gamma(\alpha)} \left(\frac{a}{\lambda}\right)^\alpha K_{\alpha-1}\left(\frac{2a}{\lambda}\right) 1_{[0,\infty)}(a). \quad (2.18)$$

This is a convex combination of a probability mass at the origin (corresponding to zero interference) and a K pdf with shape α and scale λ . This model includes the K distribution, a version of Middleton's Class-A model, and the Rayleigh distribution as special and/or limiting cases for the parameter combinations ($p = 1$, $\alpha < \infty$), ($p \ll 1$, $\alpha \rightarrow \infty$), and ($p = 1$, $\alpha \rightarrow \infty$), respectively.⁶ We will hereafter refer to these respective cases as “heavy-tailed,” “impulsive,” and “Gaussian” (or “Rayleigh”).

Inclusion of the heavy-tailed K pdf in (2.18) seems justified by the preceding theoretical and empirical discussion. Reasonable values for the shape parameter α include $\alpha = 2$ to $\alpha = 0.67$ for single-user OFDM with slow fading and fixed transmitter location, and $\alpha = 1$ to $\alpha < 0.4$ for multi-user OFDM with random transmitter locations.

Inclusion of Middleton's Class-A model via the probability mass at the origin in (2.18) captures impulsive behavior of interference that is OFF some of the time. This impulsive interference model seems justified in situations when the wireless communications signals are low-duty-cycle (*e.g.*, ultrawideband radio), or when the wireless transmitters enter the radar field-of-view only rarely, due to either a sparse wireless

⁶If we set $p \ll 1$ and $\alpha \rightarrow \infty$, our model (2.18) approximates Middleton's Class-A pdf (2.1) for $A \ll 1$ and $\Gamma \rightarrow 0$.

communications network or a small radar field-of-view (*e.g.*, short-range automotive radar, airplane altimeters). While reasonable values for the impulsiveness parameter p in (2.18) depend on the specific scenario of interest, in our subsequent analysis we examine the cases $10^{-3} \leq p \leq 1$. Since a clear pattern emerges for the effects of impulsive interference on the radar detectors studied in this chapter, extrapolation to other values of p seems straightforward.

We thus have proposed and partially justified a statistical model for wireless communications interference based on simulation results and existing theoretical models such as the Middleton and K models. We now turn to the following research question: Given this model for wireless communications interference, what are its effects on radar receivers? We address this question in the following two sections.

2.3 Effects of interference on radar: Analysis

In order to determine possible power control criteria for wireless communications interference to radar, the following two sections investigate the “do-nothing” policy of allowing radar and wireless communications to share spectrum without modifying their transmitted signals or receiver designs. The analysis significantly expands on that of [77]. The analysis is presented in this section, and the numerical results are discussed in Section 2.4. (Readers who are more interested in results than derivations may skip Sections 2.3.2 through 2.3.4 without missing the narrative of the chapter.)

2.3.1 Model

We start by defining the radar receiver architectures to be studied, as well as a statistical model for the signals of interest as they move through the radar receivers.

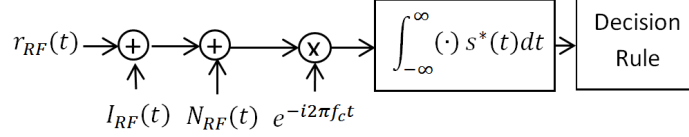


Figure 2.3. Block diagram for radar receiver

Receiver front-end

First, we assume that the sum of the radar return $r_{RF}(t)$, wireless communications interference $I_{RF}(t)$, and Gaussian noise $N_{RF}(t)$ is received by a radar antenna, converted to its complex base-band equivalent (with respect to carrier frequency f_c), and passed through a matched filter (correlator) matched to the transmitted radar signal $s(t)$. These assumptions are illustrated in the block diagram of Figure 2.3.

Here we model $N_{RF}(t)$ as AWGN with two-sided spectral density $N_0/2$. The wireless communications interference is given by

$$I_{RF}(t) = \text{Re}\{I(t)e^{i2\pi f_c t}\}, \quad (2.19)$$

with $I(t)$ modeled by (2.4)–(2.7), and

$$r_{RF}(t) = \begin{cases} 0, & \text{under } H_0 \text{ (no target),} \\ \text{Re}\{\gamma s(t)e^{i(2\pi f_c t + \Theta_S)}\}, & \text{under } H_1 \text{ (target present),} \end{cases} \quad (2.20)$$

where $\gamma \in (0, \infty)$ is an unknown, deterministic signal amplitude determined by factors such as target scattering (radar cross section), range cell size, and free space or atmospheric attenuation (path loss); $s(t)$ is the complex baseband of the known transmitted radar signal; f_c is the carrier frequency of the radar transmitter; and Θ_S is a random phase shift due to uncertainty in the position of the radar target (asynchronous reception).

Assuming that $s(t)$ and $I(t)$ are narrowband signals with respect to the carrier frequency f_c , the output of the matched filter may be written as

$$X = \frac{1}{2}\gamma E_S e^{i\Theta_S} + \frac{1}{2}I + N_{\text{noise}}, \quad (2.21)$$

where E_S is the energy (L^2 norm) of the signal $s(t)$, I is given by (2.8), and N_{noise} is a circular Gaussian random variable with mean zero and variance $\sigma^2 = N_0 E_S/4$. Equation (2.21) applies under H_1 (target present); under H_0 the first term on the right-hand side is omitted ($\gamma = 0$).

In (2.21), we may define $A_S = \gamma E_S/2$ as a deterministic quantity related to the energy received from the radar return. In the complex plane, A_S is the real magnitude of a complex phasor with phase Θ_S . Θ_S itself is modeled as random and uniformly distributed on $[0, 2\pi)$, based on the common assumption that the radar target is randomly located over a continuous range of distances much larger than the carrier wavelength $\lambda_c = c/f_c$, where c is the speed of light.

We decompose the phasor I by its magnitude and phase as

$$\frac{1}{2}I = A_I e^{i\Theta_I}, \quad (2.22)$$

where A_I is modeled using the foregoing pdf (2.18). As for the phase Θ_I , we argue that this is well modeled as uniformly distributed on $[0, 2\pi)$, based on the following observations: (i) In general, the radar will have complete uncertainty about the carrier phase of the received communications signals and will not lock onto any one carrier's phase; (ii) The communications signals arrive at the radar receiver with some random delay, which may be assumed to be randomly distributed over a continuous range of delays much greater than a carrier period $1/f_c$. Because of these observations, a uniform distribution for the composite phase Θ_I seems reasonable.

Summarizing our model so far, we will assume hereafter that the output of the matched filter (*i.e.*, the input to the decision rule) is well modeled as the following complex random variable:

$$X = \begin{cases} A_I e^{i\Theta_I} + N_{\text{noise}}, & \text{under } H_0, \\ A_S e^{i\Theta_S} + A_I e^{i\Theta_I} + N_{\text{noise}}, & \text{under } H_1, \end{cases} \quad (2.23)$$

with all quantities having been defined above. Further, we assume that all random quantities in (2.23) are independent. Finally, let us define the signal-to-noise ratio (SNR) and interference-to-noise ratio (INR) as follows:

$$\text{SNR} = \frac{A_S^2}{E[|N_{\text{noise}}|^2]} = \frac{A_S^2}{N_0 E_S/2} = \frac{\gamma^2 E_S}{2N_0}, \quad (2.24)$$

$$\text{INR} = \frac{E[A_I^2]}{E[|N_{\text{noise}}|^2]} = \frac{E[A_I^2]}{N_0 E_S/2}, \quad (2.25)$$

where we note that the denominator $E[|N_{\text{noise}}|^2] = 2\sigma^2 = N_0 E_S/2$. Also, observe that the standard case of radar detection in Gaussian noise only is a special case of our model with $A_I = 0$ ($\text{INR} \rightarrow -\infty$ dB).

Decision rule

We will examine two types of standard radar detection schemes. The first is a simple threshold test, which is optimal in the Neyman-Pearson sense for Gaussian noise when the distribution of the noise is known. For this decision rule, the amplitude of the matched filter output X in (2.23) is compared with a threshold T , and a target is declared present (H_1) if the threshold is exceeded, or absent (H_0) otherwise:

$$\phi(x) = \begin{cases} 1, & |x| > T, \\ 0, & |x| \leq T, \end{cases} \quad (2.26)$$

where T is a design parameter that sets the probability of false alarm based on the variance σ^2 of the noise.

If the noise variance σ^2 is unknown, then it becomes necessary to adaptively set the threshold T in (2.26) in order to control the probability of false alarm. One such scheme is the cell-averaging processor illustrated in Figure 2.4.

The cell-averaging processor makes a decision about whether a target is present (H_1) or not (H_0) in the delay-Doppler cell under test (CUT) by comparing the magnitude of the matched filter output X from the CUT with a threshold which is set adaptively based on the matched filter outputs Y_1, \dots, Y_N from N neighboring delay-

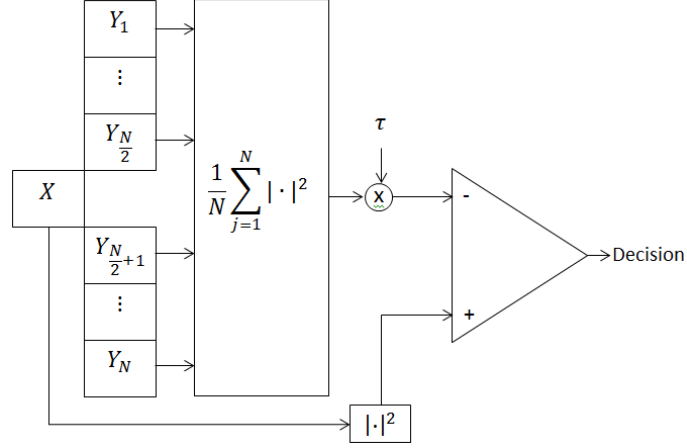


Figure 2.4. Block diagram for cell-averaging adaptive-threshold decision rule

Doppler cells. This threshold is set to be proportional to the sample average energy in the matched filter outputs Y_1, \dots, Y_N :

$$\phi(x) = \begin{cases} 1, & |x|^2 > \tau \frac{1}{N} \sum_{n=1}^N |Y_n|^2, \\ 0, & |x|^2 \leq \tau \frac{1}{N} \sum_{n=1}^N |Y_n|^2, \end{cases} \quad (2.27)$$

where the proportionality constant τ is a design parameter related to the probability of false alarm.

In AWGN only, the random variables Y_1, \dots, Y_N are i.i.d. circular Gaussian random variables with mean zero and variance σ^2 , and one can show that the statistic

$$\frac{1}{2N} \sum_{n=1}^N |Y_n|^2$$

is the maximum-likelihood estimator of the parameter σ^2 , which in this case is also unbiased and efficient (attaining the Cramer-Rao lower bound). It can be shown further that the cell-averaging processor shown in Figure 2.4 achieves a CFAR in AWGN only; for this reason the cell-averaging processor is often called a cell-averaging CFAR receiver. However, we refrain from using the term CFAR with the cell-averaging processor in this chapter because we are concerned with non-Gaussian interference, which as we will see causes the CFAR property of the cell-averaging processor to break down.

For the cell-averaging processor shown in Figure 2.4, we make the following statistical assumptions: (i) The matched filter output X of the CUT is given by (2.23). (ii) The matched filter outputs Y_1, \dots, Y_N of the neighboring cells are similarly given by (2.23), except that the neighboring cells are assumed to have H_0 always in effect (no target present). (Although in general there could be multiple targets appearing in the $N + 1$ matched filter outputs X, Y_1, \dots, Y_N , for our analysis here we make the simplifying assumption that at most one target is present at a time, and always in the CUT. The results of our analysis reflect this one important case of interest in the radar performance analysis.) (iii) Across the $N + 1$ matched filter outputs X, Y_1, \dots, Y_N , the Gaussian noise components N_{noise} in (2.23) are independent.

In addition to the above assumptions, we must specify a *joint* distribution for the various realizations of A_I appearing in the $N + 1$ matched filter outputs X, Y_1, \dots, Y_N , and in general these may be equal, correlated, or independent across the $N + 1$ cells. Although an analysis of the general case of arbitrary correlation between these $N + 1$ matched filter outputs is desirable, for the sake of analytical tractability we make the simplifying assumption of considering only the two most extreme cases:

- 1: The interference varies much more slowly than the duration of the matched filter impulse response. In this case, the amplitudes A_I may be approximated as constant across the $N + 1$ matched filter outputs X, Y_1, \dots, Y_N .
- 2: The interference varies much more quickly than the duration of the matched filter impulse response. If the statistical variation of the interference is fast enough, the amplitudes A_I may be approximated as i.i.d. across the $N + 1$ matched filter outputs X, Y_1, \dots, Y_N .

By considering these two extreme cases—that of slowly-varying interference versus quickly-varying interference (relative to the duration of the radar matched filter)—we can gain qualitative insight into the *range of possible* effects caused by interference having various coherence times. The actual behavior of any particular interference scenario will likely be somewhere between these two extremes, based on the actual

correlation properties of the particular interference. Borrowing terminology from wireless channel fading models, we refer to the former extreme as “slow” interference, and the latter extreme as “fast” interference.

Given the above assumptions, we wish to evaluate the probability of false alarm and probability of detection for both the fixed-threshold receiver and the cell-averaging processor, and this becomes a straight-forward matter of statistical derivation. We lay out this derivation in the following three sections: Section 2.3.2 presents some preliminary mathematical results in the form of modular theorems and facts in order to keep the derivation as clear as possible, and the following two Sections 2.3.3 and 2.3.4 use these mathematical results to derive the Receiver Operating Characteristic (ROC) equations in a straight-forward manner. The reader who wishes to do so may skip the derivations of the following three subsections and go directly to the results of Section 2.4.

2.3.2 Mathematical preliminaries

Fact 1 *Let Y be a circular Gaussian random variable with mean zero and variance σ^2 , and define the complex random variable $X = Y + \mu$, where μ is a real number. Then $|X|$ is a Rician random variable with parameters μ and σ , having the following pdf:*

$$f_{\text{Rice}}(r; \mu, \sigma) = \frac{r}{\sigma^2} \exp \left\{ -\frac{(r^2 + \mu^2)}{2\sigma^2} \right\} I_0 \left(\frac{r\mu}{\sigma^2} \right) 1_{[0, \infty)}(r), \quad (2.28)$$

where $I_0(\cdot)$ is the modified Bessel function of the first kind.

Corollary 1 *It follows from Fact 1 and (2.23) that under H_0 the amplitude of the matched filter output $|X|$ is conditionally Rician, given A_I and Θ_I , and has conditional pdf*

$$\begin{aligned} f_{|X||A_I, \Theta_I}^{(H_0)}(r|A_I, \Theta_I) &= f_{\text{Rice}}(r; A_I, \sigma) \\ &= f_{|X||A_I}^{(H_0)}(r|A_I), \end{aligned} \quad (2.29)$$

where the last line reflects the fact that the result is independent of the phase Θ_I .

Definition 1 *The Marcum Q-function is a common tabulated integral which gives the tail probabilities of a Rician pdf. It is defined as follows:*

$$Q_1(a, b) = \int_b^\infty x \exp \left\{ -\frac{(x^2 + a^2)}{2} \right\} I_0(ax) dx. \quad (2.30)$$

Theorem 1 *Let X and Y be two complex phasors with fixed amplitudes A_X and A_Y , and let the first phase Θ_X be fixed and the second phase Θ_Y be uniformly distributed on $[0, 2\pi)$. Then the magnitude of the sum of the two phasors, i.e., $V = |X + Y|$, has the following pdf:*

$$\begin{aligned} f_{2\text{-Phasor}}(v; A_X, A_Y) \\ = \frac{2}{\pi} \frac{v}{\sqrt{-(v^2 - (A_X - A_Y)^2)(v^2 - (A_X + A_Y)^2)}} 1_{[|A_X - A_Y|, A_X + A_Y]}(v). \end{aligned} \quad (2.31)$$

Proof We follow a derivation similar to [78]. Without loss of generality we can assume that $\Theta_X = 0$. Otherwise, we can perform a coordinate rotation of the real and imaginary axes such that A_X and A_Y are unchanged, $\Theta_X = 0$, and Θ_Y is still uniformly distributed on $[0, 2\pi)$. Thus,

$$\begin{aligned} V &= |X + Y| \\ &= |A_X + A_Y e^{i\Theta_Y}| \\ &= \sqrt{A_X^2 + A_Y^2 + 2A_X A_Y \cos \Theta_Y}, \\ F_V(v) &= P(\{V \leq v\}) \\ &= P(\{A_X^2 + A_Y^2 + 2A_X A_Y \cos \Theta_Y \leq v^2\}) \\ &= P\left(\left\{\cos \Theta_Y \leq \frac{v^2 - (A_X^2 + A_Y^2)}{2A_X A_Y}\right\}\right) \\ &= P\left(\left\{g(\Theta_Y) \geq \arccos \left[\frac{v^2 - (A_X^2 + A_Y^2)}{2A_X A_Y}\right]\right\}\right) \\ &= 1 - \frac{1}{\pi} \arccos \left[\frac{v^2 - (A_X^2 + A_Y^2)}{2A_X A_Y}\right], \end{aligned}$$

and

$$\begin{aligned} f_V(v) &= \frac{dF_V(v)}{dv} \\ &= \frac{2}{\pi} \frac{v}{\sqrt{4A_X^2 A_Y^2 - (v^2 - (A_X^2 + A_Y^2))^2}} 1_{[|A_X - A_Y|, A_X + A_Y]}(v), \end{aligned}$$

where

$$g(\Theta_Y) = \begin{cases} \Theta_Y, & \text{if } \Theta_Y \leq \pi, \\ 2\pi - \Theta_Y, & \text{if } \Theta_Y > \pi. \end{cases}$$

In the above, we have used the result that if Θ_Y is uniformly distributed on $[0, 2\pi)$, then $g(\Theta_Y)$ is uniformly distributed on $[0, \pi)$. With some algebra, we may rewrite the resulting pdf in the form of (2.31). \blacksquare

Definition 2 In (2.23) under H_1 , define the quantity

$$V = |A_S e^{i\Theta_S} + A_I e^{i\Theta_I}|. \quad (2.32)$$

Corollary 2 It follows from Theorem 1 that V in (2.32) has the following conditional pdf, given A_I and Θ_I :

$$\begin{aligned} f_{V|A_I, \Theta_I}(v|A_I, \Theta_I) & \quad (2.33) \\ &= f_{2\text{-Phasor}}(v; A_I, A_S) \\ &= \frac{2}{\pi} \frac{v}{\sqrt{-(v^2 - (A_I - A_S)^2)(v^2 - (A_I + A_S)^2)}} 1_{[|A_X - A_Y|, A_X + A_Y]}(v) \\ &= f_{V|A_I}(v|A_I), \end{aligned}$$

where the last line reflects the fact that the result is independent of the phase Θ_I .

Corollary 3 It follows from Fact 1, (2.23), and (2.32) that under H_1 the amplitude of the matched filter output $|X|$ is conditionally Rician, given V , and has conditional pdf

$$f_{|X||V}^{(H_1)}(r|v) = f_{\text{Rice}}(r; v, \sigma). \quad (2.34)$$

Theorem 2 *Let $|Y_1|, \dots, |Y_N|$ be i.i.d. and Rician with parameters μ and σ . Then the sum*

$$Z = \sum_{j=1}^N |Y_j|^2$$

is a scaled non-central chi-square random variable with characteristic function

$$\Phi_Z(\omega) = E[e^{i\omega Z}] = \frac{1}{(1 - 2i\omega\sigma^2)^N} \exp \left\{ \frac{i\omega N\mu^2}{1 - 2i\omega\sigma^2} \right\}. \quad (2.35)$$

Proof According to Fact 1, the Rician pdf of each $|Y_j|$ can be derived by defining each $|Y_j| = |X_j + \mu|$, where X_j are i.i.d. circular Gaussian random variables with mean zero and variance σ^2 , and μ is a real number.

By a simple coordinate rotation, $|Y_j|^2$ can be equivalently expressed as a sum of squares of two i.i.d. one-dimensional Gaussian random variables with mean $\mu/\sqrt{2}$ and variance σ^2 :

$$|Y_j|^2 = W_{j,1}^2 + W_{j,2}^2,$$

where $W_{j,1}$ and $W_{j,2}$ are i.i.d. Gaussian with mean $\mu/\sqrt{2}$ and variance σ^2 . Using this decomposition we can write the random variable Z as

$$Z = \sum_{j=1}^N |Y_j|^2 = \sum_{k=1}^2 \sum_{j=1}^N W_{j,k}^2.$$

This is just the sum of the squares of $2N$ i.i.d. Gaussian random variables with mean $\mu/\sqrt{2}$ and variance σ^2 . The scaled random variable $Z' = Z/\sigma^2$ then is the sum of the squares of $2N$ i.i.d. Gaussian random variables with mean $\mu/\sqrt{2\sigma^2}$ and unit variance. Reference [79, p. 207–211] states that this random variable $Z' = Z/\sigma^2$ has a non-central chi-squared distribution with $2N$ degrees of freedom and noncentrality parameter δ given by

$$\delta = \sum_{k=1}^2 \sum_{j=1}^N E^2 \left[\frac{W_{j,k}}{\sigma} \right] = 2N \frac{\mu^2/2}{\sigma^2} = \frac{N\mu^2}{\sigma^2}.$$

According to [79, p. 209], the characteristic function of Z' is

$$\Phi_{Z'}(\omega) = \frac{1}{(1 - 2i\omega)^N} \exp \left\{ \frac{i\omega N\mu^2/\sigma^2}{1 - 2i\omega} \right\},$$

so that the characteristic function of $Z = Z'\sigma^2$ is

$$\Phi_Z(\omega) = \frac{1}{(1 - 2i\omega\sigma^2)^N} \exp \left\{ \frac{i\omega N\mu^2}{1 - 2i\omega\sigma^2} \right\}.$$

■

Let us examine the *conditional* distribution of the statistic

$$Z = \sum_{n=1}^N |Y_n|^2 \quad (2.36)$$

in the cell-averaging processor from Figure 2.4, *given one value of A_I , constant across all cells*. Corollary 1 implies that the measurements $|Y_1|, \dots, |Y_N|$ are *conditionally* i.i.d. and Rician with parameters A_I and σ , *given A_I* . (Conditional independence across the N cells follows from the fact that the terms N_{noise} in (2.23) are assumed to be independent across all cells, and the pdfs of the amplitudes $|Y_1|, \dots, |Y_N|$ do not depend on the phase Θ_I , per Corollary 1.) Thus, we have the following result.

Corollary 4 *The conditional characteristic function of the statistic Z , conditioned on one value A_I , constant across all cells, is given by (2.35) with $\mu = A_I$, i.e.,*

$$\Phi_{Z|A_I}(\omega|A_I) = \frac{1}{(1 - 2i\omega\sigma^2)^N} \exp \left\{ \frac{i\omega N A_I^2}{1 - 2i\omega\sigma^2} \right\}, \quad (2.37)$$

which is the characteristic function of a scaled non-central chi-squared random variable.

Now consider the same statistic Z , but let the random variables A_I be i.i.d. across all cells. Then we have the following result.

Corollary 5 *The (unconditional) characteristic function of Z , assuming N i.i.d. realizations of the random variable A_I in the N neighboring cells Y_1, \dots, Y_N , is given by the following:*

$$\Phi_Z(\omega) = \frac{1}{(1 - 2i\omega\sigma^2)^N} \phi_{A_I^2}^N \left(\frac{i\omega}{1 - 2i\omega\sigma^2} \right), \quad (2.38)$$

where $\phi_{A_I^2}(s) = E[e^{sA_I^2}]$ is the moment generating function of A_I^2 .

Proof By Corollary 1 and Theorem 2 with $N = 1$, the *conditional* characteristic function of $|Y_1|^2$, given A_I , is

$$\Phi_{|Y_1|^2|A_I}(\omega|A_I) = \frac{1}{(1 - 2i\omega\sigma^2)} \exp \left\{ \frac{i\omega A_I^2}{1 - 2i\omega\sigma^2} \right\}.$$

Using iterated expectation we may find the *unconditional* characteristic function as follows:

$$\begin{aligned} \Phi_{|Y_1|^2}(\omega) &= E[e^{i\omega|Y_1|^2}] \\ &= E[E[e^{i\omega|Y_1|^2}|A_I]] \\ &= E[\Phi_{|Y_1|^2|A_I}(\omega|A_I)] \\ &= \int_{-\infty}^{\infty} \Phi_{|Y_1|^2|A_I}(\omega|a) f_{A_I}(a) da \\ &= \int_{-\infty}^{\infty} \frac{1}{1 - 2i\omega\sigma^2} \exp \left\{ \frac{i\omega a^2}{1 - 2i\omega\sigma^2} \right\} f_{A_I}(a) da \\ &= \frac{1}{1 - 2i\omega\sigma^2} E \left[\exp \left\{ \left(\frac{i\omega}{1 - 2i\omega\sigma^2} \right) A_I^2 \right\} \right] \\ &= \frac{1}{1 - 2i\omega\sigma^2} \phi_{A_I^2} \left(\frac{i\omega}{1 - 2i\omega\sigma^2} \right). \end{aligned}$$

Finally, we may use the fact that $|Y_1|^2, \dots, |Y_N|^2$ are i.i.d. with the above characteristic function to obtain the desired result:

$$\begin{aligned} \Phi_Z(\omega) &= E[e^{i\omega Z}] \\ &= E \left[\exp \left\{ i\omega \sum_{n=1}^N |Y_n|^2 \right\} \right] \\ &= \Phi_{|Y_1|^2}^N(\omega) \\ &= \frac{1}{(1 - 2i\omega\sigma^2)^N} \phi_{A_I^2}^N \left(\frac{i\omega}{1 - 2i\omega\sigma^2} \right), \end{aligned}$$

where $\phi_{A_I^2}(s) = E[e^{sA_I^2}]$ is the moment generating function of A_I^2 , which we allow to take a complex argument by analytic continuity. By the following lemma, this moment generating function converges for all ω , since A_I^2 is a non-negative random variable and

$$\operatorname{Re} \left(\frac{i\omega}{1 - 2i\omega\sigma^2} \right) \leq 0$$

for all $-\infty < \omega < \infty$. ■

The previous corollary defined the characteristic function of Z for the fast interference case. In order to obtain the corresponding pdf for use in numerical integration, we use a fast Fourier transform (FFT) algorithm to numerically Fourier-invert $\Phi_Z(\omega)$.

Lemma 1 *Let X be a non-negative random variable. Then its moment generating function*

$$\phi_X(s) = E[e^{sX}]$$

converges wherever $\text{Re}(s) \leq 0$.

Proof Since X is non-negative, we may write the moment generating function as follows:

$$\begin{aligned} \phi_X(s) &= E[e^{sX}] \\ &= \int_0^\infty f_X(x) e^{sx} dx, \end{aligned} \tag{2.39}$$

where $f_X(x)$ is the pdf of X , which we assume exists. The moment generating function converges if the above integral converges absolutely.

Since $f_X(x)$ is a pdf, for any $\epsilon > 0$ there exists some $0 < x_0 < \infty$ such that $f_X(x) < \epsilon$ whenever $x > x_0$. Letting $\rho = \text{Re}(s) \leq 0$,

$$\begin{aligned} &\int_0^\infty |f_X(x) e^{sx}| dx \\ &= \int_0^\infty f_X(x) e^{\rho x} dx \\ &= \int_0^{x_0} f_X(x) e^{\rho x} dx + \int_{x_0}^\infty f_X(x) e^{\rho x} dx \\ &\leq \int_0^{x_0} f_X(x) dx + \int_{x_0}^\infty \epsilon e^{\rho x} dx \\ &\leq 1 - \frac{\epsilon}{\rho} e^{\rho x_0} \\ &< \infty. \end{aligned}$$

Thus, the integral (2.39) exists for $\rho = \text{Re}(s) \leq 0$. ■

While the moment generating function $\phi_{A_I^2}(s)$ exists by Lemma 1, an analytical form is needed for computation. One can show (using [80, 8.353.4, p. 909]) that the

moment generating function of the square of a K -distributed random variable is given by

$$\phi_{K^2}(s) = \frac{1}{(-\lambda^2 s)^\alpha} \exp\left(-\frac{1}{\lambda^2 s}\right) \Gamma\left(1 - \alpha, -\frac{1}{\lambda^2 s}\right), \quad (2.40)$$

provided that $\alpha < 1$, where $\Gamma(x, y)$ is the incomplete gamma function:

$$\Gamma(x, y) = \int_y^\infty t^{x-1} e^{-t} dt. \quad (2.41)$$

Equipped with the above mathematical results, we now turn to computing the ROCs for the two receivers of interest. We start with the fixed-threshold receiver and then turn to the cell-averaging processor.

2.3.3 ROC equations for fixed-threshold detector

Consider the simple, fixed-threshold detector given by (2.26), where we have modeled the output X of the matched filter according to (2.23). We wish to determine the probability of false alarm P_{FA} and probability of detection P_{D} for this detector as a function of the threshold parameter T .

First let us calculate P_{FA} .

$$\begin{aligned} P_{\text{FA}} &= P^{(H_0)}(\{\phi(X) = 1\}) \\ &= P^{(H_0)}(\{|X| > T\}) \\ &= \int_T^\infty f_{|X|}^{(H_0)}(r) dr \\ &= \int_T^\infty \int_{-\infty}^\infty f_{|X||A_I}^{(H_0)}(r|a) f_{A_I}(a) da dr \\ &= \int_T^\infty \int_{-\infty}^\infty f_{\text{Rice}}(r; a, \sigma) f_{A_I}(a) da dr \\ &= \int_{-\infty}^\infty Q_1\left(\frac{a}{\sigma}, \frac{T}{\sigma}\right) f_{A_I}(a) da \\ &= E\left[Q_1\left(\frac{A_I}{\sigma}, \frac{T}{\sigma}\right)\right], \end{aligned}$$

where the fifth line follows from Corollary 1, and the sixth line follows by interchanging the integrals and using (2.28) and (2.30).

Now consider P_D .

$$\begin{aligned}
P_D &= P^{(H_1)}(\{\phi(X) = 1\}) \\
&= P^{(H_1)}(\{|X| > T\}) \\
&= \int_T^\infty f_{|X|}^{(H_1)}(r) dr \\
&= \int_T^\infty \int_{-\infty}^\infty \int_{-\infty}^\infty f_{|X||V,A_I}^{(H_1)}(r|v,a) f_{V|A_I}(v|a) f_{A_I}(a) da dv dr \\
&= \int_T^\infty \int_{-\infty}^\infty \int_{-\infty}^\infty f_{\text{Rice}}(r; v, \sigma) f_{2\text{-Phasor}}(v; a, A_S) f_{A_I}(a) da dv dr \\
&= \int_{-\infty}^\infty \int_{-\infty}^\infty Q_1\left(\frac{v}{\sigma}, \frac{T}{\sigma}\right) f_{2\text{-Phasor}}(v; a, A_S) f_{A_I}(a) da dv \\
&= E\left[Q_1\left(\frac{V}{\sigma}, \frac{T}{\sigma}\right)\right],
\end{aligned}$$

where the fifth line follows from Corollaries 2 and 3, and the sixth line follows by interchanging integrals and using (2.28) and (2.30).

In summary,

$$P_{\text{FA}} = \int_{-\infty}^\infty Q_1\left(\frac{a}{\sigma}, \frac{T}{\sigma}\right) f_{A_I}(a) da, \quad (2.42)$$

$$P_D = \int_{-\infty}^\infty \int_{-\infty}^\infty Q_1\left(\frac{v}{\sigma}, \frac{T}{\sigma}\right) f_{2\text{-Phasor}}(v; a, A_S) f_{A_I}(a) da dv. \quad (2.43)$$

By substituting (2.33) and (2.18) into the above, we may parametrically plot the ROC for the simple fixed-threshold receiver.

2.3.4 ROC equations for cell-averaging adaptive-threshold detector

We now turn to computing P_{FA} and P_{D} for the cell-averaging processor given by (2.27). Note that the distributions of the $N + 1$ matched filter outputs X, Y_1, \dots, Y_N depend on the interference amplitude A_I appearing in each cell. In particular,

$$\begin{aligned} f_{|Y_j||A_I}(r|A_I) &= f_{\text{Rice}}(r; A_I, \sigma), \\ f_{|X||A_I}^{(H_0)}(r|A_I) &= f_{\text{Rice}}(r; A_I, \sigma), \end{aligned} \tag{2.44}$$

$$\begin{aligned} f_{|X||A_I}^{(H_1)}(r|A_I) &= \int_{-\infty}^{\infty} f_{|X||V}^{(H_1)}(r|v) f_{V|A_I}(v|A_I) dv \\ &= \int_{-\infty}^{\infty} f_{\text{Rice}}(r; v, \sigma) f_{2\text{-Phasor}}(v; A_I, A_S) dv, \end{aligned} \tag{2.45}$$

where (2.44) follows from Corollary 1, and (2.45) follows from Corollaries 2 and 3.

As mentioned in Section 2.3.1, for the sake of analytical tractability we consider only the two extreme cases of slow (constant but random) A_I and fast (i.i.d.) A_I across the cells. Although this is only a subset of the possible scenarios, it allows for closed-form equations while illustrating the *range* of *possible* effects that interference can have on the cell-averaging processor.

Case 1: Slow interference

First, let us examine the extreme case in which the interference is “slow”, *i.e.*, one single random variable A_I applies across all $N + 1$ delay-Doppler cells. In this case, Corollary 4 applies to the statistic Z . We calculate P_D as follows:

$$\begin{aligned}
P_D &= P^{(H_1)}(\{|X| > \sqrt{(\tau/N)Z}\}) \\
&= \int_{-\infty}^{\infty} \int_{\sqrt{(\tau/N)Z}}^{\infty} f_{|X|,Z}^{(H_1)}(r, z) dr dz \\
&= \int_{-\infty}^{\infty} \int_{\sqrt{(\tau/N)Z}}^{\infty} \int_{-\infty}^{\infty} f_{|X|,Z|A_I}^{(H_1)}(r, z|a) f_{A_I}(a) da dr dz \\
&= \int_{-\infty}^{\infty} \int_{\sqrt{(\tau/N)Z}}^{\infty} \int_{-\infty}^{\infty} f_{|X||A_I}^{(H_1)}(r|a) f_{Z|A_I}(z|a) f_{A_I}(a) da dr dz \\
&= \int_{-\infty}^{\infty} \int_{\sqrt{(\tau/N)Z}}^{\infty} \int_{-\infty}^{\infty} \int_{-\infty}^{\infty} f_{\text{Rice}}(r; v, \sigma) f_{2\text{-Phasor}}(v; a, A_S) f_{Z|A_I}(z|a) \\
&\quad \cdot f_{A_I}(a) dv da dr dz \\
&= \int_{-\infty}^{\infty} \int_{-\infty}^{\infty} \int_{-\infty}^{\infty} Q_1\left(\frac{v}{\sigma}, \frac{\sqrt{(\tau/N)z}}{\sigma}\right) f_{2\text{-Phasor}}(v; a, A_S) f_{Z|A_I}(z|a) f_{A_I}(a) dv da dz \\
&= E\left[Q_1\left(\frac{V}{\sigma}, \frac{\sqrt{(\tau/N)Z}}{\sigma}\right)\right].
\end{aligned}$$

The fourth line follows from the fact that $|X|, |Y_1|, \dots, |Y_N|$ are statistically independent *conditioned on* A_I , since in (2.23) the N_{noise} terms are assumed to be independent across all cells, and the pdfs of the amplitudes $|X|, |Y_1|, \dots, |Y_N|$ are not affected by the random phase Θ_I (see Corollaries 1–3); the fifth line follows from (2.45); and the sixth line follows from (2.28) and (2.30). In the above, $f_{Z|A_I}(z|A_I)$ is the pdf corresponding to the characteristic function (2.37).

To compute P_{FA} , we take a shortcut by using the above formula for P_D with the substitution that by changing from H_1 to H_0 ,

$$f_{2\text{-Phasor}}(v; A_I, A_S) \mapsto \delta(v - A_I), \quad (2.46)$$

that is, under H_0 the quantity V from (2.32) takes on value A_I with probability one.

Using this shortcut, we get

$$\begin{aligned} P_{\text{FA}} &= \int_{-\infty}^{\infty} \int_{-\infty}^{\infty} Q_1 \left(\frac{a}{\sigma}, \frac{\sqrt{(\tau/N)z}}{\sigma} \right) f_{Z|A_I}(z|a) f_{A_I}(a) da dz \\ &= E \left[Q_1 \left(\frac{A_I}{\sigma}, \frac{\sqrt{(\tau/N)Z}}{\sigma} \right) \right]. \end{aligned}$$

In summary, for the slow interference case we can parametrically plot the ROC for the cell-averaging processor using

$$P_{\text{FA}} = \int_{-\infty}^{\infty} \int_{-\infty}^{\infty} Q_1 \left(\frac{a}{\sigma}, \frac{\sqrt{(\tau/N)z}}{\sigma} \right) f_{Z|A_I}(z|a) f_{A_I}(a) da dz, \quad (2.47)$$

$$P_{\text{D}} = \int_{-\infty}^{\infty} \int_{-\infty}^{\infty} \int_{-\infty}^{\infty} Q_1 \left(\frac{v}{\sigma}, \frac{\sqrt{(\tau/N)z}}{\sigma} \right) f_{2\text{-Phasor}}(v; a, A_S) f_{Z|A_I}(z|a) f_{A_I}(a) dv da dz, \quad (2.48)$$

along with (2.37), (2.18), and (2.33).

Case 2: Fast interference

Now, let us examine the opposite extreme case in which the interference is “fast”, *i.e.*, $N + 1$ i.i.d. realizations of the random variable A_I appear in the $N + 1$ matched

filter outputs X, Y_1, \dots, Y_N . In this case, Corollary 5 applies to the statistic Z . We compute P_D as follows:

$$\begin{aligned}
P_D &= P^{(H_1)}(\{|X| > \sqrt{(\tau/N)Z}\}) \\
&= \int_{-\infty}^{\infty} \int_{\sqrt{(\tau/N)Z}}^{\infty} f_{|X|,Z}^{(H_1)}(r, z) dr dz \\
&= \int_{-\infty}^{\infty} \int_{\sqrt{(\tau/N)Z}}^{\infty} f_{|X|}^{(H_1)}(r) f_Z(z) dr dz \\
&= \int_{-\infty}^{\infty} \int_{\sqrt{(\tau/N)Z}}^{\infty} \int_{-\infty}^{\infty} f_{|X||A_I}^{(H_1)}(r|a) f_{A_I}(a) f_Z(z) da dr dz \\
&= \int_{-\infty}^{\infty} \int_{\sqrt{(\tau/N)Z}}^{\infty} \int_{-\infty}^{\infty} \int_{-\infty}^{\infty} f_{\text{Rice}}(r; v, \sigma) f_{2\text{-Phasor}}(v; a, A_S) f_{A_I}(a) f_Z(z) dv da dr dz \\
&= \int_{-\infty}^{\infty} \int_{-\infty}^{\infty} \int_{-\infty}^{\infty} Q_1\left(\frac{v}{\sigma}, \frac{\sqrt{(\tau/N)z}}{\sigma}\right) f_{2\text{-Phasor}}(v; a, A_S) f_{A_I}(a) f_Z(z) dv da dz \\
&= E\left[Q_1\left(\frac{V}{\sigma}, \frac{\sqrt{(\tau/N)Z}}{\sigma}\right)\right].
\end{aligned}$$

The third line follows from the independence of X, Y_1, \dots, Y_N assumed in this case; the fifth line follows from (2.45); and the sixth line follows from (2.28) and (2.30). In the above, $f_Z(z)$ is the pdf corresponding to the characteristic function (2.38).

As in the slow interference case, we compute P_{FA} by substituting the shortcut (2.46) into the above formula for P_D :

$$\begin{aligned}
P_{FA} &= \int_{-\infty}^{\infty} \int_{-\infty}^{\infty} Q_1\left(\frac{a}{\sigma}, \frac{\sqrt{(\tau/N)z}}{\sigma}\right) f_{A_I}(a) f_Z(z) da dz \\
&= E\left[Q_1\left(\frac{A_I}{\sigma}, \frac{\sqrt{(\tau/N)Z}}{\sigma}\right)\right].
\end{aligned}$$

Summarizing the results for the fast interference case, we can parametrically plot the ROC for the cell-averaging processor using

$$P_{FA} = \int_{-\infty}^{\infty} \int_{-\infty}^{\infty} Q_1\left(\frac{a}{\sigma}, \frac{\sqrt{(\tau/N)z}}{\sigma}\right) f_{A_I}(a) f_Z(z) da dz, \quad (2.49)$$

$$P_D = \int_{-\infty}^{\infty} \int_{-\infty}^{\infty} \int_{-\infty}^{\infty} Q_1\left(\frac{v}{\sigma}, \frac{\sqrt{(\tau/N)z}}{\sigma}\right) f_{2\text{-Phasor}}(v; a, A_S) f_{A_I}(a) f_Z(z) dv da dz, \quad (2.50)$$

along with (2.18), (2.38), and (2.33).

We have now derived expressions for the probability of false alarm P_{FA} and probability of detection P_{D} for both classes of receivers. For the simple fixed-threshold detector, we use (2.42) and (2.43). For the cell-averaging processor with slow interference we use (2.47) and (2.48); for the cell-averaging processor with fast interference we use (2.49) and (2.50).

Using these parametric equations for P_{FA} and P_{D} derived above, we now turn to plotting some results.

2.4 Effects of interference on radar: Results

In plotting P_{FA} and P_{D} for the two radar detectors analyzed, we focus our investigation on two questions: (i) How do the *shape* parameters p and α of the interference distribution (2.18) affect detection performance? and (ii) How does the *scale* parameter λ of the interference distribution affect detection?

We devote one subsection to each of these questions in turn. Regarding the first question, we will find that non-Gaussian interference can cause the two radar detectors analyzed to behave in problematic and unintended ways, even at relatively low INR. Regarding the second question, we will see that the adaptive-threshold detector can suffer insidious losses in P_{D} , similar to results that NTIA observed in their experimental study, even when the interference is Gaussian and relatively low-INR. Finally, we also will see that the coherence time of the interference (*i.e.*, “slow” versus “fast”) has a strong influence on the radar’s behavior.

2.4.1 Effects of non-Gaussian statistical behavior

First, we look at the impact of non-Gaussian shape parameters $p < 1$ and $\alpha < \infty$ in the interference distribution (2.18) on the radar detectors’ performance. We proceed by examining how the ROCs of the two receivers change with the shape parameters p and α .

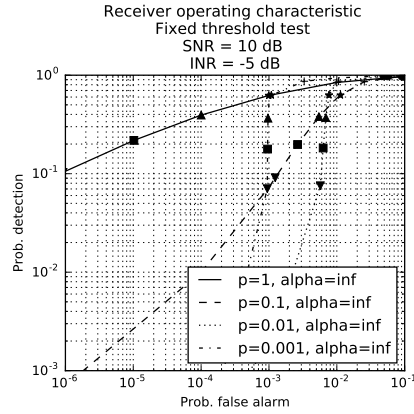
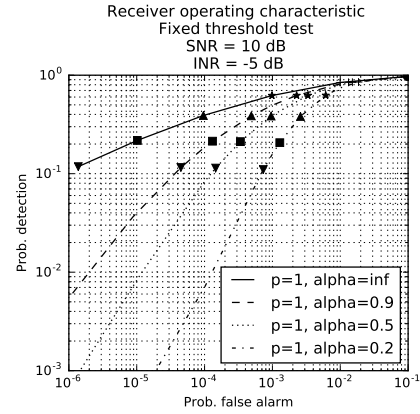
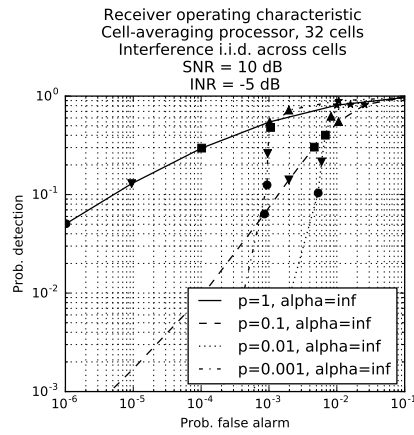
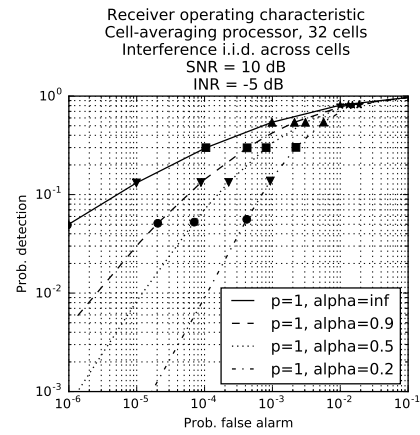
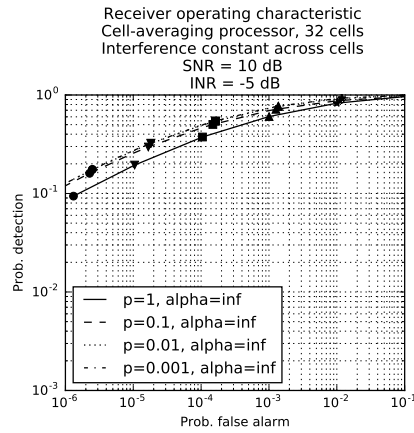
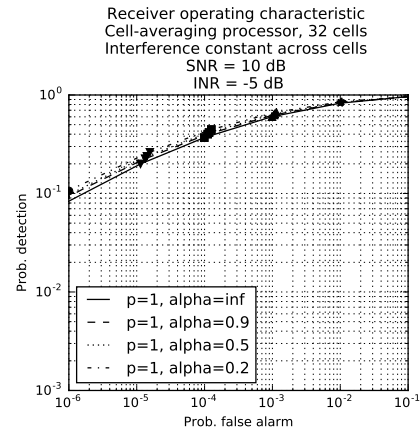
(a) Fixed-threshold test ($p \ll 1$).(b) Fixed-threshold test ($\alpha < \infty$).(c) Cell-averaging processor ($p \ll 1$).(d) Cell-averaging processor ($\alpha < \infty$).(e) Cell-averaging processor ($p \ll 1$).(f) Cell-averaging processor ($\alpha < \infty$).

Figure 2.5. ROCs for both detectors under impulsive and heavy-tailed interference.

The equations (2.42), (2.43), (2.47), (2.48), (2.49), and (2.50) are numerically integrated to plot ROCs of the two receivers. A total of 96 ROCs have been computed [3] for following sets of parameters: the fixed-threshold detector, the cell-averaging processor with fast interference, and the cell-averaging processor with slow interference; impulsive interference ($p \ll 1$ in (2.18)) and heavy-tailed interference ($\alpha < \infty$ in (2.18)); INRs of -10 , -5 , 0 , and 5 dB; and SNRs of 0 , 5 , 10 , and 15 dB.

The numerical integration of the expressions for P_{FA} and P_{D} meets with some difficulties, which Appendix A addresses. We use Monte Carlo simulation to assess the validity of the computed numerical integrals, and as shown in Appendix B, our calculations show good agreement between numerical integration and Monte Carlo simulation.

Figure 2.5 shows a representative subset of the ROCs computed. The complete set of computed results is available in [3] and Appendix C. Each plot in Figure 2.5 corresponds to a single type of receiver, a single class of interference (impulsive or heavy-tailed), as well as a single, fixed SNR = 10 dB and INR = -5 dB. Within a plot, the various curves correspond to various cases of shape parameters p and α in the interference distribution (2.18), with the mean INR held fixed across all the curves in a given plot. The Gaussian case of $p = 1$ and $\alpha \rightarrow \infty$ is always shown for the sake of comparison.

In addition, on each plot markers indicate operating points corresponding to specific choices of the threshold parameters T (fixed threshold) or τ (cell-averaging adaptive-threshold scaling parameter) across the various cases of interference distribution shapes. This allows one to interpret, for example, that if the threshold parameter T or τ had been set for some *intended* P_{FA} by assuming Gaussian interference, then one can use these markers to see what the *actual* P_{FA} would be if the interference turned out to be non-Gaussian in the field. In other words, the markers indicate the drift in operating point caused by violation of the assumption of Gaussian interference. (For example, if one set T to obtain $P_{\text{FA}} \approx 10^{-5}$ in Figure 2.5(a) assuming Gaussian interference, and if the interference instead was impulsive with

$p = 10^{-2}$, then the actual P_{FA} achieved by the detector would be roughly 6×10^{-3} , as indicated by the square markers in the figure.)

The qualitative effect of non-Gaussian interference on the ROCs can be categorized roughly into three types of behavior, depending on whether the receiver is the fixed-threshold test, the cell-averaging test with fast interference, or the cell-averaging test with slow interference. We discuss these results in turn.

Fixed-threshold detector

The results for the fixed-threshold detector are illustrated in Sub-Figures 2.5(a)–2.5(b), the former corresponding to impulsive interference ($p \ll 1$) and the latter to heavy-tailed interference ($\alpha < \infty$).

As shown in Sub-Figure 2.5(a), the ROCs for the fixed-threshold detector with impulsive interference ($p \ll 1$) tend to have a region with extremely high slope near $P_{\text{FA}} \approx p$. Furthermore, no matter what the intended false alarm probability $10^{-6} \leq P_{\text{FA}} \leq 10^{-1}$ would be under Gaussian interference, under impulsive interference one usually obtains an actual false alarm probability of $P_{\text{FA}} \approx p$, near the high-slope region of the ROC. It makes sense that the detector would operate in this high-slope region where $P_{\text{FA}} \approx p$ for most moderate values of the threshold parameter T , since under H_0 with impulsive interference, either the detector sees zero interference with probability $(1 - p)$, in which case the detector tends to declare H_0 (no target present), or the detector sees very large interference (with average power corresponding to INR/p) with probability p , in which case the detector tends to declare H_1 (target present). Thus, the probability of false alarm is governed strongly by the impulsiveness of the interference.

As shown in Sub-Figure 2.5(b), the ROCs for the fixed-threshold detector with heavy-tailed interference ($\alpha < \infty$) tend to drift to the right as the tails of the interference distribution become heavier. As in the case of impulsive interference, the actual false alarm probability under non-Gaussian interference exceeds the intended false

alarm probability under Gaussian interference, sometimes by more than an order of magnitude or two.

Cell-averaging processor with fast interference

The results for the cell-averaging processor with fast interference are illustrated in Sub-Figures 2.5(c)–2.5(d), the former corresponding to impulsive interference ($p \ll 1$) and the latter to heavy-tailed interference ($\alpha < \infty$).

As shown in these sub-figures, the ROCs for the cell-averaging processor with fast interference tend to behave qualitatively similarly to the corresponding ROCs for the simple fixed-threshold detector. For impulsive interference ($p \ll 1$), this corresponds to a high-slope region in the ROC near $P_{\text{FA}} \approx p$, as discussed previously (*cf.* Sub-Figure 2.5(c)). The reason that the cell-averaging processor exhibits the same qualitative behavior in fast interference as the fixed-threshold detector likely may be that, due to the law of large numbers, the composite threshold $(\tau/N)Z$ is relatively immune to impulsiveness in the interference, whereas the CUT is very sensitive to the impulsiveness of the interference.

Cell-averaging processor with slow interference

The results for the cell-averaging processor with slow interference are illustrated in Sub-Figures 2.5(e)–2.5(f), the former corresponding to impulsive interference ($p \ll 1$) and the latter to heavy-tailed interference ($\alpha < \infty$).

As shown in these sub-figures, the behavior of the cell-averaging processor differs significantly in the slow interference case compared with the fast interference case just discussed. The actual false alarm probability P_{FA} under non-Gaussian interference exceeds that intended under Gaussian interference. The probability of detection P_{D} also may increase due to impulsive interference, although sometimes P_{D} decreases relative to the Gaussian ROC, leading to a crossing of the Gaussian and non-Gaussian

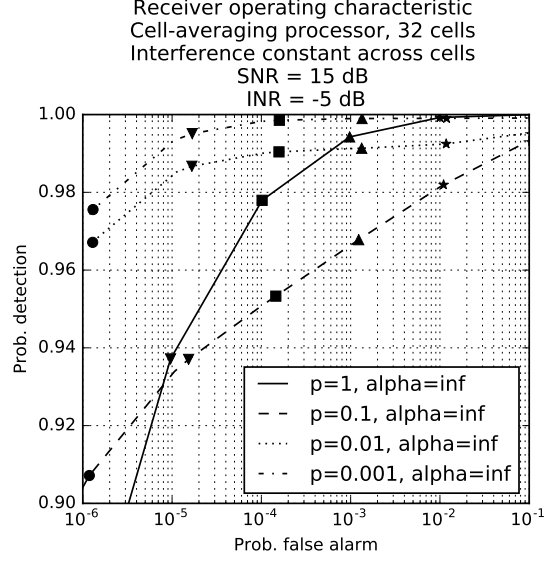


Figure 2.6. Rare crossing of non-Gaussian and Gaussian ROCs, for the case of slow, impulsive interference

ROCs in rare instances, as shown in Figure 2.6. This ROC-crossing phenomenon is explained in Appendix D.

2.4.2 Effects of changing INR

The last subsection isolated the *shape* parameters p and α in the interference distribution (2.18) to examine the effects of non-Gaussian statistical variation on the ROCs of the two radar detectors. This subsection now turns to the effect of the *scale* parameter λ of the interference pdf (2.18), which is related to INR. We will fix the shape parameters to $p = 1$ and $\alpha \rightarrow \infty$ (Gaussian interference with Rayleigh envelope) in order to isolate the effects of INR on the two types of radar detectors.

In order to evaluate the effects of INR on the two detectors' performance, we have plotted 36 plots of P_D and P_{FA} versus INR [3] for the following cases: fixed-threshold test, cell-averaging processor with fast interference, cell-averaging processor with slow interference; baseline P_{FA} (in the absence of strong interference) of about $10^{-4}, 10^{-8}, 10^{-12}$; SNRs of 5, 10, 15, and 20 dB.

For the fixed-threshold detector, both P_{FA} and P_{D} tend to increase with increasing INR. This makes sense because increasing the interference level generally causes the CUT to exceed a fixed threshold more often, leading to more decisions of H_1 (target present). Only for high SNR does P_{D} sometimes decrease slightly with increasing INR, due to destructive interference to the signal under H_1 .

For the cell-averaging processor, P_{D} decreases with increasing INR, sometimes by over an order of magnitude as INR varies from -10 to $+2$ dB, while P_{FA} either decreases or remains roughly constant with increasing INR. An example of this decrease in P_{D} caused by relatively low-level interference, without an accompanying increase in P_{FA} , is illustrated in Figure 2.7. This is an interesting result, reminiscent of the “insidious” NTIA results discussed in the Introduction. However, we note that our definition of INR (mean INR at the output of the matched filter, *cf.* (2.25)) may differ from that in [64], making a direct comparison difficult. Importantly, we observe that a drop in P_{D} occurs across all calculations involving the cell-averaging processor for both slow and fast (“white”) Gaussian interference; in fact, the decrease in P_{D} is more severe for fast interference. That such a large drop in P_{D} occurs even for white Gaussian interference shows that the NTIA results actually may not be that surprising when an adaptive threshold is used in radar detection.

The explanation for this drop in P_{D} at relatively low INR is captured graphically in Figure D.2 in Appendix D. Essentially, low-level interference causes a boost to the threshold-setting parameter Z , and this dominates over the effects of constructive and destructive interference to the signal in the CUT $|X|^2$ under H_1 .

2.5 Conclusions

We have proposed a statistical model for wireless communications interference to radar based on existing interference and clutter models and supported by original simulations. In the process, we have seen that both Gaussian and non-Gaussian statistics are plausible and deserve consideration, depending on the modeling situation, in con-

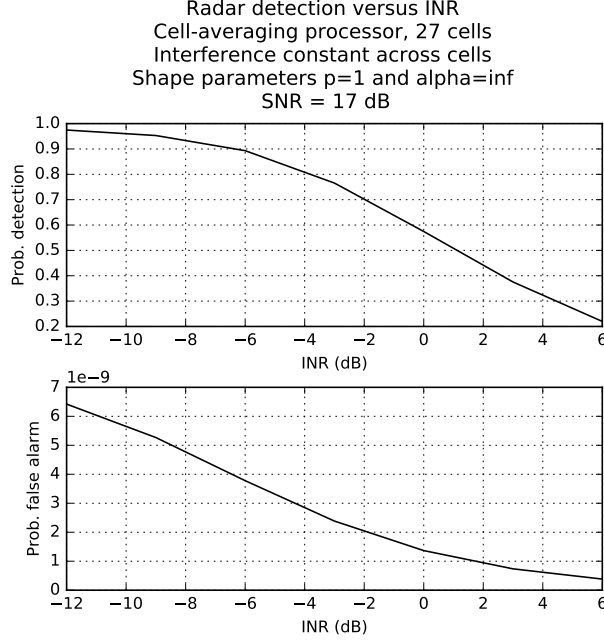


Figure 2.7. Radar P_D and P_{FA} versus INR for the case of the cell-averaging processor with 27 cells, slow Gaussian (Rayleigh) interference, a fixed threshold scalar τ , and SNR = 17 dB.

trast to previous work which has simply assumed a Gaussian interference model [47]. Non-Gaussian models can result from averaging over changing wireless propagation characteristics (such as multipath fading) or changing network conditions (such as the number or locations of transmitting sources). Whether one chooses to use a model conditioned on fixed network and channel conditions or a model based on averaging over fluctuating conditions likely will depend on the modeling application.

We also have derived equations for the probability of false alarm P_{FA} and probability of detection P_D for two types of radar receivers, given our proposed pdf for the interference. The results suggest several insights for radar-communications spectrum sharing: (i) As shown in Sub-Figures 2.5(c)–2.5(d), the cell-averaging processor, which has a CFAR in AWGN only, can have a highly variable false alarm rate when subjected to fast non-Gaussian interference. This result makes sense because the cell-averaging processor only estimates one parameter of the noise-plus-interference

distribution—the mean square value—but non-Gaussian distributions have additional kurtosis parameters which significantly impact tail probabilities. (ii) As can be seen by comparing Sub-Figures 2.5(c)–2.5(d) with Sub-Figures 2.5(e)–2.5(f), and as mentioned in Section 2.4.2, the behavior of the cell-averaging processor can vary significantly depending on the coherence time of the interference (*i.e.*, “fast” versus “slow”). (iii) Finally, as illustrated in Figure 2.7, the cell-averaging processor is susceptible to “insidious” drops in P_D at relatively low INRs, without an accompanying increase in P_{FA} . This is similar to results in the NTIA report discussed in the Introduction, although potentially different definitions of INR as well as other system differences make direct comparisons with [64] difficult. Note that the first two effects (i)–(ii) involve model mismatch between the wireless communications interference and AWGN, either through non-Gaussian interference statistics or non-white interference coherence time; the latter effect (iii), on the other hand, involves a boost to the underlying noise floor in the radar detector. Both these mechanisms of interference effects are important to consider when assessing spectrum sharing scenarios.

These results have several implications for spectrum sharing policy and technology. First, when interference is not well modeled as AWGN, the mean INR does not completely characterize the interference process, and additional interference characteristics such as kurtosis/impulsiveness and coherence time can significantly impact radar performance. Second, we have found that thresholds of INR (as defined in (2.25)) for interference protection to radar may need to be relatively low—*e.g.*, about -6 to -2 dB. Third, radar receivers may improve performance by adjusting to non-Gaussian interference environments when sharing spectrum with communications systems. One possible radar detector for non-Gaussian interference backgrounds is a matched filter followed by a more intelligent adaptive threshold than the cell-averaging processor, perhaps such as that proposed by Weber and Haykin [81]. Another possibility for radar detection in non-Gaussian interference is to use alternatives to the matched filter, such as those discussed in [82], [65, 66], and [83, 84], as these can boost detection performance over the traditional matched filter in non-Gaussian environments.

Future work could extend the model in this chapter to include: (i) Fluctuating radar target models in a pulsed radar, (ii) Arbitrary correlation in the interference, beyond simply the “fast” and “slow” extreme cases, and (iii) Additional radar detector architectures, such as an order-statistic adaptive-threshold (OS-CFAR), and interference rejection techniques. In addition, the development of novel radar signal processing to mitigate wireless communications interference also deserves attention in future research, including the application of non-linear detectors for non-Gaussian backgrounds (such as those just mentioned) to spectrum sharing scenarios.

3. OPTIMAL LINEAR DETECTION OF SIGNALS IN CYCLOSTATIONARY, LINEARLY-MODULATED, DIGITAL COMMUNICATIONS INTERFERENCE

3.1 Introduction

This chapter proposes a radar receiver that uses *temporal, whitening-based signal processing* to mitigate interference from a broad class of communications interference. The analysis and results of this chapter have been submitted for publication in [4].

3.1.1 Motivation

Many broadband wireless communications systems use some form of linear, digital modulation such as OFDM or CDMA. When such linearly modulated digital communications (LMDC) signals are sampled quickly enough (*e.g.*, faster than the pulse symbol duration T), the received sampled signals exhibit temporal correlation, and it is well known that the deflection-optimal linear detector of a known signal in correlated background consists of a whitening filter followed by a matched filter. Standard whitening filters assume a stationary model for the LMDC interference, which arises when the receiver knows only the LMDC pulse shape $g(t)$ and pulse symbol duration T , and in particular, when the delays $\{t_{d,n}\}_{n=1}^{N'}$ of the received LMDC signals are modeled as unknown, random, and uniformly distributed on $[0, T)$. If additional side information is available to the receiver (or is effectively estimated by it), such as the delays $\{t_{d,n}\}_{n=1}^N$ and mean-square pulse amplitudes $\{\mathcal{E}_{I,n}\}_{n=1}^N$ of the N ($N < N'$) most dominant LMDC signals, a more precise, cyclostationary model may accurately describe the LMDC interference. The additional side information implicit in this cyclostationary model is intuitively expected to increase the detection performance of

the whitener-plus-matched-filter relative to a detector based solely on a stationary interference model. In this chapter, we derive the whitening filter for cyclostationary LMDC interference plus stationary noise, and we seek to quantify the detection gain produced by the proposed cyclostationary whitener relative to the standard stationary whitener.

Cyclostationary theory is discussed in [85] (and related works). Much of the work applying cyclostationary theory to detection focuses on the detection *of* cyclostationary signals *in* stationary noise [86,87], rather than this chapter’s focus on detection *of* known signals *in* cyclostationary interference. One exception is the work in [88], which examines detection of known signals in cyclostationary background of a different class than is investigated in this chapter.

3.1.2 Overview

We briefly outline the primary contributions of this chapter. Section 3.2 describes the standard, stationary statistical model for LMDC interference and its associated whitening filter. Then Section 3.3 derives the whitening filter for cyclostationary LMDC interference in stationary noise. The proposed whitening filter has equivalent representations as (i) the *form* of a multiuser detector followed by an interference canceler, and (ii) a frequency-shift (FRESH) filter—both of which are presented. Section 3.4 derives and plots estimates of SINR for both the stationary-based detector and the cyclostationary-based detector. The results suggest that the cyclostationary-based detector can have significantly better performance than the stationary-based detector, particularly when the number N of dominant interfering LMDC sources is small and their INR is large relative to the stationary background (which could include both stationary LMDC interference and stationary noise). Finally, Section 3.5 concludes the chapter.

3.2 Linear whitening of stationary LMDC interference

Suppose a radar receives a signal

$$r(t) = \begin{cases} I(t) + N(t), & \text{under } H_0, \\ I(t) + N(t) + \gamma s(t), & \text{under } H_1, \end{cases} \quad (3.1)$$

where $I(t)$ is LMDC interference, $N(t)$ is circularly-symmetric, complex-valued additive white Gaussian noise (C-AWGN) with PSD \mathcal{E}_N , γ is an unknown and deterministic complex signal amplitude, and $s(t)$ is a known deterministic signal, respectively. Let us write the LMDC interference as

$$I(t) = \sum_{n=1}^N \sum_{m=-\infty}^{\infty} I_n[m] g(t - mT - t_{d,n}), \quad (3.2)$$

where $\{I_n[m]\}_{m=-\infty}^{\infty}\}_{n=1}^N$ are N independent, stationary sequences of complex-valued, circularly symmetric, zero-mean, mutually uncorrelated digital data symbols having respective mean-squares $E[|I_n[m]|^2] = \mathcal{E}_{I,n}$; $g(t)$ is a pulse shaping waveform; T is the pulse symbol duration; and $\{t_{d,n}\}_{n=1}^N$ are delays in the interval $[0, T)$. Then the optimal detector of H_1 versus H_0 , in terms of statistical deflection or SINR, first whitens the received signal $r(t)$ and the signal to be detected $s(t)$, and then correlates the whitened signals to form a statistic U , whose magnitude is compared with a threshold:

$$r_w(t) = \int_{-\infty}^{\infty} h(t, \tau) r(\tau) d\tau, \quad (3.3)$$

$$s_w(t) = \int_{-\infty}^{\infty} h(t, \tau) s(\tau) d\tau, \quad (3.4)$$

$$U = \int_{-\infty}^{\infty} r_w(t) s_w^*(t) dt, \quad (3.5)$$

$$\phi(U) = \begin{cases} 1, & |U| > u_t \\ 0, & |U| \leq u_t, \end{cases} \quad (3.6)$$

where $h(t_1, t_2)$ is the kernel of the whitening filter, and u_t is the detector threshold.

If the delays $\{t_{d,n}\}_{n=1}^N$ at which the LMDC signals reach the radar receiver are modeled as random and uniformly distributed on $[0, T)$, one can show that $I(t)$ is stationary with autocorrelation function

$$\begin{aligned} R_{II}^{(s)}(t_2 - t_1) &= E[I(t_1)I^*(t_2)] \\ &= \frac{\mathcal{E}_I}{T} \int_{-\infty}^{\infty} g(\tau)g(t_2 - t_1 + \tau) d\tau, \end{aligned} \quad (3.7)$$

where the superscript (s) distinguishes this stationary autocorrelation from a cyclostationary autocorrelation to be presented later, and where

$$\mathcal{E}_I = \sum_{n=1}^N \mathcal{E}_{I,n}. \quad (3.8)$$

Because this autocorrelation depends only on the time difference $(t_2 - t_1)$, its eigen-decomposition is given simply by Fourier analysis, and it is straightforward to show that the stationary whitening filter has the kernel:

$$h_s(t_1, t_2) = \int_{-\infty}^{\infty} \sqrt{\frac{\mathcal{E}_N}{\mathcal{E}_N + S_{II}^{(s)}(f)}} e^{i2\pi f(t_2 - t_1)} df, \quad (3.9)$$

where

$$S_{II}^{(s)}(f) = \int_{-\infty}^{\infty} R_{II}^{(s)}(\tau) e^{-i2\pi f\tau} d\tau \quad (3.10)$$

$$= \frac{\mathcal{E}_I}{T} |\tilde{G}(f)|^2 \quad (3.11)$$

is the PSD of the interference, and $\tilde{G}(f)$ is the Fourier transform of the pulse shape $g(t)$:

$$\tilde{G}(f) = \int_{-\infty}^{\infty} g(t) e^{-i2\pi ft} dt. \quad (3.12)$$

(We may scale the kernel $h_s(t_1, t_2)$ arbitrarily without affecting the SINR of the output, and we have chosen to scale it here by $\sqrt{\mathcal{E}_N}$.)

Stationary whitening of LMDC interference is well understood. However, when the delays $\{t_{d,n}\}_{n=1}^N$ of the LMDC signals are known, the LMDC interference becomes cyclostationary, having a periodic autocorrelation function, and this cyclostationarity may be exploited to improve whitening-based detection. This chapter develops the cyclostationary LMDC whitener, and it investigates the relative merits (in terms of detection performance) of cyclostationary over stationary whitening.

3.3 Linear whitening of cyclostationary LMDC interference

The form of the whitening filter for stationary LMDC interference and C-AWGN is known and was described in the previous section. In this section, we develop the whitening filter for *cyclostationary* LMDC interference and stationary interference-plus-noise. We will see that the solution to this whitening problem is rich with mathematical structure and practical implications.

It turns out that the solution to the cyclostationary LMDC whitening problem is significantly simpler if the LMDC interference is pulse-shape synchronized with respect to the receiver of interest—in other words, if every LMDC signal arrives at the radar receiver with the same delay t_d (modulo a pulse symbol duration T). This is a highly unrealistic assumption in wireless scenarios for two reasons: (i) In wireless communications networks, it is difficult and expensive to pulse-shape synchronize multiple LMDC transmitters *with respect to some centralized receiver*, such as a base station in a cellular network; (ii) Even if the LMDC transmitters are pulse-shape synchronized with respect to some centralized receiver (such as a base station), the receiver of interest which views them as interference (such as a nearby radar receiver) will likely be in another location, so that propagation delays are no longer synchronized *with respect to this receiver of interest*.

However, although it is an unrealistic scenario, we analyze the pulse-shape synchronized case first in order to gain insight and intuition into the problem, and then we turn to the more complicated and realistic asynchronous case.

3.3.1 Pulse-shape synchronized case

The autocorrelation of cyclostationary LMDC interference is given by the following theorem, assuming that the LMDC interference is pulse-shape synchronized. In this chapter, we model the pulse symbol amplitudes $I[m]$ as a white, stationary, infinite sequence of circularly symmetric complex random variables. This allows us to ignore effects of transients due to LMDC transmitters turning ON and OFF, inter-pulse

correlation due to cyclic prefixes, statistical effects of different symbol constellations, and so forth, in order to focus on the basic structure of the problem. We leave analysis of these more complicated issues to future work.

Theorem 3 *Let $I(t)$ be cyclostationary LMDC interference having the following form:*

$$I(t) = \sum_{m=-\infty}^{\infty} I[m]g(t - mT - t_d), \quad (3.13)$$

where $\{I[m]\}_{m=-\infty}^{\infty}$ is a stationary sequence of complex-valued, circularly symmetric, zero-mean, mutually uncorrelated digital data symbols having mean-square $E[|I[m]|^2] = \mathcal{E}_I$; $g(t)$ is a unit-energy pulse shaping waveform; T is the pulse symbol duration; and t_d is a deterministic delay in the interval $[0, T)$.

For $I(t)$ defined in this way, the autocorrelation $R_{II}(t_1, t_2) = E[I(t_1)I^*(t_2)]$ of $I(t)$ is given by

$$R_{II}(t_1, t_2) = \mathcal{E}_I \sum_{m=-\infty}^{\infty} g(t_1 - mT - t_d)g(t_2 - mT - t_d). \quad (3.14)$$

Proof The proof is straightforward based on the assumption that $E[I[m]I^*[n]] = \mathcal{E}_I\delta_{mn}$, where δ_{mn} is the Kronecker delta. ■

We will see that the autocorrelation function given in Theorem 3 is *singular*; that is, it has a nontrivial null space. This has two important implications for signal detection. First, *it is impossible to whiten cyclostationary LMDC interference*, in the sense that no linear operator can transform the interference $I(t)$ to produce an output having autocorrelation $\delta(t_2 - t_1)$, where $\delta(\cdot)$ denotes the Dirac delta function. Second, whitening is not actually needed for signal detection, because *perfect signal detection is possible in cyclostationary LMDC interference*. We can simply project the received signal $r(t)$ onto the null space of $R_{II}(t_1, t_2)$, and any nonzero signal component in this null space indicates the presence of a non-LMDC signal.

However, although the singular nature of $R_{II}(t_1, t_2)$ is interesting from a theoretical perspective, in practical situations LMDC interference is always observed in the presence of noise. When the noise is modeled as white, such as C-AWGN, this

has the effect of diagonal loading on the autocorrelation, forcing all its eigenvalues to be positive. In this case, whitening is possible and forms an essential part of the deflection-optimal linear detector. With the addition of C-AWGN, we can summarize the cyclostationary whitening problem as follows.

Problem 1 *Let $I(t)$ be cyclostationary LMDC interference as in Theorem 3, and let $N(t)$ be C-AWGN, independent of $I(t)$ and having PSD \mathcal{E}_N . Then the autocorrelation $R_{YY}(t_1, t_2) = E[Y(t_1)Y^*(t_2)]$ of the sum $Y(t) = I(t) + N(t)$ is*

$$R_{YY}(t_1, t_2) = \mathcal{E}_I \sum_{m=-\infty}^{\infty} g(t_1 - mT - t_d)g(t_2 - mT - t_d) + \mathcal{E}_N \delta(t_2 - t_1). \quad (3.15)$$

We wish to find the whitening kernel $h_c(t_1, t_2)$ such that, when $Y(t)$ is its input, its output

$$W(t) = \int_{-\infty}^{\infty} h_c(t, \tau)Y(\tau) d\tau \quad (3.16)$$

has autocorrelation $R_{WW}(t_1, t_2) = E[W(t_1)W^(t_2)] = c\delta(t_2 - t_1)$, for some scalar $c > 0$.*

In finite dimensional spaces, whitening is straightforward using the eigendecomposition of the covariance matrix (which is equal to the correlation matrix for zero-mean random vectors)—one simply takes the reciprocal of the square root of the eigenvalues to synthesize the whitening transformation. This same approach is possible in infinite dimensions using Mercer’s theorem [89, p. 379] (*cf.* [90, p. 534]), which gives sufficient conditions for the relevant infinite series to converge. Mercer’s Theorem is reproduced here for the sake of completeness.

Theorem 4 (*Mercer’s Theorem*) *Let $Y(t)$ be a zero-mean random process with real, bounded, and continuous autocorrelation function $R_{YY}(t_1, t_2)$. Then*

$$R_{YY}(t_1, t_2) = \sum_{k=1}^{\infty} \lambda_k \psi_k(t_1) \psi_k(t_2), \quad (3.17)$$

where the series converges uniformly and absolutely on $(t_1, t_2) \in [-Z, Z] \times [-Z, Z]$, and $\{\lambda_k\}_{k=1}^\infty$ and $\{\psi_k\}_{k=1}^\infty$ are the eigenvalues and corresponding orthonormal eigenfunctions satisfying the Fredholm integral equation

$$\lambda_k \psi_k(t) = \int_{-Z}^Z R_{YY}(t, \tau) \psi_k(\tau) d\tau, \quad (3.18)$$

for $t \in [-Z, Z]$. Here, orthonormal is taken to mean that $\int_{-Z}^Z \psi_k(t) \psi_\ell(t) dt = \delta_{k\ell}$.

Note that Problem 1 does not satisfy two conditions in Mercer's Theorem, namely, (i) that the signals be observed over a bounded time interval $[-Z, Z]$, and (ii) that the mean-square value $R_{YY}(t, t)$ of the noise be finite for all $t \in [-Z, Z]$. Thus, we temporarily modify Problem 1 to accommodate use of Mercer's Theorem. Our modifications are enumerated below.

M1: We truncate the LMDC interference to a finite set of pulse symbols $\{I[m]\}_{m=-M}^M$; that is, we replace $I(t)$ with

$$I_M(t) = \sum_{m=-M}^M I[m] g(t - mT - t_d). \quad (3.19)$$

M2: We restrict the pulse shape $g(t)$ to be zero outside of $[0, T]$.

M3: We replace the white noise with its projection onto the span of $I_M(t)$ and $s(t)$, so that the projected noise has finite mean-square.

Modifications [M1]–[M2] allow us to observe the random process $I_M(t)$ over a bounded time interval $[-Z, Z]$, where $Z = (M + 1)T$, without having any partially-overlapped symbols in the interval. Regarding [M3], we note that continuous-time white noise such as C-AWGN is an abstraction that is never observed directly in the physical world; instead, it is always “observed” indirectly at the output of a filter. The filter essentially projects the white noise onto a subspace, so that the observed, projected noise has finite average power (as is expected for physical processes). In our problem, the white noise will only be observed at the output of the whitening-plus-matched filter, and so we may reasonably project it onto the span of $I_M(t)$ and $s(t)$

to perform our analysis (call this subspace \mathcal{IS}). We disregard any components of the C-AWGN orthogonal to \mathcal{IS} by the intuition of the Irrelevance Theorem (cf. [91, p. 57-58]).

Based on these modifications [M1]–[M3], we pose a modified problem statement as follows.

Modified Problem 1 *Let $I_M(t)$ be as in (3.19), and let $P_{\mathcal{IS}}[N(t)]$ be the projection of C-AWGN $N(t)$, independent of $I_M(t)$ and having PSD \mathcal{E}_N , onto \mathcal{IS} , the span of $I_M(t)$ and $s(t)$. Then the autocorrelation $R_{\bar{Y}\bar{Y}}(t_1, t_2) = E[\bar{Y}(t_1)\bar{Y}^*(t_2)]$ of $\bar{Y}(t) = I_M(t) + P_{\mathcal{IS}}[N(t)]$ is*

$$R_{\bar{Y}\bar{Y}}(t_1, t_2) = \mathcal{E}_I \sum_{m=-M}^M g(t_1 - mT - t_d)g(t_2 - mT - t_d) + \mathcal{E}_N P_{\mathcal{IS}}(t_1, t_2), \quad (3.20)$$

where $P_{\mathcal{IS}}(t_1, t_2)$ is the kernel of the projection operator $P_{\mathcal{IS}}[\cdot]$. Now we wish to find the whitening kernel $\bar{h}_c(t_1, t_2)$ such that, when $\bar{Y}(t)$ is its input, its output

$$\bar{W}(t) = \int_{-Z}^Z \bar{h}_c(t, \tau) \bar{Y}(\tau) d\tau \quad (3.21)$$

has autocorrelation $R_{\bar{W}\bar{W}}(t_1, t_2) = E[\bar{W}(t_1)\bar{W}^*(t_2)] = cP_{\mathcal{IS}}(t_1, t_2)$, for some scalar $c > 0$, where $Z = (M + 1)T$.

Modifications [M1]–[M3] allow us to pose Modified Problem 1 in a way that is solvable via Mercer's Theorem. After solving Modified Problem 1 in this way, we intuitively generalize away from the modifications [M1]–[M3] to propose a solution to the original Problem 1. Then, we formally prove that the proposed solution to Problem 1 is correct.

In order to solve Modified Problem 1 via Mercer's Theorem, one must solve the Fredholm integral equation (3.18). The next lemma provides this derivation.

Lemma 2 *Let $R_{\bar{Y}\bar{Y}}(t_1, t_2)$ be as in Modified Problem 1. Then we have the following eigendecomposition:*

$$R_{\bar{Y}\bar{Y}}(t_1, t_2) = \lambda_0 x_0(t_1)x_0(t_2) + \lambda_1 \sum_{m=-M}^M x_{1,m}(t_1)x_{1,m}(t_2), \quad (3.22)$$

where the eigenvalues are $\lambda_1 = \mathcal{E}_N + \mathcal{E}_I$ and $\lambda_0 = \mathcal{E}_N$, the range-space eigenfunctions are

$$x_{1,m}(t) = g(t - mT - t_d), \quad (3.23)$$

and the null-space eigenfunction $x_0(t)$ is the normalized version $x_0(t) = x'_0(t)/\|x'_0\|$ of

$$x'_0(t) = s(t) - \sum_{m=-M}^M x_{1,m}(t) \int_{-Z}^Z x_{1,m}(\tau) s(\tau) d\tau. \quad (3.24)$$

Here $Z = (M+1)T$, $s(t)$ is the signal to be detected, and the norm $\|\cdot\|$ is defined by

$$\|x\|^2 = \int_{-Z}^Z |x(t)|^2 dt. \quad (3.25)$$

Proof We start by showing that $x_{1,m}(t)$ is an eigenfunction of the autocorrelation

$$\begin{aligned} R_{I_M I_M}(t_1, t_2) &= E[I_M(t_1)I_M^*(t_2)] \\ &= \mathcal{E}_I \sum_{m=-M}^M g(t_1 - mT - t_d)g(t_2 - mT - t_d), \end{aligned} \quad (3.26)$$

for each $m \in \{-M, \dots, 0, \dots, M\}$:

$$\begin{aligned} &\int_{-Z}^Z R_{I_M I_M}(t, \tau) x_{1,m}(\tau) d\tau \\ &= \int_{-Z}^Z \mathcal{E}_I \sum_{n=-M}^M g(t - nT - t_d)g(\tau - nT - t_d)g(\tau - mT - t_d) d\tau \\ &= \mathcal{E}_I \sum_n g(t - nT - t_d) \int_{-Z}^Z g(\tau - nT - t_d)g(\tau - mT - t_d) d\tau \\ &= \mathcal{E}_I \sum_n g(t - nT - t_d)\delta_{nm} \\ &= \mathcal{E}_I g(t - mT - t_d) \\ &= \mathcal{E}_I x_{1,m}(t), \end{aligned}$$

where in the third step we have used the fact that $g(t)$ is zero outside $[0, T)$ and has unit energy. Thus, $x_{1,m}(t)$ is an eigenfunction of $R_{I_M I_M}(t_1, t_2)$ having eigenvalue $\mu_m = \mathcal{E}_I$, for all $m \in \{-M, \dots, 0, \dots, M\}$. We observe that $\{x_{1,m}(t)\}_{m=-M}^M$ is an orthonormal set.

Further, by simple inspection we have that

$$R_{I_M I_M}(t_1, t_2) = \sum_{m=-M}^M \mu_m x_{1,m}(t_1) x_{1,m}(t_2),$$

so that the set $\{x_{1,m}(t)\}_{m=-M}^M$ spans the entire range space of $R_{I_M I_M}(t_1, t_2)$. (Indeed, any LMDC signal of this form is simply a linear combination of the eigenfunctions $\{x_{1,m}(t)\}_{m=-M}^M$.) Thus, the set of eigenfunctions $\{x_{1,m}(t)\}_{m=-M}^M$ provides an orthonormal basis for the range space of $R_{I_M I_M}(t_1, t_2)$.

Adding the projected C-AWGN component $\mathcal{E}_N P_{\mathcal{IS}}(t_1, t_2)$ to the autocorrelation has the effect of diagonal loading, adding \mathcal{E}_N to all eigenvalues whose corresponding eigenfunctions are within \mathcal{IS} . This can be seen from the observation that for any $x \in \mathcal{IS}$, $t \in [-Z, Z]$,

$$\int_{-Z}^Z P_{\mathcal{IS}}(t, \tau) x(\tau) d\tau = x(t). \quad (3.27)$$

Thus, it remains to find a basis for the intersection of \mathcal{IS} with the null space of $R_{I_M I_M}(t_1, t_2)$. This intersection is one-dimensional, and consists of the component of the signal $s(t)$ which is orthogonal to the range space of $R_{I_M I_M}(t_1, t_2)$. This implies that the signal $x'_0(t)$ given in the statement of the lemma is a basis for the intersection of \mathcal{IS} with the null space of $R_{I_M I_M}(t_1, t_2)$. Normalizing $x'_0(t)$ completes the orthonormal basis for the space \mathcal{IS} . ■

From the previous lemma, we observe that the space \mathcal{IS} actually is finite-dimensional, and so in this case we have no need of the convergence part of Mercer's Theorem. The eigendecomposition of the previous lemma is useful because it allows us to solve Modified Problem 1 almost by inspection, simply by inverting the eigenvalues and taking their square root.

Corollary 6 *The filter which whitens $\bar{Y}(t)$ in the sense of Modified Problem 1 is an LTV system whose kernel $\bar{h}_c(t_1, t_2)$ is given by:*

$$\begin{aligned}\bar{h}_c(t_1, t_2) &= \frac{1}{\sqrt{\mathcal{E}_N}} x_0(t_1) x_0(t_2) + \frac{1}{\sqrt{\mathcal{E}_N + \mathcal{E}_I}} \sum_{m=-M}^M x_{1,m}(t_1) x_{1,m}(t_2) \\ &= \frac{1}{\sqrt{\mathcal{E}_N}} P_{IS}(t_1, t_2) \\ &\quad + \left(\frac{1}{\sqrt{\mathcal{E}_N + \mathcal{E}_I}} - \frac{1}{\sqrt{\mathcal{E}_N}} \right) \sum_{m=-M}^M g(t_1 - mT - t_d) g(t_2 - mT - t_d).\end{aligned}\tag{3.28}$$

Proof The proof is straight-forward given the following eigendecomposition of the projection kernel $P_{IS}(t_1, t_2)$:

$$P_{IS}(t_1, t_2) = x_0(t_1) x_0(t_2) + \sum_{m=-M}^M x_{1,m}(t_1) x_{1,m}(t_2).\tag{3.29}$$

■

While the LTV filter (3.28) solves Modified Problem 1, we can generalize this filter to solve the original Problem 1. Intuitively, we might expect to generalize from modification [M1] by taking the limit $M \rightarrow \infty$. We also might expect to generalize from modification [M3] by replacing the projection kernel $P_{IS}(t_1, t_2)$ in (3.28) with the identity kernel $\delta(t_2 - t_1)$. Indeed, we can formally prove that these intuitive generalizations of (3.28) do in fact solve the original Problem 1, provided that modification [M2] is still assumed. (For now, we do not generalize from the modification [M2], as this generalization complicates the analysis, but leave this for the analysis of the case of asynchronous pulse shapes.)

Theorem 5 *Let $g(t)$ be zero outside of the interval $[0, T)$. Then the filter which whitens $Y(t)$ in the sense of Problem 1 is an LTV system whose kernel $h_c(t_1, t_2)$ is given by:*

$$\begin{aligned}h_c(t_1, t_2) &= \frac{1}{\sqrt{\mathcal{E}_N}} \delta(t_2 - t_1) \\ &\quad + \left(\frac{1}{\sqrt{\mathcal{E}_N + \mathcal{E}_I}} - \frac{1}{\sqrt{\mathcal{E}_N}} \right) \sum_{m=-\infty}^{\infty} g(t_1 - mT - t_d) g(t_2 - mT - t_d).\end{aligned}\tag{3.30}$$

Proof One can show by simple substitution that the autocorrelation $R_{WW}(t_1, t_2)$ of $W(t)$ in Problem 1 is indeed $\delta(t_2 - t_1)$, when $h_c(t_1, t_2)$ is defined in this way. The idempotence of $(1/\mathcal{E}_I) \cdot R_{II}(t_1, t_2)$ provides helpful shortcuts in the derivation—that is, the property that

$$\int_{-\infty}^{\infty} R_{II}(t_1, \tau) R_{II}(\tau, t_2) d\tau = \mathcal{E}_I R_{II}(t_1, t_2). \quad (3.31)$$

■

Some remarks are in order at this point on the form of the whitening filter, some practical implications of this form, and some mathematical intuition.

First, the output of the whitening filter is essentially a weighted sum of two pieces, the first piece simply a scaled version of the original signal, and the second piece transformed by an LTV system. By choosing the coefficients in front of these two pieces very carefully, the autocorrelation of the transformed output $W(t)$ has perfect cancellation of the non-white components so that only the white component is left. However, this perfect cancellation and whitening is possible only by a careful choice of the weighting coefficients in $h_c(t_1, t_2)$. Let us look more carefully at these coefficients.

The ratio of the two weighting coefficients in $h_c(t_1, t_2)$ is

$$\begin{aligned} \gamma &= \frac{1/\sqrt{\mathcal{E}_N + \mathcal{E}_I} - 1/\sqrt{\mathcal{E}_N}}{1/\sqrt{\mathcal{E}_N}} \\ &= -1 + \sqrt{\frac{1}{1 + \mathcal{E}_I/\mathcal{E}_N}}. \end{aligned}$$

Thus, in order to set the weights in $h_c(t_1, t_2)$ correctly, the receiver must know $\mathcal{E}_I/\mathcal{E}_N$ accurately, which is a type of INR. This presents a technical challenge for receiver design. In general, it will not be possible to know the INR *a priori*, and so it must be estimated adaptively by the receiver. Thus, *the cyclostationary whitener must have knowledge of both the interference delay t_d and the INR $\mathcal{E}_I/\mathcal{E}_N$.*

In addition, note that in the case of zero C-AWGN, the noise PSD $\mathcal{E}_N = 0$, so that a nonzero whitening filter can be designed such that its output $W(t) = 0$ with probability one. (This may be seen by multiplying the whitening kernel (3.30) by

$\sqrt{\mathcal{E}_N}$, setting $\mathcal{E}_N = 0$, and then observing that the whitener output has PSD $\mathcal{E}_N = 0$.) In other words, when there is no noise, the LMDC interference $I(t)$ lies in the null space of $h_c(t_1, t_2)$. In this case, the linear transformation $h_c(t_1, t_2)$ has the effect of cancelling the LMDC interference, but other non-LMDC signals are transformed to a non-zero output. This implies that detection of signals $s(t)$ in the presence of LMDC interference $I(t)$ only and no noise can be done perfectly, *provided that the delay t_d is known*.

Thus, for the case of pulse-shape synchronized $I(t)$, we have posed whitening Problem 1, modified it via modifications [M1]–[M3] to accomodate Mercer’s Theorem, used Mercer’s Theorem to solve the resulting Modified Problem 1, intuitively generalized from modifications [M1] and [M3] to propose a solution to the original Problem 1, and formally proven that this proposed solution is correct. The resulting whitening filter requires knowledge of both the delay and the INR of the interference, and in the theoretical case of only interference and no noise, it achieves perfect signal detection.

These results so far have been based on the simplifying but unrealistic assumption that the LMDC interference is pulse-shape synchronized with respect to the radar receiver. We now relax this assumption and examine the more realistic, asynchronous case. In the process, we will find a way to relax modifying assumption [M2] as well.

3.3.2 Asynchronous case

As mentioned in the introduction to this section, the pulse-shape synchronized case of the previous sub-section is not realistic in practical wireless scenarios. Thus, we now turn to the asynchronous case, in which multiple LMDC signals arrive at the radar receiver with different delays.

Theorem 6 *Let $I(t)$ be cyclostationary LMDC interference having the following form:*

$$I(t) = \sum_{n=1}^N \sum_{m=-\infty}^{\infty} I_n[m]g(t - mT - t_{d,n}), \quad (3.32)$$

where $\{\{I_n[m]\}_{m=-\infty}^{\infty}\}_{n=1}^N$ are N independent, stationary sequences of complex-valued, circularly symmetric, zero-mean, mutually uncorrelated digital data symbols having respective mean-square values of $E[|I_n[m]|^2] = \mathcal{E}_{I,n}$; $g(t)$ is a unit-energy pulse shaping waveform; T is the pulse symbol duration; and $\{t_{d,n}\}_{n=1}^N$ are deterministic delays in the interval $[0, T)$.

Then the autocorrelation of $I(t)$ is as follows:

$$R_{II}(t_1, t_2) = \sum_{n=1}^N \mathcal{E}_{I,n} \sum_{m=-\infty}^{\infty} g(t_1 - mT - t_{d,n})g(t_2 - mT - t_{d,n}). \quad (3.33)$$

Proof The single-user case of $N = 1$ is discussed in Theorem 3. Since the N LMDC users are independent and zero-mean, the autocorrelation of the sum is the sum of the autocorrelations of the N LMDC users' signals. ■

As in the pulse-shape synchronized case, the autocorrelation of $I(t)$ given by Theorem 6 is singular. However, in practical situations, $I(t)$ is always observed in the presence of noise, and white noise forces all the eigenvalues of the autocorrelation to be positive. With the addition of C-AWGN, we can pose the multi-user, asynchronous, cyclostationary LMDC whitening problem as follows.

Problem 2 Let $I(t)$ be multi-user, asynchronous, cyclostationary LMDC interference as in Theorem 6, and let $N(t)$ be C-AWGN, independent of $I(t)$ and having PSD \mathcal{E}_N . Then the autocorrelation of the sum $Y(t) = I(t) + N(t)$ is

$$R_{YY}(t_1, t_2) = \sum_{n=1}^N \mathcal{E}_{I,n} \sum_{m=-\infty}^{\infty} g(t_1 - mT - t_{d,n})g(t_2 - mT - t_{d,n}) + \mathcal{E}_N \delta(t_2 - t_1). \quad (3.34)$$

We wish to find the whitening kernel $h_c(t_1, t_2)$ such that, when $Y(t)$ is its input, its output

$$W(t) = \int_{-\infty}^{\infty} h_c(t, \tau)Y(\tau) d\tau \quad (3.35)$$

has autocorrelation $R_{WW}(t_1, t_2) = c\delta(t_2 - t_1)$, for some scalar $c > 0$.

As before, although we would like to use Mercer's Theorem to construct the whitening filter $h_c(t_1, t_2)$, Problem 2 does not satisfy two conditions in Mercer's Theorem—namely, a bounded time interval in which the signals are observed, and a finite mean-square value of the noise. Thus, once again we modify the problem using modifications [M1]–[M3], enumerated in the previous sub-section, except that for [M1] we now use the signal

$$I_M(t) = \sum_{n=1}^N \sum_{m=-M}^M I_n[m]g(t - mT - t_{d,n}). \quad (3.36)$$

The result of these modifications is Modified Problem 2, stated next.

Modified Problem 2 *Let $I_M(t)$ be as in (3.36), and let $P_{\mathcal{IS}}[N(t)]$ be the projection of C-AWGN $N(t)$, independent of $I_M(t)$ and having PSD \mathcal{E}_N , onto \mathcal{IS} , the span of $I_M(t)$ and $s(t)$. Then the autocorrelation of $\bar{Y}(t) = I_M(t) + P_{\mathcal{IS}}[N(t)]$ is*

$$R_{\bar{Y}\bar{Y}}(t_1, t_2) = \sum_{n=1}^N \mathcal{E}_{I,n} \sum_{m=-M}^M g(t_1 - mT - t_{d,n})g(t_2 - mT - t_{d,n}) + \mathcal{E}_N P_{\mathcal{IS}}(t_1, t_2), \quad (3.37)$$

where $P_{\mathcal{IS}}(t_1, t_2)$ is the kernel of the projection operator $P_{\mathcal{IS}}[\cdot]$. Now we wish to find the whitening kernel $\bar{h}_c(t_1, t_2)$ such that, when $\bar{Y}(t)$ is its input, its output

$$\bar{W}(t) = \int_{-Z}^Z \bar{h}_c(t, \tau) \bar{Y}(\tau) d\tau \quad (3.38)$$

has autocorrelation $R_{\bar{W}\bar{W}}(t_1, t_2) = cP_{\mathcal{IS}}(t_1, t_2)$ for some scalar $c > 0$, where $Z = (M + 1)T$.

We can write the *form* of the solution to Modified Problem 2 using Mercer's Theorem. After doing so, we intuitively generalize away from the simplifying modifications [M1]–[M3] to propose the *form* of the solution to the original Problem 2. Then, we use this form to derive the exact solution to Problem 2.

In order to solve Modified Problem 2 using Mercer's Theorem, one must solve the Fredholm integral equation (3.18), and the next lemma provides this derivation.

Note that for now we specify only the *form* of the eigendecomposition to within some unspecified set of coefficients $\{\{\{\kappa_{m,\ell,n}\}_{m=1}^{N(2M+1)}\}_{\ell=1}^N\}_{n=-M}^M$ and some unspecified set of eigenvalues $\{\mu_m\}_{m=1}^{N(2M+1)}$. Later, we will solve for the relevant mathematical combinations of these quantities when defining the whitening filter.

Lemma 3 *Let $R_{\bar{Y}\bar{Y}}(t_1, t_2)$ be as in Modified Problem 2. Then we have the following eigendecomposition:*

$$R_{\bar{Y}\bar{Y}}(t_1, t_2) = \lambda_0 x_0(t_1)x_0(t_2) + \sum_{m=1}^{N(2M+1)} \lambda_{1,m} x_{1,m}(t_1)x_{1,m}(t_2), \quad (3.39)$$

where the null-space eigenvalue $\lambda_0 = \mathcal{E}_N$; the range-space eigenvalues $\lambda_{1,m} = \mu_m + \mathcal{E}_N$ are left unspecified for now; the orthonormal range-space eigenfunctions are

$$x_{1,m}(t) = \sum_{\ell=1}^N \sum_{n=-M}^M \kappa_{m,\ell,n} g(t - nT - t_{d,\ell}), \quad (3.40)$$

for an appropriate choice of the coefficients $\kappa_{m,\ell,n}$, which we assume exists for the moment; and the null-space eigenfunction $x_0(t)$ is the normalized version $x_0(t) = x'_0(t)/\|x'_0\|$ of

$$x'_0(t) = s(t) - \sum_{m=1}^{N(2M+1)} x_{1,m}(t) \int_{-Z}^Z x_{1,m}(\tau) s(\tau) d\tau, \quad (3.41)$$

where $Z = (M+1)T$, $s(t)$ is the signal to be detected, and the norm $\|\cdot\|$ is defined by

$$\|x\|^2 = \int_{-Z}^Z |x(t)|^2 dt. \quad (3.42)$$

Proof We derive the form of the range-space eigenfunctions. The null space analysis is similar to that in the pulse-shape synchronized case (see Lemma 2).

The form of the range-space eigenfunctions can be computed as follows:

$$\begin{aligned}
& \int_{-Z}^Z R_{I_M I_M}(t, \tau) x_{1,m}(\tau) d\tau \\
&= \int_{-Z}^Z \sum_{\ell=1}^N \mathcal{E}_{I,\ell} \sum_{n=-M}^M g(t - nT - t_{d,\ell}) g(\tau - nT - t_{d,\ell}) x_{1,m}(\tau) d\tau \\
&= \sum_{\ell=1}^N \sum_{n=-M}^M g(t - nT - t_{d,\ell}) \left(\mathcal{E}_{I,\ell} \int_{-Z}^Z x_{1,m}(\tau) g(\tau - nT - t_{d,\ell}) d\tau \right) \\
&= \mu_m x_{1,m}(t).
\end{aligned}$$

The form of $x_{1,m}(t)$ follows by properly defining the coefficients $\kappa_{m,\ell,n}$. We assume for the moment that it is possible to define the $\kappa_{m,\ell,n}$ in a self-consistent way such that different $x_{1,m}(t)$ are orthonormal. Note that there are at most $N(2M+1)$ linearly independent $x_{1,m}(t)$, corresponding to the dimension of the space of coefficients $\{\{\kappa_{m,\ell,n}\}_{\ell=1}^N\}_{n=-M}^M$. ■

From the previous lemma, we again observe that the space \mathcal{IS} is finite-dimensional, and so we have no need of the convergence part of Mercer's Theorem in this case. The eigendecomposition of the previous lemma is useful because it allows us to specify the *form* of the solution to Modified Problem 2, simply by inverting the eigenvalues and taking their square root.

Corollary 7 *The form of the kernel which whitens $\bar{Y}(t)$, in the sense of Modified Problem 2, is as follows:*

$$\bar{h}_c(t_1, t_2) = \frac{1}{\sqrt{\mathcal{E}_N}} P_{\mathcal{IS}}(t_1, t_2) + \sum_{m,n=1}^N \sum_{p,q=-M}^M c_{m,n,p,q} g(t_1 - pT - t_{d,m}) g(t_2 - qT - t_{d,n}), \quad (3.43)$$

for some choice of coefficients $c_{m,n,p,q} = c_{n,m,q,p}$, which is left unspecified for now.

Proof Using the following eigendecomposition of the projection kernel $P_{\mathcal{IS}}(t_1, t_2)$:

$$P_{\mathcal{IS}}(t_1, t_2) = x_0(t_1)x_0(t_2) + \sum_{m=1}^{N(2M+1)} x_{1,m}(t_1)x_{1,m}(t_2), \quad (3.44)$$

we can derive the form of the filter $\bar{h}_c(t_1, t_2)$ as follows:

$$\begin{aligned}\bar{h}_c(t_1, t_2) &= \frac{1}{\sqrt{\mathcal{E}_N}} x_0(t_1) x_0(t_2) + \sum_{m=1}^{N(2M+1)} \frac{1}{\sqrt{\mu_m + \mathcal{E}_N}} x_{1,m}(t_1) x_{1,m}(t_2) \\ &= \frac{1}{\sqrt{\mathcal{E}_N}} P_{IS}(t_1, t_2) + \sum_{m=1}^{N(2M+1)} \left(\frac{1}{\sqrt{\mu_m + \mathcal{E}_N}} - \frac{1}{\sqrt{\mathcal{E}_N}} \right) x_{1,m}(t_1) x_{1,m}(t_2).\end{aligned}$$

After multiplying the kernel by the constant $\sqrt{\mathcal{E}_N}$, we can simplify the second term further:

$$\begin{aligned}\sqrt{\mathcal{E}_N} \bar{h}_c(t_1, t_2) - P_{IS}(t_1, t_2) &= \sum_{\ell=1}^{N(2M+1)} \gamma_\ell x_{1,\ell}(t_1) x_{1,\ell}(t_2) \\ &= \sum_{\ell} \gamma_\ell \sum_{m=1}^N \sum_{p=-M}^M \kappa_{\ell,m,p} g(t_1 - pT - t_{d,m}) \sum_{n=1}^N \sum_{q=-M}^M \kappa_{\ell,n,q} g(t_2 - qT - t_{d,n}) \\ &= \sum_{\ell, m, n, p, q} \gamma_\ell \kappa_{\ell,m,p} \kappa_{\ell,n,q} g(t_1 - pT - t_{d,m}) g(t_2 - qT - t_{d,n}) \\ &= \sum_{m, n, p, q} c'_{m,n,p,q} g(t_1 - pT - t_{d,m}) g(t_2 - qT - t_{d,n}),\end{aligned}$$

where

$$\gamma_\ell = -1 + \sqrt{\frac{1}{1 + \mu_\ell / \mathcal{E}_N}},$$

and

$$c'_{m,n,p,q} = \sum_{\ell=1}^{N(2M+1)} \gamma_\ell \kappa_{\ell,m,p} \kappa_{\ell,n,q}.$$

Writing $c_{m,n,p,q} = c'_{m,n,p,q} / \sqrt{\mathcal{E}_N}$ gives the desired result. Note that $c_{m,n,p,q} = c_{n,m,q,p}$.

■

Assuming that the coefficients $c_{m,n,p,q}$ can be chosen appropriately, the LTV filter (3.43) solves Modified Problem 2. We can intuitively generalize the form of this filter to propose the form of the solution to the original Problem 2, as before, by taking the limit $M \rightarrow \infty$ and by replacing the projection kernel $P_{IS}(t_1, t_2)$ with the identity kernel $\delta(t_2 - t_1)$. Further, in the resulting *form* for $h_c(t_1, t_2)$, we can write down the

conditions that the coefficients $c_{m,n,p,q}$ must satisfy to accomplish whitening. The next lemma provides the details. We observe that Lemma 4 is general enough not to require any of the modifications [M1]–[M3].

Lemma 4 *Let $Y(t)$ be the sum of multi-user, asynchronous, cyclostationary LMDC interference and C-AWGN, as in Problem 2. Then the whitening filter that solves Problem 2 has the following kernel:*

$$h_c(t_1, t_2) = \delta(t_2 - t_1) + \sum_{m,n=1}^N \sum_{p,q=-\infty}^{\infty} c_{m,n,p,q} g(t_1 - pT - t_{d,m}) g(t_2 - qT - t_{d,n}), \quad (3.45)$$

where the coefficients $c_{m,n,p,q} = c_{n,m,q,p}$ satisfy the following system of difference equations:

$$\begin{aligned} 0 = & \mathcal{E}_{I,i} \delta_{ij} \delta_{kl} + \mathcal{E}_N (c_{i,j,k,\ell} + c_{j,i,\ell,k}) \\ & + \sum_{m,p} \mathcal{E}_{I,i} c_{j,m,\ell,p} \langle g, S_{(p-k)T+\Delta_{mi}} g \rangle \\ & + \sum_{n,q} \mathcal{E}_{I,j} c_{i,n,k,q} \langle g, S_{(\ell-q)T+\Delta_{jn}} g \rangle \\ & + \mathcal{E}_N \sum_{m,n,p,q} c_{i,n,k,q} c_{j,m,\ell,p} \langle g, S_{(p-q)T+\Delta_{mn}} g \rangle \\ & + \sum_{m,n,p,q,r,s} \mathcal{E}_{I,r} c_{i,n,k,q} c_{j,m,\ell,p} \langle g, S_{(s-q)T+\Delta_{rn}} g \rangle \langle g, S_{(p-s)T+\Delta_{mr}} g \rangle, \end{aligned} \quad (3.46)$$

where $i, j, m, n, r \in \{1, \dots, N\}$ and $k, \ell, p, q, s \in \mathbb{Z}$, and we define the notation:

$$\Delta_{mn} = t_{d,m} - t_{d,n}, \quad (3.47)$$

$$\langle g, S_x g \rangle = \int_{-\infty}^{\infty} g(\tau) g(\tau - x) d\tau. \quad (3.48)$$

In other words, the random process

$$W(t) = \int_{-\infty}^{\infty} h_c(t, \tau) Y(\tau) d\tau \quad (3.49)$$

has autocorrelation $R_{WW}(t_1, t_2) = \mathcal{E}_N \delta(t_2 - t_1)$.

Proof Without loss of generality, we may multiply $h_c(t_1, t_2)$ by any scalar and still accomplish whitening. By the preceding arguments, and scaling by $\sqrt{\mathcal{E}_N}$, we propose the form (3.45) for $h_c(t_1, t_2)$.

Given this form of whitening filter, we compute the autocorrelation $R_{WW}(t_1, t_2)$ from Problem 2 and solve for the coefficients $c_{m,n,p,q}$ that force

$$R_{WW}(t_1, t_2) = \mathcal{E}_N \delta(t_2 - t_1). \quad (3.50)$$

The derivation of $R_{WW}(t_1, t_2)$ is tedious and so is left to Appendix E. In the resulting equation, we desire the difference

$$R_{WW}(t_1, t_2) - \mathcal{E}_N \delta(t_2 - t_1)$$

to be equal to zero. Since each (i, j, k, ℓ) -th term in this difference is linearly independent from the rest, the overall sum is equal to zero if and only if each of the (i, j, k, ℓ) -th coefficients is identically zero. Setting all the (i, j, k, ℓ) -th coefficients equal to zero gives the system of difference equations given in the statement of the lemma. ■

The previous lemma gives the form of the whitening filter for Problem 2 to within an unknown set of coefficients $c_{m,n,p,q}$, and it converts the problem of finding these coefficients to one of solving a system of difference equations. We can solve this system of difference equations using Hilbert space theory, leading to the following theorem, which fully specifies the whitening filter for multi-user, asynchronous, cyclostationary LMDC interference and C-AWGN. This algorithm is the primary result of this chapter.

Theorem 7 *Let $Y(t) = I(t) + N(t)$, where $I(t)$ is multi-user, asynchronous, cyclostationary LMDC interference as described in Theorem 6, and $N(t)$ is C-AWGN, independent of $I(t)$ and having PSD \mathcal{E}_N . Then the LTV whitening filter has the kernel*

$$h_c(t_1, t_2) = \delta(t_2 - t_1) + \sum_{m,n=1}^N \sum_{p,q=-\infty}^{\infty} c_{m,n,p,q} g(t_1 - pT - t_{d,m}) g(t_2 - qT - t_{d,n}), \quad (3.51)$$

where the coefficients $c_{m,n,p,q}$ are calculated from the algorithm to follow. That is, the filtered random process

$$W(t) = \int_{-\infty}^{\infty} h_c(t, \tau) Y(\tau) d\tau \quad (3.52)$$

has autocorrelation $R_{WW}(t_1, t_2) = \mathcal{E}_N \delta(t_2 - t_1)$.

Algorithm for computing whitener coefficients:

1. Compute the matrix-valued functions $\mathbf{E}[p], \mathbf{G}[p] \in \mathbb{C}^{N \times N \times \mathbb{Z}}$ whose (m, n, p) -th components are given by

$$\mathbf{E}_{m,n}[p] = \mathcal{E}_{I,n} \delta_{mn} \delta_{0p}, \quad (3.53)$$

$$\mathbf{G}_{m,n}[p] = \langle g, S_{pT + \Delta_{mn}} g \rangle, \quad (3.54)$$

where bold font denotes matrices, and $\mathbf{A}_{m,n}[p]$ is the (m, n) -th component of the matrix $\mathbf{A}[p]$.

2. Compute the DTFTs

$$\tilde{\mathbf{E}}(f) = \sum_{p=-\infty}^{\infty} \mathbf{E}[p] e^{-i2\pi f p}, \quad (3.55)$$

$$\tilde{\mathbf{G}}(f) = \sum_{p=-\infty}^{\infty} \mathbf{G}[p] e^{-i2\pi f p}. \quad (3.56)$$

3. For every $f \in [-1/2, 1/2)$, compute the eigendecomposition

$$\tilde{\mathbf{E}}^{1/2}(f) \tilde{\mathbf{G}}(f) \tilde{\mathbf{E}}^{1/2}(f) = \tilde{\mathbf{Q}}_1(f) \tilde{\mathbf{\Lambda}}(f) \tilde{\mathbf{Q}}_1^H(f), \quad (3.57)$$

where $\tilde{\mathbf{Q}}_1(f)$ is a unitary eigenvector matrix, and

$$\tilde{\mathbf{\Lambda}}(f) = \text{diag}\{\lambda_1(f), \dots, \lambda_r(f), 0, \dots, 0\} \quad (3.58)$$

is a diagonal eigenvalue matrix with rank $r \leq N$. Since $\tilde{\mathbf{G}}(f) \geq 0$ (proven in Appendix F), it follows that $\tilde{\mathbf{\Lambda}}(f) \geq 0$. The matrix

$$\tilde{\mathbf{Q}}_2(f) = \tilde{\mathbf{E}}^{1/2}(f) \tilde{\mathbf{Q}}_1(f), \quad (3.59)$$

now jointly diagonalizes $\tilde{\mathbf{G}}(f)$ and $\tilde{\mathbf{E}}^{-1}(f)$ [92, p. 33-36]:

$$\tilde{\mathbf{Q}}_2^H(f) \tilde{\mathbf{E}}^{-1}(f) \tilde{\mathbf{Q}}_2(f) = \mathbf{I}, \quad (3.60)$$

$$\tilde{\mathbf{Q}}_2^H(f) \tilde{\mathbf{G}}(f) \tilde{\mathbf{Q}}_2(f) = \tilde{\mathbf{\Lambda}}(f). \quad (3.61)$$

4. For every $f \in [-1/2, 1/2)$, compute the generalized inverse [93] and square-root matrices

$$\tilde{\mathbf{G}}_{\lambda_0}^\dagger(f) = \tilde{\mathbf{Q}}_2(f) \tilde{\mathbf{\Lambda}}_{\lambda_0}^\dagger(f) \tilde{\mathbf{Q}}_2^H(f), \quad (3.62)$$

$$\tilde{\mathbf{U}}_{\lambda_0}(f) = \tilde{\mathbf{Q}}_2(f) \left(\mathcal{E}_N \tilde{\mathbf{\Lambda}}_{\lambda_0}^\dagger(f) \right)^{1/2} \tilde{\mathbf{Q}}_1^H(f), \quad (3.63)$$

$$\tilde{\mathbf{V}}_{\lambda_0}(f) = \tilde{\mathbf{Q}}_2(f) \left(\mathcal{E}_N \tilde{\mathbf{\Lambda}}_{\lambda_0}^\dagger(f) + \mathbf{I} \right)^{1/2} \tilde{\mathbf{Q}}_1^H(f), \quad (3.64)$$

where

$$\tilde{\mathbf{\Lambda}}_{\lambda_0}^\dagger(f) = \text{diag}\{1/\lambda_1(f), \dots, 1/\lambda_r(f), 1/\lambda_0, \dots, 1/\lambda_0\}, \quad (3.65)$$

and $0 < \lambda_0 \ll 1$. These matrices satisfy the following relations:

$$\tilde{\mathbf{G}}(f) \tilde{\mathbf{G}}_{\lambda_0}^\dagger(f) \tilde{\mathbf{G}}(f) = \tilde{\mathbf{G}}(f), \quad (3.66)$$

$$\tilde{\mathbf{U}}_{\lambda_0}(f) \tilde{\mathbf{U}}_{\lambda_0}^H(f) = \mathcal{E}_N \tilde{\mathbf{G}}_{\lambda_0}^\dagger(f), \quad (3.67)$$

$$\tilde{\mathbf{V}}_{\lambda_0}(f) \tilde{\mathbf{V}}_{\lambda_0}^H(f) = \mathcal{E}_N \tilde{\mathbf{G}}_{\lambda_0}^\dagger(f) + \tilde{\mathbf{E}}(f). \quad (3.68)$$

5. For every $f \in [-1/2, 1/2)$, compute the matrix

$$\tilde{\mathbf{C}}(f) = \lim_{\lambda_0 \rightarrow 0} \left[\tilde{\mathbf{U}}_{\lambda_0}(f) \tilde{\mathbf{V}}_{\lambda_0}^{-1}(f) - \mathbf{I} \right] \tilde{\mathbf{G}}_{\lambda_0}^\dagger(f). \quad (3.69)$$

6. Find the coefficients $c_{m,n,p,q}$ by the inverse DTFT

$$c_{m,n,p,q} = \mathbf{C}_{m,n}[p-q] = \int_{-1/2}^{1/2} \tilde{\mathbf{C}}_{m,n}(f) e^{i2\pi f(p-q)} df. \quad (3.70)$$

Proof All that remains after the preceding Lemma 4 is to find the coefficients $c_{m,n,p,q}$ which satisfy (3.46). An elegant solution to (3.46) may be obtained by expressing the scalars appearing in that equation as components of linear operators.

Define a Hilbert space \mathcal{X} indexed by $(j, \ell) \in \{1, \dots, N\} \times \mathbb{Z}$ and defined by the inner product

$$\langle \mathbf{x}, \mathbf{y} \rangle = \sum_{j=1}^N \sum_{\ell=-\infty}^{\infty} x_{j,\ell} y_{j,\ell},$$

where $x_{j,\ell}$, $y_{j,\ell}$ are the (j, ℓ) -th components of vectors $\mathbf{x}, \mathbf{y} \in \mathcal{X}$, respectively. We will refer to the index over the finite set $\{1, \dots, N\}$ as the *user index*, since in (3.51) it

corresponds to the N LMDC users in the interference process $I(t)$; similarly, we will refer to the index over the countable set \mathbb{Z} as the *pulse-lag index*, since in (3.51) it corresponds to a time shift of an integer number of pulse durations T . Given this definition of \mathcal{X} , any linear operator $A : \mathcal{X} \rightarrow \mathcal{X}$ has a representation

$$y_{j,\ell} = \sum_{k=1}^N \sum_{m=-\infty}^{\infty} A_{j,k,\ell,m} x_{k,m},$$

where $A_{j,k,\ell,m}$ is the kernel of the operator A , and $y_{j,\ell}$, $x_{j,\ell}$ are the (j, ℓ) -th components of two vectors $\mathbf{x}, \mathbf{y} = A\mathbf{x} \in \mathcal{X}$, respectively. Using this notation, and defining the self-adjoint operators $C, G, E : \mathcal{X} \rightarrow \mathcal{X}$ as having kernels

$$\begin{aligned} C_{m,n,p,q} &= c_{m,n,p,q}, \\ G_{m,n,p,q} &= \langle g, S_{(p-q)T+\Delta_{mn}} g \rangle, \\ E_{m,n,p,q} &= \mathcal{E}_{I,n} \delta_{mn} \delta_{pq}, \end{aligned}$$

respectively, we can rewrite (3.46) as follows:

$$\begin{aligned} 0 &= E + \mathcal{E}_N(C + C^*) + EG^*C^* + CG^*E \\ &\quad + \mathcal{E}_N CG^*C^* + CG^*EG^*C^* \\ &= C(GEG^* + \mathcal{E}_N G)C^* + C(GE + \mathcal{E}_N I) \\ &\quad + (GE + \mathcal{E}_N I)^*C^* + E, \end{aligned} \tag{3.71}$$

where I is the identity operator, asterisk denotes adjoint operator, and we have used the self-adjoint relations $C = C^*$, $G = G^*$, and $E = E^*$.

Equation (3.71) can be simplified further by the observation that the operators C , G , and E are (i) finite-dimensional in the user index, and (ii) time-invariant in the pulse-lag index. (The time invariance of C in the pulse-lag index follows from the time-invariance of all the other operators appearing in (3.71) in that index.) This suggests that arithmetic involving such operators may be simplified using matrix multiplication (due to finite-dimensionality in one index) and Fourier analysis (due to time-invariance in the other index). Indeed, we can formally derive a matrix representation of these operators in a frequency domain.

Step #1: Representation of operator composition.

Let $A, B : \mathcal{X} \rightarrow \mathcal{X}$ be two operators which have real-valued kernels that are time-invariant in the pulse-lag index. Then their kernels may be represented using the matrix-valued functions

$$\begin{aligned} A_{m,n,p,q} &= \mathbf{A}_{m,n}[p - q], \\ B_{m,n,p,q} &= \mathbf{B}_{m,n}[p - q]. \end{aligned}$$

Further, the composition $D = AB$ of these two operators has the following kernel:

$$\begin{aligned} D_{m,n,p,q} &= (AB)_{m,n,p,q} \\ &= \sum_{k=1}^N \sum_{\ell=-\infty}^{\infty} \mathbf{A}_{m,k}[p - \ell] \mathbf{B}_{k,n}[\ell - q] \\ &= \int_{-1/2}^{1/2} \sum_k \tilde{\mathbf{A}}_{m,k}(u) \tilde{\mathbf{B}}_{k,n}(u) e^{i2\pi u(p-q)} du, \end{aligned}$$

where in the second step we have substituted using the DTFTs of $\mathbf{A}[p]$ and $\mathbf{B}[p]$:

$$\begin{aligned} \tilde{\mathbf{A}}(f) &= \sum_{p=-\infty}^{\infty} \mathbf{A}[p] e^{-i2\pi f p}, \\ \tilde{\mathbf{B}}(f) &= \sum_{p=-\infty}^{\infty} \mathbf{B}[p] e^{-i2\pi f p}. \end{aligned}$$

We can use the definition of matrix multiplication to write the above as

$$\begin{aligned} D_{m,n,p,q} &= \mathbf{D}_{m,n}[p - q], \\ \mathbf{D}[p - q] &= \int_{-1/2}^{1/2} \tilde{\mathbf{A}}(f) \tilde{\mathbf{B}}(f) e^{i2\pi f(p-q)} df. \end{aligned}$$

This shows that the composition $D = AB$ may be computed using *matrix multiplication in the frequency domain*.

Step #2: Representation of operator adjoint.

Let $A : \mathcal{X} \rightarrow \mathcal{X}$ have real-valued kernel that is time-invariant in the pulse-lag index, and let $B = A^*$. Then

$$\begin{aligned} \int_{-1/2}^{1/2} \tilde{\mathbf{B}}_{m,n}(f) e^{i2\pi f(p-q)} df &= \mathbf{B}_{m,n}[p-q] \\ &= \mathbf{A}_{n,m}^*[q-p] \\ &= \int_{-1/2}^{1/2} \tilde{\mathbf{A}}_{n,m}^*(f) e^{i2\pi f(p-q)} df, \end{aligned}$$

where we have used the fact that since $\mathbf{A}_{n,m}[p]$ is real-valued, $\mathbf{A}_{n,m}[p] = \mathbf{A}_{n,m}^*[p]$. This shows that the adjoint of A corresponds to its *conjugate-transpose in the frequency domain*.

Step #3: Representation of (3.71) in matrix form.

Using the previous two steps, we approach (3.71) by converting it to a matrix equation in the frequency domain. First, we express the kernels of C , G , and E using the notation

$$\begin{aligned} \mathbf{C}_{m,n}[p-q] &= C_{m,n,p,q} = c_{m,n,p,q}, \\ \mathbf{G}_{m,n}[p-q] &= G_{m,n,p,q} = \langle g, S_{(p-q)T+\Delta_{mn}} g \rangle, \\ \mathbf{E}_{m,n}[p-q] &= E_{m,n,p,q} = \mathcal{E}_{I,n} \delta_{mn} \delta[p-q], \end{aligned}$$

where $\delta[n] = \delta_{n0}$ is the discrete-time delta function. We are now able to re-write (3.71) by transforming into the frequency domain and applying matrix arithmetic:

$$\begin{aligned} \mathbf{0} &= \tilde{\mathbf{C}}(f) \left[\tilde{\mathbf{G}}(f) \tilde{\mathbf{E}}(f) \tilde{\mathbf{G}}^H(f) + \mathcal{E}_N \tilde{\mathbf{G}}(f) \right] \tilde{\mathbf{C}}^H(f) \\ &\quad + \tilde{\mathbf{C}}(f) \left[\tilde{\mathbf{G}}(f) \tilde{\mathbf{E}}(f) + \mathcal{E}_N \mathbf{I} \right] \\ &\quad + \left[\tilde{\mathbf{G}}(f) \tilde{\mathbf{E}}(f) + \mathcal{E}_N \mathbf{I} \right]^H \tilde{\mathbf{C}}(f)^H + \tilde{\mathbf{E}}(f), \end{aligned} \tag{3.72}$$

where $\tilde{\mathbf{E}}(f)$, $\tilde{\mathbf{G}}(f)$ are defined in the statement of the theorem, $\tilde{\mathbf{C}}(f)$ is defined similarly, and the superscript H denotes conjugate transpose. Thus, all that remains to fully specify the coefficient matrix $\tilde{\mathbf{C}}(f)$, and hence $c_{m,n,p,q} = \mathbf{C}_{m,n}[p-q]$, is to solve the above matrix equation at every $f \in [-1/2, 1/2]$.

Step #4: Solution to (3.71) by completing the square in (3.72)—Case of invertible $\tilde{\mathbf{G}}(f)$.

For the case of invertible $\tilde{\mathbf{G}}(f)$, $r = N$, so λ_0 and the limit do not enter into (3.62)–(3.69). In this case, we can solve the matrix equation (3.72) by completing the square at each $f \in [-1/2, 1/2)$. Dropping the dependence on f for a moment for notational simplicity, we have

$$\begin{aligned}
\mathbf{0} &= \tilde{\mathbf{C}} \left[\tilde{\mathbf{G}} \tilde{\mathbf{E}} \tilde{\mathbf{G}}^H + \mathcal{E}_N \tilde{\mathbf{G}} \right] \tilde{\mathbf{C}}^H \\
&\quad + \tilde{\mathbf{C}} \left[\tilde{\mathbf{G}} \tilde{\mathbf{E}} + \mathcal{E}_N \mathbf{I} \right] + \left[\tilde{\mathbf{G}} \tilde{\mathbf{E}} + \mathcal{E}_N \mathbf{I} \right]^H \tilde{\mathbf{C}}^H + \tilde{\mathbf{E}} \\
&= \tilde{\mathbf{C}} \tilde{\mathbf{G}} \tilde{\mathbf{V}} \tilde{\mathbf{V}}^H \tilde{\mathbf{G}}^H \tilde{\mathbf{C}}^H + \tilde{\mathbf{C}} \tilde{\mathbf{G}} \tilde{\mathbf{V}} \tilde{\mathbf{V}}^H \\
&\quad + \left(\tilde{\mathbf{V}} \tilde{\mathbf{V}}^H \right)^H \tilde{\mathbf{G}}^H \tilde{\mathbf{C}}^H + \tilde{\mathbf{E}} \\
&= \left[\tilde{\mathbf{C}} \tilde{\mathbf{G}} \tilde{\mathbf{V}} + \tilde{\mathbf{V}} \right] \left[\tilde{\mathbf{C}} \tilde{\mathbf{G}} \tilde{\mathbf{V}} + \tilde{\mathbf{V}} \right]^H + \tilde{\mathbf{E}} - \tilde{\mathbf{V}} \tilde{\mathbf{V}}^H \\
&= \left[\tilde{\mathbf{C}} \tilde{\mathbf{G}} \tilde{\mathbf{V}} + \tilde{\mathbf{V}} \right] \left[\tilde{\mathbf{C}} \tilde{\mathbf{G}} \tilde{\mathbf{V}} + \tilde{\mathbf{V}} \right]^H - \tilde{\mathbf{U}} \tilde{\mathbf{U}}^H,
\end{aligned}$$

where we have used (3.66)–(3.68) from the statement of the theorem. The solution

$$\begin{aligned}
\tilde{\mathbf{C}} \tilde{\mathbf{G}} \tilde{\mathbf{V}} + \tilde{\mathbf{V}} &= \tilde{\mathbf{U}} \\
\tilde{\mathbf{C}} &= \left[\tilde{\mathbf{U}} \tilde{\mathbf{V}}^{-1} - \mathbf{I} \right] \tilde{\mathbf{G}}^{-1}
\end{aligned}$$

follows directly. This must be computed at each $f \in [-1/2, 1/2)$ before $\tilde{\mathbf{C}}(f)$ can be Fourier-inverted to obtain the coefficients $c_{m,n,p,q}$.

Step #5: When $\tilde{\mathbf{G}}(f)$ is singular, the limit (3.69) exists, provided that $\mathcal{E}_N > 0$.

For the case of singular $\tilde{\mathbf{G}}(f)$, we cannot use its matrix inverse as in the previous step. However, when we replace this inverse with a properly constructed generalized inverse [93], and when we also properly construct the square root matrices $\tilde{\mathbf{U}}_{\lambda_0}(f)$ and $\tilde{\mathbf{V}}_{\lambda_0}(f)$, we can guarantee convergence in (3.69) such that the limit $\tilde{\mathbf{C}}(f)$ satisfies (3.72). In this step, we show that the definitions (3.62)–(3.64)—which are based on the joint diagonalization of $\tilde{\mathbf{G}}(f)$ and $\tilde{\mathbf{E}}^{-1}(f)$ [92, p. 33–36]—imply convergence of (3.69). In the next step, we show that the limit (3.69) satisfies (3.72).

Joint diagonalization allows us to compute the limit (3.69) directly as follows. Again, dropping the functional dependence on f , we have

$$\begin{aligned}\tilde{C} &= \lim_{\lambda_0 \rightarrow 0} \left[\tilde{Q}_2 \sqrt{\mathcal{E}_N \tilde{\Lambda}_{\lambda_0}^\dagger} \tilde{Q}_1^H \left(\tilde{Q}_2 \sqrt{\mathcal{E}_N \tilde{\Lambda}_{\lambda_0}^\dagger + \mathbf{I}} \tilde{Q}_1^H \right)^{-1} - \mathbf{I} \right] \tilde{Q}_2 \tilde{\Lambda}_{\lambda_0}^\dagger \tilde{Q}_2^H \\ &= \lim_{\lambda_0 \rightarrow 0} \tilde{Q}_2 \left[\sqrt{\frac{\mathcal{E}_N \tilde{\Lambda}_{\lambda_0}^\dagger}{\mathcal{E}_N \tilde{\Lambda}_{\lambda_0}^\dagger + \mathbf{I}}} - \mathbf{I} \right] \tilde{\Lambda}_{\lambda_0}^\dagger \tilde{Q}_2^H.\end{aligned}$$

The convergence is only affected by the middle expression involving only diagonal matrices. Because these matrices are diagonal, they multiply element-wise, and the convergence reduces to a scalar case. Examining the diagonal elements involving λ_0 , we compute the limit using L'Hospital's rule:

$$\lim_{\lambda_0 \rightarrow 0} \left(\sqrt{\frac{\mathcal{E}_N}{\mathcal{E}_N + \lambda_0}} - 1 \right) \frac{1}{\lambda_0} = -\frac{1}{2\mathcal{E}_N}.$$

Hence the limit (3.69) exists, but note that this depends critically on $\mathcal{E}_N > 0$.

Step #6: Solution to (3.71) via (3.72)—Case of singular $\tilde{\mathbf{G}}(f)$.

Finally, given that the limit (3.69) exists, we prove that it satisfies (3.72). First, we define the matrices

$$\tilde{C}_{\lambda_0}(f) = \left[\tilde{U}_{\lambda_0}(f) \tilde{V}_{\lambda_0}^{-1}(f) - \mathbf{I} \right] \tilde{\mathbf{G}}_{\lambda_0}^\dagger(f), \quad (3.73)$$

$$\tilde{\mathbf{G}}_{\lambda_0}(f) = \left(\tilde{Q}_2^H(f) \right)^{-1} \tilde{\Lambda}_{\lambda_0}(f) \tilde{Q}_2^{-1}(f), \quad (3.74)$$

where

$$\tilde{\Lambda}_{\lambda_0}(f) = \text{diag}\{\lambda_1(f), \dots, \lambda_r(f), \lambda_0, \dots, \lambda_0\} \quad (3.75)$$

is the same as $\tilde{\Lambda}(f)$, except with zero eigenvalues replaced by λ_0 . With these definitions we have (cf. 3.69, 3.61)

$$\tilde{C}(f) = \lim_{\lambda_0 \rightarrow 0} \tilde{C}_{\lambda_0}(f), \quad (3.76)$$

$$\tilde{\mathbf{G}}(f) = \lim_{\lambda_0 \rightarrow 0} \tilde{\mathbf{G}}_{\lambda_0}(f). \quad (3.77)$$

Therefore, we can show (dropping the dependence on f again for notational simplicity) that

$$\begin{aligned}
& \tilde{\mathbf{C}} \left[\tilde{\mathbf{G}} \tilde{\mathbf{E}} \tilde{\mathbf{G}}^H + \varepsilon_N \tilde{\mathbf{G}} \right] \tilde{\mathbf{C}}^H + \tilde{\mathbf{C}} \left[\tilde{\mathbf{G}} \tilde{\mathbf{E}} + \varepsilon_N \mathbf{I} \right] + \left[\tilde{\mathbf{G}} \tilde{\mathbf{E}} + \varepsilon_N \mathbf{I} \right]^H \tilde{\mathbf{C}}^H + \tilde{\mathbf{E}} \\
&= \left(\lim_{\lambda_0 \rightarrow 0} \tilde{\mathbf{C}}_{\lambda_0} \right) \left[\left(\lim_{\lambda_0 \rightarrow 0} \tilde{\mathbf{G}}_{\lambda_0} \right) \tilde{\mathbf{E}} \left(\lim_{\lambda_0 \rightarrow 0} \tilde{\mathbf{G}}_{\lambda_0}^H \right) + \varepsilon_N \left(\lim_{\lambda_0 \rightarrow 0} \tilde{\mathbf{G}}_{\lambda_0} \right) \right] \left(\lim_{\lambda_0 \rightarrow 0} \tilde{\mathbf{C}}_{\lambda_0}^H \right) \\
&\quad + \left(\lim_{\lambda_0 \rightarrow 0} \tilde{\mathbf{C}}_{\lambda_0} \right) \left[\left(\lim_{\lambda_0 \rightarrow 0} \tilde{\mathbf{G}}_{\lambda_0} \right) \tilde{\mathbf{E}} + \varepsilon_N \mathbf{I} \right] \\
&\quad + \left[\left(\lim_{\lambda_0 \rightarrow 0} \tilde{\mathbf{G}}_{\lambda_0} \right) \tilde{\mathbf{E}} + \varepsilon_N \mathbf{I} \right]^H \left(\lim_{\lambda_0 \rightarrow 0} \tilde{\mathbf{C}}_{\lambda_0}^H \right) + \tilde{\mathbf{E}} \\
&= \lim_{\lambda_0 \rightarrow 0} \left(\tilde{\mathbf{C}}_{\lambda_0} \left[\tilde{\mathbf{G}}_{\lambda_0} \tilde{\mathbf{E}} \tilde{\mathbf{G}}_{\lambda_0}^H + \varepsilon_N \tilde{\mathbf{G}}_{\lambda_0} \right] \tilde{\mathbf{C}}_{\lambda_0}^H \right. \\
&\quad \left. + \tilde{\mathbf{C}}_{\lambda_0} \left[\tilde{\mathbf{G}}_{\lambda_0} \tilde{\mathbf{E}} + \varepsilon_N \mathbf{I} \right] \right. \\
&\quad \left. + \left[\tilde{\mathbf{G}}_{\lambda_0} \tilde{\mathbf{E}} + \varepsilon_N \mathbf{I} \right]^H \tilde{\mathbf{C}}_{\lambda_0}^H + \tilde{\mathbf{E}} \right) \\
&= 0.
\end{aligned}$$

The first step follows from (3.76)–(3.77); the second step follows from properties of limits; and the third step follows from the observation that the large matrix expression inside the parantheses equals zero for every $\lambda_0 > 0$ (see Step #4), and hence it also equals zero in the limit as $\lambda_0 \rightarrow 0$. ■

The algorithm of the previous theorem provides a way to combine the energy and delay information of the interference (represented by the energy matrix-valued function $\mathbf{E}[n]$ and delayed-inner-product matrix-valued function $\mathbf{G}[n]$) with the PSD information of the noise (represented by ε_N) into a whitening filter architecture.

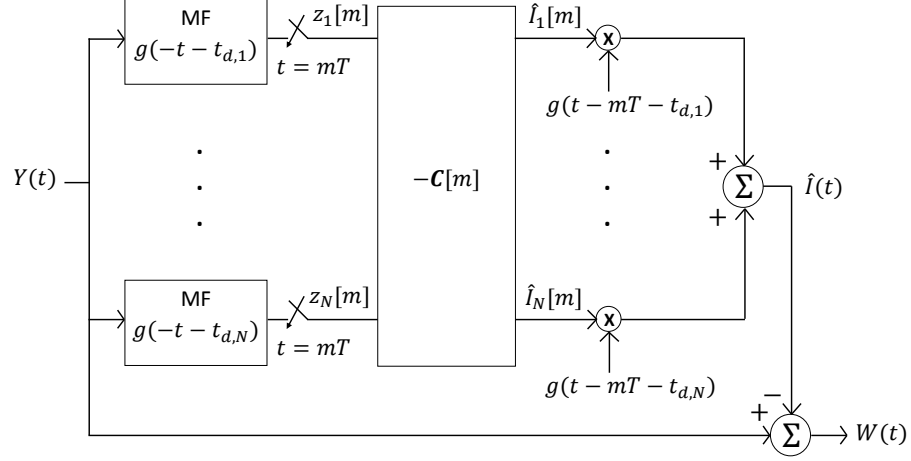


Figure 3.1. Interpretation of the cyclostationary whitener of Theorem 7 as the *form* of a multiuser detector followed by an interference canceler, cf [94, p. 235, 244, 295].

Note that we may rewrite the receiver of Theorem 7 in the following steps, which are illustrated in Figure 3.1:

$$z_n[q] = \int_{-\infty}^{\infty} Y(\tau) g(\tau - qT - t_{d,n}) d\tau, \quad (3.78)$$

$$\hat{l}_m[p] = - \sum_{n=1}^N \sum_{q=-\infty}^{\infty} \mathbf{C}_{m,n}[p - q] z_n[q], \quad (3.79)$$

$$\hat{l}(t) = \sum_{m=1}^N \sum_{p=-\infty}^{\infty} \hat{l}_m[p] g(t - pT - t_{d,m}), \quad (3.80)$$

$$W(t) = Y(t) - \hat{l}(t). \quad (3.81)$$

This has the form of a multiuser detector followed by an interference canceler—compare Figure 3.1, for example, with the diagrams of [94, p. 235, 244, 295]. However, we note that: (i) The distinctiveness of our “multiuser detector” is its particular matrix-valued impulse response $\mathbf{C}[m]$; (ii) We have derived this impulse response $\mathbf{C}[m]$ not from a multiuser detection problem, but from a *single-user* detection problem with a specific cyclostationary background interference; (iii) The derivation, as

presented, does not guarantee that the quantities $\hat{I}_n[m]$ are in fact good estimates of the pulse amplitudes $I_n[m]$ in any sense. These observations notwithstanding, it is intriguing that the solution to our single-user detection problem has the *form* of a multiuser detector and interference canceler. Future work should investigate this relationship more fully.

For practical implementation, the limit (3.69) may be approximated using diagonal loading for the generalized inverse $\tilde{\mathbf{A}}_{\lambda_0}^\dagger(f)$:

$$\tilde{\mathbf{A}}_{\lambda_0}^\dagger(f) \approx \left(\tilde{\mathbf{A}}(f) + \lambda_0 \max \left\{ \tilde{\mathbf{A}}(f) \right\} \mathbf{I} \right)^{-1}, \quad (3.82)$$

for some fixed $0 < \lambda_0 \ll 1$, where the maximum selects the largest eigenvalue from along the diagonal of $\tilde{\mathbf{A}}(f)$. In addition to approximating the limit using a fixed, small λ_0 , this diagonal loading also has the desirable effect of stabilizing the inverse numerically.

As in the simpler, pulse-shape synchronized case, we can gain intuitive insight into the benefit of knowing the energy and delay information $\{\mathcal{E}_{I,n}\}_{n=1}^N$ and $\{t_{d,n}\}_{n=1}^N$ by considering the hypothetical case of asymptotically¹ zero noise ($\mathcal{E}_N \rightarrow 0$). Applying the previous theorem, as $\mathcal{E}_N \rightarrow 0$ we obtain a non-vanishing filter $h_c(t_1, t_2)$ whose output can be made arbitrarily small as the noise grows smaller. (This can be seen via (3.62)–(3.69), which imply that the whitening filter is non-vanishing as $\mathcal{E}_N \rightarrow 0$ —see Step #5 of the proof of Theorem 7—and via the statement in the theorem that the output of $h_c(t_1, t_2)$ has PSD $\mathcal{E}_N \rightarrow 0$.) This suggests that in asynchronous cyclostationary LMDC interference, it may be possible to achieve arbitrarily close to perfect detection by making the noise arbitrarily small—*provided that the energy and delay information of the interference is known*. This is similar to the analogous result we obtained in the much simpler single-user or synchronized case.

The foregoing insights prompt the question: How can we model the detection gain produced by knowledge of the side information $\{\mathcal{E}_{I,n}\}_{n=1}^N$ and $\{t_{d,n}\}_{n=1}^N$ relative to the case when this energy and timing information is unknown? This question is inves-

¹Note that in this asynchronous case, we cannot set $\mathcal{E}_N = 0$ in general, due to the condition in Step #5 of the proof of Theorem 7.

tigated in Section 3.4. Before turning to the performance analysis, though, we first include brief subsections on (i) representation of the cyclostationary whitening filter (3.51)–(3.70) using FRESH filtering, and (ii) a demonstration that the cyclostationary whitening filter (3.51)–(3.70) is general enough to cover the case of cyclostationary LMDC interference plus any *arbitrary, non-white* stationary component.

3.3.3 Representation of whitener as FRESH filter

The kernel $h_c(t_1, t_2)$ from (3.51)–(3.70) inherits some periodic structure from the cyclostationary model of the LMDC interference, and this periodicity allows us to represent $h_c(t_1, t_2)$ as a FRESH filter. The mathematical foundation for the FRESH filter version of $h_c(t_1, t_2)$ is described in the following theorem.

Theorem 8 *Let an LTV filter kernel be periodic with period T in the sense that $h(t_1 + T, t_2 + T) = h(t_1, t_2)$. Then the spectrum $\tilde{W}(f)$ of the filter output*

$$w(t) = \int_{-\infty}^{\infty} h(t, s)y(s) ds \quad (3.83)$$

has the representation

$$\tilde{W}(f) = \sum_{k=-\infty}^{\infty} \tilde{H}^{(k/T)} \left(- \left(f - \frac{k}{2T} \right) \right) \tilde{Y} \left(f - \frac{k}{T} \right), \quad (3.84)$$

where

$$\tilde{W}(f) = \int_{-\infty}^{\infty} w(t) e^{-i2\pi ft} dt, \quad (3.85)$$

$$\tilde{Y}(f) = \int_{-\infty}^{\infty} y(t) e^{-i2\pi ft} dt, \quad (3.86)$$

$$\tilde{H}^{(k/T)}(f) = \frac{1}{T} \int_{-\infty}^{\infty} \int_{-T/2}^{T/2} h \left(t - \frac{\tau}{2}, t + \frac{\tau}{2} \right) e^{-i2\pi(kt/T + f\tau)} dt d\tau. \quad (3.87)$$

Proof By the specified periodicity of $h(t_1, t_2)$, we have the Fourier series representation:

$$h \left(t - \frac{\tau}{2}, t + \frac{\tau}{2} \right) = \sum_{k=-\infty}^{\infty} h^{(k/T)}(\tau) e^{i2\pi kt/T}, \quad (3.88)$$

$$h^{(k/T)}(\tau) = \frac{1}{T} \int_{-T/2}^{T/2} h \left(t - \frac{\tau}{2}, t + \frac{\tau}{2} \right) e^{-i2\pi kt/T} dt. \quad (3.89)$$

Thus, the filter output $w(t)$ can be written as:

$$w(t) = \sum_{k=-\infty}^{\infty} \int_{-\infty}^{\infty} h^{(k/T)}(s-t)y(s)e^{i2\pi k(t+s)/2T} ds. \quad (3.90)$$

Taking a Fourier transform gives the desired result. ■

The previous theorem states that linear, periodically time-varying (LPTV) filters have representations as FRESH filters. FRESH filters essentially consist of a bank of frequency-shifters followed by linear, time-invariant (LTI) filters, as illustrated in Figure 3.2. We can show that the cyclostationary whitener $h_c(t_1, t_2)$ is LPTV and hence has a FRESH implementation by Theorem 8: By making the change of variables $\ell = p - q$ in (3.51) and using (3.70), we can write

$$h_c(t_1, t_2) - \delta(t_2 - t_1) = \sum_{m,n,\ell,p} \mathbf{C}_{m,n}[\ell] g(t_1 - pT - t_{d,m}) g(t_2 - (p - \ell)T - t_{d,n}), \quad (3.91)$$

where the index ℓ ranges over all the integers, and the other indices m, n, p are as in (3.51). From this equation one can see that $h_c(t_1 + T, t_2 + T) = h_c(t_1, t_2)$ is indeed LPTV.

Using the notation of Theorem 8, and substituting h_c for h everywhere, we can derive a FRESH filter implementation of $h_c(t_1, t_2)$ as follows:

$$\begin{aligned} \tilde{H}_c^{(k/T)}(f) &= \frac{1}{T} \int_{-\infty}^{\infty} \int_{-T/2}^{T/2} h_c\left(t - \frac{\tau}{2}, t + \frac{\tau}{2}\right) e^{-i2\pi(kt/T + f\tau)} dt d\tau \\ &= \delta[k] + \sum_{m,n=1}^N \sum_{\ell=-\infty}^{\infty} \mathbf{C}_{m,n}[\ell] \tilde{H}_{m,n,\ell}^{(k/T)}(f), \end{aligned} \quad (3.92)$$

where

$$\begin{aligned} \tilde{H}_{m,n,\ell}^{(k/T)}(f) &= \frac{1}{T} \int_{-\infty}^{\infty} \int_{-T/2}^{T/2} \sum_{p=-\infty}^{\infty} g\left(t - \frac{\tau}{2} - pT - t_{d,m}\right) g\left(t + \frac{\tau}{2} - (p - \ell)T - t_{d,n}\right) \\ &\quad \cdot e^{-i2\pi(kt/T + f\tau)} dt d\tau \end{aligned}$$

$$\begin{aligned}
&= \frac{1}{T} \int_{-\infty}^{\infty} \sum_{p=-\infty}^{\infty} \int_{-T/2-pT-t_{d,m}}^{T/2-pT-t_{d,m}} g\left(s - \frac{\tau}{2}\right) g\left(s + \frac{\tau}{2} + \ell T - t_{d,n} + t_{d,m}\right) \\
&\quad \cdot e^{-i2\pi k(s+pT+t_{d,m})/T} e^{-i2\pi f\tau} dt d\tau \\
&= \frac{1}{T} \int_{-\infty}^{\infty} \int_{-\infty}^{\infty} g\left(s - \frac{\tau}{2}\right) g\left(s + \frac{\tau}{2} + \ell T - t_{d,n} + t_{d,m}\right) \\
&\quad \cdot e^{-i2\pi ks/T} e^{-i2\pi f\tau} e^{-i2\pi kt_{d,m}/T} ds d\tau \\
&= \frac{1}{T} \int_{-\infty}^{\infty} g(u) e^{i2\pi(f-k/2T)u} du \int_{-\infty}^{\infty} g(v) e^{-i2\pi(f+k/2T)v} dv \\
&\quad \cdot e^{-i2\pi(f+k/2T)t_{d,n}} e^{i2\pi(f-k/2T)t_{d,m}} e^{i2\pi(f+k/2T)\ell T} \\
&= \frac{1}{T} \tilde{G}^* \left(f - \frac{k}{2T}\right) \tilde{G} \left(f + \frac{k}{2T}\right) \\
&\quad \cdot e^{i2\pi(f+k/2T)\ell T} e^{i2\pi(f-k/2T)t_{d,m}} e^{-i2\pi(f+k/2T)t_{d,n}},
\end{aligned} \tag{3.93}$$

where in the first and third steps we make the changes of variables

$$\begin{aligned}
s &= t - pT - t_{d,m}, \\
u &= s - \frac{\tau}{2}, \\
v &= s + \frac{\tau}{2} + \ell T - t_{d,n} + t_{d,m}.
\end{aligned}$$

Combining (3.92) with (3.93) gives

$$\begin{aligned}
\tilde{H}_c^{(k/T)}(f) &= \delta[k] + \frac{1}{T} \tilde{G}^* \left(f - \frac{k}{2T}\right) \tilde{G} \left(f + \frac{k}{2T}\right) \\
&\quad \cdot \sum_{m,n=1}^N \sum_{\ell=-\infty}^{\infty} \mathbf{C}_{m,n}[\ell] e^{i2\pi(fT+k/2)\ell} e^{i2\pi(f-k/2T)t_{d,m}} e^{-i2\pi(f+k/2T)t_{d,n}} \\
&= \delta[k] + \frac{1}{T} \tilde{G}^* \left(f - \frac{k}{2T}\right) \tilde{G} \left(f + \frac{k}{2T}\right) \\
&\quad \cdot \sum_{m,n=1}^N \tilde{\mathbf{C}}_{m,n} \left(-Tf - \frac{k}{2}\right) e^{i2\pi(f-k/2T)t_{d,m}} e^{-i2\pi(f+k/2T)t_{d,n}},
\end{aligned} \tag{3.94}$$

where we have used (3.70) in the last step. When we combine this with (3.84)–(3.87), and using the fact that $g(t)$ is real-valued, we get

$$\begin{aligned}
\tilde{W}(f) &= \tilde{Y}(f) \\
&+ \frac{1}{T} \tilde{G}(f) \sum_{k=-\infty}^{\infty} \tilde{Y} \left(f - \frac{k}{T}\right) \tilde{G}^* \left(f - \frac{k}{T}\right) \tilde{\mathbf{s}}^H(f) \tilde{\mathbf{C}}(Tf - k) \tilde{\mathbf{s}} \left(f - \frac{k}{T}\right),
\end{aligned} \tag{3.95}$$

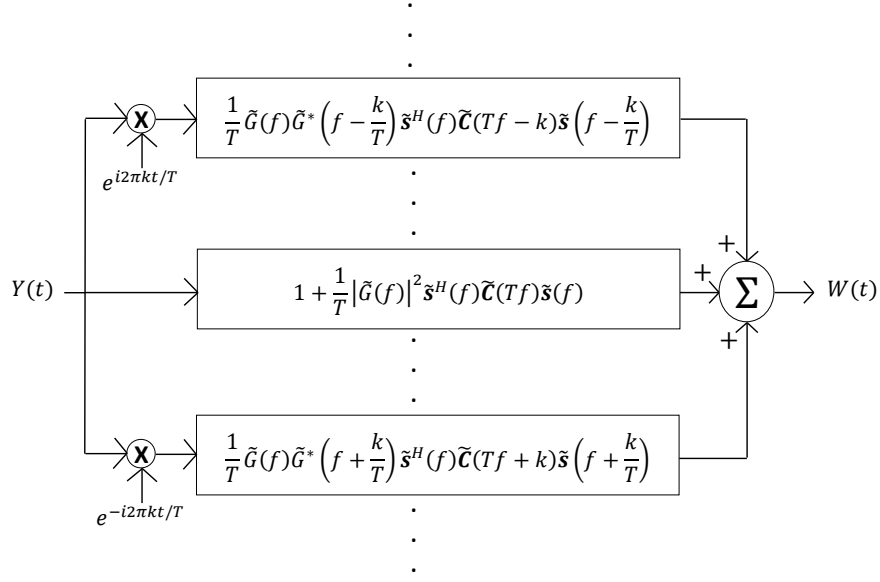


Figure 3.2. FRESH filter implementation of the cyclostationary whitener of Theorem 7. A FRESH filter essentially consists of a bank of frequency shifters followed by LTI filters.

where we note the periodicity $\tilde{\mathbf{C}}(Tf - k) = \tilde{\mathbf{C}}(Tf)$ for all $k \in \mathbb{Z}$, and we define the unevenly-sampled sinusoidal vectors $\tilde{\mathbf{s}}(f)$ as having components, for $n = 1, \dots, N$:

$$\tilde{s}_n(f) = e^{i2\pi f t_{d,n}}. \quad (3.96)$$

This FRESH architecture of the cyclostationary whitener is illustrated in Figure 3.2.

In practice, only a finite subset $\mathcal{K} \subset \{k/T : k \in \mathbb{Z}\}$ of cycle frequencies (k/T) in (3.95) will be important. Thus, using the FRESH implementation (3.95), cyclostationary whitening can be performed using $|\mathcal{K}|$ LTI convolutions, where $|\mathcal{K}|$ is the cardinality of the set \mathcal{K} .²

²In the authors' simulations, this FRESH implementation may provide some boost in computational speed.

3.3.4 Extension of whitener to a mixture of stationary and cyclostationary LMDC interference

Suppose a radar receives interference from a large network of many LMDC transmitters, and it can estimate the energy scalars $\{\mathcal{E}_{I,n}\}_{n=1}^N$ and delays $\{t_{d,n}\}_{n=1}^N$ of only the N most dominant transmitting LMDC sources (which dominate the interference through, for example, the near-far problem—*cf.* [95, p. 533]). Then it makes sense to model the composite LMDC interference as a mixture of a cyclostationary component (corresponding to the N most dominant transmitters whose parameters are estimated by the radar) and a stationary component (corresponding to the remaining, less dominant transmitters, whose parameters cannot be estimated by the radar). That is, we model the interference-plus-noise as

$$Y(t) = I_c(t) + I_s(t) + N(t), \quad (3.97)$$

where $I_c(t)$ is cyclostationary LMDC interference with autocorrelation given by (3.33), $I_s(t)$ is stationary LMDC interference with autocorrelation given by a version of (3.7)—namely,

$$R_{I_s I_s}^{(s)}(t_2 - t_1) = \frac{\mathcal{E}_{I,\text{rem}}}{T} \int_{-\infty}^{\infty} g(\tau) g(t_2 - t_1 + \tau) d\tau, \quad (3.98)$$

where $\mathcal{E}_{I,\text{rem}}$ is the sum of the mean-square pulse amplitudes of the remaining, less dominant LMDC sources, after the N most dominant sources are subtracted out—and $N(t)$ is C-AWGN having PSD \mathcal{E}_N , with all signals in (3.97) being zero-mean and independent of each other.

We can show that the deflection-optimal linear detector of signals in this modified stationary-cyclostationary LMDC interference and C-AWGN has the same form as previously derived. To show this, without loss of generality, we pass the received interference-plus-noise $Y(t)$ through an invertible stationary whitening filter having LTI impulse response (*cf.* (3.9)–(3.11))

$$h_s(\tau) = \int_{-\infty}^{\infty} \sqrt{\frac{\mathcal{E}_N}{\mathcal{E}_N + (\mathcal{E}_{I,\text{rem}}/T) \cdot |\tilde{G}(f)|^2}} e^{i2\pi f\tau} df. \quad (3.99)$$

The result of this invertible filtering operation is the new interference-plus-noise signal

$$\begin{aligned}\bar{\bar{Y}}(t) &= \sum_{n=1}^N \sum_{m=-\infty}^{\infty} I_n[m] \int_{-\infty}^{\infty} g(t - mT - t_{d,n} - \tau) h_s(\tau) d\tau \\ &\quad + \bar{\bar{N}}(t),\end{aligned}\tag{3.100}$$

where $\bar{\bar{N}}(t)$ is additive white noise (not necessarily Gaussian) with PSD \mathcal{E}_N , and the remaining cyclostationary component has autocorrelation function

$$\begin{aligned}R_{\bar{\bar{I}}\bar{\bar{I}}}(t_1, t_2) &= \sum_{n=1}^N \bar{\bar{\mathcal{E}}}_{I,n} \sum_{m=-\infty}^{\infty} \bar{\bar{g}}(t_1 - mT - t_{d,n}) \\ &\quad \cdot \bar{\bar{g}}(t_2 - mT - t_{d,n}),\end{aligned}\tag{3.101}$$

which is the same as (3.33), except with a new set of energy scalars and a new pulse shape, given by

$$\bar{\bar{\mathcal{E}}}_{I,n} = \mathcal{E}_{I,n} \left\| \int_{-\infty}^{\infty} g(t - \tau) h_s(\tau) d\tau \right\|^2, \tag{3.102}$$

$$\bar{\bar{g}}(t) = \frac{\int_{-\infty}^{\infty} g(t - \tau) h_s(\tau) d\tau}{\left\| \int_{-\infty}^{\infty} g(t - \tau) h_s(\tau) d\tau \right\|}. \tag{3.103}$$

This argument shows that the above-derived detector of signals in cyclostationary LMDC interference and C-AWGN is also optimal for a mixture of cyclostationary and stationary LMDC interference. Further, the same argument is adapted easily to include a mixture of cyclostationary LMDC interference with any arbitrary stationary component.

3.4 Performance analysis

We evaluate the performance of the detector based on the cyclostationary whitener $h_c(t_1, t_2)$ versus that based on the stationary whitener $h_s(t_1, t_2)$. Since whitening-based detectors optimize the statistical criterion of deflection, we use statistical deflection as our performance metric. The deflection d of a decision statistic U used for hypothesis testing is defined as

$$d = \frac{|E_1[U] - E_0[U]|^2}{\text{Var}_0[U]}, \tag{3.104}$$

where $E_j[U]$ and $\text{Var}_j[U]$ denote the mean and variance of U under hypothesis $H_j, j \in \{0, 1\}$. As we will see, the deflection d leads to a natural definition of SINR. The goal of our analysis is to derive the gain in deflection or SINR produced by using $h_c(t_1, t_2)$ over $h_s(t_1, t_2)$. We use a combination of theoretical analysis and Monte Carlo simulation (where necessary) to evaluate this performance gain.

3.4.1 Theoretical analysis of deflection

We first analyze the statistical deflection of the stationary-based and cyclostationary-based detectors theoretically.

To find the deflection of the either detector (the analysis is the same for both), we compute the mean and variance of U in (3.5) under H_0 and its mean under H_1 . Under H_0 :

$$\begin{aligned} E_0[U] &= \int \int E_0[r_w(t)] h^*(t, \tau) s^*(\tau) d\tau dt \\ &= 0, \\ E_0[|U|^2] &= \int \int \int \int E_0[r_w(\alpha) r_w^*(\beta)] h^*(\alpha, \tau) h(\beta, \sigma) \\ &\quad \cdot s^*(\tau) s(\sigma) d\tau d\sigma d\alpha d\beta \\ &= \mathcal{E}_N \int \int \int h^*(\alpha, \tau) h(\alpha, \sigma) s^*(\tau) s(\sigma) d\tau d\sigma d\alpha, \end{aligned}$$

where in this sub-section (3.4.1) all integrals are over the entire real line unless otherwise specified, and we have used the fact that under H_0 , $r_w(t)$ in (3.3) is zero-mean and stationary with PSD \mathcal{E}_N . Under H_1 :

$$\begin{aligned} E_1[U] &= \int \int E_1[r_w(t)] h^*(t, \tau) s^*(\tau) d\tau dt \\ &= \int \int \int \gamma s(\sigma) h(t, \sigma) h^*(t, \tau) s^*(\tau) d\tau d\sigma dt. \end{aligned}$$

The deflection d , then, is given in terms of a type of SINR:

$$d = \frac{|\gamma|^2}{\mathcal{E}_N} \left\| \int h(t, \tau) s(\tau) d\tau \right\|^2, \quad (3.105)$$

where here the norm is defined by

$$\|x\|^2 = \int_{-\infty}^{\infty} |x(t)|^2 dt. \quad (3.106)$$

The deflection (3.105) is the ratio of the energy of the *whitened* signal $\gamma s_w(t)$ (cf. (3.4)) to the noise PSD \mathcal{E}_N .

So far the analysis has assumed a fixed set of parameters \mathcal{E}_I , $\{\mathcal{E}_{I,n}\}_{n=1}^N$, and $\{t_{d,n}\}_{n=1}^N$ used to define the filters $h_s(t_1, t_2)$ and $h_c(t_1, t_2)$ in (3.9)–(3.11) and (3.51)–(3.70). We argue for two reasons that it makes sense to model these LMDC parameters as random. The first reason is theoretical: These parameters may fluctuate over time as LMDC transmitters turn ON and OFF, move through space, undergo changing power control and timing jitter, etc., and these temporal fluctuations may be modeled using probability distributions. The second reason is practical: In order to compute performance curves of the deflections d_s and d_c for the respective whitening algorithms, a deterministic model of these parameters would make it necessary to plot curves for a large number of parameter combinations, whereas modeling them as random allows us to plot a few ensemble averages that include many of the various special cases. For these reasons, we adopt random models for the parameters \mathcal{E}_I , $\{\mathcal{E}_{I,n}\}_{n=1}^N$, and $\{t_{d,n}\}_{n=1}^N$.

For the case of random parameters \mathcal{E}_I , $\{\mathcal{E}_{I,n}\}_{n=1}^N$, and $\{t_{d,n}\}_{n=1}^N$, the unconditional deflection d is given by taking the expectation of (3.105) over these parameters:³

$$d = \frac{|\gamma|^2}{\mathcal{E}_N} E \left[\left\| \int h(t, \tau) s(\tau) d\tau \right\|^2 \right]. \quad (3.107)$$

Therefore, the gain in deflection (SINR) from using a cyclostationary-based detector over a stationary-based detector is the ratio

$$\frac{d_c}{d_s} = \frac{E \left[\left\| \int h_c(t, \tau) s(\tau) d\tau \right\|^2 \right]}{E \left[\left\| \int h_s(t, \tau) s(\tau) d\tau \right\|^2 \right]}. \quad (3.108)$$

³Technically, iterated expectation has to be used separately, twice in the numerator and once in the denominator of (3.104), but in this case one of the expectations in the numerator is zero, and the expectation in the denominator cancels perfectly.

3.4.2 Statistical models for LMDC parameters

To choose specific probability distributions for the parameters \mathcal{E}_I , $\{\mathcal{E}_{I,n}\}_{n=1}^N$, and $\{t_{d,n}\}_{n=1}^N$, we briefly consider the types of physical phenomena governing their fluctuations.

First, we look at the energy scalars \mathcal{E}_I used in (3.9)–(3.11) and $\{\mathcal{E}_{I,n}\}_{n=1}^N$ used in (3.51)–(3.70), and we note that the former energy scalar is simply the sum of the latter, *cf.* (3.8). In a large wireless network, these energy scalars will fluctuate over time due to changing path loss, shadowing, multipath fading, and power control as the LMDC transmitters turn ON and OFF, move around, and adapt to changing network conditions. The dominant fluctuations in LMDC power received by the radar are likely to be dictated by: (i) Direct path loss from the LMDC transmitters to the radar, and (ii) Power control, which is likely to be governed largely by path loss from the LMDC mobiles to the LMDC base stations. For sake of simplicity, we ignore power control effects in this chapter and choose to focus on path loss as the dominant statistical effect driving variations in LMDC power received at the radar.

We adopt the following statistical model for the energy scalars $\{\mathcal{E}_{I,n}\}_{n=1}^N$. We model the radial distances $\{R_n\}_{n=1}^N$ of the N LMDC transmitters to the radar as the radial distances of N i.i.d. points, uniformly distributed over a sector of an annulus having inner and outer radii R_{\min} and R_{\max} , to the common center of the concentric circles defining that annulus sector. Then we adopt a path loss model of $\alpha_n = 1/R_n^{2\nu}$ power attenuation with distance.⁴ We scale the path loss attenuations using

$$\mathcal{E}_{I,n} = c\alpha_n, \quad (3.109)$$

where the scalar c is chosen to set a specified input INR:

$$\text{INR} = \frac{\sum_{n=1}^N E[\mathcal{E}_{I,n}]}{\mathcal{E}_N} = \frac{NcE[\alpha_n]}{\mathcal{E}_N}, \quad (3.110)$$

which is the sum of the average energies in the N LMDC users' modulated pulse shapes divided by the noise PSD.

⁴The guard radius R_{\min} is necessary to preserve finite second-order moments, given the path loss model we are using, *cf.* [67, 70–72].

Regarding the delays $\{t_{d,n}\}_{n=1}^N$, we argue that these are well modeled by a uniform probability distribution. This seems justified by the observation that the LMDC transmitters are not synchronized with the radar receiver and are turning ON and OFF at random over epochs much longer than a pulse duration T . Therefore, we model the $\{t_{d,n}\}_{n=1}^N$ as i.i.d. and uniformly distributed on $[0, T)$.

3.4.3 Method of evaluating expectation in (3.107)

Given these statistical distributions for the parameters $\{\mathcal{E}_{I,n}\}_{n=1}^N$, and $\{t_{d,n}\}_{n=1}^N$, the expectation in (3.107) is nontrivial to compute. This is because these random parameters enter into the definition of the whitener in highly nonlinear ways—consider (3.51)–(3.70) used to define the cyclostationary whitening filter. Due to the intractability of closed-form solutions, we use Monte Carlo integration to evaluate the expectation in (3.107).

To compute Monte Carlo integrals, we generate L i.i.d. collections of the parameters $\{\{\mathcal{E}_{I,n,\ell}\}_{n=1}^N, \{t_{d,n,\ell}\}_{n=1}^N\}_{\ell=1}^L$ using the statistical distributions just described, and we form the L corresponding stationary and cyclostationary filters $\{h_{s,\ell}(t_1, t_2), h_{c,\ell}(t_1, t_2)\}_{\ell=1}^L$. Then for each filter $h_{s,\ell}(t_1, t_2)$ ($h_{c,\ell}(t_1, t_2)$) we compute the deflection $d_{s,\ell}$ ($d_{c,\ell}$) according to (3.105). Finally, we compute the mean and standard error:

$$\hat{d}_s = \frac{1}{L} \sum_{\ell=1}^L d_{s,\ell} \quad (3.111)$$

$$\hat{\sigma}_{\hat{d}_s} = \sqrt{\frac{1}{L} \cdot \left(\frac{1}{L-1} \sum_{\ell=1}^L |d_{s,\ell} - \hat{d}_s|^2 \right)}, \quad (3.112)$$

and similarly for \hat{d}_c and its standard error. Here, the standard error estimates the standard deviation of the estimate \hat{d}_s (\hat{d}_c) and gives a sense of the error in this estimate. These estimates can be plotted parametrically versus INR by adjusting the scalar c in (3.109)–(3.110).

3.4.4 Choice of waveforms

In order to evaluate the expressions (3.105)–(3.107) for deflection, one must specify the signals $s(t)$ and $g(t)$. Although these waveforms could be quite general, for simplicity in this chapter we use signals similar to those used in some current radar and communications systems. Future work could investigate ways to optimize the deflection d over these waveforms $s(t)$ and $g(t)$.

For the radar signal $s(t)$, we use an LFM chirp with chirp rate β and duration T_{LFM} ,

$$s(t) = e^{i\pi\beta(t-T_{\text{LFM}}/2)^2} 1_{[0, T_{\text{LFM}}]}(t), \quad (3.113)$$

which has time-bandwidth product $\Pi = \beta T_{\text{LFM}}^2$. We choose the signal amplitude γ to set a specified input SNR:

$$\text{SNR} = \frac{\|\gamma s(t)\|^2}{\mathcal{E}_N} = \frac{|\gamma|^2 T_{\text{LFM}}}{\mathcal{E}_N}. \quad (3.114)$$

For the communications pulse shaping waveform $g(t)$, we investigate the following two choices:

$$g_1(t) = \sqrt{\frac{2}{T}} \sin\left(\frac{\pi t}{T}\right) 1_{[0, T]}(t), \quad (3.115)$$

$$g_2(t) = \sqrt{\frac{1}{T}} \cos\left(\frac{\pi t}{2T}\right) 1_{[-T, T]}(t). \quad (3.116)$$

These pulses are similar, except that the latter pulse shape has overlap between pulses and has half the bandwidth of the former ($1/T$ instead of $2/T$).

3.4.5 Implementation of whiteners

The stationary whitener (3.9)–(3.11) and cyclostationary whitener (3.51)–(3.70) are implemented using discrete-time processing on a computer, so that integrals can be reduced to sums, and Fourier transforms can be computed using the DFT implemented as an FFT.⁵ The cyclostationary whitener is implemented using the FRESH implementation (3.95), and due to discrete-time processing, only $|\mathcal{K}| = TF_s$ distinct

cycle frequencies (k/T) exist. In order to make the FRESH formula (3.95) work using DFTs, the delays $\{t_{d,n}\}_{n=1}^N$ have to be rounded to an integer multiple of $1/F_s$. However, since TF_s is large—on the order of 10^3 samples per pulse—we expect that forcing the delays $\{t_{d,n}\}_{n=1}^N$ to be on-grid in this manner should have a negligible impact on our estimates of deflection.

Validation of our computer implementation of the whiteners (3.9)–(3.11) and (3.51)–(3.70) is presented in Appendix G.

3.4.6 Results

We plot \hat{d}_s and \hat{d}_c versus input INR, and the results are shown in Figures 3.3–3.4. Error bars, which are tiny, correspond to the estimated standard errors $\hat{\sigma}_{\hat{d}_s}$ and $\hat{\sigma}_{\hat{d}_c}$. In these figures, the following parameter values are used: $L = 100$ i.i.d. samples per estimate; a simulation sample rate of $F_s = 102.4$ GHz (chosen to be large in order to simulate continuous time); an LMDC pulse symbol rate of $1/T = 100$ MHz; a ratio of maximum to minimum radial distances of $R_{\max}/R_{\min} = 5$, with a pathloss exponent of $\nu = 1$ (spherical propagation), yielding a total dynamic range of $(R_{\max}/R_{\min})^{2\nu} = 14$ dB for random fluctuations in path loss due to variations in transmitter location; a received radar signal $\gamma s(t)$ with input SNR of 10 dB. In Figure 3.3, the signal $s(t)$ has LFM chirp rate of $\beta = 100$ MHz/ μ s and chirp duration of $T_{\text{LFM}} = 1$ μ s, combining to give a bandwidth of 100 MHz and a time-bandwidth product of $\Pi = 100$; in Figure 3.4, the signal $s(t)$ has LFM chirp rate of $\beta = 200$ MHz/ μ s and chirp duration of $T_{\text{LFM}} = 0.5$ μ s, combining to give a bandwidth of 100 MHz and a time-bandwidth product of $\Pi = 50$. Note that the half-sine pulse shape $g_1(t)$ has bandwidth $2/T = 200$ MHz, while the half-cosine pulse shape $g_2(t)$ has bandwidth $1/T = 100$ MHz, which are twice and equal to the bandwidth of $s(t)$, respectively.

⁵For some pulse shapes $g(t)$, not used in this chapter, the matrix-valued function $\tilde{\mathbf{G}}(f)$ from (3.56) is more accurately computed using closed-form Fourier transforms $\tilde{G}(f)$ of $g(t)$ along with (F.3) from Appendix F, rather than using a DFT to compute (3.56). This is the case for pulse shapes $g(t)$ which are band-limited but not time-limited, such as a root-raised-cosine pulse shape, since for these pulse shapes taking a DFT of time-domain samples would introduce distortions due to windowing.

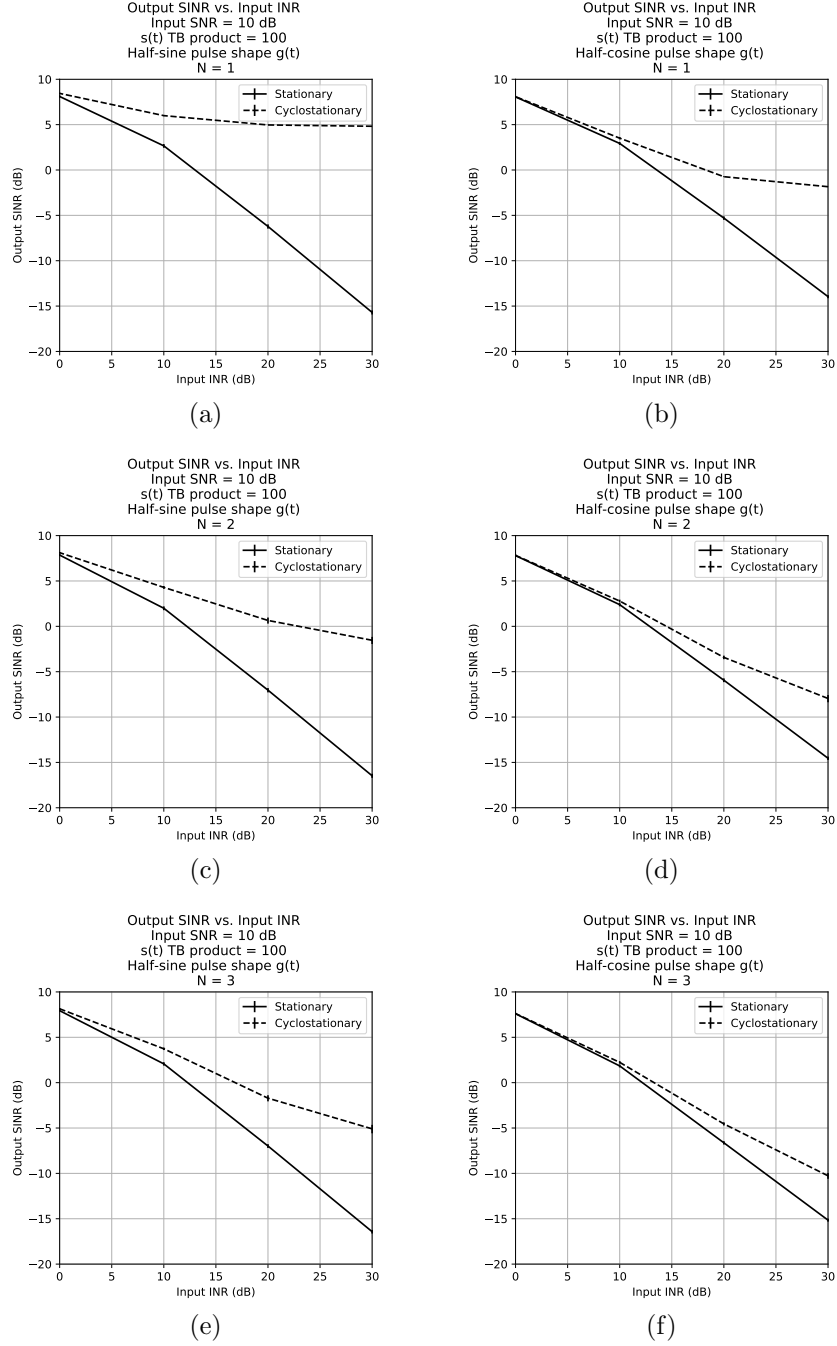


Figure 3.3. Estimated deflection (output SINR) \hat{d}_s and \hat{d}_c versus input INR, for $s(t)$ having time-bandwidth product $\Pi = 100$. (a) $N = 1$ and $g(t) = g_1(t)$ (half-sine pulse shape). (b) $N = 1$ and $g(t) = g_2(t)$ (half-cosine pulse shape). (c) $N = 2$ and $g(t) = g_1(t)$ (half-sine pulse shape). (d) $N = 2$ and $g(t) = g_2(t)$ (half-cosine pulse shape). (e) $N = 3$ and $g(t) = g_1(t)$ (half-sine pulse shape). (f) $N = 3$ and $g(t) = g_2(t)$ (half-cosine pulse shape).

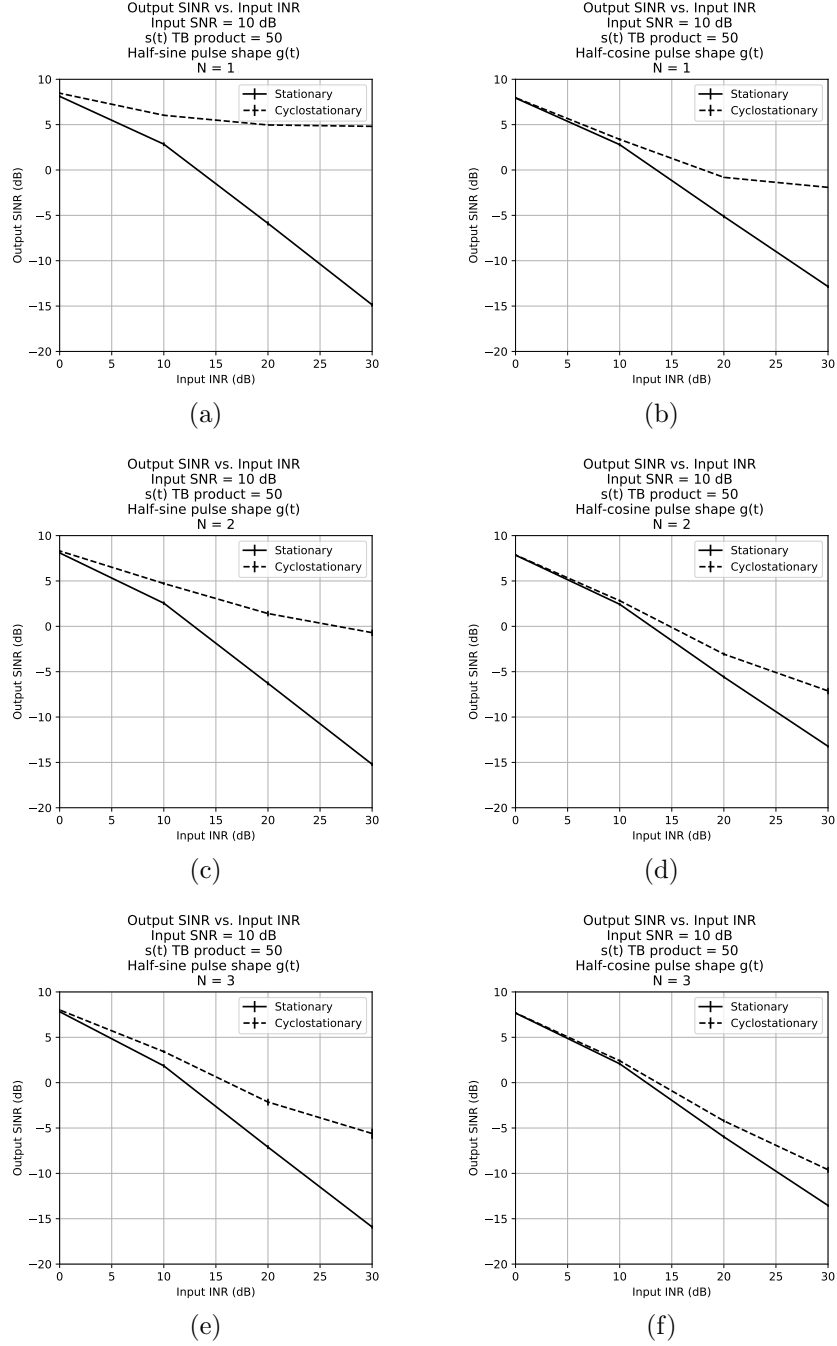


Figure 3.4. Estimated deflection (output SINR) \hat{d}_s and \hat{d}_c versus input INR, for $s(t)$ having time-bandwidth product $\Pi = 50$. (a) $N = 1$ and $g(t) = g_1(t)$ (half-sine pulse shape). (b) $N = 1$ and $g(t) = g_2(t)$ (half-cosine pulse shape). (c) $N = 2$ and $g(t) = g_1(t)$ (half-sine pulse shape). (d) $N = 2$ and $g(t) = g_2(t)$ (half-cosine pulse shape). (e) $N = 3$ and $g(t) = g_1(t)$ (half-sine pulse shape). (f) $N = 3$ and $g(t) = g_2(t)$ (half-cosine pulse shape).

In Figures 3.3–3.4, we observe the following: (i) The cyclostationary whitener leads to detection performance that is at least as good as the stationary whitener, in terms of deflection; (ii) The superiority of the cyclostationary whitener increases with increasing INR; (iii) The superiority of the cyclostationary whitener decreases with increasing N ; (iv) The superiority of the cyclostationary whitener is greater for the half-sine pulse shape $g_1(t)$ than for the half-cosine pulse shape $g_2(t)$; (v) The time-bandwidth product Π of the radar signal $s(t)$ has only a minor impact on the performance of the whiteners (where $\Pi = 100$ in Figure 3.3 and $\Pi = 50$ in Figure 3.4).

The deterioration of cyclostationary-based detection performance as N increases makes sense intuitively from the multiuser detector interpretation of Figure 3.1: As N increases, the signal $s(t)$ is projected onto a greater number of shifts of the pulse shape $g(t)$, and transformations of these projections are then subtracted out from $s(t)$, leaving less of the original signal energy at the output of the whitener. In the limit as $N \rightarrow \infty$, the signal $s(t)$ is projected onto all possible shifts of the pulse shape, and transformations of all possible projections are then subtracted out from $s(t)$. These results seem to suggest that the stationary whitener is the limiting form of the cyclostationary whitener, when the number N of LMDC delays is large.

Therefore, the results of Figures 3.3–3.4 suggest that radar detection can benefit from cyclostationary whitening when LMDC interference is characterized by both (i) a low number N of dominant interfering sources, and (ii) a high INR of these N sources, relative to the stationary remainder of the interference-plus-noise. This scenario could potentially arise, for example, in a near-far situation (*cf.* [95, p. 533]). The results of Figures 3.3–3.4 also suggest that the performance of the cyclostationary whitener is dependent on the signals used by the communications (and most likely also, radar) systems, implying that future work could optimize these waveforms for radar-communications spectral coexistence.

3.5 Conclusions

We have fully derived the deflection-optimal linear detector of signals in cyclostationary LMDC interference and stationary interference-plus-noise, which consists of a novel whitening filter followed by the traditional matched filter. We have given two mathematically equivalent representations of the proposed cyclostationary whitening filter, in terms of: (i) The *form* of a multiuser detector followed by an interference canceler, and (ii) A FRESH filter. Performance results indicate that detection based on the proposed cyclostationary whitening filter performs at least as well as detection based on standard stationary whitening, and sometimes better. The cyclostationary whitener leads to the most significant improvements in detection performance over stationary whitening when the number of dominant cyclostationary LMDC sources is low, and when they have a high received power relative to the stationary background. This situation potentially could arise in a near-far scenario when a few LMDC transmitters occasionally wander close to a radar receiver.

In order to fully develop the cyclostationary whitener algorithm derived and evaluated in this chapter, future work could investigate a number of further topics. These include:

1. Estimation of the model order N (*i.e.*, the number of dominant LMDC signals).
2. Estimation of the $2N + 1$ model parameters \mathcal{E}_N , $\{\mathcal{E}_{I,n}\}_{n=1}^N$, and $\{t_{d,n}\}_{n=1}^N$, given the model order N .
3. Algorithms for tracking the parameters \mathcal{E}_N , N , $\{\mathcal{E}_{I,n}\}_{n=1}^N$, and $\{t_{d,n}\}_{n=1}^N$ as they evolve through time.
4. Evaluation of the impact of estimation errors on the performance of the cyclostationary whitener/detector.
5. Joint waveform design for both the LMDC pulse shape $g(t)$ and the radar signal $s(t)$. Ideally, optimal waveforms $g(t)$ and $s(t)$ would achieve the optimal

trade-off between communications and radar system performances in a spectrum sharing scenario.

6. Investigation of the connection between cyclostationary whitening and multiuser detection (see Figure 3.1).

4. CONCLUSIONS

In an increasingly crowded RF environment, spectrum sharing provides one of many possible solutions to increasing spectral efficiency, with all of its economic and social benefits. This dissertation has made two substantive chapters of contributions to research on radar-communications spectrum sharing, focusing in particular on the problem of radar detection in the presence of wireless communications interference. In this closing chapter, we summarize the major findings of this dissertation, make some connections between Chapters 2–3, and propose some general directions for future work on this topic.

4.1 Summary of contributions

Chapter 2 proposed a model for wireless communications interference and its effects on adaptive-threshold radar detection. In modeling wireless communications interference statistically, both existing theoretical models in the literature and our original simulations suggested that communications interference could have both Gaussian and non-Gaussian behavior, depending on the specific modeling application. Based on our proposed model, we derived analytical expressions for the probability of false alarm and the probability of detection of a fixed-threshold radar detector and a cell-averaging adaptive-threshold radar detector. When we plotted the resulting ROC curves, we found that two general mechanisms impacted interference effects on radar. First, since the radar detectors analyzed were optimized for detection in AWGN only, when interference was either non-Gaussian or non-white, model mismatch led to unexpected results such as increased false alarm rates. Second, a boost to the underlying noise floor due to communications interference sometimes caused significant detection losses at relatively low INR, without an accompanying increase in the false alarm rate.

Chapter 3 proposed a novel algorithm for detecting radar signals in the presence of cyclostationary, linearly-modulated, digital communications (LMDC) interference. The assumed cyclostationary model required reliable estimation of $2N$ parameters, where N is the number of distinct LMDC delays. The deflection-optimal detector in such interference consisted of a novel whitening filter, which had equivalent representations in terms of both multiuser detection and FRESH filtering, followed by a matched filter. Performance results suggested that the proposed cyclostationary-based detector could outperform the standard equivalent detector based on a stationary interference model, particularly when the number N of dominant LMDC signals was small and their INR was large relative to the stationary remainder of the interference-plus-noise.

4.2 Connections between Chapters 2–3

Chapters 2–3 share at least two common threads. The first is that *inaccuracies and inefficiencies in models of wireless communications interference are opportunities for improved detector design*. By modeling inaccuracies we mean lack of fit to the physical world; by modeling inefficiencies we refer to suboptimal use of the available information.

In Chapter 2, modeling inaccuracies surfaced when communications interference was not well modeled by AWGN, the model on which the fixed-threshold and cell-averaging detectors were based. As such, we suggested that improved detection could be achieved by adopting more accurate models of communications interference. For example, similarities between the interference models discussed in Chapter 2 and existing radar clutter models suggest that detectors from the radar clutter literature may also hold promise for spectrum sharing applications.

In Chapter 3, modeling inefficiencies arose in the stationary model for LMDC interference when the delays and INRs of the dominant LMDC interfering sources could be reliably estimated. In this case, a more efficient use of the available informa-

tion resulted in a cyclostationary interference model, and we demonstrated that this cyclostationary model leads to better detection performance. Thus, in both Chapters 2 and 3, interference modeling deficiencies had ramifications for radar detection.

A second thread common through Chapters 2–3 that *non-LTI filtering may facilitate spectrum sharing between radar and wireless communications*. In Chapter 2, the plausibility of non-Gaussian communications interference motivated the suggestion of non-linear radar detectors. In Chapter 3, a cyclostationary interference model resulted in a time-varying detector. In both cases, either through non-linearity or time-variation, the proposed detectors were non-LTI.

One could argue that non-LTI filters are necessary if radar and communications systems are to use common frequencies at a common time and location. The rationale for this claim is as follows. If the communications and radar receivers are LTI exclusively, then it is well-known that the receivers' eigenfunctions are the complex exponentials. An implications of this mathematical result is that radar and communications signals sharing a common Fourier basis (range of sinusoidal frequencies) cannot be completely separated using LTI filters. Put another way, the only way to separate spectrally coexistent radar and communications signals is to employ non-LTI receivers. For linear receivers this argument implies the use of time-varying processing, which involves a change of basis from the Fourier basis (sinusoidal frequencies) as well as synchronization in the receivers. In fact, non-FDMA multiple access techniques, such as TDMA and CDMA, may be viewed as employing such alternative, non-sinusoidal basis functions, to which the receivers must synchronize.

Thus, the results of both Chapters 2 and 3 suggest that improved interference modeling as well as non-LTI detector designs may play an important role in interference mitigation for radar-communications spectrum sharing.

4.3 Directions for future work

In addition to some of the specific topics for future work mentioned at the end of Chapters 2–3, here we outline some broad directions for future research. First, models of wireless communications interference deserve further attention. Several theoretical interference models (such as the Middleton and alpha-stable models) suffer from limitations or inaccuracies, and empirical models are difficult to extend beyond the specific experimental data used to construct them. As more accurate, robust, and tractable interference models are developed, they may provide insights and tools for improved receiver design.

Second, several directions for spectrum-sharing radar receiver design remain to be explored. These include the use of non-linear detectors for non-Gaussian interference environments, including possibly detectors from the radar clutter literature, as well as time-frequency methods, cyclostationarity, multiuser detection, and MIMO beamforming.

Together, interference modeling and interference mitigation have potential to improve joint radar-communications performance in spectrum sharing applications. As interference is more effectively managed by the radar and communications systems of tomorrow, people will enjoy increasing benefits from increasingly efficient use of the RF spectrum.

REFERENCES

REFERENCES

- [1] N. Nartasilpa, S. Shahi, A. Salim, D. Tuninetti, N. Devroye, D. Erricolo, D. P. Zilz, and M. R. Bell, “Let’s Share CommRad: Co-Existing Communications and Radar Systems,” in *IEEE Radar Conference (RadarCon)*, Oklahoma City, OK, USA, apr 2018.
- [2] D. P. Zilz and M. R. Bell, “Statistical Modeling of Wireless Communications Interference and Its Effects on Adaptive-Threshold Radar Detection,” *IEEE Transactions on Aerospace and Electronic Systems*, vol. 54, no. 2, pp. 890–911, apr 2018.
- [3] —, “Statistical Results on the Performance of an Adaptive-Threshold Radar Detector in the Presence of Wireless Communications Interference,” Purdue University, Department of Electrical and Computer Engineering Technical Reports, Paper 482, Tech. Rep., nov 2017. [Online]. Available: <http://docs.lib.purdue.edu/ecetr/482>
- [4] —, “Optimal Linear Detection of Signals in Cyclostationary, Linearly-Modulated, Digital Communications Interference,” *Submitted to IEEE Transactions on Aerospace and Electronic Systems*, 2018.
- [5] J. Bezanson, A. Edelman, S. Karpinski, and V. B. Shah, “Julia: A Fresh Approach to Numerical Computing,” *SIAM Review*, vol. 59, no. 1, pp. 65–98, feb 2017. [Online]. Available: <http://julialang.org>
- [6] A. Meurer, C. Smith, M. Paprocki, O. Čertík, S. Kirpichev, M. Rocklin, A. Kumar, S. Ivanov, J. Moore, S. Singh, T. Rathnayake, S. Vig, B. Granger, R. Muller, F. Bonazzi, H. Gupta, S. Vats, F. Johansson, F. Pedregosa, M. Curry, A. Terrel, Š. Roučka, A. Saboo, I. Fernando, S. Kulal, R. Cimrman, and A. Scopatz, “SymPy: Symbolic Computing in Python,” *PeerJ Computer Science*, vol. 3, p. e103, jan 2017.
- [7] “Distributions: A Julia Package for Probability Distributions and Associated Functions.” [Online]. Available: <https://github.com/JuliaStats/Distributions.jl>
- [8] “DSP: A Julia Package for Filter Design, Periodograms, Window Functions, and Other Digital Signal Processing Functionality.” [Online]. Available: <https://github.com/JuliaDSP/DSP.jl>
- [9] M. Galassi, J. Davies, J. Theiler, B. Gough, G. Jungman, P. Alken, M. Booth, and F. Rossi, *GNU Scientific Library Reference Manual*, 3rd ed. Network Theory Ltd., 2009.
- [10] W. Hart, T. Hofmann, F. Johansson, C. Fieker, O. Motsak, and Others, “Nemo: Julia Bindings for Various Mathematical Libraries.” [Online]. Available: <https://github.com/wbhart/Nemo.jl>

- [11] “StatsFuns: A Julia Package for Mathematical Functions Related to Statistics.” [Online]. Available: <https://github.com/JuliaStats/StatsFuns.jl>
- [12] S. G. Johnson, “Cubature: A Simple C Package for Adaptive Multidimensional Integration.” [Online]. Available: <https://github.com/stevengj/cubature>
- [13] “Interpolations: Fast, Continuous Interpolation of Discrete Datasets in Julia.” [Online]. Available: <https://github.com/JuliaMath/Interpolations.jl>
- [14] “Roots: Root Finding Functions for Julia.” [Online]. Available: <https://github.com/JuliaMath/Roots.jl>
- [15] “StatsBase: Basic Statistics for Julia.” [Online]. Available: <https://github.com/JuliaStats/StatsBase.jl>
- [16] T. E. Oliphant, *A Guide to NumPy*. USA: Trelgol Publishing, 2006.
- [17] E. Jones, T. Oliphant, P. Peterson, and Others, “SciPy: Open Source Scientific Tools for Python.” [Online]. Available: <http://www.scipy.org>
- [18] S. Seabold and J. Perktold, “Statsmodels: Econometric and Statistical Modeling with Python,” in *Proceedings of the 9th Python in Science Conference*, 2010.
- [19] F. Johansson and Others, “Mpmath: A Python Library for Arbitrary-Precision Floating-Point Arithmetic,” dec 2013. [Online]. Available: <http://mpmath.org>
- [20] J. D. Hunter, “Matplotlib: A 2D Graphics Environment,” *Computing in Science & Engineering*, vol. 9, no. 3, pp. 90–95, jun 2007.
- [21] E. Halepovic, C. Williamson, and M. Ghaderi, “Wireless Data Traffic: A Decade of Change,” *IEEE Network*, vol. 23, no. 2, pp. 20–26, mar 2009.
- [22] “Cisco Visual Networking Index: Global Mobile Data Traffic Forecast Update, 2016–2021 White Paper,” feb 2017. [Online]. Available: <http://www.cisco.com/c/en/us/solutions/collateral/service-provider/visual-networking-index-vni/mobile-white-paper-c11-520862.html>
- [23] S. Haykin, “Cognitive Radio: Brain-Empowered Wireless Communications,” *IEEE Journal on Selected Areas in Communications*, vol. 23, no. 2, pp. 201–220, feb 2005.
- [24] D. Cabric, S. M. Mishra, and R. W. Brodersen, “Implementation Issues in Spectrum Sensing for Cognitive Radios,” in *Conference Record of the Thirty-Eighth Asilomar Conference on Signals, Systems and Computers*. IEEE, nov 2004, pp. 772–776.
- [25] A. Ghasemi and E. S. Sousa, “Collaborative Spectrum Sensing for Opportunistic Access in Fading Environments,” in *First IEEE International Symposium on New Frontiers in Dynamic Spectrum Access Networks (DYSPAN)*. IEEE, nov 2005, pp. 131–136.
- [26] H. S. Dhillon, R. K. Ganti, F. Baccelli, and J. G. Andrews, “Modeling and Analysis of K-Tier Downlink Heterogeneous Cellular Networks,” *IEEE Journal on Selected Areas in Communications*, vol. 30, no. 3, pp. 550–560, apr 2012.

- [27] H. S. Dhillon and J. G. Andrews, "Downlink Rate Distribution in Heterogeneous Cellular Networks under Generalized Cell Selection," *IEEE Wireless Communications Letters*, vol. 3, no. 1, pp. 42–45, feb 2014.
- [28] T. L. Marzetta, "Noncooperative Cellular Wireless with Unlimited Numbers of Base Station Antennas," *IEEE Transactions on Wireless Communications*, vol. 9, no. 11, pp. 3590–3600, nov 2010.
- [29] H. Q. Ngo, E. G. Larsson, and T. L. Marzetta, "Energy and Spectral Efficiency of Very Large Multiuser MIMO Systems," *IEEE Transactions on Communications*, vol. 61, no. 4, pp. 1436–1449, apr 2013.
- [30] J. Choi, Z. Chance, D. J. Love, and U. Madhow, "Noncoherent Trellis Coded Quantization: A Practical Limited Feedback Technique for Massive MIMO Systems," *IEEE Transactions on Communications*, vol. 61, no. 12, pp. 5016–5029, dec 2013.
- [31] J. Choi, D. J. Love, and P. Bidigare, "Downlink Training Techniques for FDD Massive MIMO Systems: Open-Loop and Closed-Loop Training With Memory," *IEEE Journal of Selected Topics in Signal Processing*, vol. 8, no. 5, pp. 802–814, oct 2014.
- [32] J. Choi, D. J. Love, and T. Kim, "Trellis-Extended Codebooks and Successive Phase Adjustment: A Path From LTE-Advanced to FDD Massive MIMO Systems," *IEEE Transactions on Wireless Communications*, vol. 14, no. 4, pp. 2007–2016, apr 2015.
- [33] S. Hur, T. Kim, D. J. Love, J. V. Krogmeier, T. A. Thomas, and A. Ghosh, "Millimeter Wave Beamforming for Wireless Backhaul and Access in Small Cell Networks," *IEEE Transactions on Communications*, vol. 61, no. 10, pp. 4391–4403, oct 2013.
- [34] S. Rangan, T. S. Rappaport, and E. Erkip, "Millimeter-Wave Cellular Wireless Networks: Potentials and Challenges," *Proceedings of the IEEE*, vol. 102, no. 3, pp. 366–385, mar 2014.
- [35] A. Ghosh, T. A. Thomas, M. C. Cudak, R. Ratasuk, P. Moorut, F. W. Vook, T. S. Rappaport, G. R. MacCartney, S. Sun, and S. Nie, "Millimeter-Wave Enhanced Local Area Systems: A High-Data-Rate Approach for Future Wireless Networks," *IEEE Journal on Selected Areas in Communications*, vol. 32, no. 6, pp. 1152–1163, jun 2014.
- [36] B. Obama, "Presidential Memorandum: Unleashing the Wireless Broadband Revolution," *The White House, Office of the Press Secretary*, jun 2010. [Online]. Available: <https://obamawhitehouse.archives.gov/the-press-office/presidential-memorandum-unleashing-wireless-broadband-revolution>
- [37] —, "Presidential Memorandum: Expanding America's Leadership in Wireless Innovation," *The White House, Office of the Press Secretary*, jun 2013. [Online]. Available: <https://obamawhitehouse.archives.gov/the-press-office/2013/06/14/presidential-memorandum-expanding-americas-leadership-wireless-innovation>

- [38] NTIA, “An Assessment of the Near-Term Viability of Accommodating Wireless Broadband Systems in the 1675–1710 MHz, 1755–1780 MHz, 3500–3650 MHz, and 4200–4220 MHz, 4380–4400 MHz Bands,” NTIA Fast Track Report, Tech. Rep., oct 2010.
- [39] FCC, “Report and Order,” *FCC 14-31, GN Docket No. 13-185*, mar 2014.
- [40] FCC and NTIA, “Public Notice: Coordination Procedures in the 1695–1710 MHz and 1755–1780 MHz Bands,” *DA 14-1023, GN Docket No. 13-185*, jul 2014.
- [41] FCC, “Report and Order, and Second Further Notice of Proposed Rulemaking,” *FCC 15-47, GN Docket No. 12-354*, apr 2015.
- [42] E. F. Drocella, J. C. Richards, R. L. Sole, F. Najmy, A. Lundy, and P. M. McKenna, “3.5 GHz Exclusion Zone Analyses and Methodology,” NTIA Report 15-517, Tech. Rep., jun 2015.
- [43] J. M. Peha, “Spectrum Management Policy Options,” *IEEE Communications Surveys*, vol. 1, no. 1, pp. 2–8, 1998.
- [44] H. Griffiths, L. Cohen, S. Watts, E. Mokole, C. Baker, M. Wicks, and S. Blunt, “Radar Spectrum Engineering and Management: Technical and Regulatory Issues,” *Proceedings of the IEEE*, vol. 103, no. 1, pp. 85–102, jan 2015.
- [45] R. Saruthirathanaworakun, J. M. Peha, and L. M. Correia, “Opportunistic primary-secondary spectrum sharing with a rotating radar,” in *2012 International Conference on Computing, Networking and Communications (ICNC)*. IEEE, jan 2012, pp. 1025–1030. [Online]. Available: <http://ieeexplore.ieee.org/lpdocs/epic03/wrapper.htm?arnumber=6167362>
- [46] J. M. Peha, “Spectrum Sharing in the Gray Space,” *Telecommunications Policy*, vol. 37, no. 2-3, pp. 167–177, mar 2013.
- [47] F. Hessar and S. Roy, “Spectrum Sharing Between a Surveillance Radar and Secondary Wi-Fi Networks,” *IEEE Transactions on Aerospace and Electronic Systems*, vol. 52, no. 3, pp. 1434–1448, jun 2016.
- [48] J. H. Reed, A. W. Clegg, A. V. Padaki, T. Yang, R. Nealy, C. Dietrich, C. R. Anderson, and D. M. Mearns, “On the Co-Existence of TD-LTE and Radar Over 3.5 GHz Band: An Experimental Study,” *IEEE Wireless Communications Letters*, vol. 5, no. 4, pp. 368–371, aug 2016.
- [49] F. Paisana, N. J. Kaminski, N. Marchetti, and L. A. DaSilva, “Signal Processing for Temporal Spectrum Sharing in a Multi-Radar Environment,” *IEEE Transactions on Cognitive Communications and Networking*, vol. 3, no. 2, pp. 123–137, jun 2017.
- [50] F. Paisana, N. Marchetti, and L. A. DaSilva, “Radar, TV and Cellular Bands: Which Spectrum Access Techniques for Which Bands?” *IEEE Communications Surveys & Tutorials*, vol. 16, no. 3, pp. 1193–1220, 2014.
- [51] B. Bahrak, S. Bhattarai, A. Ullah, J.-M. Park, J. Reed, and D. Gurney, “Protecting the Primary Users’ Operational Privacy in Spectrum Sharing,” in *IEEE International Symposium on Dynamic Spectrum Access Networks (DYSPAN)*. IEEE, apr 2014, pp. 236–247.

- [52] S. D. Blunt, P. Yatham, and J. Stiles, "Intrapulse Radar-Embedded Communications," *IEEE Transactions on Aerospace and Electronic Systems*, vol. 46, no. 3, pp. 1185–1200, jul 2010.
- [53] S. Gogineni, M. Rangaswamy, and A. Nehorai, "Multi-Modal OFDM Waveform Design," in *IEEE Radar Conference (RadarCon)*. IEEE, apr 2013.
- [54] K.-W. Huang, M. Bica, U. Mitra, and V. Koivunen, "Radar Waveform Design in Spectrum Sharing Environment: Coexistence and Cognition," in *IEEE Radar Conference (RadarCon)*. IEEE, may 2015, pp. 1698–1703.
- [55] R. A. Romero and K. D. Shepherd, "Friendly Spectrally Shaped Radar Waveform With Legacy Communication Systems for Shared Access and Spectrum Management," *IEEE Access*, vol. 3, pp. 1541–1554, aug 2015.
- [56] A. Hassanien, M. G. Amin, Y. D. Zhang, and F. Ahmad, "Dual-Function Radar-Communications: Information Embedding Using Sidelobe Control and Waveform Diversity," *IEEE Transactions on Signal Processing*, vol. 64, no. 8, pp. 2168–2181, apr 2016.
- [57] B. Li, A. P. Petropulu, and W. Trappe, "Optimum Co-Design for Spectrum Sharing Between Matrix Completion Based MIMO Radars and a MIMO Communication System," *IEEE Transactions on Signal Processing*, vol. 64, no. 17, pp. 4562–4575, sep 2016.
- [58] M. R. Bell, "Information Theory and Radar Waveform Design," *IEEE Transactions on Information Theory*, vol. 39, no. 5, pp. 1578–1597, sep 1993.
- [59] H. Deng and B. Himed, "Interference Mitigation Processing for Spectrum-Sharing Between Radar and Wireless Communications Systems," *IEEE Transactions on Aerospace and Electronic Systems*, vol. 49, no. 3, pp. 1911–1919, jul 2013.
- [60] Z. Geng, H. Deng, and B. Himed, "Adaptive Radar Beamforming for Interference Mitigation in Radar-Wireless Spectrum Sharing," *IEEE Signal Processing Letters*, vol. 22, no. 4, pp. 484–488, apr 2015.
- [61] N. Nartasilpa, D. Tuninetti, N. Devroye, and D. Erricolo, "On the Error Rate of a Communication System Suffering from Additive Radar Interference," in *IEEE Global Communications Conference (GLOBECOM)*. IEEE, dec 2016.
- [62] A. R. Chiriyath, B. Paul, and D. W. Bliss, "Radar-Communications Convergence: Coexistence, Cooperation, and Co-Design," *IEEE Transactions on Cognitive Communications and Networking*, vol. 3, no. 1, pp. 1–12, mar 2017.
- [63] "Characteristics of Non-Meteorological Radiolocation Radars, and Characteristics and Protection Criteria for Sharing Studies for Aeronautical Radionavigation and Radars in the Radiodetermination Service Operating in the Frequency Band 2700–2900 MHz," *Recommendation ITU-R M.1464-2*, feb 2015.
- [64] F. H. Sanders, R. L. Sole, B. L. Bedford, D. Franc, and T. Pawlowitz, "Effects of RF Interference on Radar Receivers," NTIA Report TR-06-444, Tech. Rep., sep 2006.

- [65] K. J. Sangston and K. R. Gerlach, "Coherent Detection of Radar Targets in a Non-Gaussian Background," *IEEE Transactions on Aerospace and Electronic Systems*, vol. 30, no. 2, pp. 330–340, apr 1994.
- [66] —, "Non-Gaussian Noise Models and Coherent Detection of Radar Targets," Naval Research Lab Report NRL/FR/5341-92-9367, Washington, D.C., Tech. Rep., nov 1992.
- [67] M. Haenggi and R. K. Ganti, "Interference in Large Wireless Networks," *Foundations and Trends in Networking*, vol. 3, no. 2, pp. 127–248, 2008.
- [68] J. Ilow and D. Hatzinakos, "Analytic Alpha-Stable Noise Modeling in a Poisson Field of Interferers or Scatterers," *IEEE Transactions on Signal Processing*, vol. 46, no. 6, pp. 1601–1611, jun 1998.
- [69] P. C. Pinto, C.-C. Chong, A. Giorgetti, M. Chiani, and M. Z. Win, "Narrow-band Communication in a Poisson Field of Ultrawideband Interferers," in *IEEE International Conference on Ultra-Wideband*. IEEE, sep 2006, pp. 387–392.
- [70] H. Inaltekin and S. B. Wicker, "The Behavior of Unbounded Path-Loss Models and the Effect of Singularity on Computed Network Interference," in *4th Annual IEEE Communications Society Conference on Sensor, Mesh and Ad Hoc Communications and Networks*. IEEE, jun 2007, pp. 431–440.
- [71] J. Venkataraman, M. Haenggi, and O. Collins, "Shot Noise Models for Outage and Throughput Analyses in Wireless Ad Hoc Networks," in *IEEE Military Communications Conference*. IEEE, oct 2006, pp. 1–7.
- [72] P. Cardieri, "Modeling Interference in Wireless Ad Hoc Networks," *IEEE Communications Surveys & Tutorials*, vol. 12, no. 4, pp. 551–572, 2010.
- [73] D. Middleton, "Statistical-Physical Models of Electromagnetic Interference," *IEEE Transactions on Electromagnetic Compatibility*, vol. EMC-19, no. 3, pp. 106–127, aug 1977.
- [74] —, "Statistical-Physical Models of Man-Made and Natural Radio Noise, Part II: First-Order Probability Models of the Envelope and Phase," Office of Telecommunications, OT Report 76-86, Tech. Rep., apr 1976.
- [75] M. Sekine and Y. Mao, *Weibull Radar Clutter*. London: Peter Peregrinus Ltd., 1990.
- [76] W. J. J. Roberts and S. Furui, "Maximum Likelihood Estimation of K-Distribution Parameters Via the Expectation-Maximization Algorithm," *IEEE Transactions on Signal Processing*, vol. 48, no. 12, pp. 3303–3306, dec 2000.
- [77] M. R. Bell, N. Devroye, D. Erricolo, T. Koduri, S. Rao, and D. Tuninetti, "Results on Spectrum Sharing between a Radar and a Communications System," in *International Conference on Electromagnetics in Advanced Applications (ICEAA)*. IEEE, aug 2014, pp. 826–829.
- [78] J. S. Daba and M. R. Bell, "Statistics of the Scattering Cross-Section of a Small Number of Random Scatterers," *IEEE Transactions on Antennas and Propagation*, vol. 43, no. 8, pp. 773–783, aug 1995.

- [79] K. Krishnamoorthy, *Handbook of Statistical Distributions with Applications*. Boca Raton, FL: Chapman & Hall/CRC, 2006.
- [80] I. S. Gradshteyn and I. M. Ryzhik, *Table of Integrals, Series, and Products*, 8th ed., D. Zwillinger and V. Moll, Eds. Waltham, MA: Academic Press, 2014.
- [81] P. Weber and S. Haykin, "Ordered Statistic CFAR Processing for Two-Parameter Distributions with Variable Skewness," *IEEE Transactions on Aerospace and Electronic Systems*, vol. AES-21, no. 6, pp. 819–821, nov 1985.
- [82] S. A. Kassam, *Signal Detection in Non-Gaussian Noise*, J. B. Thomas, Ed. New York, NY: Springer-Verlag, 1988.
- [83] E. Conte, M. Lops, and G. Ricci, "Asymptotically Optimum Radar Detection in Compound-Gaussian Clutter," *IEEE Transactions on Aerospace and Electronic Systems*, vol. 31, no. 2, pp. 617–625, apr 1995.
- [84] S. Kraut, L. L. Scharf, and L. T. McWhorter, "Adaptive Subspace Detectors," *IEEE Transactions on Signal Processing*, vol. 49, no. 1, pp. 1–16, jan 2001.
- [85] W. A. Gardner, Ed., *Cyclostationarity in Communications and Signal Processing*. New York, NY: IEEE Press, 1994.
- [86] W. A. Gardner, "Signal Interception: A Unifying Theoretical Framework for Feature Detection," *IEEE Transactions on Communications*, vol. 36, no. 8, pp. 897–906, aug 1988.
- [87] E. Axell, G. Leus, E. G. Larsson, and H. V. Poor, "Spectrum Sensing for Cognitive Radio: State-of-the-Art and Recent Advances," *IEEE Signal Processing Magazine*, vol. 29, no. 3, pp. 101–116, may 2012.
- [88] L. Izzo, L. Paura, and M. Tanda, "Signal Detection in Partially Known Cyclostationary Non-Gaussian Noise," in *Proceedings of the IEEE 1990 National Aerospace and Electronics Conference*. Dayton, OH, USA: IEEE, may 1990, pp. 116–119.
- [89] H. V. Poor, *An Introduction to Signal Detection and Estimation*, J. B. Thomas, Ed. New York, NY: Springer-Verlag, 1988.
- [90] H. L. Van Trees, K. L. Bell, and Z. Tian, *Detection, Estimation, and Modulation Theory—Part I: Detection, Estimation, and Filtering Theory*, 2nd ed. Hoboken, NJ: John Wiley & Sons, Inc., 2013.
- [91] C. W. Helstrom, *Elements of Signal Detection and Estimation*. Englewood Cliffs, NJ: Prentice-Hall, Inc., 1995.
- [92] K. Fukunaga, *Introduction to Statistical Pattern Recognition*, 1st ed. New York, NY: Academic Press, Inc., 1972.
- [93] R. M. Pringle and A. A. Rayner, *Generalized Inverse Matrices with Applications to Statistics*, A. Stuart, Ed. London: Charles Griffin & Company Limited, 1971.
- [94] S. Verdú, *Multiuser Detection*. Cambridge, UK: Cambridge University Press, 1998.

- [95] R. L. Peterson, R. E. Ziemer, and D. E. Borth, *Introduction to Spread Spectrum Communications*. Englewood Cliffs, NJ: Prentice-Hall, Inc., 1995.
- [96] G. M. Ljung and G. E. P. Box, "On a Measure of Lack of Fit in Time Series Models," *Biometrika*, vol. 65, no. 2, pp. 297–303, aug 1978.

APPENDICES

A. PRACTICAL CONSIDERATIONS IN NUMERICAL INTEGRATION

Numerical integration of (2.42), (2.43), (2.47), (2.48), (2.49), and (2.50) can be complicated by difficulties such as slow convergence and incorrect error estimates which can cause adaptive quadrature/cubature algorithms to reach premature stopping conditions. (Such has been observed in some integrations using Matlab.) We have found the Cubature package of MIT's Julia programming language [5, 12] to provide an accurate and relatively fast solution. We use the `pcubature()` routine with appropriately selected relative tolerances to obtain numerical integral values which agree with Monte Carlo simulation to within standard statistical variation of the Monte Carlo estimates (*cf.* Appendix B).

In order to transform the integrals into a form acceptable for the `pcubature()` routine—namely, a smooth integrand and a hypercubic region of integration—the following mathematical manipulations are employed. First, the Marcum Q-function is expanded as an integral according to (2.30). Second, changes of variables are applied as follows:

$$\begin{aligned} t' &= \frac{a^b}{1 + a^b}, \\ u' &= \begin{cases} \frac{x^2 - T^2}{1 + x^2}, & \text{for (2.42), (2.43),} \\ \frac{x^2 - (\tau/N)z}{1 + x^2}, & \text{for (2.47), (2.48), (2.49), (2.50),} \end{cases} \\ v' &= \frac{z}{1 + z}, \\ w' &= 1 - \frac{1}{\pi} \arccos \left[\frac{v^2 - (A_S^2 + a^2)}{2A_S a} \right], \end{aligned}$$

where the exponent b is chosen so as to remove possible singularities in the pdf (2.18) of A_I :

$$b = \begin{cases} \alpha, & \alpha \leq 1/2, \\ 1, & \alpha > 1/2. \end{cases}$$

Also, in some cases involving (2.42) and (2.43), T is so far in the tail of the distributions that $1 - P_{FA}$ and $1 - P_D$ must be computed in place of P_{FA} and P_D , using extended-precision floating point integrands.

B. AGREEMENT OF MONTE CARLO SIMULATION WITH NUMERICAL INTEGRATION

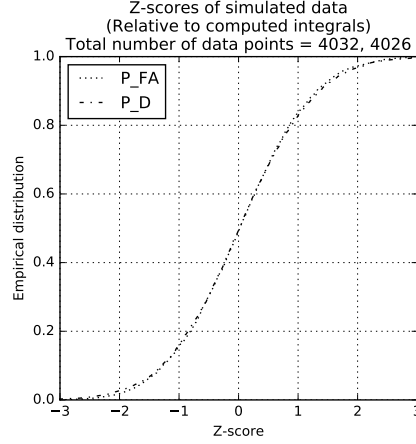


Figure B.1. Z-scores of Monte Carlo estimates of P_{FA} and P_D , assuming the values for P_{FA} and P_D obtained by numerical integration are correct. Six values of z_{P_D} are not computable since the corresponding numerically integrated values of P_D are barely greater than unity, by a negligible amount that is consistent with the Monte Carlo estimates (which are unity or barely less than unity) and do not affect conclusions drawn by the ROC plots.

In order to check the validity of our numerical integrals, we check them against Monte Carlo simulation as follows: First, we generate n_t i.i.d. realizations of the random phasors given by (2.23) and process them using decision rules (2.26) and (2.27). Then we use the following estimates of P_{FA} and P_D :

$$\hat{P}_{FA} = \frac{1}{n_t} \sum_{j=1}^{n_t} \phi_j \left(X_j^{(H_0)} \right), \quad (\text{B.1})$$

$$\hat{P}_D = \frac{1}{n_t} \sum_{j=1}^{n_t} \phi_j \left(X_j^{(H_1)} \right), \quad (\text{B.2})$$

where $\phi_j(X_j) \in \{0, 1\}$ denotes the detector's j -th decision. Finally, we compute Z-scores of the Monte Carlo estimates, assuming that the true values of the parameters are given by the results of the numerical integration:

$$z_{P_{FA}} = \frac{\hat{P}_{FA} - P_{FA}}{\sigma_{P_{FA}}}, \quad (\text{B.3})$$

$$z_{P_D} = \frac{\hat{P}_D - P_D}{\sigma_{P_D}}, \quad (\text{B.4})$$

$$\sigma_{P_{FA}}^2 = P_{FA}(1 - P_{FA})/n_t, \quad (\text{B.5})$$

$$\sigma_{P_D}^2 = P_D(1 - P_D)/n_t, \quad (\text{B.6})$$

The results of our computed Z-scores over the 96 ROCs computed in Section 2.4.1 are shown in Figure B.1. Since n_t is chosen to be very large ($n_t = 10^7$), the Z-scores should approximately follow the standard normal distribution by the CLT. Indeed, as shown in Figure B.1, about 68% of the Z-scores fall between -1 and 1, about 95% of the Z-scores fall between -2 and 2, and about 99.7% of the Z-scores fall between -3 and 3—as expected for a standard normal distribution. Thus, our numerical integration agrees with Monte Carlo simulation to within standard statistical variation.

Similar results are obtained for the 36 plots of P_D and P_{FA} versus INR discussed in Section 2.4.2.

**C. FULL SET OF CALCULATED P_{FA} AND P_{D} FOR
FIXED-THRESHOLD RADAR DETECTOR AND
CELL-AVERAGING ADAPTIVE-THRESHOLD RADAR
DETECTOR**

Effects of non-Gaussian interference on radar detection

Fixed-threshold test with impulsive interference ($p < 1$)

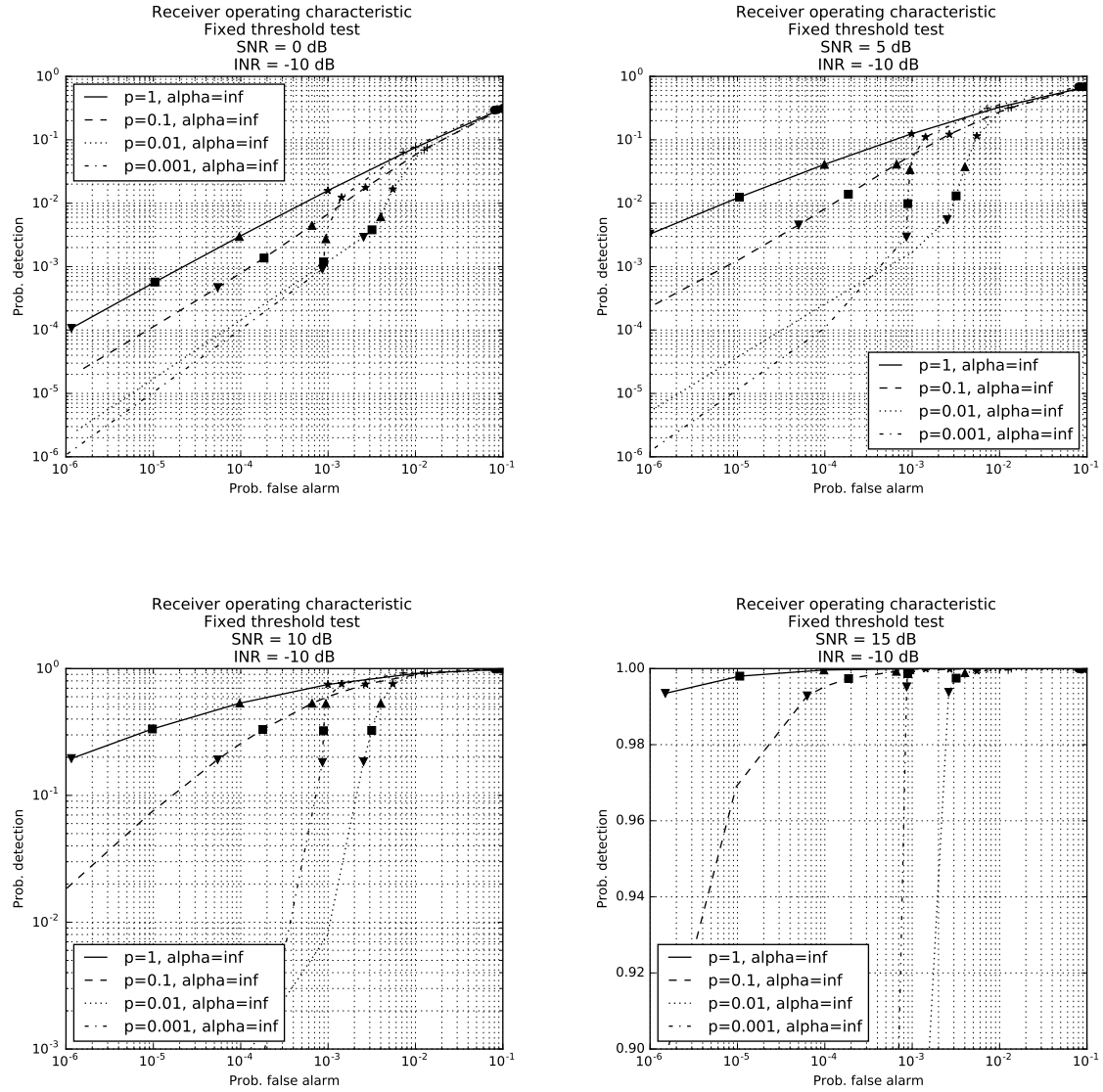


Figure C.1. ROCs for fixed-threshold test with impulsive interference (INR = -10 dB; SNR = 0, 5, 10, 15 dB)

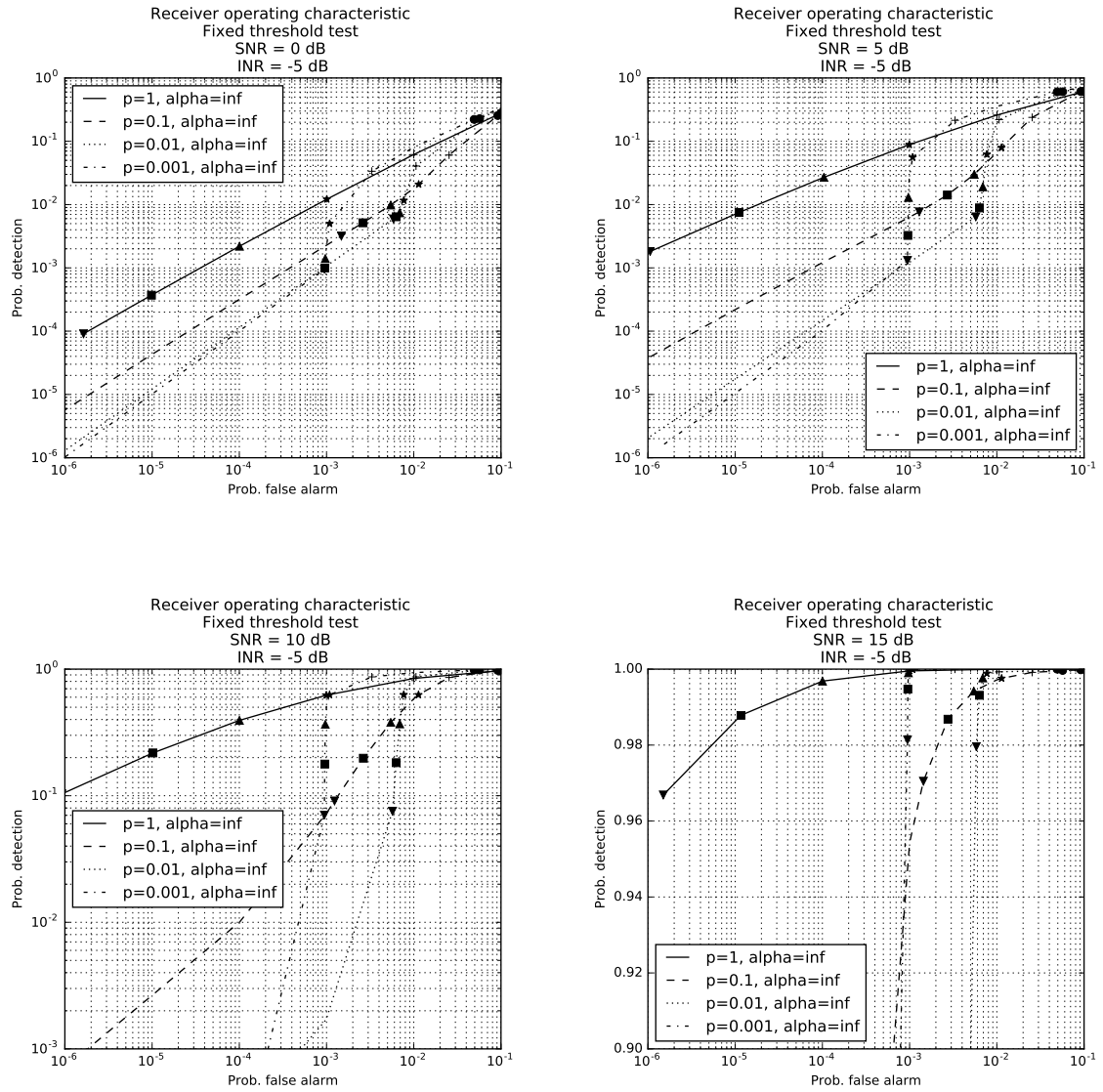


Figure C.2. ROCs for fixed-threshold test with impulsive interference (INR = -5 dB; SNR = 0, 5, 10, 15 dB)

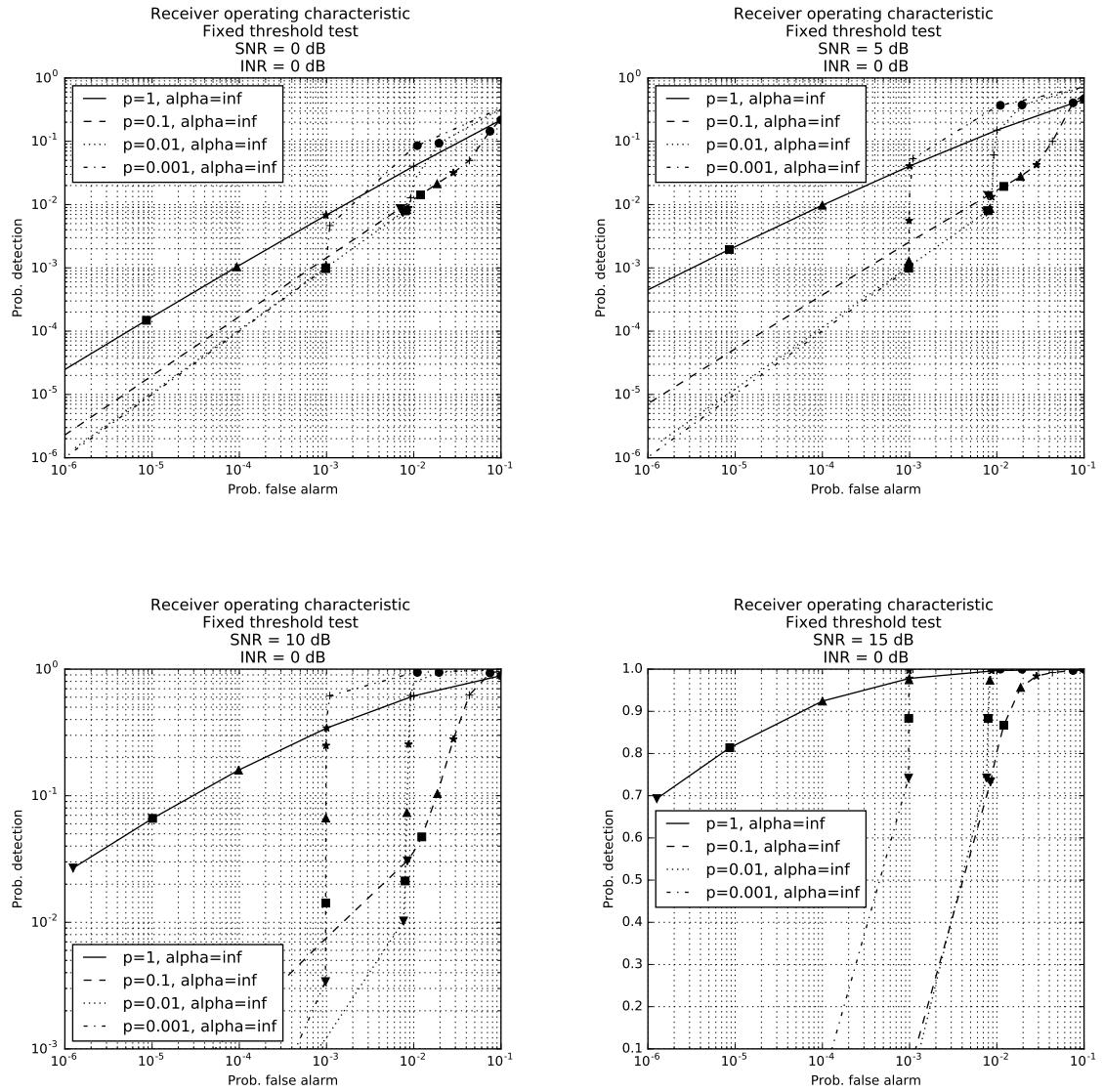


Figure C.3. ROCs for fixed-threshold test with impulsive interference (INR = 0 dB; SNR = 0, 5, 10, 15 dB)

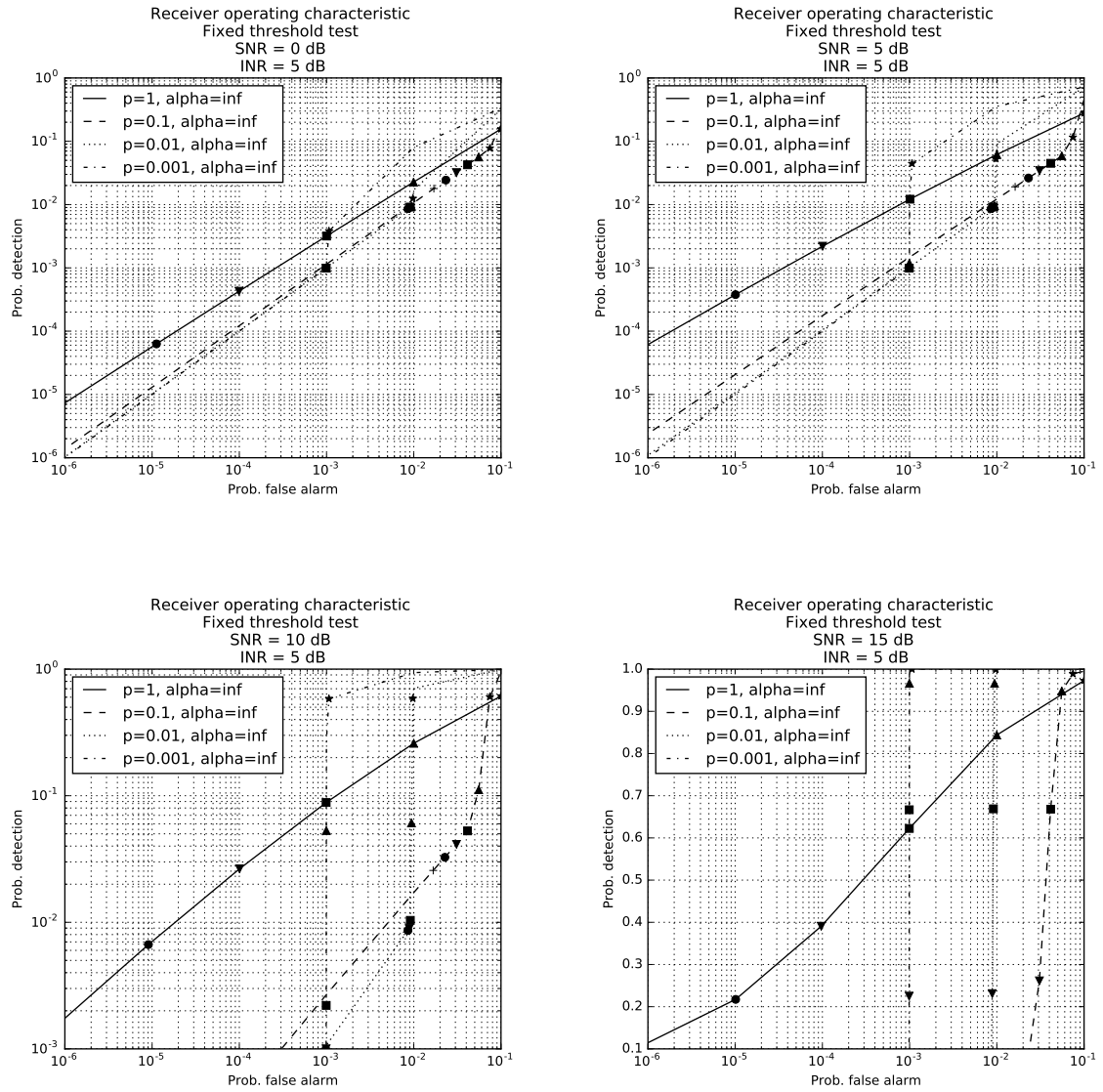


Figure C.4. ROCs for fixed-threshold test with impulsive interference (INR = 5 dB; SNR = 0, 5, 10, 15 dB)

Fixed-threshold test with heavy-tailed interference ($\alpha < \infty$)

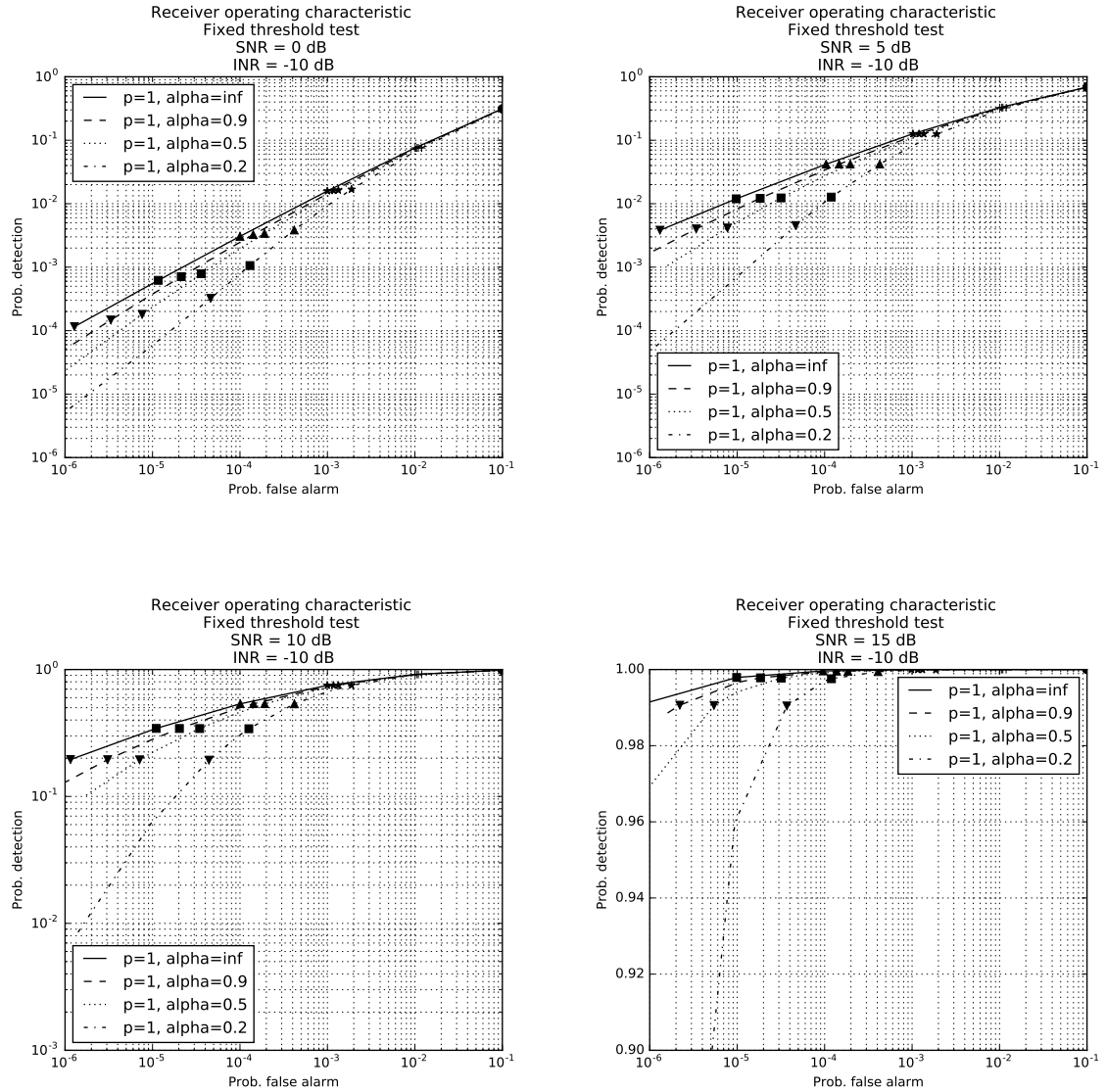


Figure C.5. ROCs for fixed-threshold test with heavy-tailed interference (INR = -10 dB; SNR = 0, 5, 10, 15 dB)

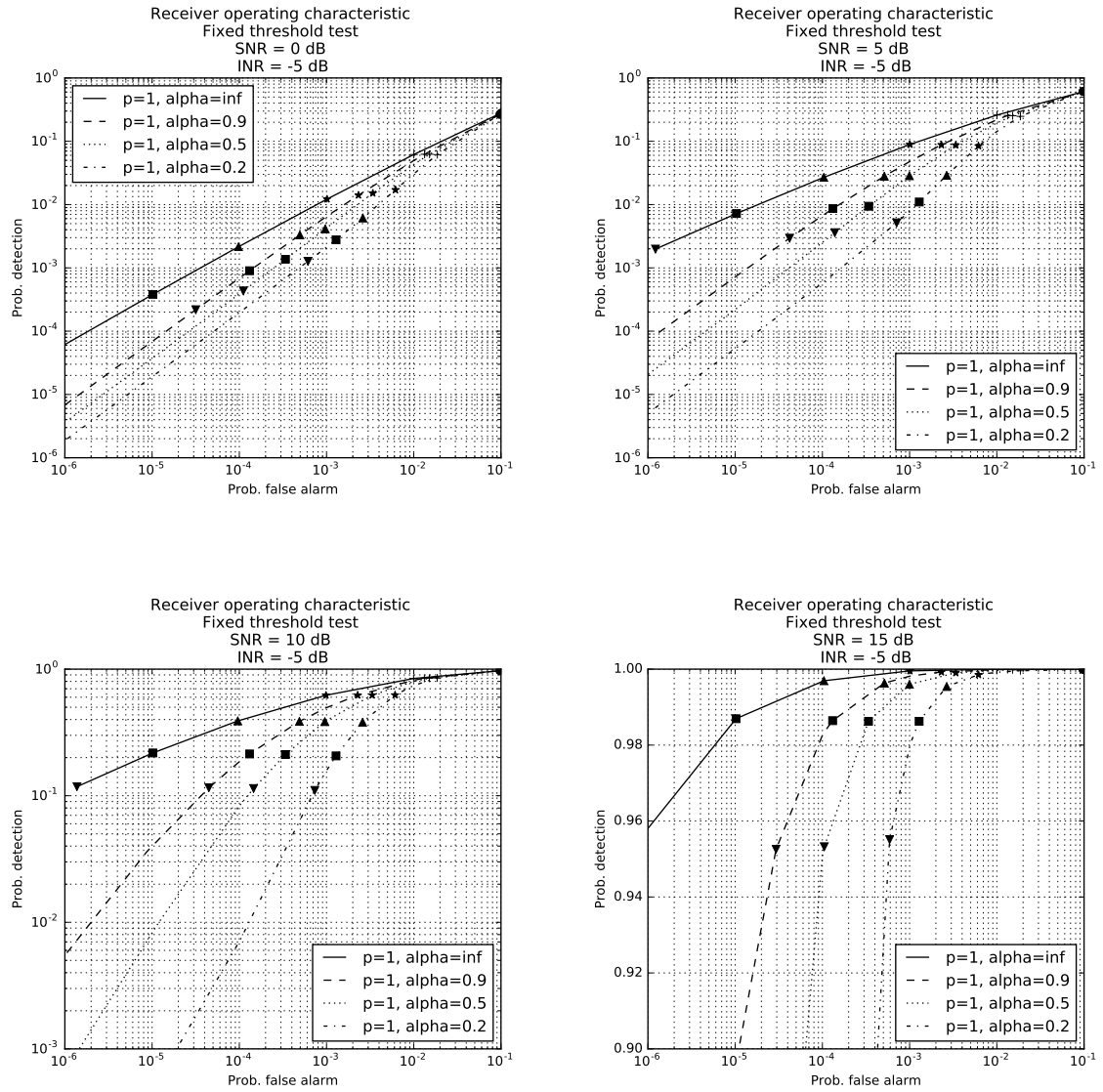


Figure C.6. ROCs for fixed-threshold test with heavy-tailed interference (INR = -5 dB; SNR = 0, 5, 10, 15 dB)

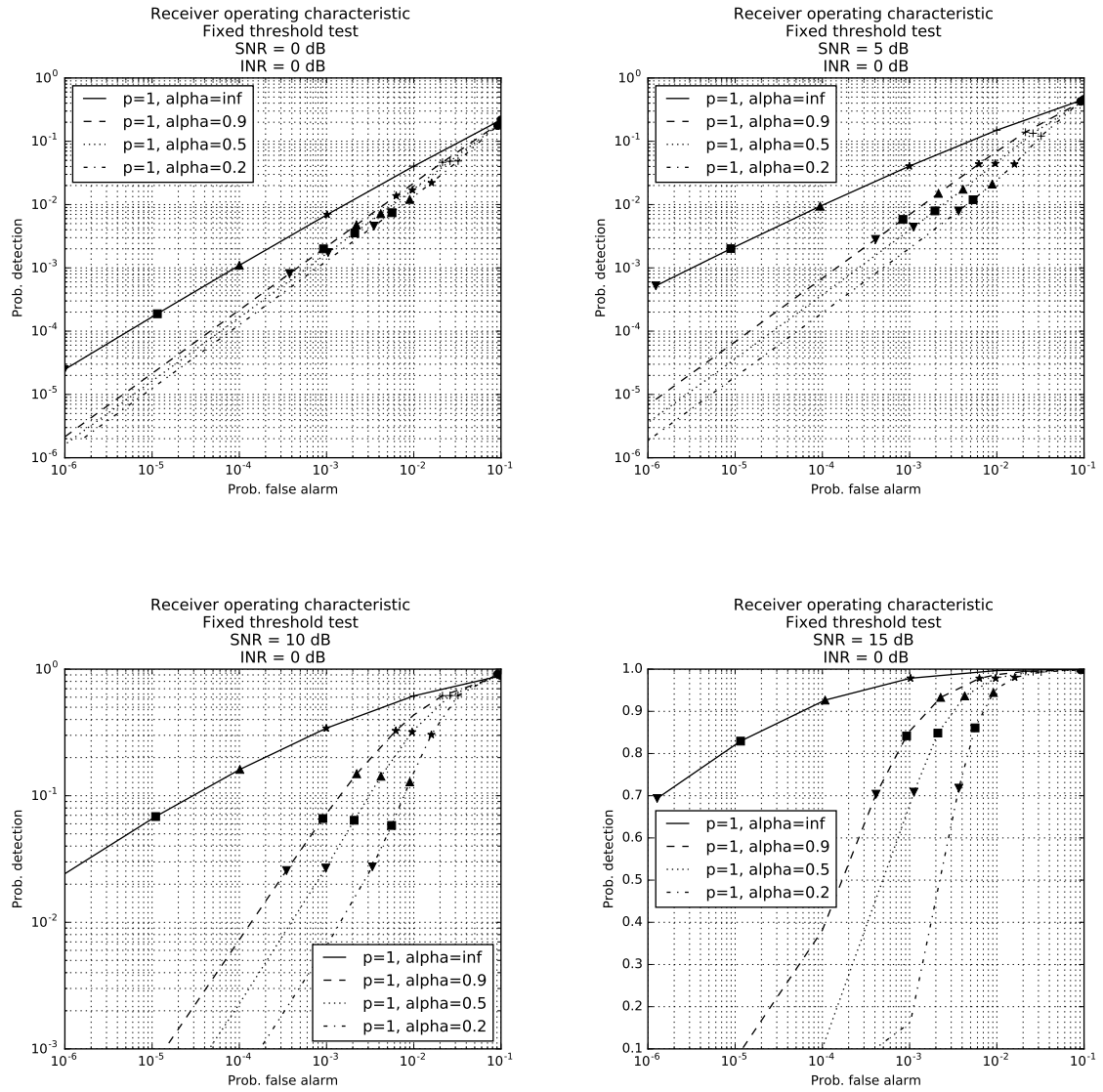


Figure C.7. ROCs for fixed-threshold test with heavy-tailed interference (INR = 0 dB; SNR = 0, 5, 10, 15 dB)

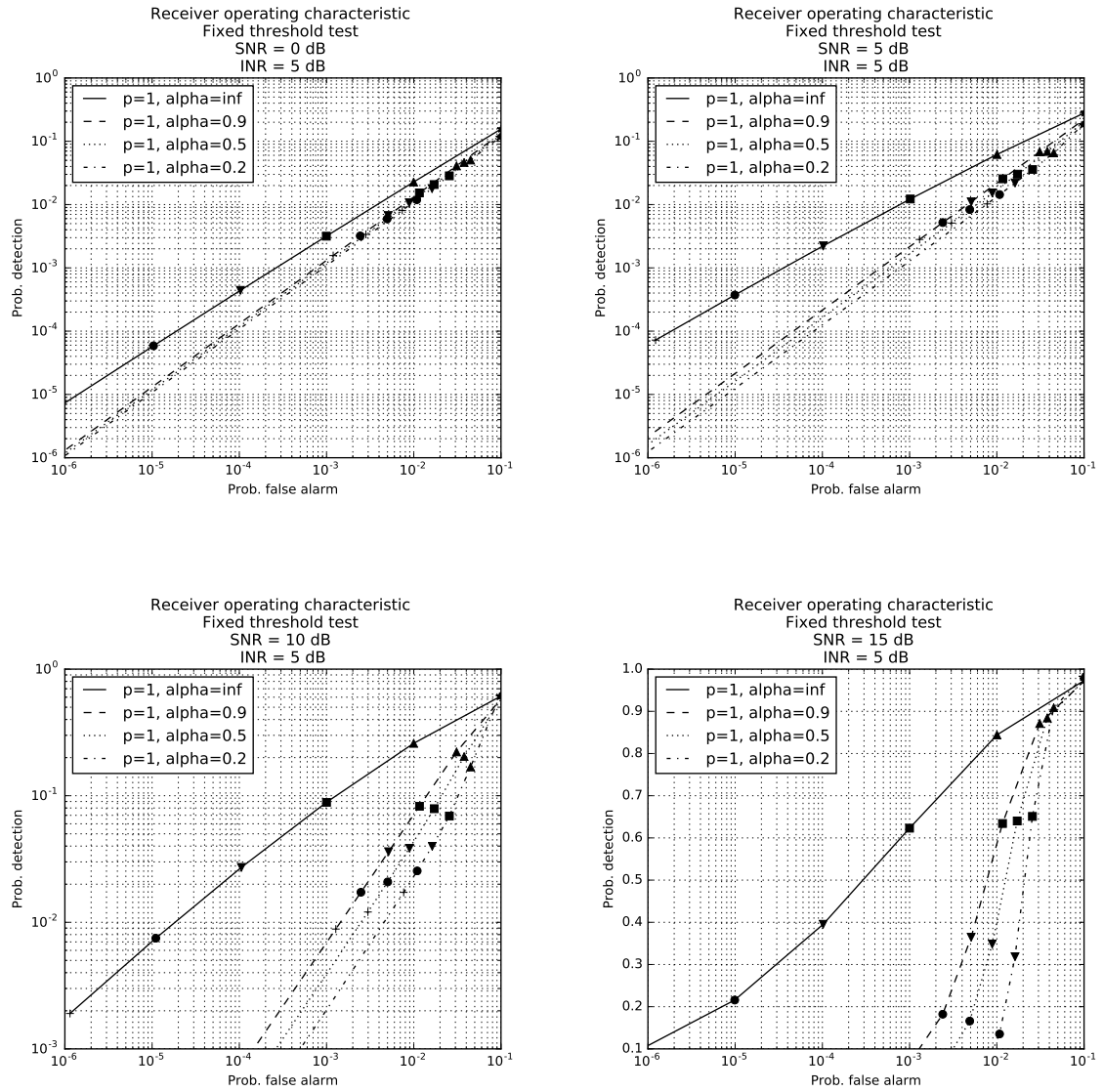


Figure C.8. ROCs for fixed-threshold test with heavy-tailed interference (INR = 5 dB; SNR = 0, 5, 10, 15 dB)

Cell-averaging adaptive-threshold test with “fast,” impulsive interference ($p < 1$)

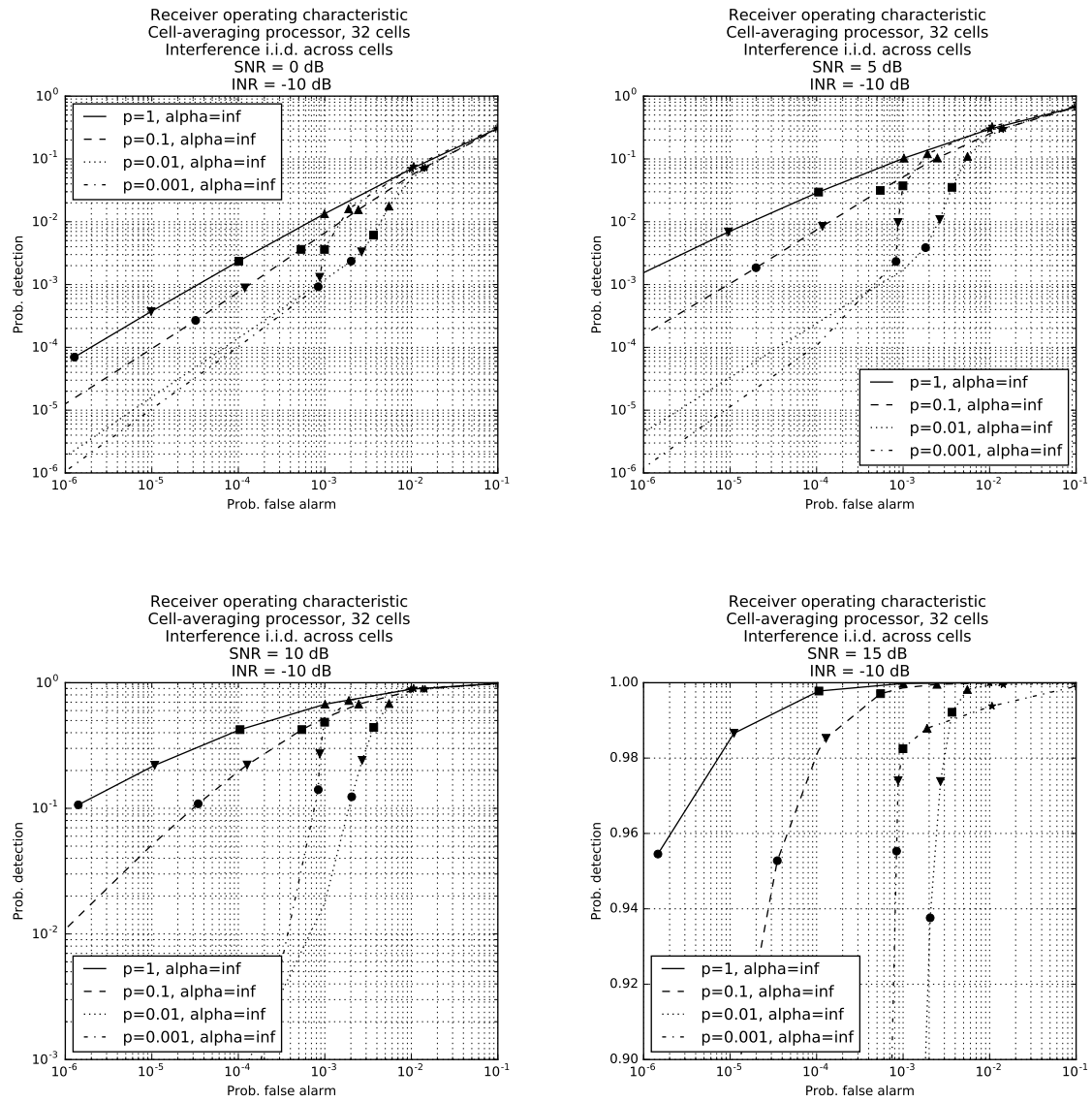


Figure C.9. ROCs for cell-averaging processor with “fast,” impulsive interference (INR = -10 dB; SNR = 0, 5, 10, 15 dB)

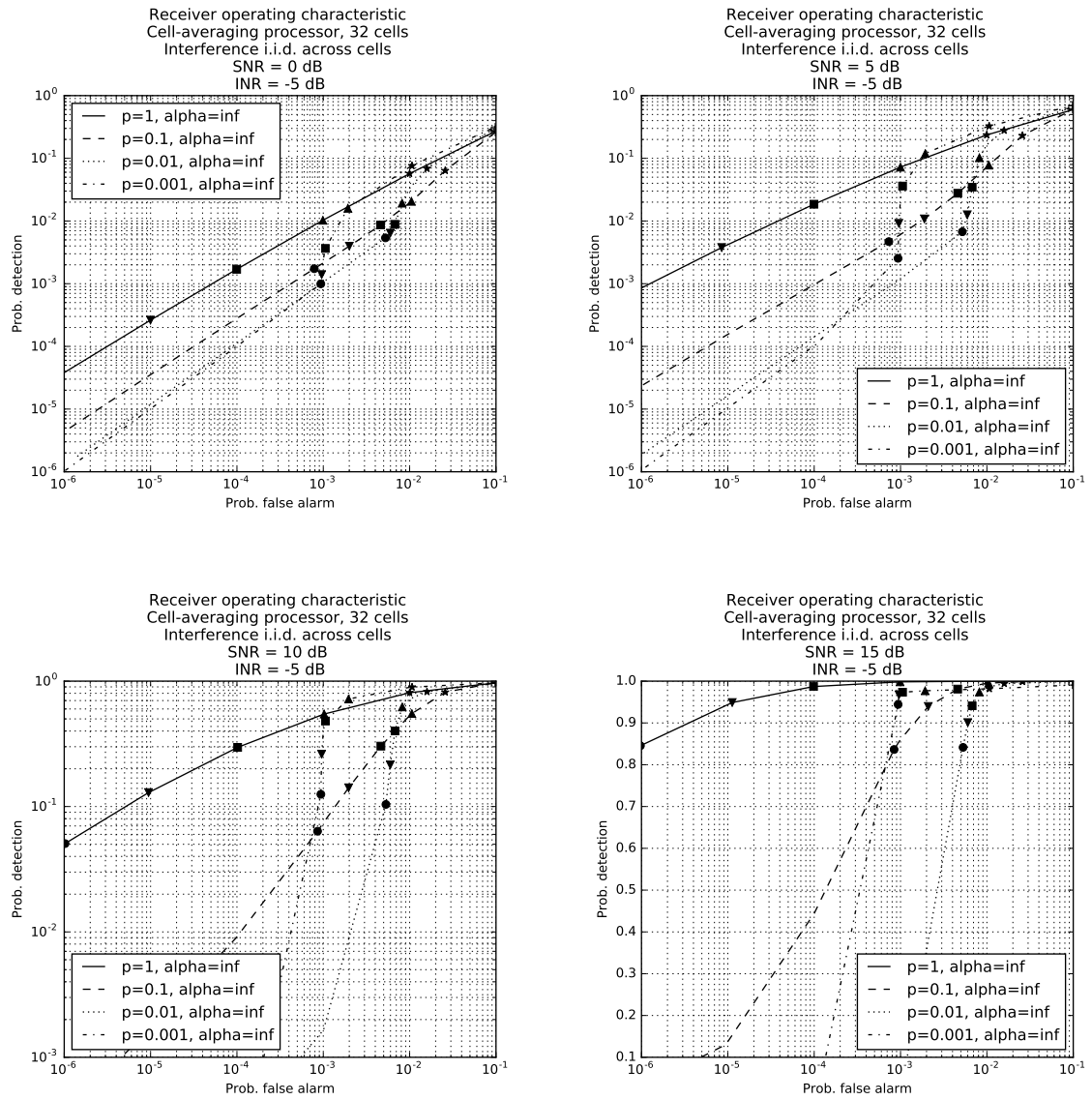


Figure C.10. ROCs for cell-averaging processor with “fast,” impulsive interference (INR = -5 dB; SNR = 0, 5, 10, 15 dB)

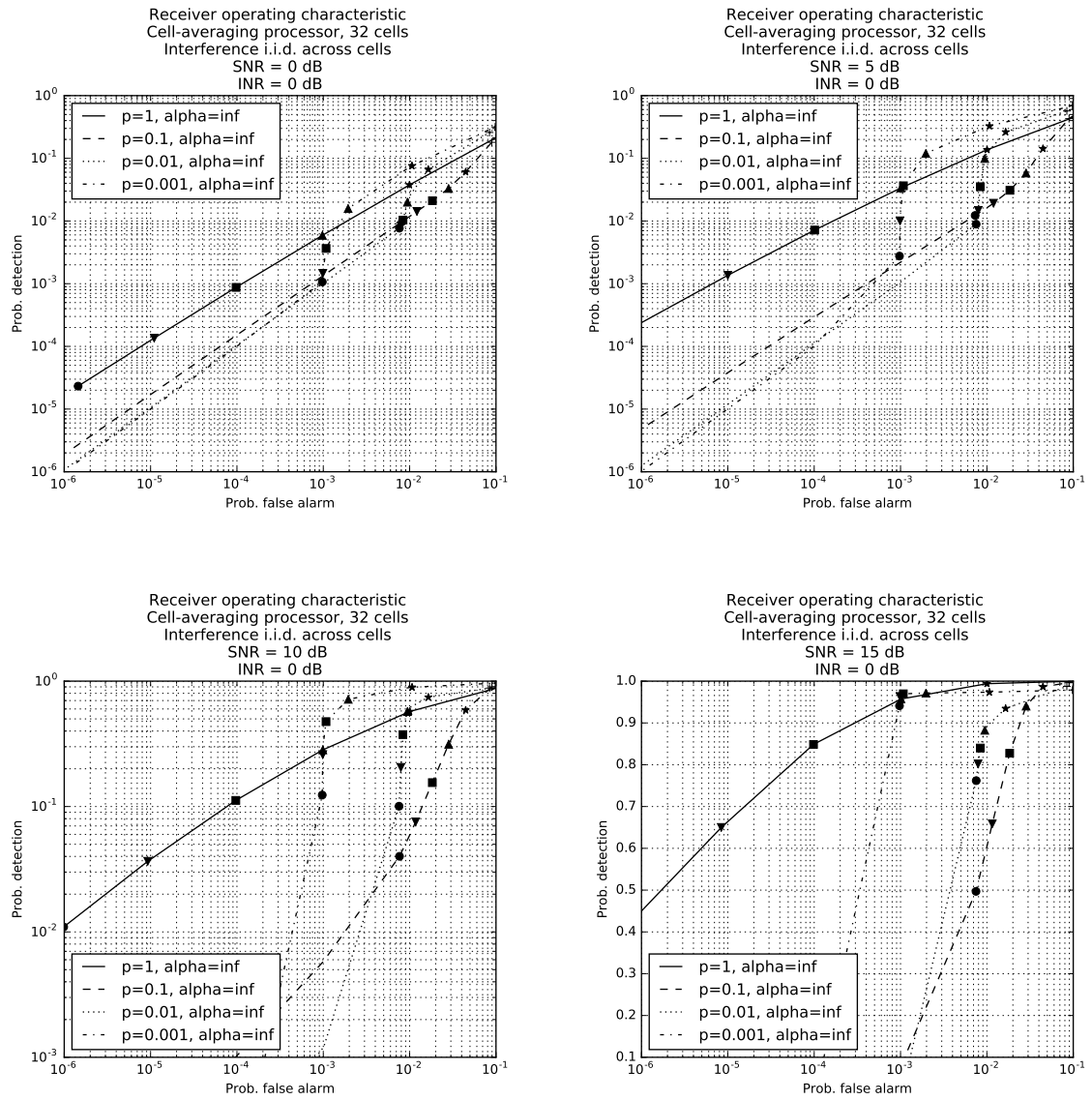


Figure C.11. ROCs for cell-averaging processor with “fast,” impulsive interference (INR = 0 dB; SNR = 0, 5, 10, 15 dB)

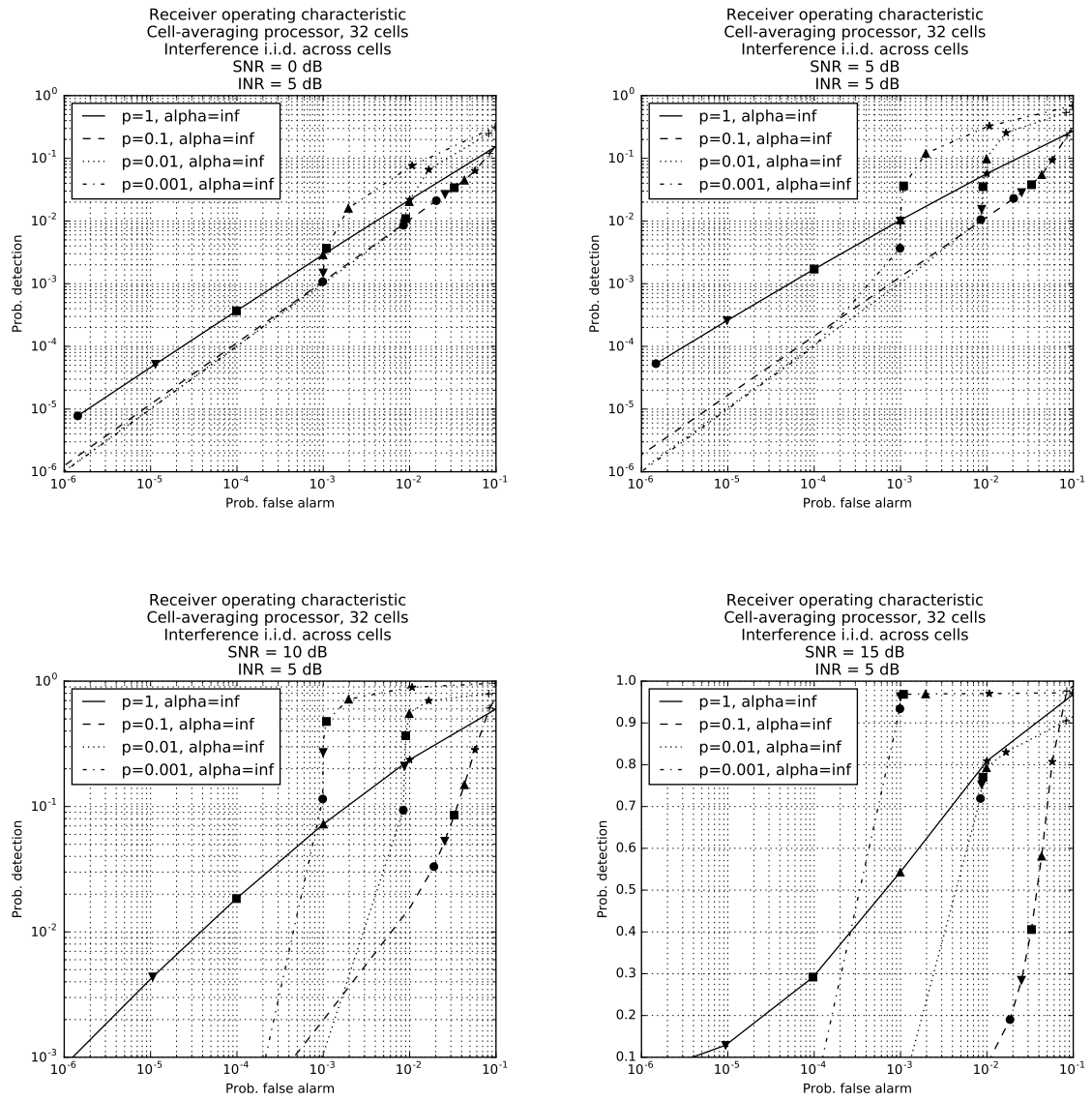


Figure C.12. ROCs for cell-averaging processor with “fast,” impulsive interference (INR = 5 dB; SNR = 0, 5, 10, 15 dB)

Cell-averaging adaptive-threshold test with “fast,” heavy-tailed interference ($\alpha < \infty$)

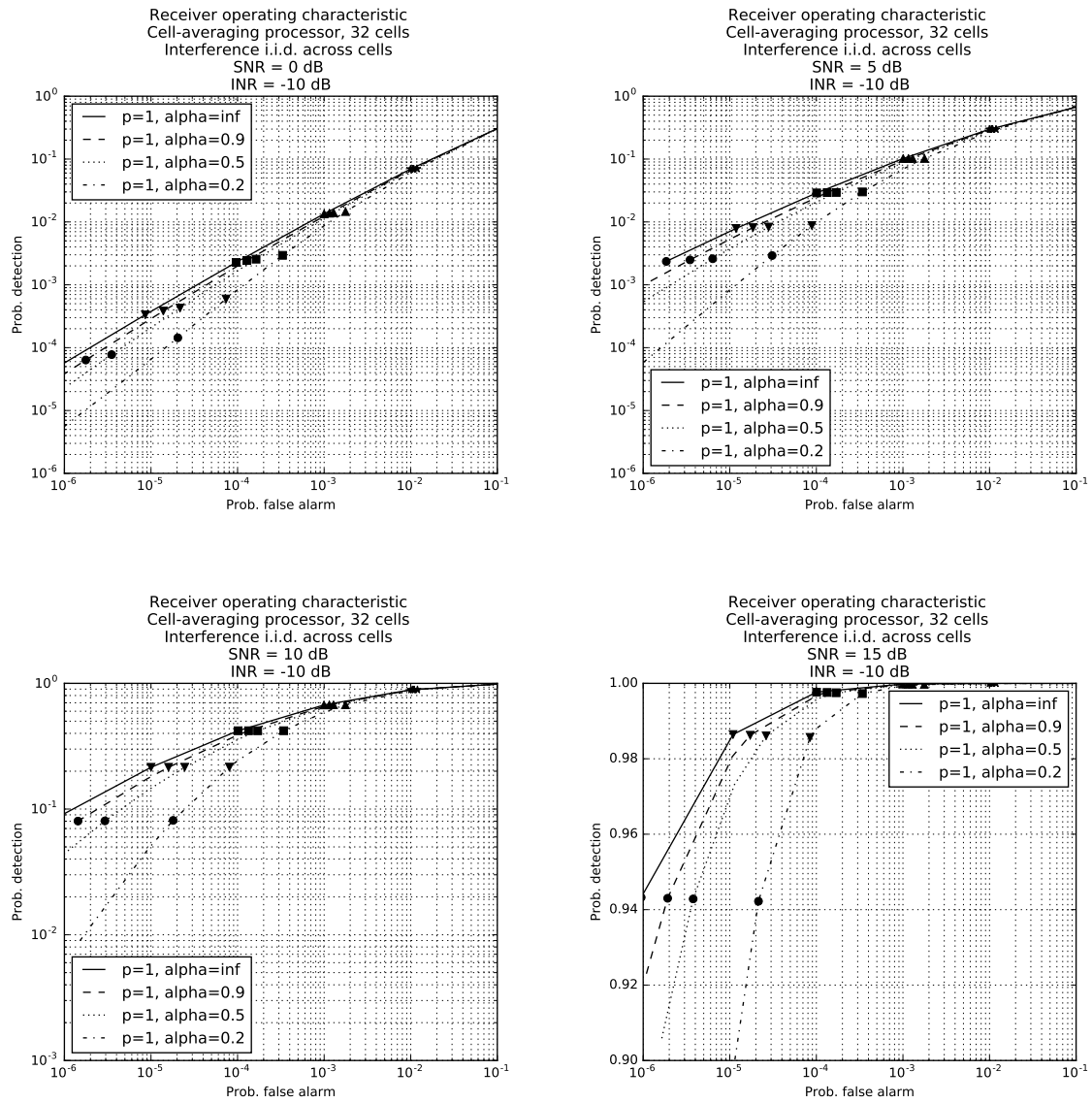


Figure C.13. ROCs for cell-averaging processor with “fast,” heavy-tailed interference (INR = -10 dB; SNR = 0, 5, 10, 15 dB)

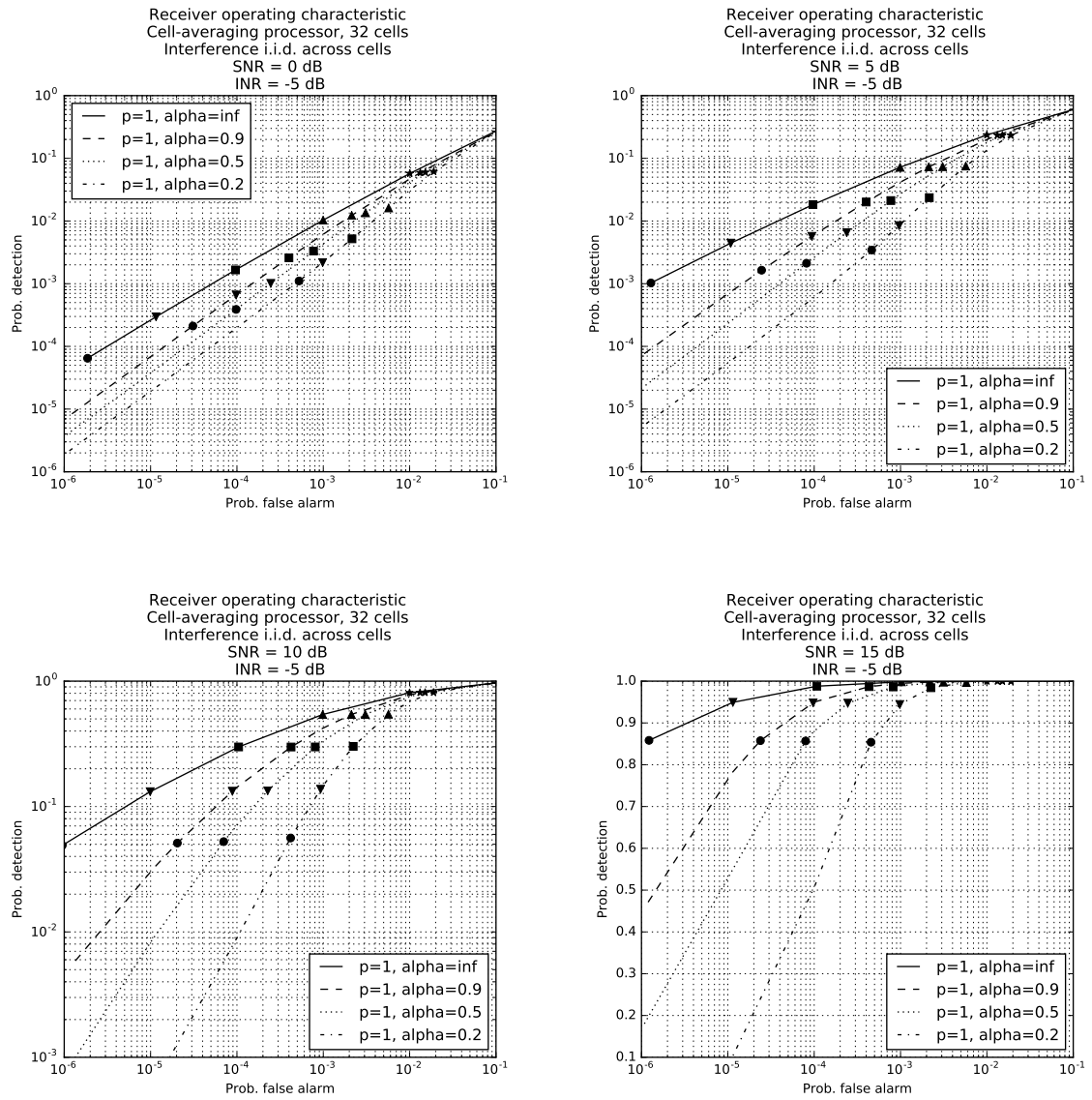


Figure C.14. ROCs for cell-averaging processor with “fast,” heavy-tailed interference (INR = -5 dB; SNR = 0, 5, 10, 15 dB)

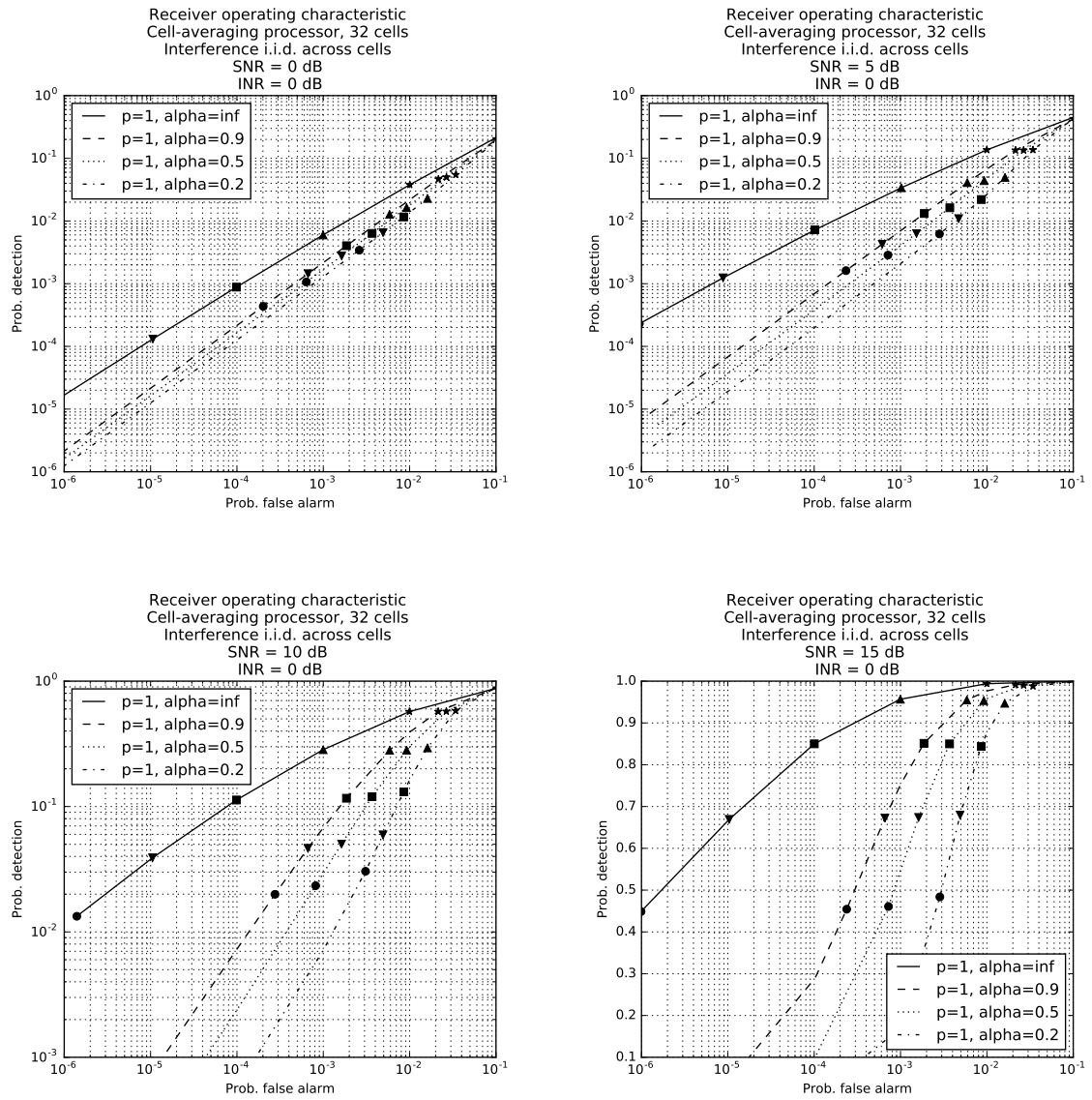


Figure C.15. ROCs for cell-averaging processor with “fast,” heavy-tailed interference (INR = 0 dB; SNR = 0, 5, 10, 15 dB)

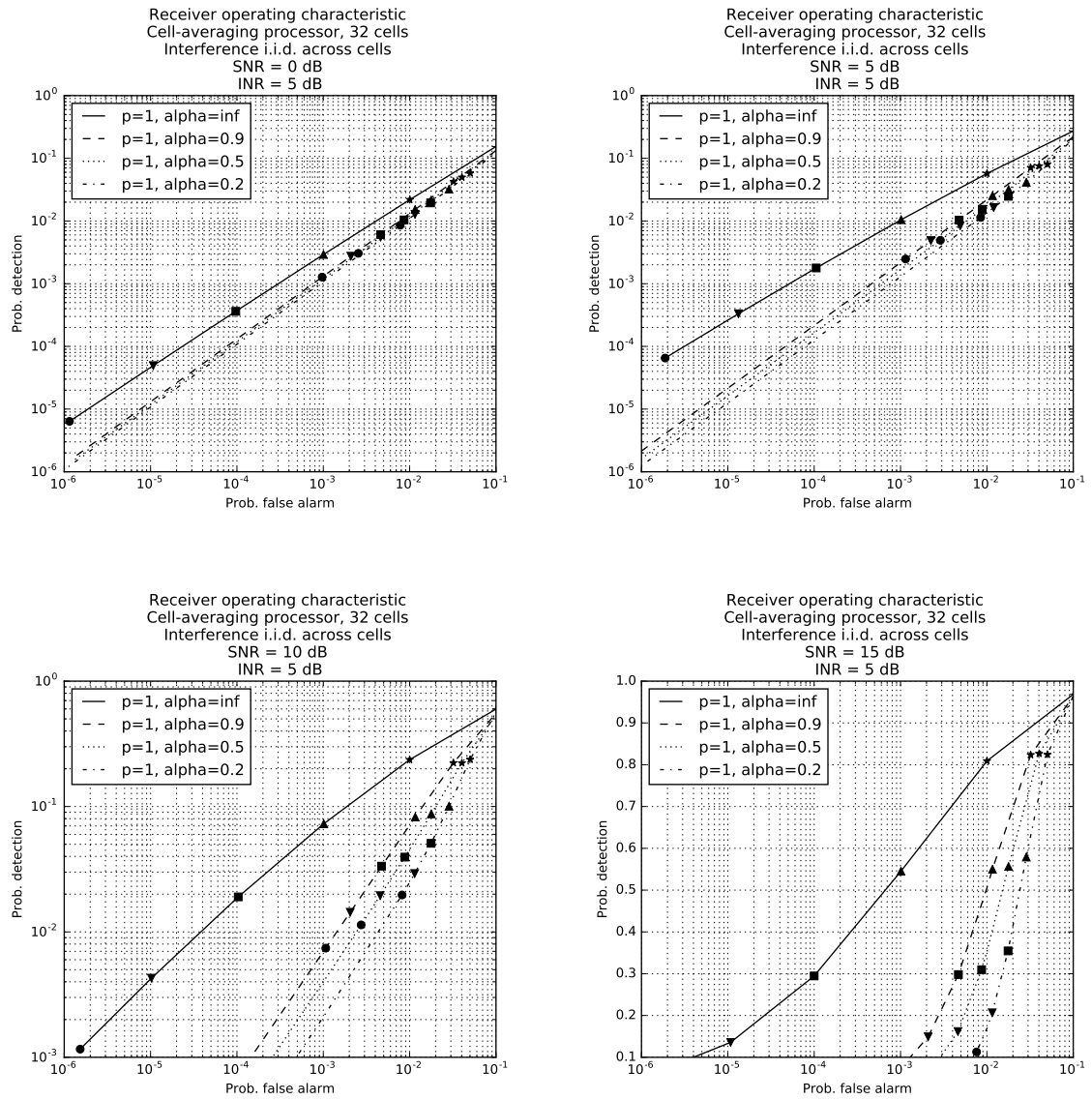


Figure C.16. ROCs for cell-averaging processor with “fast,” heavy-tailed interference (INR = 5 dB; SNR = 0, 5, 10, 15 dB)

Cell-averaging adaptive-threshold test with “slow,” impulsive interference ($p < 1$)

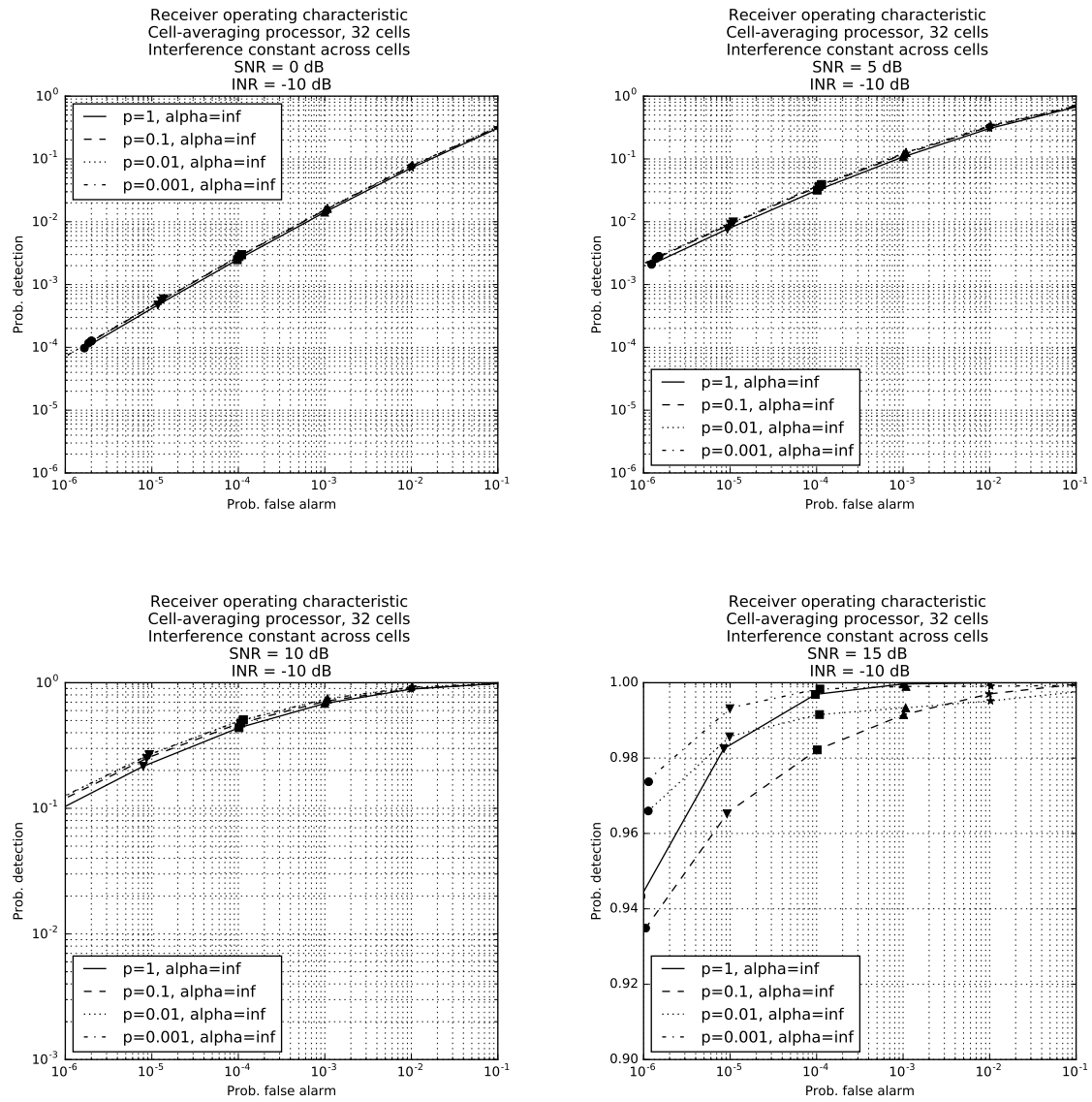


Figure C.17. ROCs for cell-averaging processor with “slow,” impulsive interference (INR = -10 dB; SNR = 0, 5, 10, 15 dB)

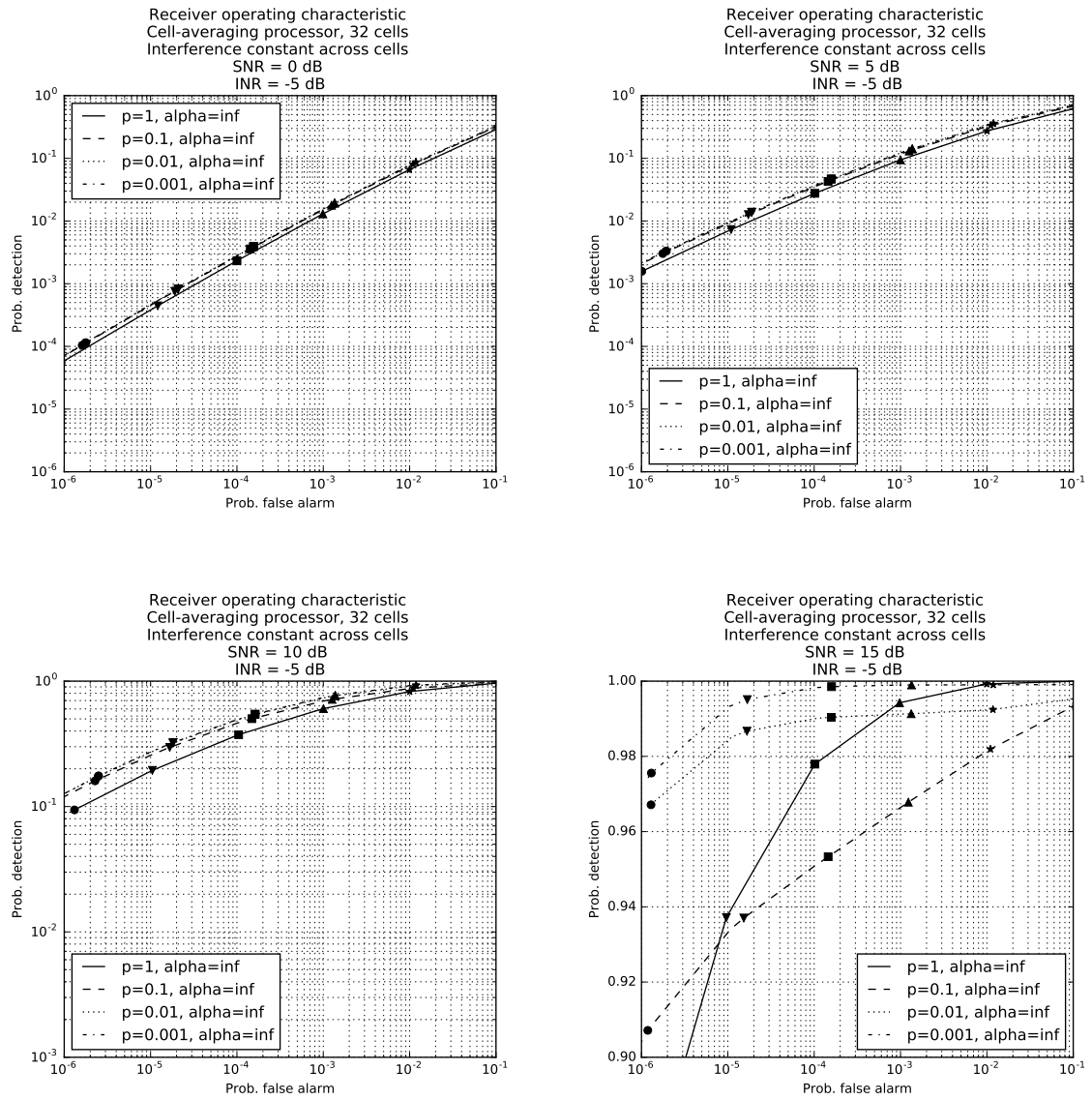


Figure C.18. ROCs for cell-averaging processor with “slow,” impulsive interference (INR = -5 dB; SNR = 0, 5, 10, 15 dB)

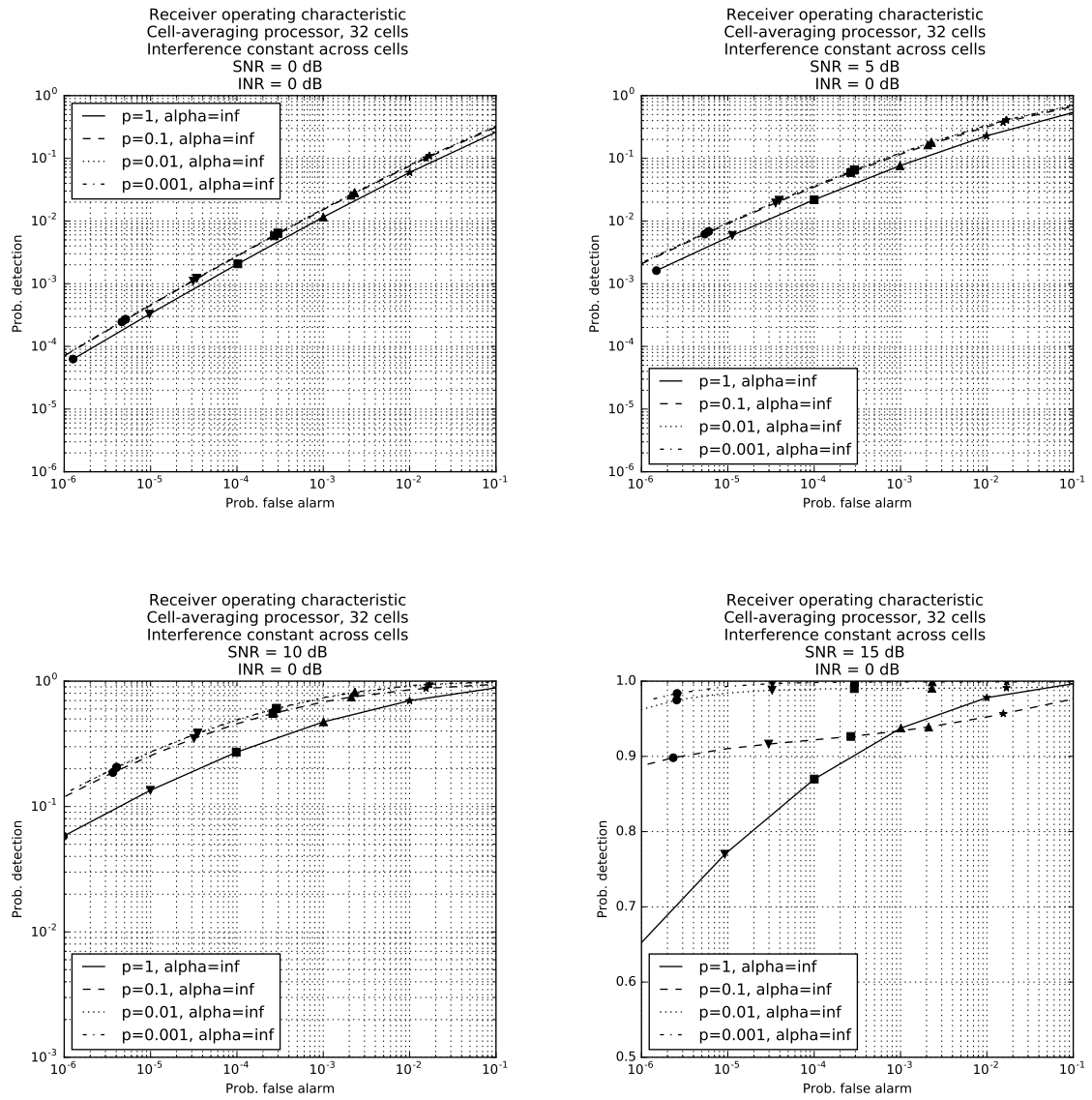


Figure C.19. ROCs for cell-averaging processor with “slow,” impulsive interference (INR = 0 dB; SNR = 0, 5, 10, 15 dB)

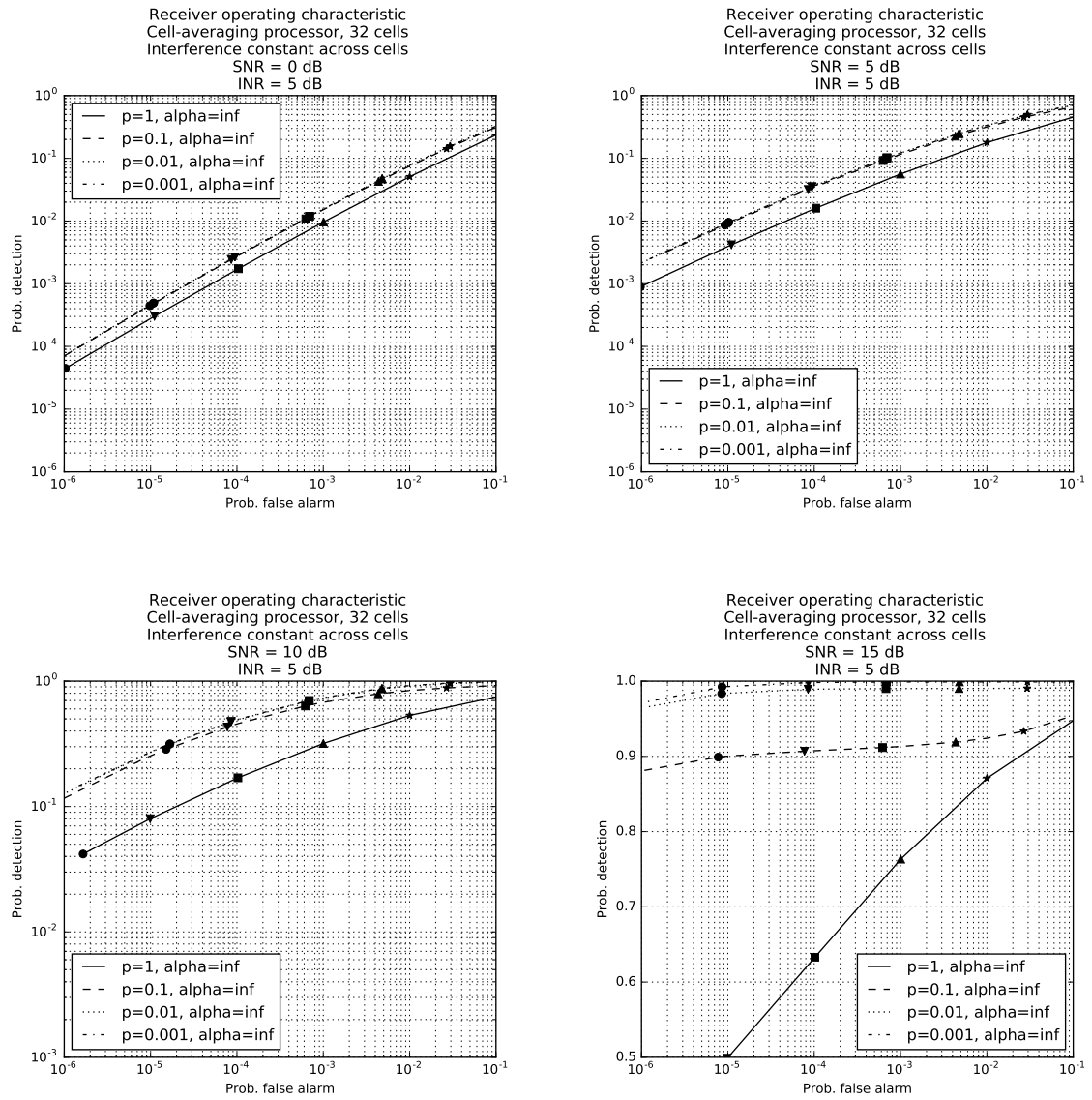


Figure C.20. ROCs for cell-averaging processor with “slow,” impulsive interference (INR = 5 dB; SNR = 0, 5, 10, 15 dB)

Cell-averaging adaptive-threshold test with “slow,” heavy-tailed interference ($\alpha < \infty$)

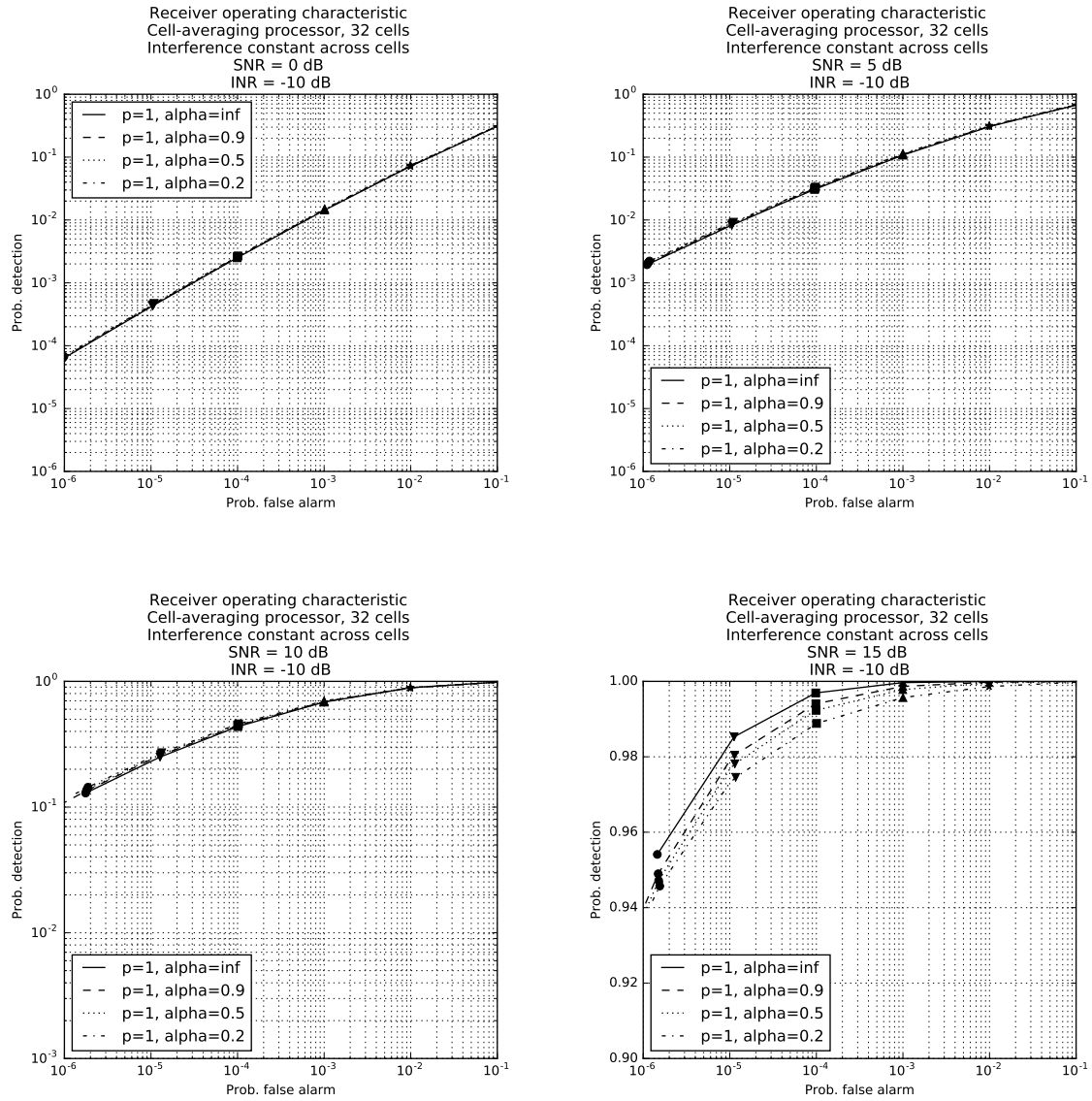


Figure C.21. ROCs for cell-averaging processor with “slow,” heavy-tailed interference (INR = -10 dB; SNR = 0, 5, 10, 15 dB)

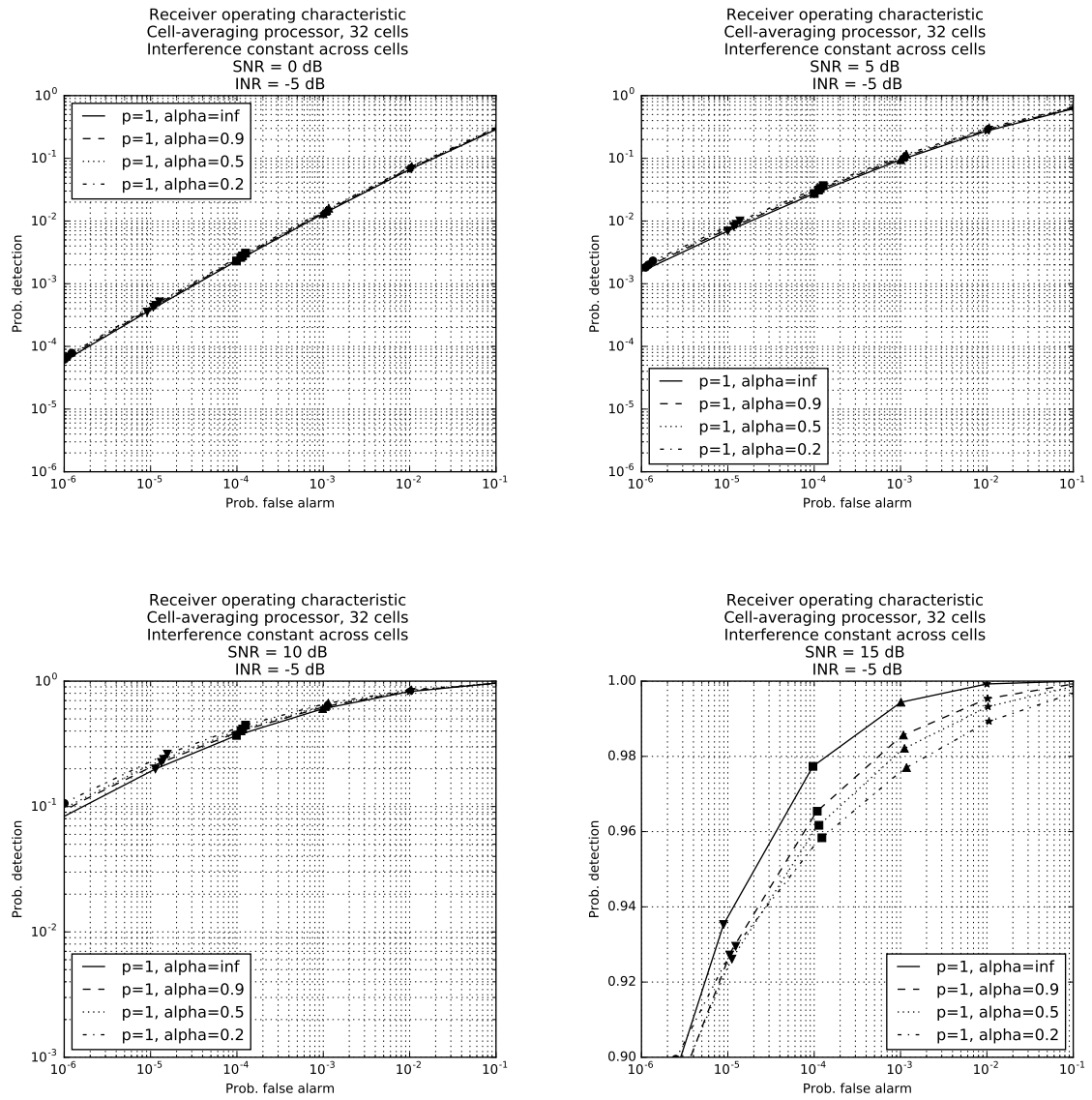


Figure C.22. ROCs for cell-averaging processor with “slow,” heavy-tailed interference (INR = -5 dB; SNR = 0, 5, 10, 15 dB)

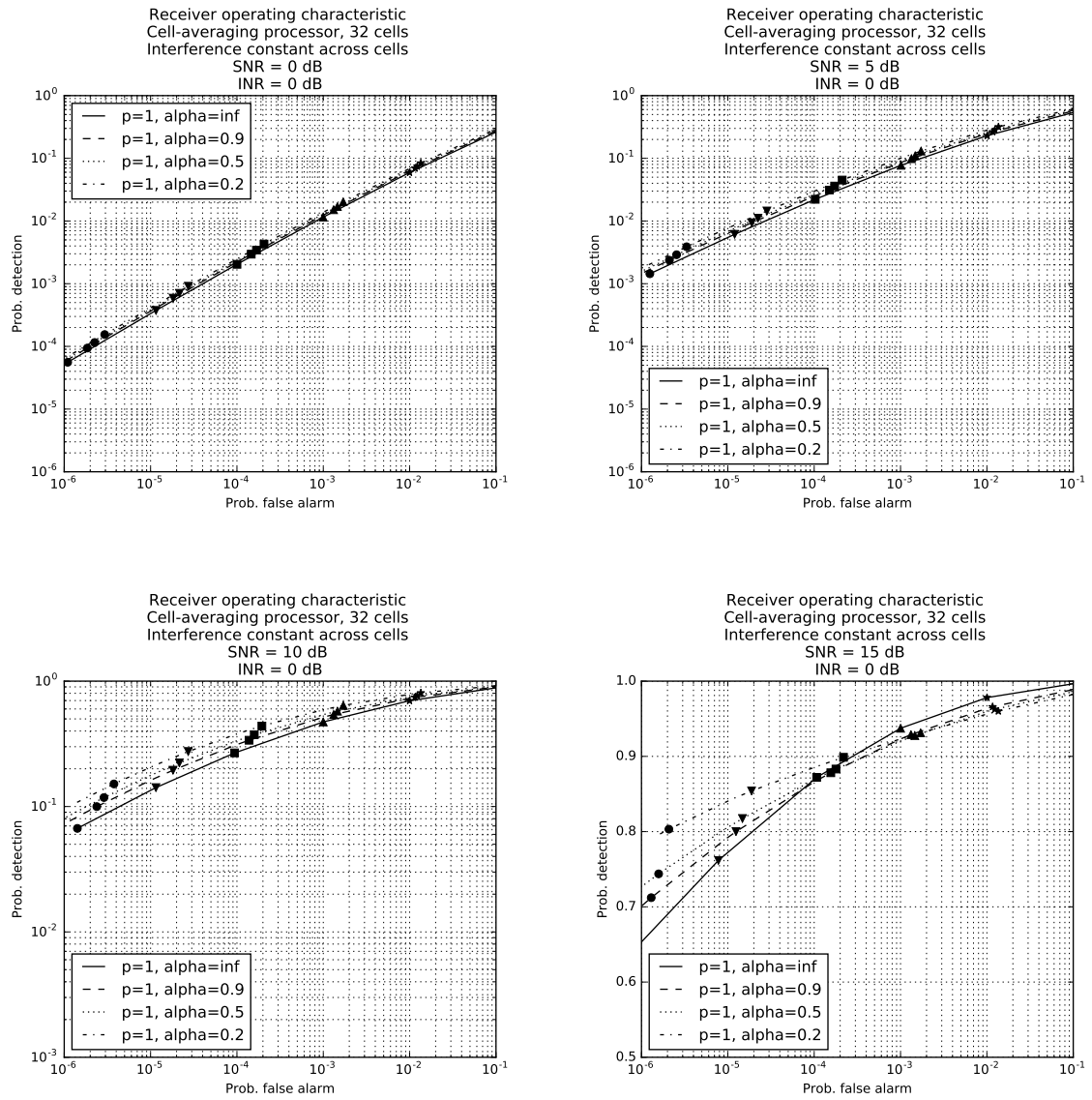


Figure C.23. ROCs for cell-averaging processor with “slow,” heavy-tailed interference (INR = 0 dB; SNR = 0, 5, 10, 15 dB)

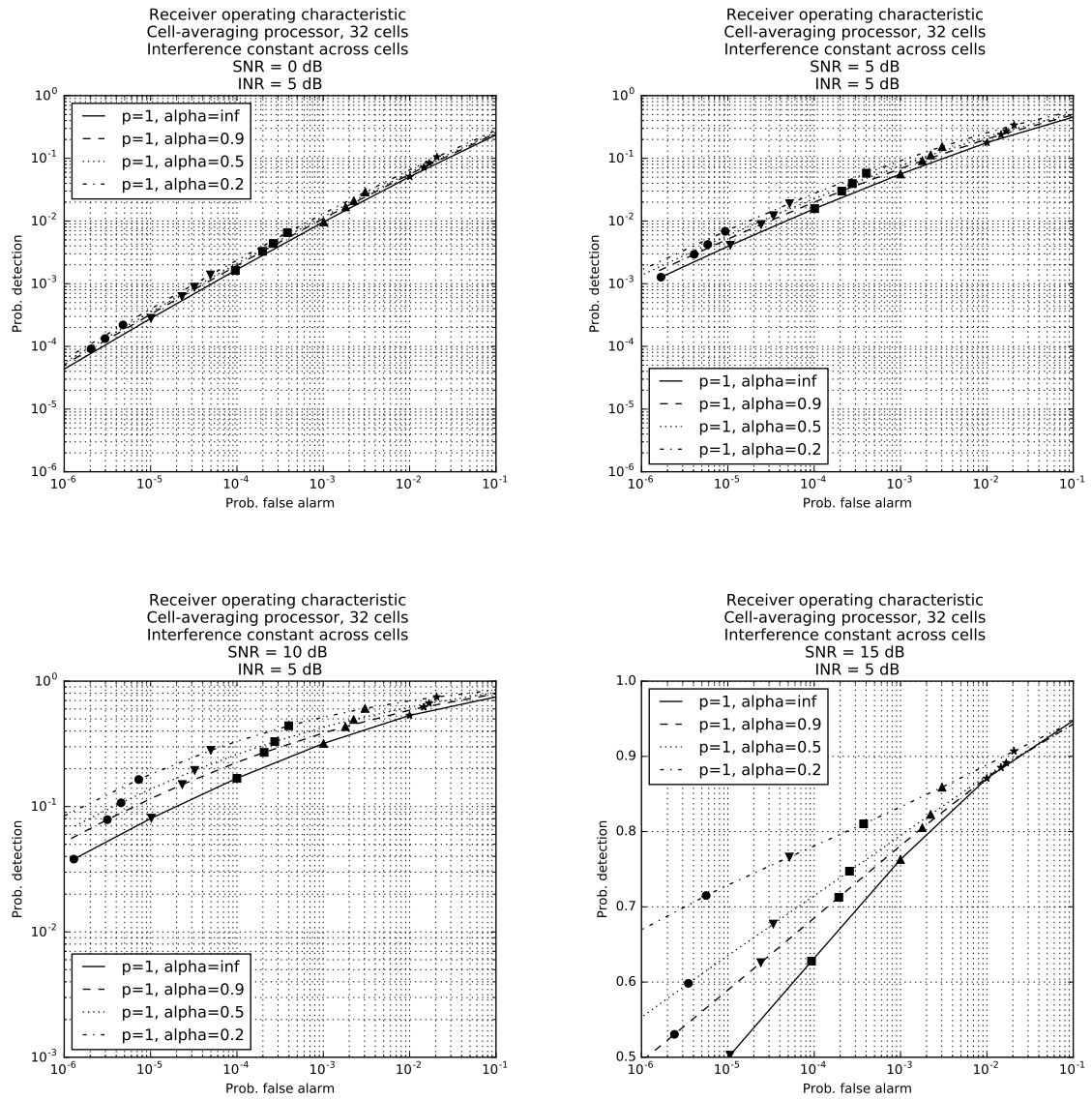


Figure C.24. ROCs for cell-averaging processor with “slow,” heavy-tailed interference (INR = 5 dB; SNR = 0, 5, 10, 15 dB)

Effects of INR on radar detection

Fixed-threshold test with Gaussian interference ($p = 1, \alpha \rightarrow \infty$)

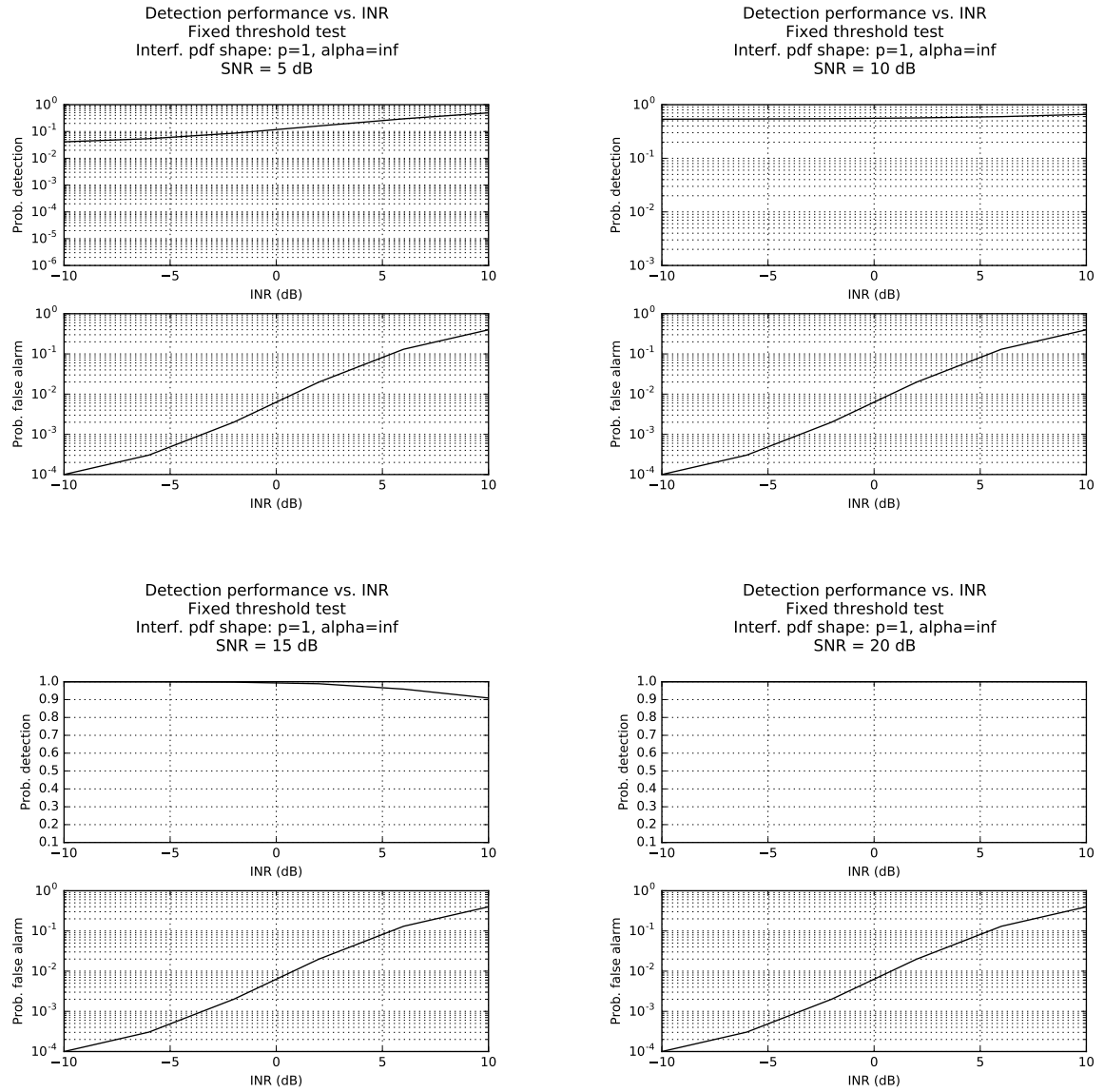


Figure C.25. P_D and P_{FA} versus INR for fixed-threshold test (SNR = 5, 10, 15, 20 dB, baseline $P_{FA} = 10^{-4}$)

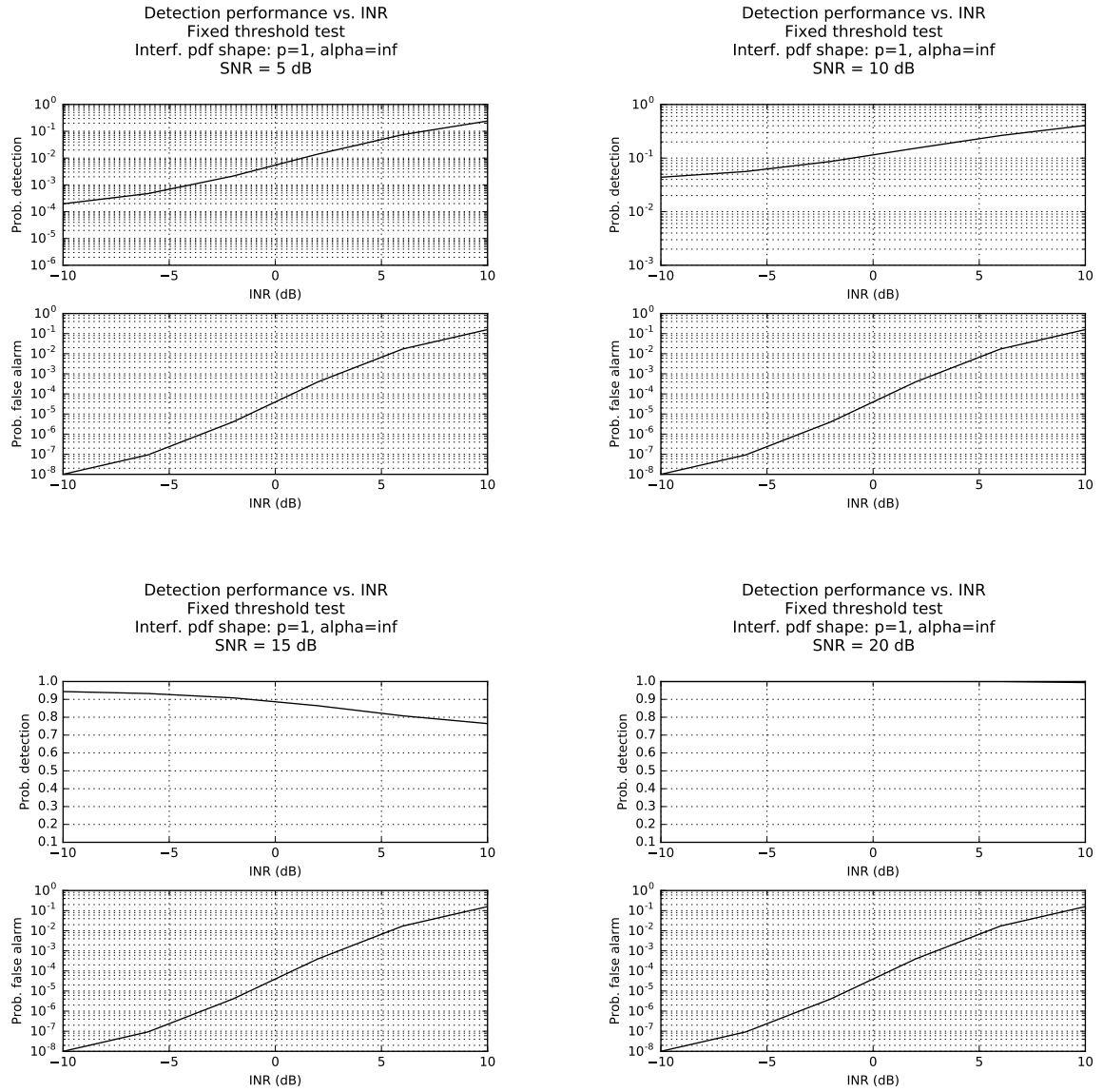


Figure C.26. P_D and P_{FA} versus INR for fixed-threshold test (SNR = 5, 10, 15, 20 dB, baseline $P_{FA} = 10^{-8}$)

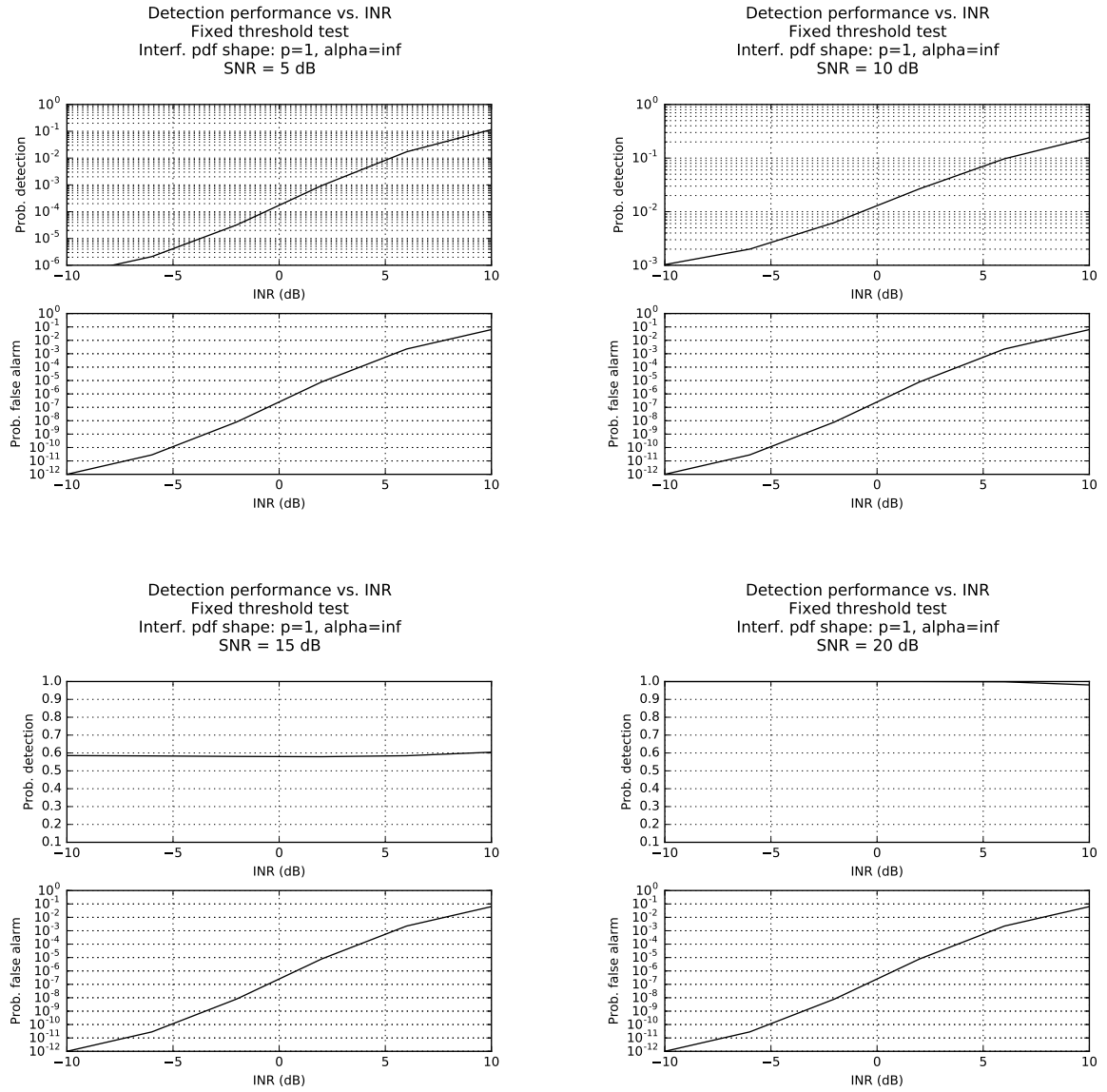


Figure C.27. P_D and P_{FA} versus INR for fixed threshold test (SNR = 5, 10, 15, 20 dB, baseline $P_{FA} = 10^{-12}$)

Cell-averaging adaptive-threshold test with “fast,” Gaussian interference

($p = 1, \alpha \rightarrow \infty$)

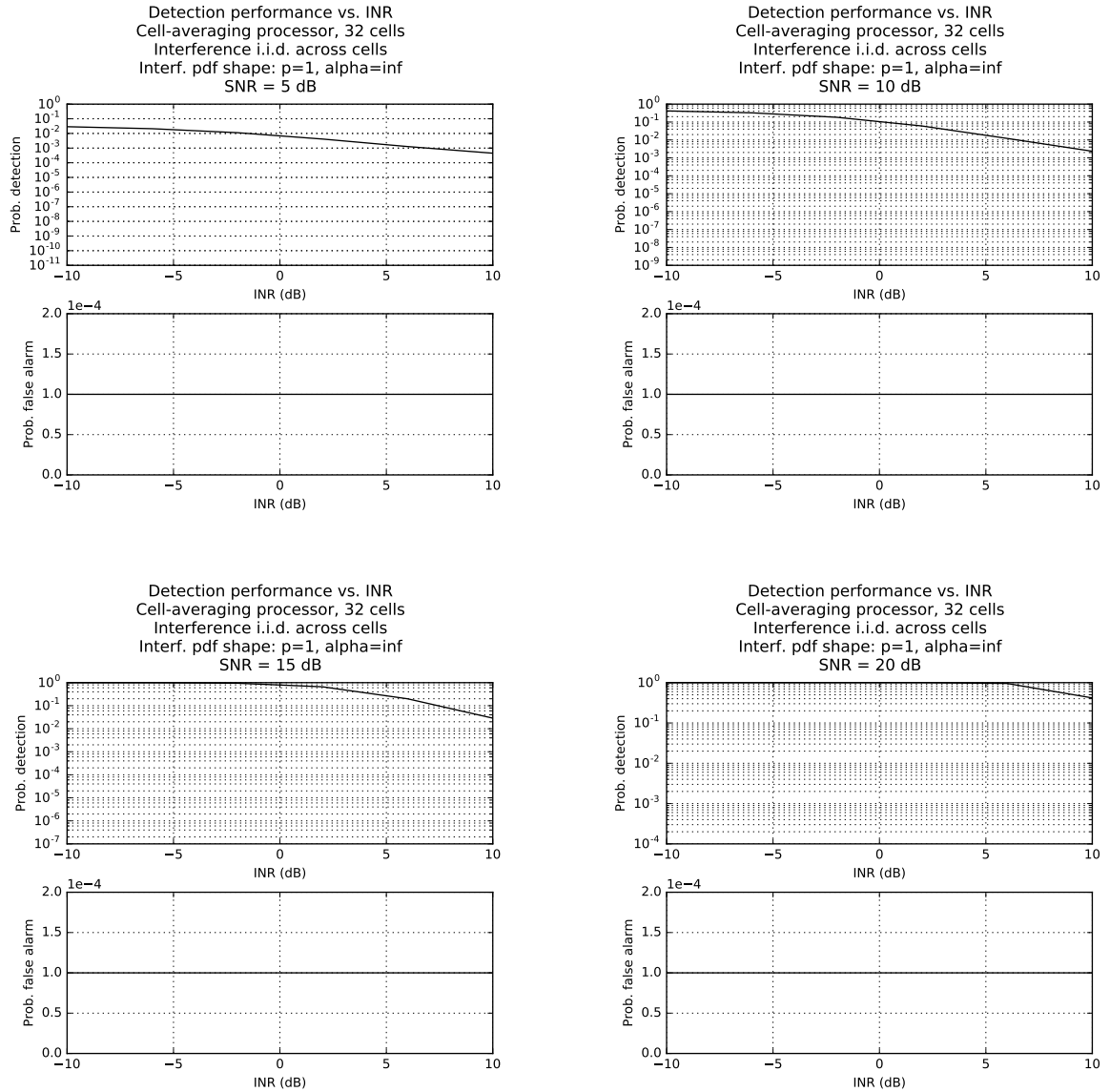


Figure C.28. P_D and P_{FA} versus INR for cell-averaging processor with “fast” interference (SNR = 5, 10, 15, 20 dB, baseline $P_{FA} = 10^{-4}$)

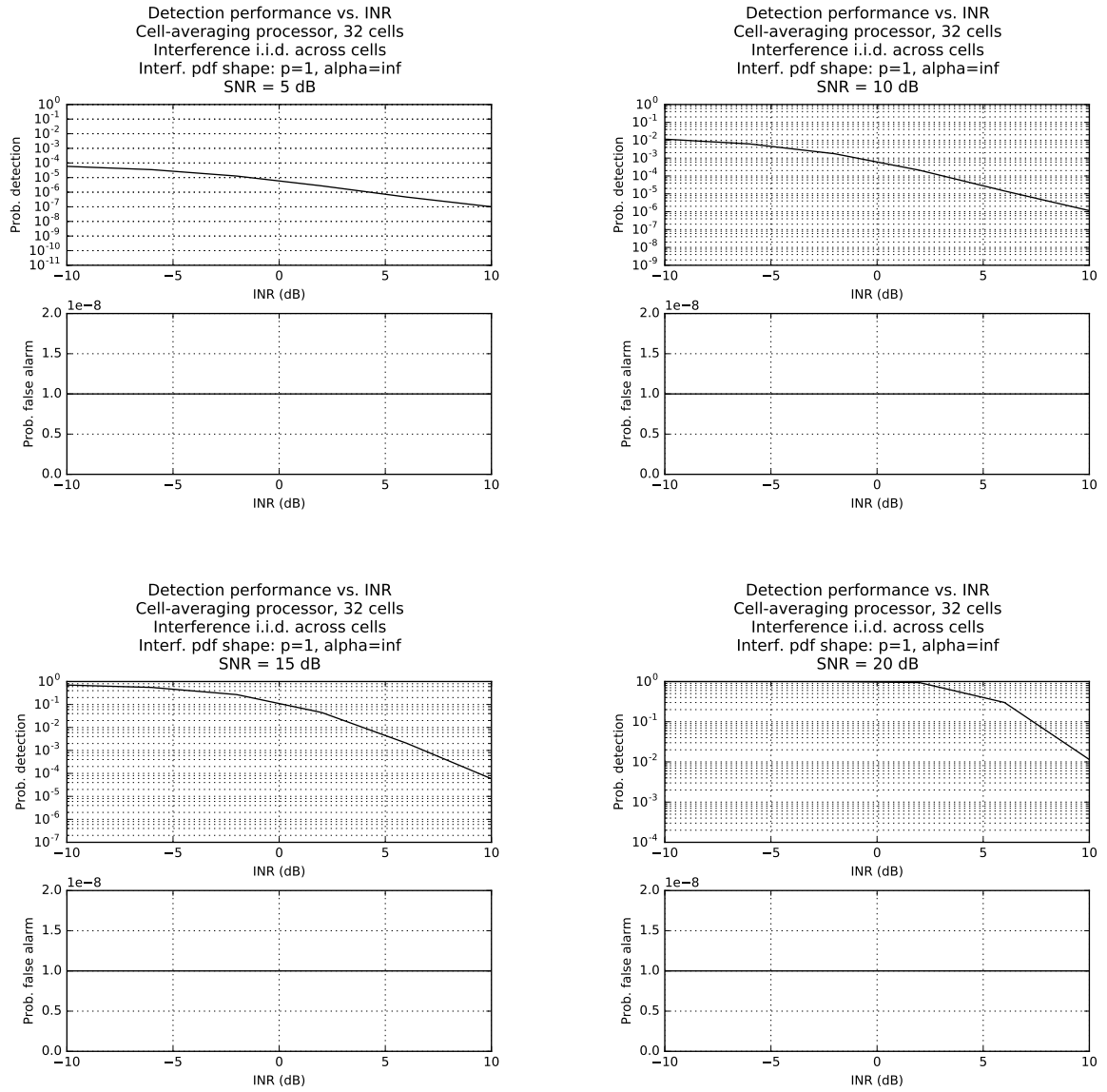


Figure C.29. P_D and P_{FA} versus INR for cell-averaging processor with “fast” interference (SNR = 5, 10, 15, 20 dB, baseline $P_{FA} = 10^{-8}$)

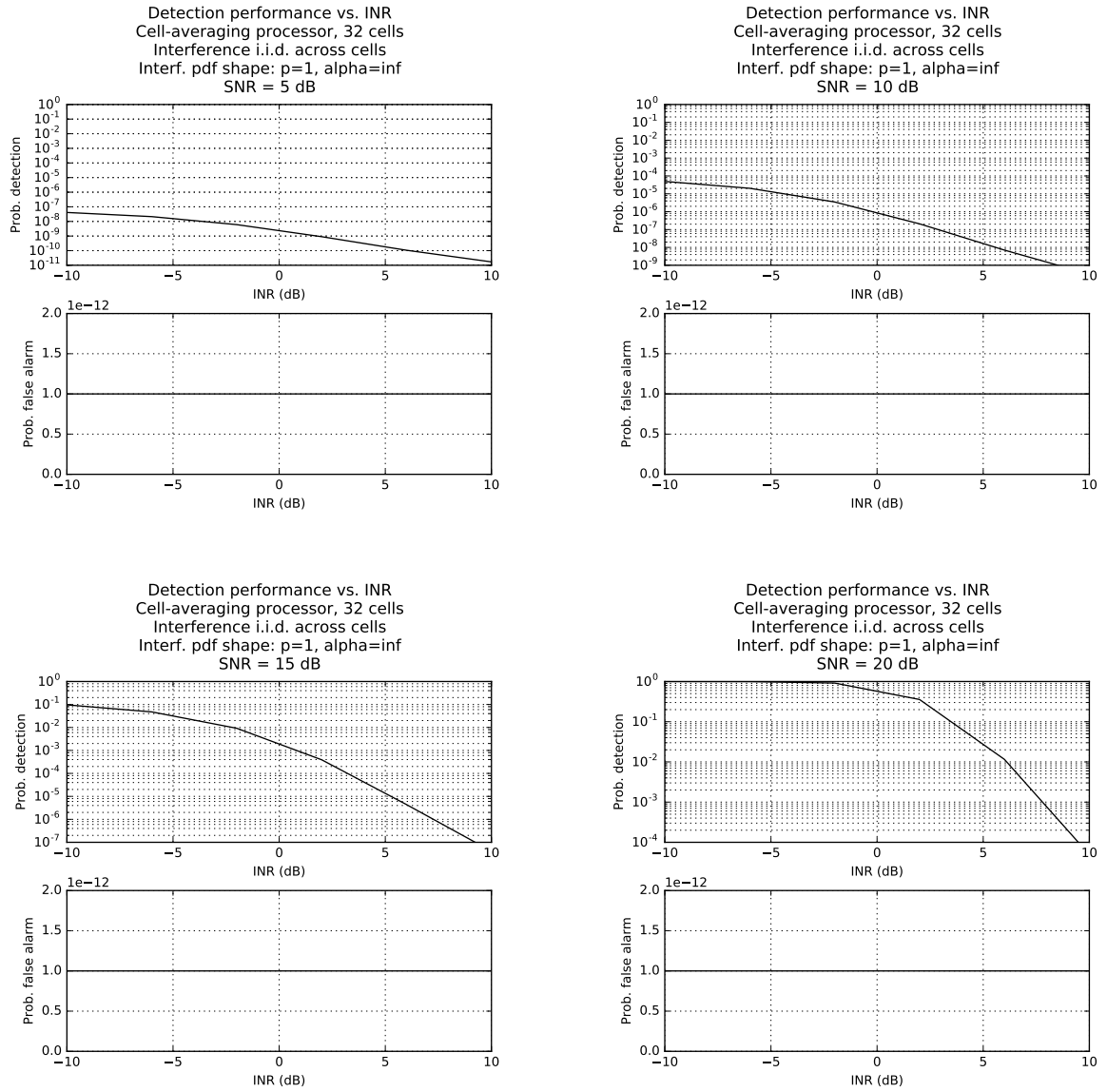


Figure C.30. P_D and P_{FA} versus INR for cell-averaging processor with “fast” interference (SNR = 5, 10, 15, 20 dB, baseline $P_{FA} = 10^{-12}$)

Cell-averaging adaptive-threshold test with “slow,” Gaussian interference
 $(p = 1, \alpha \rightarrow \infty)$

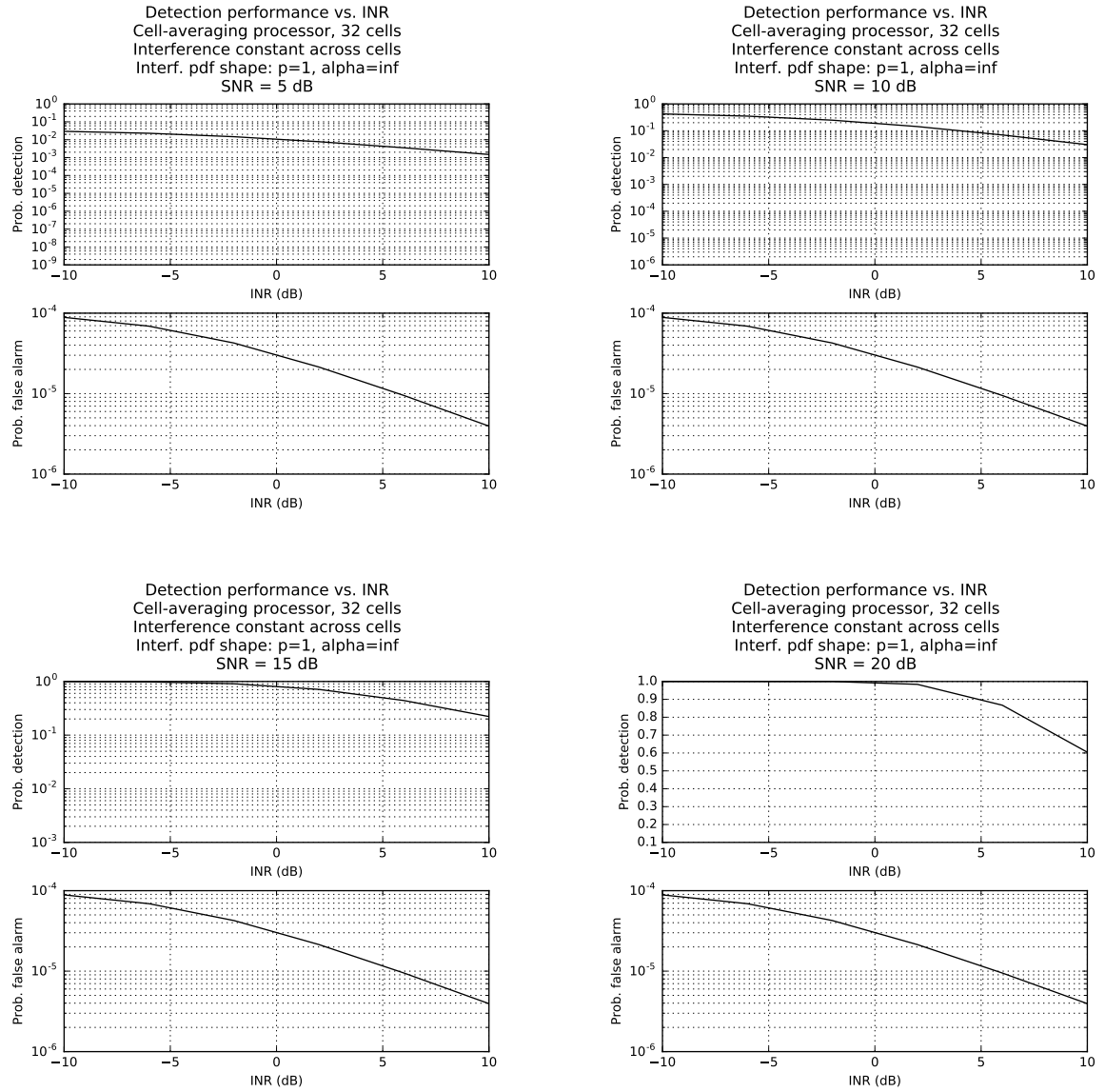


Figure C.31. P_D and P_{FA} versus INR for cell-averaging processor with “slow” interference (SNR = 5, 10, 15, 20 dB, baseline $P_{FA} = 10^{-4}$)

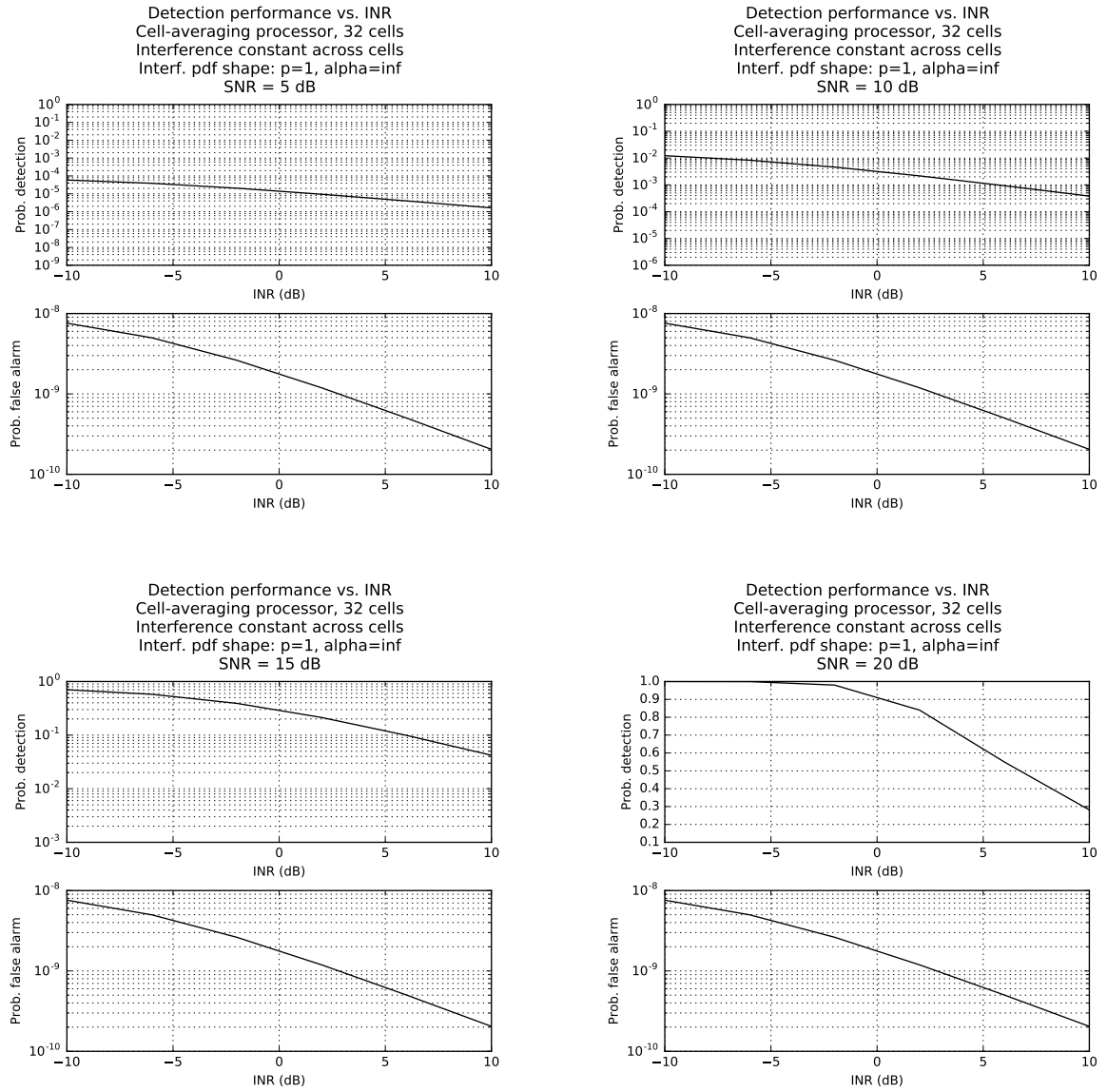


Figure C.32. P_D and P_{FA} versus INR for cell-averaging processor with “slow” interference (SNR = 5, 10, 15, 20 dB, baseline $P_{FA} = 10^{-8}$)

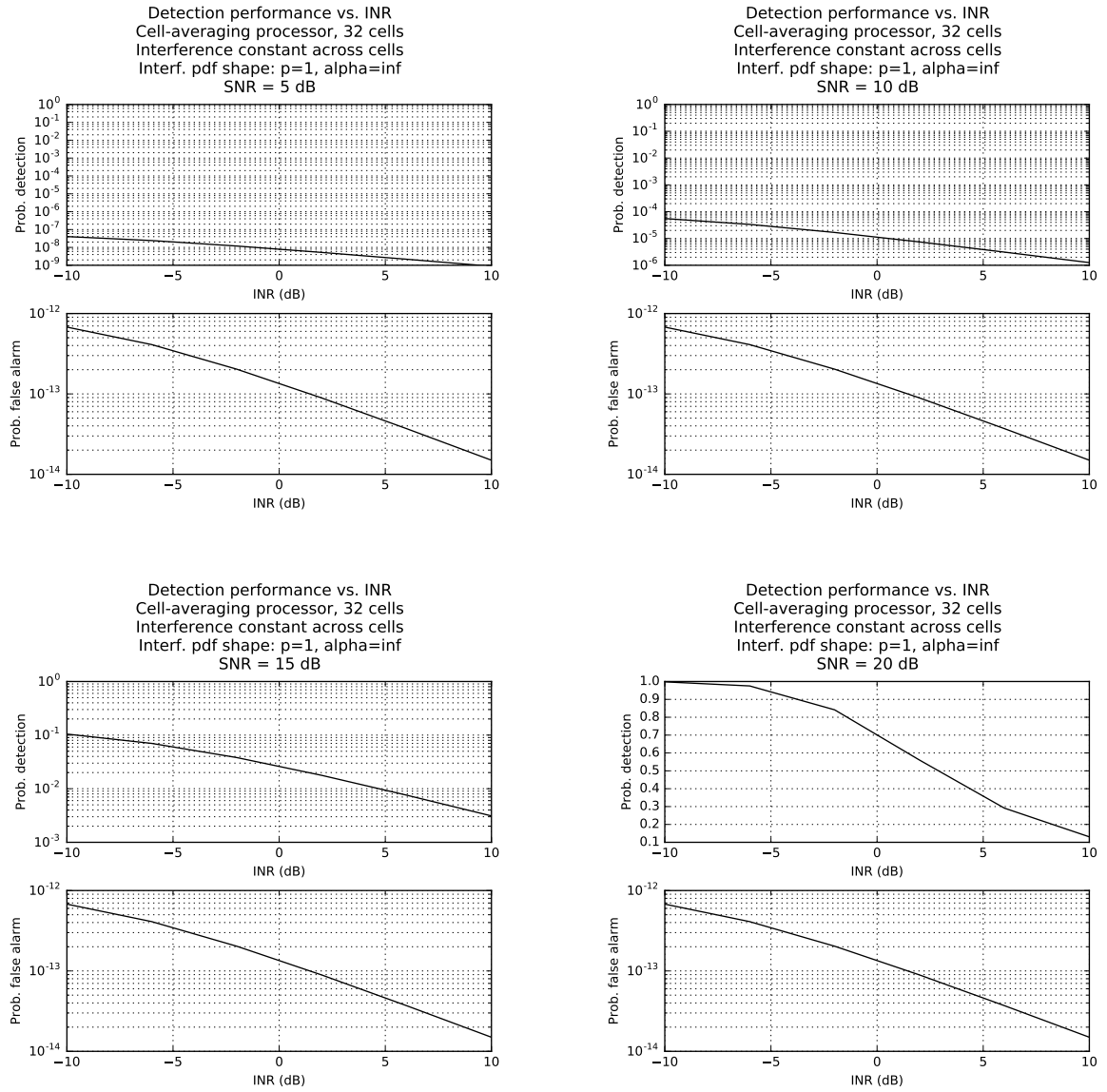


Figure C.33. P_D and P_{FA} versus INR for cell-averaging processor with “slow” interference (SNR = 5, 10, 15, 20 dB, baseline $P_{FA} = 10^{-12}$)

D. UNDERSTANDING THE ROC CROSSING CAUSED BY SLOW INTERFERENCE

As discussed in Section 2.4.1, slow, low-level interference occasionally can cause the ROC for non-Gaussian interference to cross under the ROC for Gaussian interference. This is illustrated in Figure 2.6.

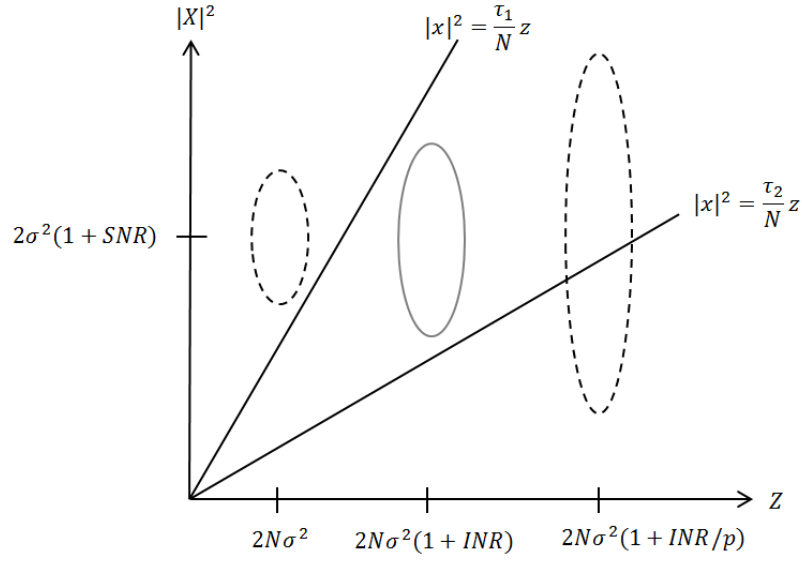


Figure D.1. Diagram explaining the crossing of the ROCs in Figure 2.6 for Gaussian versus impulsive interference, for the case of the cell-averaging processor with slow interference.

This crossing in the Gaussian and non-Gaussian ROCs for the cell-averaging processor with slow interference can be explained by examining the statistics of $|X|^2$ and Z . The conceptual diagram in Figure D.1 illustrates the statistical distribution of the random variables $|X|^2$ (the CUT) and Z (the total energy in the neighboring cells) under H_1 . The ellipses represent the approximate peaks in the two-dimensional pdf of $|X|^2$ and Z . Two cases are shown. (i) Dashed pdf: The dashed ellipses represent

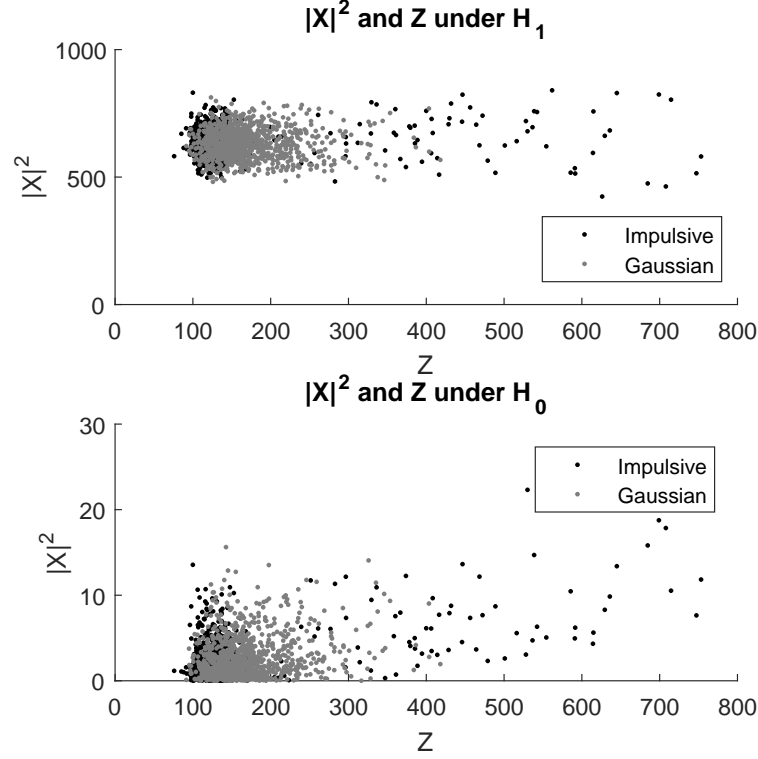


Figure D.2. The distributions under H_1 (top) and H_0 (bottom) of many i.i.d. samples of $|X|^2$ and Z for the cell-averaging processor with slow interference. The top figure corresponds to the qualitative description of Figure D.1.

the case of impulsive interference. With probability $(1 - p)$, all $N + 1$ cells see zero interference, so the $(|X|^2, Z)$ pairs cluster around the dashed ellipse on the left—they are to the left on the Z -axis because there is no interference to boost the threshold parameter Z , and they are close together on the $|X|^2$ -axis because the CUT experiences little destructive or constructive interference to the signal. Conversely, with probability p , all $N + 1$ cells see interference with strength INR/p , so the $(|X|^2, Z)$ pairs cluster around the dashed ellipse on the right—they are to the right on the Z -axis because strong interference boosts the threshold parameter Z , and they are spread out on the $|X|^2$ -axis because of the large range of destructive and constructive interference to the signal in the CUT. (ii) Solid pdf: The solid ellipse represents

the case of Gaussian interference with strength INR; here the $(|X|^2, Z)$ pairs form a cluster in between the two dashed ellipses, with a moderate boost to the threshold parameter Z , and moderate destructive and constructive interference to the signal in the CUT.

The probability of detection is the probability that $|X|^2 > (\tau/N)Z$. Geometrically, this is the volume under the two-dimensional pdf of $|X|^2$ and Z in the region where $|X|^2 > (\tau/N)Z$. The figure shows two different choices of threshold scalar τ , corresponding to two different choices of probability of false alarm. (i) Small probability of false alarm: τ_1 in the figure shows a large threshold scalar, corresponding to a lower false alarm probability. For this choice of threshold scalar, the dashed pdf has more volume above the line $|X|^2 = (\tau_1/N)Z$ than the solid pdf. This means that at lower false alarm probabilities, P_D for Gaussian interference will be less than P_D for the impulsive interference. (ii) Greater probability of false alarm: τ_2 in the figure shows a smaller choice of threshold scalar, resulting in a greater false alarm probability. For this choice of threshold scalar, the solid pdf has more volume above the line $|X|^2 = (\tau_2/N)Z$ than the dashed pdf. This means that at greater false alarm probabilities, P_D for Gaussian interference will exceed P_D for the impulsive interference.

Thus, because slow interference affects *all* cells simultaneously, it stretches the pdf of $|X|^2$ and Z along the Z -axis into an elongated trapezoid under H_1 , which stays centered based on the SNR along the $|X|^2$ -axis. The qualitative diagram of Figure D.1 is illustrated more concretely by the numerical simulation shown in Figure D.2.

E. DETAILED DERIVATION FROM THE DEVELOPMENT OF THE CYCLOSTATIONARY LMDC WHITENER

In Lemma 4, the computation of the autocorrelation $R_{WW}(t_1, t_2)$ proceeds by the following steps, where all integrals are over the real line:

$$\begin{aligned}
& R_{WW}(t_1, t_2) - \mathcal{E}_N \delta(t_2 - t_1) \\
&= \int \int h_c(t_1, \alpha) h_c(t_2, \beta) R_{YY}(\alpha, \beta) d\alpha d\beta - \mathcal{E}_N \delta(t_2 - t_1) \\
&= \int \int \left[\delta(\alpha - t_1) + \sum_{m,n,p,q} c_{m,n,p,q} g(t_1 - pT - t_{d,m}) g(\alpha - qT - t_{d,n}) \right] \\
&\quad \cdot \left[\delta(\beta - t_2) + \sum_{m',n',p',q'} c_{m',n',p',q'} g(t_2 - p'T - t_{d,m'}) g(\beta - q'T - t_{d,n'}) \right] \\
&\quad \cdot \left[\mathcal{E}_N \delta(\beta - \alpha) + \sum_{r,s} \mathcal{E}_{I,r} g(\alpha - sT - t_{d,r}) g(\beta - sT - t_{d,r}) \right] d\alpha d\beta \\
&\quad - \mathcal{E}_N \delta(t_2 - t_1) \\
&= \sum_{r,s} \mathcal{E}_{I,r} g(t_1 - sT - t_{d,r}) g(t_2 - sT - t_{d,r}) \\
&\quad + \mathcal{E}_N \sum_{m',n',p',q'} c_{m',n',p',q'} g(t_2 - p'T - t_{d,m'}) g(t_1 - q'T - t_{d,n'}) \\
&\quad + \sum_{r,m',s,p'} \left(\sum_{n',q'} \mathcal{E}_{I,r} c_{m',n',p',q'} \langle g, S_{(q'-s)T + \Delta_{n',r}} g \rangle \right) \\
&\quad \cdot g(t_1 - sT - t_{d,r}) g(t_2 - p'T - t_{d,m'}) \\
&\quad + \mathcal{E}_N \sum_{m,n,p,q} c_{m,n,p,q} g(t_1 - pT - t_{d,m}) g(t_2 - qT - t_{d,n}) \\
&\quad + \sum_{m,r,p,s} \left(\sum_{n,q} \mathcal{E}_{I,r} c_{m,n,p,q} \langle g, S_{(s-q)T + \Delta_{rn}} g \rangle \right) \\
&\quad \cdot g(t_1 - pT - t_{d,m}) g(t_2 - sT - t_{d,r})
\end{aligned}$$

$$\begin{aligned}
& + \mathcal{E}_N \sum_{m,m',p,p'} \left(\sum_{n,n',q,q'} c_{m,n,p,q} c_{m',n',p',q'} \langle g, S_{(q'-q)T+\Delta_{n'n}} g \rangle \right) \\
& \quad \cdot g(t_1 - pT - t_{d,m}) g(t_2 - p'T - t_{d,m'}) \\
& + \sum_{m,m',p,p'} \sum_{r,n',s,q'} \left(\sum_{n,q} \mathcal{E}_{I,r} c_{m,n,p,q} \langle g, S_{(s-q)T+\Delta_{rn}} g \rangle \right) c_{m',n',p',q'} \\
& \quad \cdot \langle g, S_{(q'-s)T+\Delta_{n'r}} g \rangle g(t_1 - pT - t_{d,m}) g(t_2 - p'T - t_{d,m'}) \\
= & \sum_{i,j,k,\ell} \mathcal{E}_{I,j} \delta_{ij} \delta_{k\ell} g(t_1 - kT - t_{d,i}) g(t_2 - \ell T - t_{d,j}) \\
& + \mathcal{E}_N \sum_{i,j,k,\ell} c_{j,i,\ell,k} g(t_1 - kT - t_{d,i}) g(t_2 - \ell T - t_{d,j}) \\
& + \sum_{i,j,k,\ell} \left(\sum_{n',q'} \mathcal{E}_{I,i} c_{j,n',\ell,q'} \langle g, S_{(q'-k)T+\Delta_{n'i}} g \rangle \right) \\
& \quad \cdot g(t_1 - kT - t_{d,i}) g(t_2 - \ell T - t_{d,j}) \\
& + \mathcal{E}_N \sum_{i,j,k,\ell} c_{i,j,k,\ell} g(t_1 - kT - t_{d,i}) g(t_2 - \ell T - t_{d,j}) \\
& + \sum_{i,j,k,\ell} \left(\sum_{n,q} \mathcal{E}_{I,j} c_{i,n,k,q} \langle g, S_{(\ell-q)T+\Delta_{jn}} g \rangle \right) \\
& \quad \cdot g(t_1 - kT - t_{d,i}) g(t_2 - \ell T - t_{d,j}) \\
& + \mathcal{E}_N \sum_{i,j,k,\ell} \left(\sum_{n,n',q,q'} c_{i,n,k,q} c_{j,n',\ell,q'} \langle g, S_{(q'-q)T+\Delta_{n'n}} g \rangle \right) \\
& \quad \cdot g(t_1 - kT - t_{d,i}) g(t_2 - \ell T - t_{d,j}) \\
& + \sum_{i,j,k,\ell} \left(\sum_{n,n',q,q',r,s} \mathcal{E}_{I,r} c_{i,n,k,q} c_{j,n',\ell,q'} \langle g, S_{(s-q)T+\Delta_{rn}} g \rangle \langle g, S_{(q'-s)T+\Delta_{n'r}} g \rangle \right) \\
& \quad \cdot g(t_1 - kT - t_{d,i}) g(t_2 - \ell T - t_{d,j}).
\end{aligned}$$

F. PROOF ON POSITIVE SEMIDEFINITENESS

The following lemma on positive semidefiniteness is used in Theorem 7.

Lemma 5 *The matrix $\tilde{\mathbf{G}}(f)$ appearing in Theorem 7 is positive semidefinite for every $f \in [-1/2, 1/2]$.*

Proof First, we define the continuous-time function

$$\gamma(\tau) = \langle g, S_\tau g \rangle = \int_{-\infty}^{\infty} g(t)g(t - \tau) dt. \quad (\text{F.1})$$

This is simply the convolution of the pulse shape $g(t)$ with a time-reversed version of itself.

Second, we write the continuous-time Fourier transform $\tilde{\Gamma}(f)$ of $\gamma(\tau)$ as

$$\tilde{\Gamma}(f) = \int_{-\infty}^{\infty} \gamma(\tau) e^{-i2\pi f\tau} d\tau = |\tilde{G}(f)|^2, \quad (\text{F.2})$$

where $\tilde{G}(f)$ is the Fourier transform of $g(t)$.

Third, we note that the entries of $\mathbf{G}[n]$ are discrete-time samples taken from the continuous-time function $\gamma(\tau)$, and so using sampling theory we write, from (3.54) and (3.56),

$$\begin{aligned} \tilde{\mathbf{G}}_{m,n}(\nu) &= \sum_{p=-\infty}^{\infty} \gamma(pT + \Delta_{mn}) e^{-i2\pi\nu p} \\ &= \frac{1}{T} \sum_{k=-\infty}^{\infty} \tilde{\Gamma}\left(\frac{\nu - k}{T}\right) e^{i2\pi(\nu - k)\Delta_{mn}/T} \\ &= \frac{1}{T} \sum_{k=-\infty}^{\infty} \left| \tilde{G}\left(\frac{\nu - k}{T}\right) \right|^2 e^{i2\pi(\nu - k)\Delta_{mn}/T}, \end{aligned} \quad (\text{F.3})$$

where we have used (F.2) in the last step.

Fourth, given $\nu \in [-1/2, 1/2]$, we define the continuous-time-continuous-frequency functions

$$\psi_\nu(t, f) = \frac{1}{\sqrt{T}} \sum_{k=-\infty}^{\infty} \tilde{G}\left(\frac{\nu - k}{T}\right) e^{i2\pi(\nu - k)t/T} e^{i2\pi kf}. \quad (\text{F.4})$$

Finally, we complete the proof as follows. For any $c_m, c_n \in \mathbb{C}$ and $\nu \in [-1/2, 1/2)$, we have

$$\begin{aligned}
& \sum_{m=1}^N \sum_{n=1}^N c_m c_n^* \tilde{\mathbf{G}}_{m,n}(\nu) \\
&= \frac{1}{T} \sum_{m,n} c_m c_n^* \sum_{k=-\infty}^{\infty} \left| \tilde{G}\left(\frac{\nu-k}{T}\right) \right|^2 e^{i2\pi(\nu-k)\Delta_{m,n}/T} \\
&= \frac{1}{T} \sum_{m,n,k} c_m c_n^* \sum_{\ell=-\infty}^{\infty} \delta_{k\ell} \tilde{G}\left(\frac{\nu-k}{T}\right) e^{i2\pi(\nu-k)t_{d,m}/T} \\
&\quad \cdot \tilde{G}^*\left(\frac{\nu-\ell}{T}\right) e^{-i2\pi(\nu-\ell)t_{d,n}/T} \\
&= \frac{1}{T} \sum_{m,n,k,\ell} c_m c_n^* \int_{-1/2}^{1/2} e^{i2\pi kf} \tilde{G}\left(\frac{\nu-k}{T}\right) e^{i2\pi(\nu-k)t_{d,m}/T} \\
&\quad \cdot e^{-i2\pi \ell f} \tilde{G}^*\left(\frac{\nu-\ell}{T}\right) e^{-i2\pi(\nu-\ell)t_{d,n}/T} df \\
&= \sum_{m,n} c_m c_n^* \int_{-1/2}^{1/2} \psi_\nu(t_{d,m}, f) \psi_\nu^*(t_{d,n}, f) df \\
&= \int_{-1/2}^{1/2} \left| \sum_{n=1}^N c_n \psi_\nu(t_{d,n}, f) \right|^2 df \\
&\geq 0,
\end{aligned}$$

where the first step follows from (F.3), and the fourth step follows from (F.4). ■

Note that $\tilde{\mathbf{G}}(f)$ is singular at some $f = \nu \in [-1/2, 1/2)$ if and only if there exists some set of nonzero coefficients $\{c_n\}_{n=1}^N$ such that

$$0 = \sum_{n=1}^N c_n \psi_\nu(t_{d,n}, f) \quad (\text{F.5})$$

for all $f \in [-1/2, 1/2)$. This is the case, for example, for $\tilde{\mathbf{G}}(0)$ when $N = 2$ and $g(t)$ is a sinc-wave pulse shape having spectrum

$$\tilde{G}(f) = \sqrt{T} 1_{[-1/2T, 1/2T]}(f). \quad (\text{F.6})$$

To see this, simply set $c_1 = -c_2 = 1$ in (F.5). This possibility of singular $\tilde{\mathbf{G}}(f)$ motivates the use of a generalized inverse in the cyclostationary whitener, *cf.* (3.62)–(3.69).

G. MONTE CARLO VALIDATION OF WHITENERS

Our deflection results presented in Figures 3.3–3.4 assume valid whitening filters $h_s(t_1, t_2)$ and $h_c(t_1, t_2)$. In order to validate our computer code for these two filters, this appendix presents statistical methods we use to check our results.

Simulation setup

First, given L' i.i.d. realizations of the LMDC parameters $\{\{\mathcal{E}_{I,n,\ell}\}_{n=1}^{N(\ell)}, \{t_{d,n,\ell}\}_{n=1}^{N(\ell)}\}_{\ell=1}^{L'}$, we generate random interference and noise using the following steps. We sample all continuous-time signals at sampling rate F_s .

To generate the ℓ -th random LMDC interference $I_\ell(t)$, we simulate $N(\ell)$ independent LMDC signals as

$$I_{n,\ell}(t) = \sum_{m=0}^M I_{n,\ell}[m]g(t - mT - t_{d,n,\ell}), \quad (\text{G.1})$$

for each $n = 1, \dots, N(\ell)$, where $\{I_{n,\ell}[m]\}_{m=0}^M$ are i.i.d. circular Gaussian random variables with mean zero and mean-square $\mathcal{E}_{I,n,\ell}$. Then, we sum the $N(\ell)$ users' signals to get the composite interference

$$I_\ell(t) = \sum_{n=1}^{N(\ell)} I_{n,\ell}(t). \quad (\text{G.2})$$

To generate the ℓ -th random C-AWGN $N_\ell(t)$, we generate i.i.d. circular Gaussian random variables with mean zero and mean-square $\mathcal{E}_N F_s$, where F_s is the sample rate.

Next, for each $\ell = 1, \dots, L'$, we independently simulate LMDC interference $I_\ell(t)$ and C-AWGN $N_\ell(t)$ as above, sum the interference and noise, and pass the sum through the whitening filters $h_{s,\ell}(t_1, t_2)$ and $h_{c,\ell}(t_1, t_2)$ computed using the parameters $\{\mathcal{E}_{I,n,\ell}\}_{n=1}^{N(\ell)}$ and $\{t_{d,n,\ell}\}_{n=1}^{N(\ell)}$. The output of these filters, then, is

$$W_{s,\ell}(t) = \int_{-\infty}^{\infty} h_{s,\ell}(t, \tau) (I_\ell(\tau) + N_\ell(\tau)) d\tau, \quad (\text{G.3})$$

and similarly for $W_{c,\ell}(t)$. Then we examine the whitened signals $\{W_{s,\ell}(t)\}_{\ell=1}^{L'}$ and $\{W_{c,\ell}(t)\}_{\ell=1}^{L'}$ and test for whiteness using the following two statistical methods.

Statistical test 1: Autocorrelation test

The first test for whiteness is based on [96]. For each $W_{s,\ell}(t)$ (or $W_{c,\ell}(t)$), we form a statistic $Q_{s,\ell}$ ($Q_{c,\ell}$) given by

$$W'_{s,\ell}(t) = \text{Re}\{W_{s,\ell}(t)\} + \text{Im}\{W_{s,\ell}(t)\}, \quad (\text{G.4})$$

$$r_{s,k} = \frac{\sum_{t=k+1}^{n'} W'_{s,\ell}(t/F_s) W'_{s,\ell}((t-k)/F_s)}{\sum_{t=1}^{n'} W'^2_{s,\ell}(t/F_s)}, \quad (\text{G.5})$$

$$Q_{s,\ell} = n'(n' + 2) \sum_{k=1}^{m'} (n' - k)^{-1} r_{s,k}^2, \quad (\text{G.6})$$

where n' is the discrete-time length of the signal, and m' is the number of lags used in the estimate. Provided that $m' \ll n'$, the statistics $\{Q_{s,\ell}\}_{\ell=1}^{L'}$ ($\{Q_{c,\ell}\}_{\ell=1}^{L'}$) should follow a $\chi^2_{m'}$ distribution [96]. Therefore, we form a one-sided p-value $p_{s,\ell}$ ($p_{c,\ell}$)

$$p_{s,\ell} = 1 - F_{\chi^2_{m'}}(Q_{s,\ell}), \quad (\text{G.7})$$

for each $\ell = 1, \dots, L'$, where $F_{\chi^2_{m'}}(\cdot)$ is the cdf of a $\chi^2_{m'}$ random variable. Then we use a Kolmogorov-Smirnov test to see if the sequence $\{p_{s,\ell}\}_{\ell=1}^{L'}$ ($\{p_{c,\ell}\}_{\ell=1}^{L'}$) is consistent with a Uniform[0, 1] distribution.

Statistical test 2: Periodogram test

Sometimes whiteness, or lack thereof, is more visible in the frequency domain than in the time domain. Thus, in order to complement our time-domain autocorrelation analysis, we also test for whiteness using the following *ad hoc* method based

on the frequency-domain periodogram. For each $W_{s,\ell}(t)$ (or $W_{c,\ell}(t)$), we compute the frequency-smoothed periodogram $P_{s,\ell}[k]$ ($P_{c,\ell}[k]$):

$$\tilde{P}_{s,\ell}[k] = \frac{1}{n'F_s} \left| \sum_{t=1}^{n'} W_{s,\ell}(t/F_s) e^{-i2\pi k(t-1)/n'} \right|^2, \quad (\text{G.8})$$

$$P_{s,\ell}[k] = (\tilde{P}_{s,\ell} \circledast w)[k], \quad (\text{G.9})$$

where \circledast denotes circular convolution, and $w[k]$ is a suitably chosen unit-area frequency window. Then we compute the maximum deviation measure $\nu_{s,\ell}$ ($\nu_{c,\ell}$):

$$\bar{P}_{s,\ell} = \frac{1}{n'} \sum_{k=1}^{n'} P_{s,\ell}[k], \quad (\text{G.10})$$

$$\nu_{s,\ell} = \left[\max_{k=1,\dots,n'} |P_{s,\ell}[k] - \bar{P}_{s,\ell}| \right]^{-1}, \quad (\text{G.11})$$

for each $\ell = 1, \dots, L'$. Since the exact distribution of the $\{\nu_{s,\ell}\}_{\ell=1}^{L'}$ ($\{\nu_{c,\ell}\}_{\ell=1}^{L'}$) is not known, we generate a reference set $\{\nu_{\text{ref},\ell}\}_{\ell=1}^{L''}$ from truly white noise processes $\{W_{\text{ref},\ell}(t)\}_{\ell=1}^{L''}$ having PSD \mathcal{E}_N , sample rate F_s , and discrete-time length n' , and we use a two-sample Kolmogorov-Smirnov test to see if the sequences $\{\nu_{s,\ell}\}_{\ell=1}^{L'}$ (or $\{\nu_{c,\ell}\}_{\ell=1}^{L'}$) and $\{\nu_{\text{ref},\ell}\}_{\ell=1}^{L''}$ are consistent with the same underlying distribution.

Results

In plotting each sub-plot of Figures 3.3–3.4, we use $L = 100$ i.i.d. sample functions of LMDC interference plus C-AWGN. In order to save computation time, within each subplot these $L = 100$ i.i.d. sample functions are recycled across the eight points plotted, corresponding to stationary and cyclostationary whitening, and INRs of 0, 10, 20, and 30 dB. Due to this time-saving signal recycling, statistical tests for whiteness are not independent across the eight cases for which signals are recycled. Independence notwithstanding, the statistical whiteness Tests 1 and 2 both pass at a significance level of 0.05 for all eight cases and for both Figure 3.3 and Figure 3.4. For Figure 3.3, Test 1 uses parameters $L' = 600$ ($L = 100$ i.i.d. trials per subplot, times 6 subplots), $n' = 102\,400$, and $m' = 2\,048$, while Test 2 uses the same values

of L' and n' with $L'' = 10^3$. For Figure 3.4, the test parameters are the same, except for $n' = 51\,200$, due to the shortening of the signals relative to Figure 3.3.

Figure G.1 shows the whiteness measures $\{p_{s,\ell}\}_{\ell=1}^{L'}$ and $\{p_{c,\ell}\}_{\ell=1}^{L'}$ (Sub-Figure (a)) and $\{\nu_{s,\ell}\}_{\ell=1}^{L'}$ and $\{\nu_{c,\ell}\}_{\ell=1}^{L'}$ (Sub-Figure (b)) for INRs of 0, 10, 20, and 30 dB for the $L' = 600$ trials used to compute Figure 3.3. Figure G.2 shows the corresponding whiteness measures for the $L' = 600$ trials used to compute Figure 3.4. Note the good visual agreement between the chi-squared whiteness p-values $\{p_{s,\ell}\}_{\ell=1}^{L'}$ and $\{p_{c,\ell}\}_{\ell=1}^{L'}$ with a Uniform[0, 1] distribution, and the good agreement between the periodogram whiteness measures $\{\nu_{s,\ell}\}_{\ell=1}^{L'}$ and $\{\nu_{c,\ell}\}_{\ell=1}^{L'}$ with the reference set $\{\nu_{\text{ref},\ell}\}_{\ell=1}^{L''}$, whose empirical cdf is shown as a thin dashed line.¹

¹We also have used some *ad hoc* statistical tests based on order statistics to check the distribution of the chi-squared whiteness p-values $\{p_{s,\ell}\}_{\ell=1}^{L'}$ and $\{p_{c,\ell}\}_{\ell=1}^{L'}$. Although these tests are not independent of each other nor of the other tests presented above, the results may suggest a lack of perfect whiteness in the whitener outputs $\{W_{s,\ell}(t)\}_{\ell=1}^{L'}$ and $\{W_{c,\ell}(t)\}_{\ell=1}^{L'}$. However, as shown in the results of Tests 1–2 and Figures G.1–G.2, these whitener outputs are close enough to white that our estimates of \hat{d}_s and \hat{d}_c remain valid.

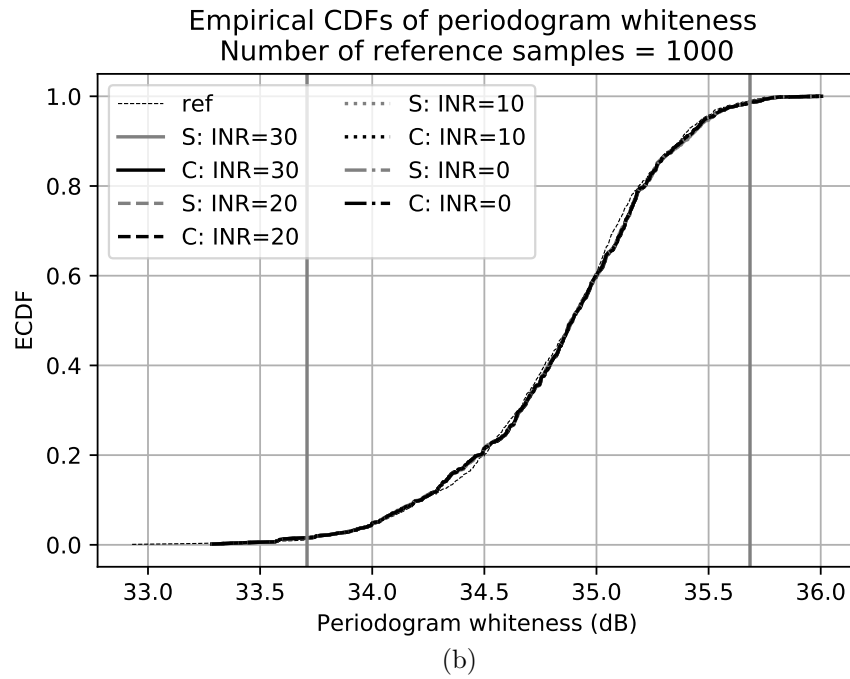
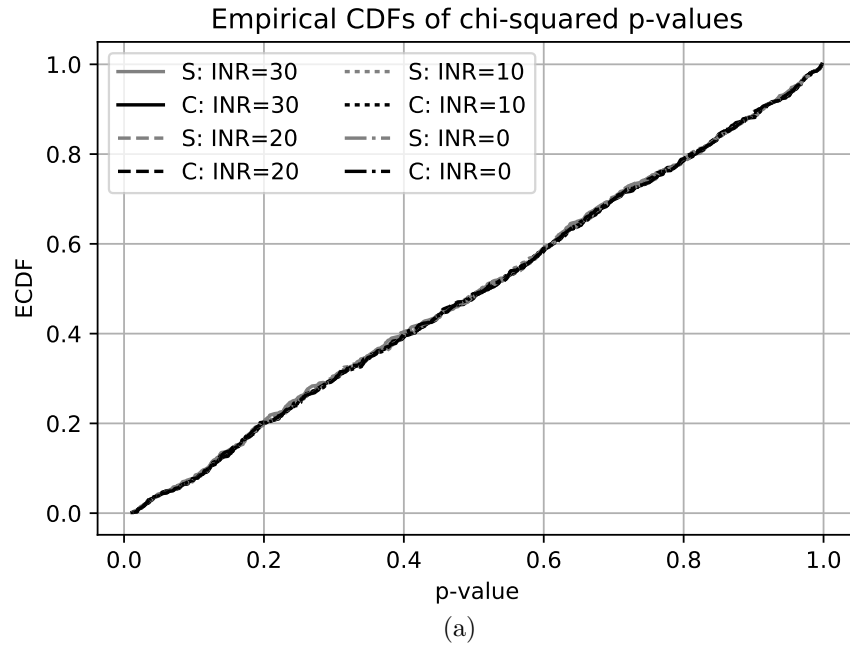


Figure G.1. Empirical cumulative distribution functions (CDFs) of whiteness measures for Figure 3.3. (a) $\{p_{s,\ell}\}_{\ell=1}^{L'}$ and $\{p_{c,\ell}\}_{\ell=1}^{L'}$ for INRs of 0, 10, 20, and 30 dB. (b) $\{\nu_{s,\ell}\}_{\ell=1}^{L'}$ and $\{\nu_{c,\ell}\}_{\ell=1}^{L'}$ for INRs of 0, 10, 20, and 30 dB, along with the reference set $\{\nu_{\text{ref},\ell}\}_{\ell=1}^{L''}$.

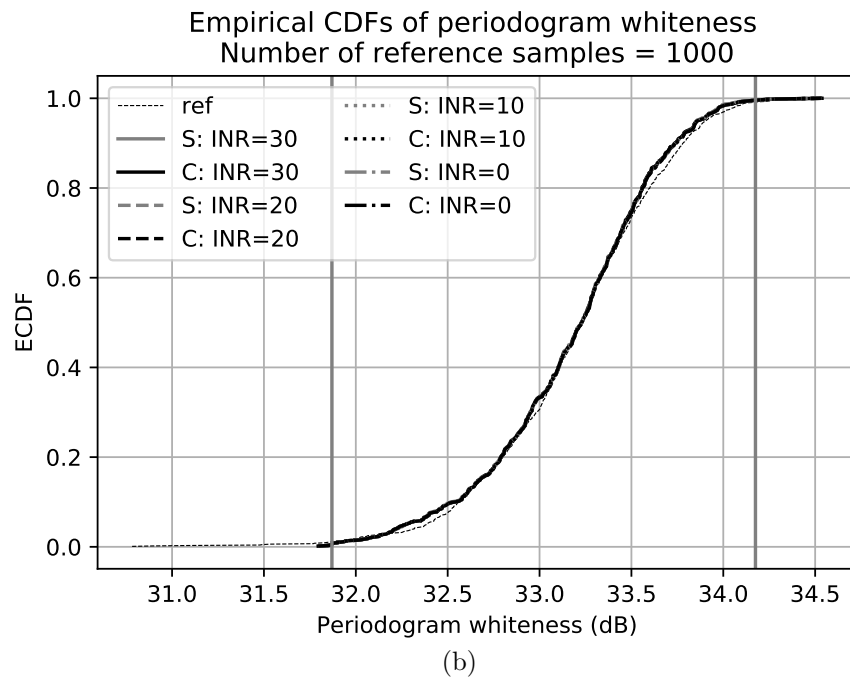
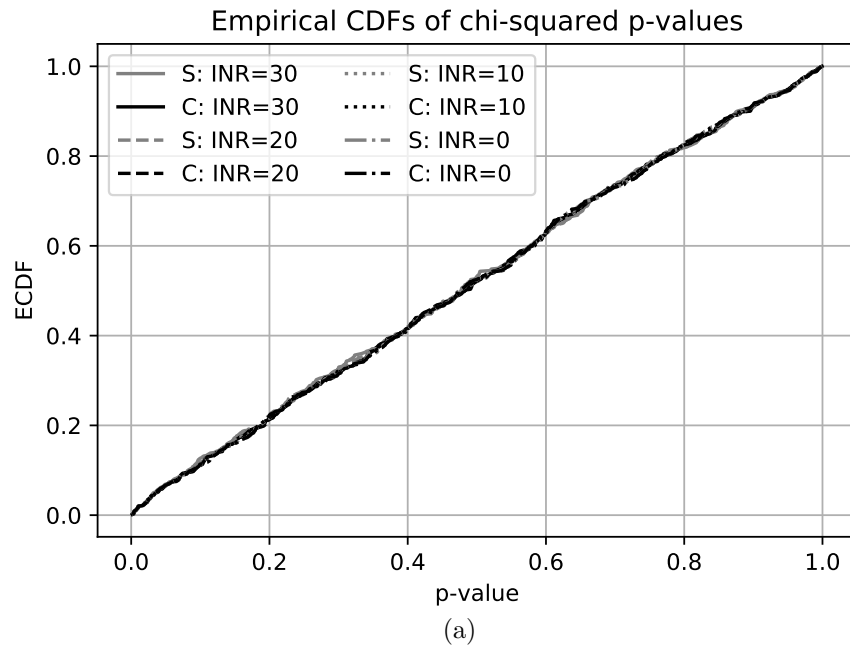


Figure G.2. Empirical cumulative distribution functions (CDFs) of whiteness measures for Figure 3.4. (a) $\{p_{s,\ell}\}_{\ell=1}^{L'}$ and $\{p_{c,\ell}\}_{\ell=1}^{L'}$ for INRs of 0, 10, 20, and 30 dB. (b) $\{\nu_{s,\ell}\}_{\ell=1}^{L'}$ and $\{\nu_{c,\ell}\}_{\ell=1}^{L'}$ for INRs of 0, 10, 20, and 30 dB, along with the reference set $\{\nu_{\text{ref},\ell}\}_{\ell=1}^{L''}$.

VITA

VITA

David P. Zilz was born the eldest of four siblings to Paul and Peggy Zilz in 1987. He graduated from Taylor University (Upland, Indiana) with the B.S. degree in engineering physics in 2011. During his undergraduate education, he held internships at the Center for Integrated Nanotechnologies (Albuquerque, New Mexico) and the National Institute of Standards and Technology (Boulder, Colorado). While pursuing his Ph.D. at Purdue University (West Lafayette, Indiana), he has held internships in cybersecurity, as well as at the RAND Corporation (Santa Monica, California) and the Air Force Research Laboratory (Wright-Patterson Air Force Base, Ohio). He also has received multiple awards for his teaching at Purdue.